Structural studies on iron-based exhaust gas catalysts by means of X-ray absorption spectroscopy

Zur Erlangung des akademischen Grades eines

DOKTORS DER NATURWISSENSCHAFTEN

(Dr. rer. nat.)

Fakultät für Chemie und Biowissenschaften

Karlsruher Institut für Technologie (KIT) - Universitätsbereich

genehmigte

DISSERTATION

von

M.Sc. Alexey Boubnov

aus

Moskau

Dekan: Prof. Dr. Peter Roesky

Referent: Prof. Dr. Jan-Dierk Grunwaldt

Korreferent: Prof. Dr. Clemens Heske

Tag der mündlichen Prüfung: 20. Oktober 2014

Dieses Werk ist lizenziert unter einer Creative Commons Namensnennung –
Weitergabe unter gleichen Bedingungen 3.0 Deutschland Lizenz
(CC BY-SA 3.0 DE): http://creativecommons.org/licenses/by-sa/3.0/de/

Foreword

I would like to thank Professor Dr. Jan-Dierk Grunwaldt for giving me the opportunity to do a Ph.D. study on *in situ* X-ray absorption spectroscopy (XAS) in his group at KIT. This work was additionally supervised by Dr. Stefan Mangold and Dr. Henning Lichtenberg, partly by Dr. Maria Casapu and Dr. Gian Luca Chiarello, and especially in the beginning by Prof. Dr. Matthias Bauer and Prof. Dr. Sven Kureti. I thank Professor Dr. Clemens Heske for assessing this work as a co-referee.

Much valuable experience and knowledge was shared with me in discussions with Andreas Pacher and Marina Tepluchin during our common projects. Thanks to Sabrina Conrad and Andreas Gänzler, whom I have partly supervised on their diploma projects, producing exciting results. I would like to thank the whole group for creating a pleasant working atmosphere.

A large part of my experimental work was done during beam times at synchrotron radiation facilities in collaboration with other Ph.D. students and post-doctoral fellows, from KIT and other Universities, applying XAS in their projects. These many campaigns will remain in my memory as times of interesting science as well as times where I grew intellectually and socially. This would have not been possible without the many weeks spent with Drs. Martin Høj, Jakob Munkholt Christensen, Jan Stötzel, Nikolai Musko, Matthias Beier, Qiongxiao Wu, Kirsten Schuh, Loubna Gharnati, the EXAFS-team - Drs. Dmitry Doronkin and Hudson Carvalho, and many others.

I would like to thank people from other departments at KIT for helping me with parts of my work: Dr. Valeriu Mereacre for recording and interpreting the Mössbauer spectra, Drs. Christoph Jacob, Matthew Kundrat and Andrew Atkins for tirelessly carrying out DFT calculations to support two of the presented works. Thanks to Dr. Boris Reznik for discussions on TEM and XRD data interpretation. Essential for several studies were mineral reference samples, which were kindly provided by Dr. Farahnaz Daliran and Dr. Kirsten Drüppel (KIT) as well as by Dr. N. E. Nikol'skaya and Dr. T. A. Burova (FGUP "VIMS", Russia) and V. I. Yashina (MGRI-RSGPU, Russia).

In connection to the many setups and instruments developed for the *in situ* measurements, I would like to thank Alexander Jaks with his team at the mechanical workshop, as well as technicians Kevin Utermann, Jan Pesek, Hans Herberger and Jörg Finsterle for help and inspiration from the design to the commissioning of micro-reactors and gas dosing systems.

Special thanks to the beamline scientists Dr. Maarten Nachtegaal (SLS), Dr. Stephen Doyle (ANKA), Dr. Adam Webb and Dr. Michael Murphy (HASYLAB), Dr. Herman Emerich, Dr. Wouter van Beek, Dr. Pieter Glatzel and Dr. Erik Gallo (ESRF) and many others along with technical staff for their invaluable support, interesting discussions and unforgettable beam times. The synchrotron radiation sources ANKA, SLS, HASYLAB and ESRF are acknowledged for providing beamtime. Funding of this project by KIT and the German Federal Ministry of Education and Research (BMBF, projects "MatAkt" and "ZeitKatMat") is gratefully acknowledged.

Finally I thank my parents, my wife and daughters for constantly supporting and motivating me during my Ph.D. study.

Abstract

In this thesis, several steps toward a better understanding of Fe-based catalysts in automotive exhaust gas after-treatment are outlined. These materials can potentially replace noble metals and improve zeolite materials. A strong focus is laid on iron oxide supported on γ-Al_2O_3 which is studied with respect to the location and structure of its Fe-sites, as well as its redox-behaviour for potential applications in e.g. the removal of NO_x by selective catalytic reduction with ammonia (NH_3-SCR) and catalytic CO oxidation. As an extension of these studies, also a deeper insight into the reaction mechanism of NH_3-SCR over the well-known Fe/ZSM-5 catalyst is obtained by novel characterisation techniques.

As part of this work, a dedicated experimentation platform has been established at the synchrotron light source ANKA (Karlsruhe, Germany), which allows to combine *in situ* X-ray absorption spectroscopy and catalytic studies in one experiment. Being a further development of existing concepts at other synchrotrons, this concept supports the acceleration of catalyst research, as the sample environment is provided on-site and therefore attracts user groups which are not specialised in these techniques to add *in situ* XAS to their research.

If spectroscopic data is acquired of the working catalyst, extraction of structural information on the iron-based catalysts from the acquired spectra remains a challenge. Therefore, different analysis tools for elaborate quantitative and qualitative analysis of extended X-ray absorption fine structure (EXAFS) and X-ray absorption near-edge structure (XANES) spectra were tested.

To assess the structure of Fe sites in Fe/Al_2O_3 by EXAFS, models describing the atomic neighbourhood are required. Due to the limited knowledge of the structure and the many different ways one can imagine the structure, a systematic selection of all possible structures was carried out to find the best one. A large number of molecular models of Fe sites on/in γ-Al_2O_3 matrices were built, partly with the geometry optimised using density-functional theory (DFT), and the simulated EXAFS spectra of these models were tested in a preliminary selection against the measured EXAFS spectra of the catalysts. This selection validated the models where the Fe atoms were located at octahedral sites of the support and eliminated those at tetrahedral sites. An EXAFS refinement of the best few models has shown that mixtures of highly dispersed FeO_4 and FeO_5 moieties, partially as clusters of several Fe atoms, are the dominating species in these materials.

The lower signal-to-noise ratio in absorption spectra measured during a catalytic reaction complicates the extraction of structural information from the EXAFS region. Alternatively, the oxidation state and first-shell coordination number of Fe species can be obtained using the pre-edge feature. This information becomes especially useful during a catalytic reaction, when a combination of XANES and EXAFS for probing this information is limited by insufficient data quality. A variogram-based analysis of the pre-edge region based on spectra of reference compounds has been proven in this work to reveal this structural information, circumventing problems of low data quality and resolution where the electronic transitions cannot be identified. As an example, it was shown that during a temperature-programmed reduction (TPR) of Fe/Al_2O_3, the FeO_x moieties are reduced from Fe^{3+} to Fe^{2+}, retaining a Fe-O coordination number of ca. 5.

On the other hand, this pre-edge analysis method was very valuable in the analysis of combined high-energy-resolution fluorescence-detected (HERFD)-XANES and valence-to-core X-ray emission spectroscopy (V2C-XES). A thorough analysis of the oxidation state and local coordination of the Fe species in a Fe/ZSM-5 catalyst under NH_3-SCR reaction conditions has assisted in elucidating the structure of the Fe species including interpretation of the V2C-XES spectra. The results further allowed understanding the structure of intermediate species and therefore also the reaction mechanism.

In summary, this work shows that X-ray absorption spectroscopy significantly contributes to the structural understanding of catalysts. Along with the complex apparatus for detecting physical and chemical phenomena during a catalytic reaction with high accuracy and reproducibility, careful application of data analysis tools allows contributing to a better understanding of catalysts.

Kurzfassung

Ziel dieser Arbeit war es, zu einem tieferen Verständnis der Wirkungsweise eisenbasierter Katalysatoren als mögliche Alternative zu herkömmlichen Edelmetall- und Zeolith-basierten Systemen in der Abgasnachbehandlung zu gelangen. Dabei wurden Eisenoxidpartikel auf γ-Al_2O_3 als Trägermaterial bzgl. der Lage und Struktur der Fe-Spezies sowie ihres Redox-Verhaltens untersucht. Dies spielt eine wichtige Rolle im Hinblick auf potentielle Anwendungen, z.B. bei der Reduktion von Stickoxiden (NO_x) durch selektive katalytische Reduktion mit Ammoniak (NH_3-SCR) und bei der katalytischen Oxidation von Kohlenmonoxid (CO). Erweitert wurden diese Studien durch die Untersuchung des Reaktionsmechanismus der selektiven katalytischen Reduktion von NO mittels NH_3 an dem bekannten Fe/ZSM-5 Katalysatorsystem mittels neuartiger Synchrotron-basierter Charakterisierungsmethoden.

Im Rahmen dieser Arbeit wurde eine Experimentierplattform für katalytische Studien mittels *in situ*-Röntgenabsorptionsspektroskopie an der ANKA-Synchrotronstrahlungsquelle (Karlsruher Institut für Technologie) aufgebaut. Als eine Weiterentwicklung bestehender Konzepte an anderen Synchrotronstrahlungsquellen ist diese Plattform Teil einer speziellen Infrastruktur für Katalyseforschung, die Nutzergruppen verschiedene Apparaturen für spezielle Probenumgebungen für *in situ* Röntgenabsortionsspektroskopie zur Verfügung stellt und daher diese Methoden auch Nutzergruppen aus der Katalyse ohne oder mit wenig Synchrotronsstrahlungserfahrung zugänglich macht.

Die Gewinnung von Strukturinformationen aus den gemessenen Absorptionsspektren an Eisenkatalysatoren erwies sich als überaus anspruchsvoll. Daher wurden unterschiedliche Methoden zur quantitativen und qualitativen Auswertung der Daten, sowohl im Vor- und Nahkantenbereich (*engl*. X-ray absorption near-edge structure, XANES) als auch im Bereich der kantenferneren Röntgenabsorptionsfeinstruktur (*engl.* extended X-ray absorption fine structure, EXAFS), auf ihre Effizienz untersucht.

Die Analyse der Struktur von Eisen-Clustern als katalytisch aktive Zentren mit EXAFS erfordert ein Modell der atomaren Umgebung der Absorberatome. Aufgrund der begrenzten Vorkenntnisse der Struktur und der Vielzahl möglicher Strukturen wurde eine systematische Auswahl aus allen denkbaren Möglichkeiten durchgeführt. Dazu wurde eine große Anzahl von Molekülmodellen für Eisenzentren auf/ in einer γ-Al_2O_3-Matrix erstellt, teilweise mit theoriegestützter (*engl.* density-functional theory, DFT) Geometrieoptimierung. Eine Auswahl

simulierter EXAFS-Spektren auf Basis dieser Modelle wurde mit den gemessenen EXAFS-Spektren des Katalysators verglichen. Insbesondere Modelle mit Eisenatomen an den Oktaederstellen des γ-Al_2O_3-Trägermaterials zeigten beste Überstimmung, während Modelle mit Eisenatomen an Tetraederstellen ausgeschlossen werden konnten. Eine EXAFS-Auswertung einer engeren Auswahl der am besten passenden Modelle zeigte, dass in diesen Katalysatoren eine Mischung aus FeO_4 und FeO_5 Spezies hochgradig dispergiert und teilweise als Gruppen aus mehreren Eisenatomen vorliegt.

Das niedrigere Signal-Rausch-Verhältnis in Absorptionsspektren, die während einer katalytischen Reaktion gemessen werden, erschwert die Gewinnung von Strukturinformationen aus dem EXAFS-Bereich. Alternativ können Oxidationszustände und Koordinationszahlen der FeO_x-Gruppen, die wichtig für die Untersuchung der Eisenzentren während einer katalytischen Reaktion sind, aus Vorkantenspektren gewonnen werden. Über eine Variogramm-Analyse der Vorkantenbereiche können einige Probleme, die auf geringe Datenqualität und Auflösung zurückzuführen sind und eine Identifizierung der beteiligten elektronischen Übergänge erheblich erschweren, umgangen werden. So konnte z.B. gezeigt werden, dass während einer Temperatur-programmierten Reduktion (TPR) die Fe^{3+}-Eisenzentren zu Fe^{2+} reduziert werden, während die lokale Koordinationszahl von etwa 5 erhalten wird.

Diese Vorkantenanalyse erwies sich zudem als sehr wertvoll bei der Auswertung von XANES-Spektren, die mittels HERFD (*engl.* high-energy-resolution fluorescence-detection) kombiniert mit Valenz-zu-Kern Röntgenemissionsspektroskopie (*engl.* valence-to-core X-ray emission spectroscopy, V2C-XES,) gemessen wurden. Eine gründliche Bestimmung der Oxidationsstufe und der lokalen Koordination der Eisenzentren in Fe/ZSM-5 Katalysatoren während SCR haben zur Beschreibung der Eisenzentren und der Interpretation der V2C-Spektren beigetragen. Weiterhin trugen die Resultate zu einem tieferen Verständnis des Reaktionsmechanismus bei.

Zusammenfassend zeigt die vorliegende Arbeit, dass die Röntgenabsorptionsspektroskopie eine Schlüsselrolle bei Untersuchungen zu Struktur und Mechanismus von Katalysatoren spielt. In Verbindung mit den speziellen *in situ*-spektroskopischen Apparaturen zur genauen und reproduzierbaren Charakterisierung der während katalytischer Reaktionen ablaufenden physikalischen und chemischen Prozesse leisten die hier beschriebenen Methoden zur Auswertung der Absorptionsdaten einen wichtigen Beitrag zu einem detaillierten Verständnis dieser Phänomene.

Contents

1. Introduction 8
1.1. Iron-based catalysts for exhaust after-treatment 8
1.2. Objectives of this work 10
1.3. X-ray absorption spectroscopy (XAS) 11
1.4. Advanced tools for *in situ* XAS 23
1.5. Structure of this thesis 28
2. Materials and methods 29
2.1. Capillary micro-reactor setup with Gas Blower 30
2.2. High-pressure transmission-XAS setup 31
2.3. Pre-requisites for catalysis research at synchrotron beamlines 32
2.4. Mobile integral setup for experimental control 33
2.5. XAS measurements and data analysis 34
2.6. Catalyst synthesis and characterisation 39
2.7. Experiments with *in situ* XAS micro-reactors 41
3. Structure of Fe centres in Fe/Al_2O_3-based catalysts for automotive application 48
3.1. Catalytic performance of Fe supported on BEA zeolite and γ-Al_2O_3 48
3.2. Reducibility of Fe sites on BEA zeolite and γ-Al_2O_3 49
3.3. Identification of the structure of Fe on γ-Al_2O_3 by EXAFS 51
3.4. Conclusion 76
4. Fe K-pre-edge analysis for application in heterogeneous catalysis 77
4.1. Challenges in analysis of iron species by pre-edge XAS 77
4.2. Pre-edge treatment for structural analysis – a historical overview 79
4.3. Pre-edge analysis procedures for catalytic studies 97
4.4. Comparison of pre-edge extraction models 102
4.5. Structural trends derived from pre-edge information 106
4.6. Validation of pre-edge analysis using further reference compounds 118
4.7. Evolution of Fe in 1% Fe/Al_2O_3 and 0.5% Fe/BEA during reduction 123
4.8. Structure of Fe/ZSM-5 during NH_3-SCR probed by HERFD-XANES and V2C-XES 130
4.9. Conclusion 132
5. General conclusions and outlook 133

1. Introduction

1.1. Iron-based catalysts for exhaust after-treatment

Iron-based catalysts play a key role in several exhaust gas after-treatment systems like Fe-zeolites for SCR of NO_x with NH_3 and hydrocarbons (Shelef, 1995, Marturano *et al.*, 2001, Battiston, Bitter, de Groot*, et al.*, 2003, Pirngruber *et al.*, 2004, Brandenberger *et al.*, 2008, Høj *et al.*, 2009), CO oxidation (Wagloehner *et al.*, 2008, Royer & Duprez, 2011, Tepluchin *et al.*, 2014) and bulk chemical processes such as Fischer-Tropsch synthesis (Dong *et al.*, 2011), ammonia synthesis (Mittasch & Frankenburg, 1950, Jacobsen *et al.*, 2001, Schlögl, 2003), as well as ammonia decomposition (Simonsen *et al.*, 2012).

With increasingly stringent emission regulations, harmful emissions from vehicles and industry must be reduced by catalytic after-treatment processes. Among other catalysts, iron-based catalysts have received strong attention in this field. Iron oxide-based zeolite-supported catalysts are commercially applied for e.g. the abatement of nitric oxide (NO) and nitrogen dioxide (NO_2) from lean-burn engines (Schwidder *et al.*, 2005, Santhosh Kumar *et al.*, 2006, Johnson, 2008, Brandenberger *et al.*, 2008, Grossale *et al.*, 2008, Lox *et al.*, 2008, Balle *et al.*, 2009) and decomposition of nitrous oxide (N_2O) from e.g. nitric acid production (Perbandt *et al.*, 2013). Due to their low cost and low environmental impact, alumina-supported iron oxide-based catalysts (Fe/Al_2O_3) are prospective candidates for exhaust gas after-treatment. Besides removal of NOx by selective catalytic reduction (SCR) (Worch *et al.*, 2014), this catalytic system was found interesting for e.g. CO oxidation (Tepluchin *et al.*, 2014) and ammonia synthesis (Homs *et al.*, 1993). However, the activity of this catalyst system for SCR is lower compared to that of noble-metal analogues (Worch *et al.*, 2014) and is more prone to sulphur-poisoning (Okazaki *et al.*, 1997). The interaction of the catalytic centres with the support is another influencial factor on the catalytic activity as the Fe sites on exhibit different reactivity on different oxide supports (Liu *et al.*, 2007). In order to evaluate and improve the applicability of the Fe/Al_2O_3 catalysts for SCR, fundamental knowledge of the structure, reactivity and the reaction mechanisms is required.

The structure of the catalyst (the metal constituting the active centres and the support) is known to have an influence on the reactivity at different temperatures, allowing to tune e.g. the low-temperature or high-temperature activity (Brandenberger *et al.*, 2008, Worch *et al.*, 2014). The nuclearity of the catalytic sites likewise plays a role for the reaction. Different synthesis procedures can lead to different distributions of iron centres on the support, e.g. high

loadings of Fe precursor result in haematite-phase clusters with high surface area, whereas low amounts of iron lead to highly-dispersed oxidic clusters. It was shown that the SCR performance is directly correlated to the density of isolated Fe sites (Høj *et al.*, 2009, Brandenberger *et al.*, 2010) on zeolites, whereas the bulk crystalline iron oxide phases do not contribute to catalytic activity. Also the role of the catalyst support remains an open question. The interaction of the catalytic centres with the support is important since the support itself has a direct influence on the catalytic activity, and the isolated Fe sites on γ-Al_2O_3 exhibit a different behaviour compared to those on zeolite (Liu *et al.*, 2007).

Finally, the optimisation of the catalyst requires the understanding of the reaction mechanism (Metkar *et al.*, 2011, Ruggeri *et al.*, 2012). In order to determine the role of the Fe centres, the adsorption modes of intermediate species must be studied specifically, i.e. independently of species adsorbed to the support, which can be achieved by infrared and UV-Vis spectroscopy (Hunger & Weitkamp, 2001). Relationships between the structure and reactivity are are thus required.

An experiment probing the structure of the catalyst by spectroscopic techniques during operation (*operando* spectroscopy) is critical for establishing such relationships. *Operando* spectroscopy reveals the chemical state of the catalyst under reaction conditions, which can often deviate significantly from the chemical state before or after the reaction. In this respect it should be emphasised that a catalyst is not part of the net reaction of educts to products, but interacts with the molecular intermediates and is an intermediate, a state that can be probed only during reaction. *Operando* spectroscopy is closely related to *in situ* spectroscopy, which is spectroscopy under well-defined reaction conditions, but not necessarily technically relevant.

The present work is focused on the exploitation of X-ray absorption spectroscopy (XAS) at the Fe K-edge to specifically probe the Fe centres in the catalysts and describe the catalyst function from the perspective of the Fe centres. XAS is a powerful tool to characterise the local-range order in materials, in particular catalysts under reaction conditions, e.g. (Englisch *et al.*, 1996, Grunwaldt *et al.*, 2000, Grunwaldt & Clausen, 2002, Topsøe, 2003, Weckhuysen, 2003, Bañares, 2005, Grunwaldt & Frenkel, 2009, Deutschmann & Grunwaldt, 2013) and references therein). XAS can be used to study catalysts *in situ* and under challenging *operando* reaction conditions, since X-rays penetrate many window materials suitable for catalytic reactors specially designed for spectroscopic/catalytic experiments (Grunwaldt &

Clausen, 2002, Grunwaldt *et al.*, 2003, Grunwaldt *et al.*, 2004, Grunwaldt & Baiker, 2005, Bare & Ressler, 2009).

1.2. Objectives of this work

The aim of this Ph.D. project was two-fold. On the one hand the appropriate infrastructure at KIT should be established to conduct *in situ* studies at ANKA and other synchrotron radiation sources. For this purpose, *in situ* setups were built up and a platform established that allows in general structure-activity relationships at ANKA. On the other hand the scope of the thesis was to analyse the structure and reactivity of Fe centres in Fe/Al_2O_3 catalysts with low Fe-loadings, in order to gain insight into their function and understand why the catalytic performance is different from that of well-known systems, e.g. zeolite-based ones. An *operando* study of the Fe centres in a Fe/ZSM-5 catalyst by recently developed photon-in-photon-out techniques pushed the understanding of the critical reaction steps during NH_3-SCR. At all steps, data analysis techniques that were developed in the present work were implemented to interpret the measurement results.

Applying X-ray absorption spectroscopy (XAS) at the Fe K absorption edge, low Fe-loadings (0.1-1% Fe by weight) had to be selected in the Fe/Al_2O_3 catalyst in order to specifically probe Fe species dispersed on the surface. Extended X-ray absorption fine structure (EXAFS) spectroscopy is applied to extract the binding site of the Fe species on the γ-Al_2O_3 support, as the bond distances and coordination numbers within a few Ångströms of the absorber atom can thus be probed. To compliment existing analysis tools, a strong focus is laid on realistic input models for refinement of the EXAFS spectra. Many hypothetical structures of Fe sites interacting with γ-Al_2O_3 can be formulated, but little *a priori* knowledge is available on the actual situation. Therefore, in an approach presented in this thesis, a library of possible structures, part of which is refined by DFT calculations, is objectively tested against the experimental data. This approach allows to view and compare several models simultaneously, and thus to proceed with detailed analysis of a few interesting candidates and to reject the less suitable ones.

In a next step, the reducibility of the Fe centres is studied during temperature-programmed reduction (TPR) by following changes in the pre-edge region of the X-ray absorption near-edge structure (XANES). Both the oxidation state and the coordination geometry of the Fe sites are monitored during the structural transformation. The low amount of the Fe component, fast data acquisition and sample inhomogeneities exert an impact on the data

quality and the reliability of the structural information extracted. The use of high-resolution conditions becomes increasingly limited, as that competes with beam intensity and spectral quality. Furthermore, *in situ* XAS studies in catalysis research are commonly carried out at standard EXAFS beamlines, where special measures for increasing the instrumental resolution are not taken. Quantitative and qualitative analysis using pre-edge variograms is well-known on high-resolution data, applied in studies of geological samples, historical artefacts and catalysts. The present work demonstrates that this chemical information is also accessible in standard-resolution data and can be applied with a high degree of objectivity, having little preliminary knowledge of the sample.

Finally, the optimised pre-edge analysis is used in a combination of high-energy-resolution fluorescence-detected (HERFD) XANES spectroscopy and valence-to-core X-ray emission spectroscopy (V2C-XES) to probe the ligands around Fe in the Fe/ZSM-5 system during NH_3-SCR reaction conditions. The oxidation state and coordination number gained from the pre-edge promoted the interpretation of the V2C spectra, unravelling the intermediate species during the reaction of adsorbed NOx and ammonia-derived chemical species.

1.3. X-ray absorption spectroscopy (XAS)

X-ray absorption spectroscopy (XAS) is a powerful method to characterise the local atomic environment of selected absorber atoms (Teo, 1981, Koningsberger & Prins, 1988, Englisch *et al.*, 1996). X-rays are electromagnetic radiation, conventionally divided into the region of soft X-rays (photon energies below a few keV, e.g. 284 eV at the carbon K-edge or the 543 eV at the oxygen K-edge) and hard X-rays (several keV, e.g. 2472 eV at the sulphur K-edge to e.g. 25514 eV at the Ag K-edge). Especially in the hard X-ray regime, XAS is widely used to study heterogeneous catalysts because it probes atoms and their local surroundings in a material, and the radiation penetrates many window materials, which becomes especially important under reaction conditions (Bazin *et al.*, 1996, Clausen *et al.*, 1998, Grunwaldt & Clausen, 2002, Grunwaldt *et al.*, 2004, Weckhuysen, 2004, Grunwaldt & Baiker, 2005, Bare & Ressler, 2009, Meunier, 2010).

XAS exploits the core-electron, which is excited during X-ray absorption by a selected element, to probe the electronic structure of the valence band of that element (XANES) and the local atomic neighbourhood (EXAFS). Using EXAFS, the type, number and distances to neighbouring atoms at a radius of ca. 6 Å is determined. This element-specific analysis is applicable to materials in crystalline, amorphous, liquid, dissolved and gaseous phase. A

complementary technique to XAS is X-ray diffraction (XRD), which probes crystal phases by scattering of the incoming X-ray beam according to Bragg's law, determining inter-lattice distances (Teo, 1981). XRD requires long-range order and minimum crystallite size of ca. 1 nm. The combined application of these methods will be briefly brought to attention in Sections 1.4.3 and 2.7.4.

XANES probes the unoccupied valence electronic states and is complementary to valence-to-core X-ray emission spectroscopy (V2C-XAS), probing the occupied valence electronic states (Bauer, 2014). This application of XANES spectroscopy to complement V2C-XAS will be covered in Chapter 4.

1.3.1. The X-ray absorption process

When atoms absorb X-ray photons of energy E, the energy is transferred to a core electron (in a 1s shell in K-edge spectroscopy or a $2p_{3/2}$ shell in L_3-edge spectroscopy), which is excited into the continuum as a photoelectron. This process is known as the photoelectric effect. The atomic absorption cross-section σ_a is a function of the atomic number Z, scaling as Z^4. The fact that each absorption edge is unique for a specific element makes XAS element-specific. Furthermore, the absorption cross-section rapidly decays with increasing photon energy E, scaling as $1/E^3$. If the absorption cross-section from a series of elements is weighted by $1/E^3$ and Z^4, it becomes constant as a function of photon energy, separated by edge jumps, as shown in Figure 1 (Als-Nielsen & McMorrow, 2001).

The energy transferred from the incident photon to the absorbing atom is decomposed as

$$E = E_0 + \frac{\hbar^2 k^2}{2m},$$

where E_0 is the electron binding energy, $\hbar^2k^2/2m$ is the kinetic energy of the photoelectron, $\hbar$ Planck's constant divided by 2π, k the photoelectron wave number and m the mass of the electron. At $E = E_0$, called the absorption edge, there is an abrupt increase in absorption (edge jump). An X-ray absorption spectrum of α-Fe_2O_3 measured at the Fe K-edge is shown in Figure 2a.

X-ray absorption spectra are an excellent source of chemical information, which is probed by the excited photoelectron. Close to the absorption edge, in the X-ray absorption near-edge structure (XANES) spectrum (Figure 2a), the low-energy core electron probes the unoccupied electronic states. Below atomic ionisation, unoccupied states in the valence shells of the atom

are probed to reveal the oxidation state and local coordination geometry of the absorbing atom. Examples of valence shells are the 3d-shell of first-row transition metals, giving rise to pre-edge features in K-edge spectra (such as for Fe, Figure 2b) or the 5d-shell of third-row transition metals such as Pt, probed by the first strong resonance of L_3-edge spectra.

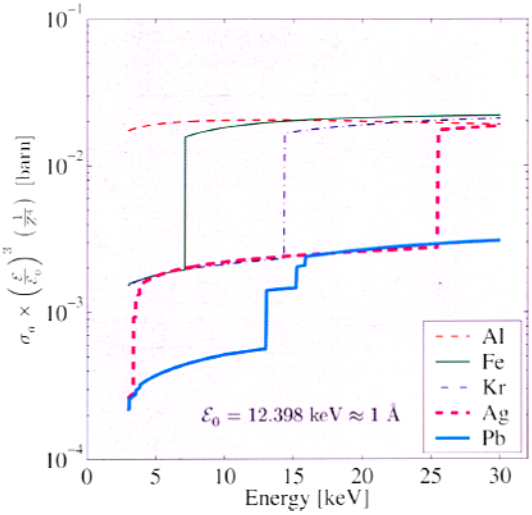

Figure 1 Absorption cross-section from some elements plotted together, weighted by $1/E^3$ and Z^4, this weighting completely removes the $1/E^3$ and Z^4 dependence. Atomic numbers for the given elements are $_{13}$Al, $_{26}$Fe, $_{36}$Kr, $_{47}$Ag, $_{82}$Pb. The denominator E_0 in the E^3-weighting term is the energy of an X-ray with a wavelength of 1Å, arbitrarily chosen to make the weighting term a dimensionless number; it is not to be confused with the absorption edge E_0. Units of cross-section are barn; 1 barn = 10^{-24}cm^2. (Als-Nielsen & McMorrow, 2001). Reprinted from Elements of X-ray Physics, J. Als-Nielsen and D. McMorrow, Photoelectric absorption, p. 203, Copyright (2001), with permission from John Wiley & Sons, Ltd.

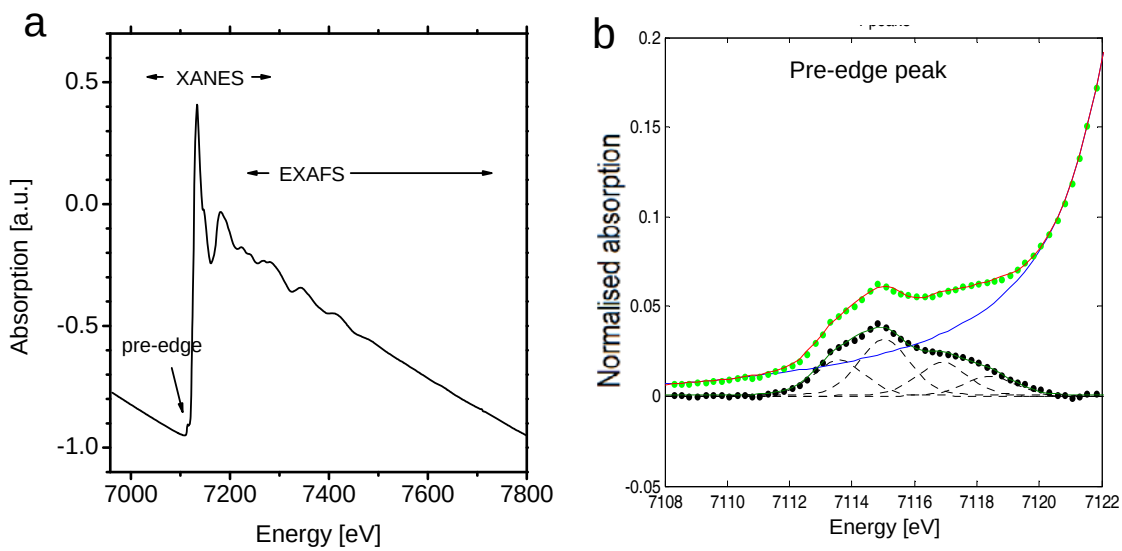

Figure 2 X-ray absorption spectrum of α-Fe_2O_3 at the Fe K-edge (E_0 = 7112 eV) as raw data showing the pre-edge, XANES and EXAFS regions (a) and the extracted and de-convolved pre-edge feature (b).

After atomic ionisation, the photoelectron is excited into unoccupied electronic states, which are sensitive to the oxidation state, length and angles of the bonds to the nearest-neighbour atoms (Waychunas *et al.*, 1983, Benfatto & Della Longa, 2001). In this regime, photoelectrons with low kinetic energy (below 50 eV) have a long mean free path (can exceed 1 nm) and experience multiple scattering from neighbouring atoms. The complex electronic structure arising from multiple-scattering effects (together with pre-edge, edge position, white line intensity, etc.) is often unique for specific chemical and the complete XANES spectrum serves as a "fingerprint" for their analysis (Río *et al.*, 2005). The pre-edge peak (below the K-edge) contains singular information about the oxidation state and coordination geometry of the metal ions and is therefore a clear indicator of these properties, also in cases where the XANES spectra cannot be used as a fingerprint, i.e. no reference spectra for comparison are available (Westre *et al.*, 1997, Wilke *et al.*, 2001), as for less-usual metal environments such as in complexes, non-crystalline materials, dopants, etc.

At sufficiently high kinetic energies, in the extended X-ray absorption fine structure regime (EXAFS, Figure 2a and Figure 4), single-scattering from neighbouring atoms starts to dominate, and local-order structural atomic information on the length-scale of several Ångströms can be obtained.

The excited state formed in the absorption process is a hole in the core shell level. This hole is filled with an electron from a higher energy level in relaxation processes, emitting a fluorescence photon or secondary electrons to conserve energy. Fluorescence photons studied in XES probe the electronic levels from which the electron originates and the fluorescence intensity can be used to indirectly measure absorption.

The next three sub-sections present the theoretical background for pre-edge spectroscopy, X-ray emission and EXAFS spectroscopy of iron-containing materials in detail, as these methods have been extensively used for the present work.

1.3.2. Pre-edge features

Pre-edge features in K-edge XANES spectra (Figure 2b) correspond to 1s → 3d transitions, which are important to probe the chemistry of the first-row transition metals, as for these elements the 3d-orbital is the valence shell. Since probability of this transition is very sensitive to the geometry of the local atomic environment of the absorber atom, an intensive pre-edge peak can be an indicator of tetrahedral (4-fold) coordination, whereas a weak pre-edge peak can indicate octahedral (6-fold) coordination.

The 1s → 3d transition is a quadrupolar transition, involving a change in angular momentum by $\Delta l = +2$. However, quadrupole transitions are very weak in comparison with dipolar transitions, such as the 1s → 4p transition, during which a change in angular momentum by $\Delta l = +1$ occurs. If the absorber atom is coordinated in geometry with a centre of inversion (e.g. octahedral), a weak pre-edge peak will show that the transition is of purely quadrupolar character. However, if the inversion centre is distorted by a change in the number and arrangement of ligands, e.g. if Fe is coordinated in fivefold or fourfold geometry, 3d-4p molecular orbital hybridisation (mixing) can occur, facilitating dipolar transitions of the 1s → 4p type with a significantly higher intensity. A linear relationship between the degree of 3d-4p hybridisation and the pre-edge intensity has been shown (Roe *et al.*, 1984) (Figure 3a); the 3d-4p hybridisation increased with decreasing Fe coordination number from 6 (ligands typically in an octahedral (O_h) arrangement) to 5 (several symmetries) and 4 (tetrahedral (T_d), trigonal pyramid and in some cases square planar) (Westre *et al.*, 1997) (Figure 3b). This allows one to directly correlate pre-edge intensities and local coordination number of the Fe ion.

The position of the pre-edge peak can be used as a direct indicator of the Fe oxidation state, making an unambiguous distinction between Fe^{2+} (average pre-edge position 7112 eV) and Fe^{3+} (average pre-edge position 7113.5 eV) possible (Wilke *et al.*, 2001). For Fe compounds, this distinction is possible because the coordination geometry does not influence the pre-edge peak position, and the oxidation state and coordination geometry of the Fe ions can be obtained independently of each other using the pre-edge. This is in contrast to other 3d-metals, e.g. for Ti^{4+} and Ni^{2+}, where both the position and intensity are affected by the coordination geometry (Yamamoto, 2008). For these ions, this is explained by the location of the Fermi level between the 3d and 4p energy-levels, resulting in a strong energy-dependence of the transition probability on the degree of 3d-4p mixing. In the case of Fe, the Fermi energy is located below both of these levels

Crystal-field theory predicts the electronic states into which 3d-electrons split, when the ion is surrounded by ligands in a specific geometry, as shown in Figure 3. The Fe K-pre-edge features of compounds containing Fe in various oxidation states (Fe^{2+}, Fe^{3+} and mixtures), as well as coordination numbers (4-, 5-, 6-coordinated and higher) were studied in the light of crystal-field theory (Westre *et al.*, 1997, Arrio *et al.*, 2000, Galoisy *et al.*, 2001). Many strong transitions from the 1s core shell into the predicted states were clearly observed as pre-edge features in high-resolution experimental data, but the experimental resolution has often limited identification of the weak transitions. Further work (Wilke *et al.*, 2001) has introduced

the interpretation of general trends in the intensity and position of the Fe K-pre-edge feature for quantification of oxidation state and coordination geometry, circumventing the complexity of *ab initio* calculations by using reference compounds. One chapter in this thesis is dedicated to this topic.

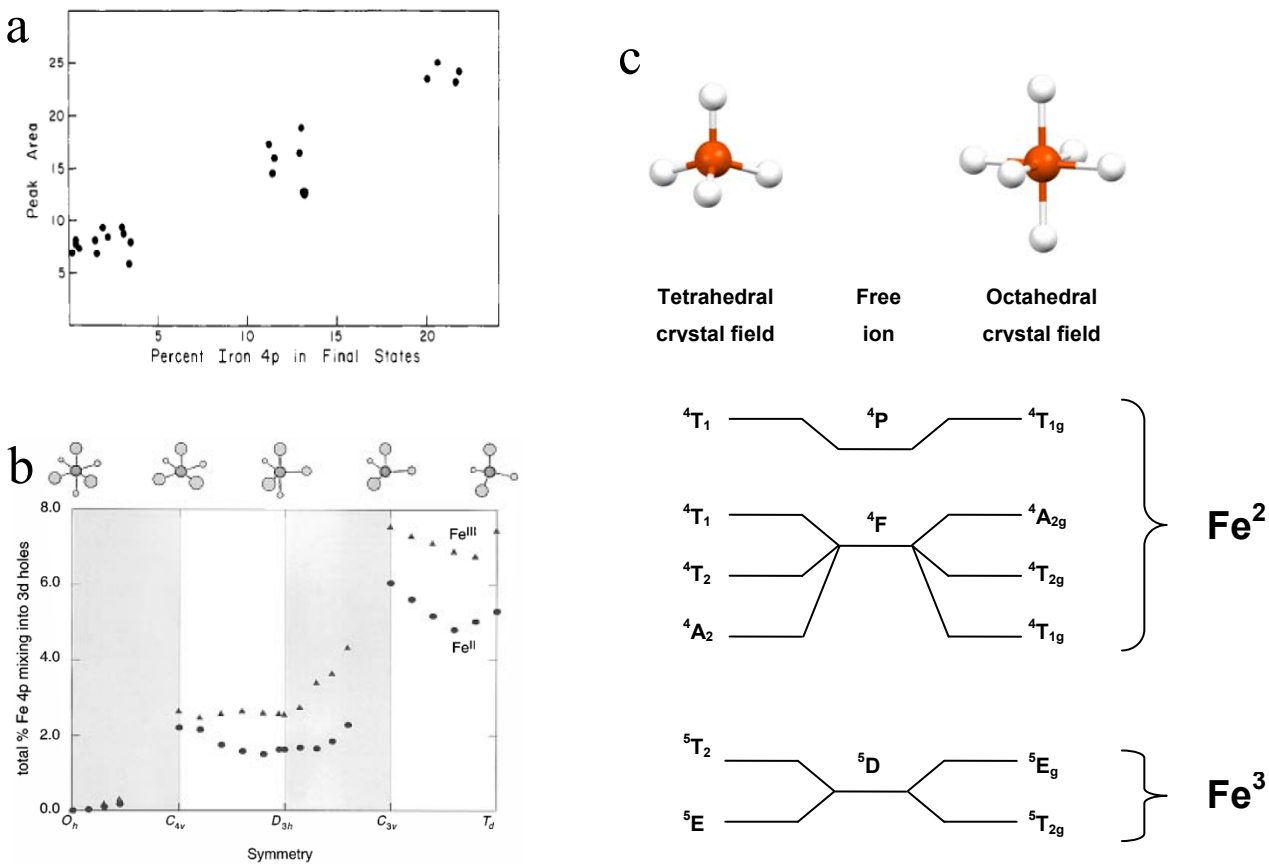

Figure 3 Linear relationship between the 3d-4p mixing and the pre-edge intensity (Roe *et al.*, 1984) (a), the increasing 3d-4p mixing as the coordination decreases from 6-fold over 5-fold to 4-fold geometries (Westre *et al.*, 1997) (b), and the electronic transitions predicted by crystal field theory comprising the Fe K-pre-edge features of Fe^{2+} and Fe^{3+} species in tetrahedral (T_d) and octahedral (O_h) coordination. (a) Reprinted with permission from A. L. Roe, D. J. Schneider, R. J. Mayer, J. W. Pyrz, J. Widom and L. Que, X-ray absorption spectroscopy of iron-tyrosinate proteins, Journal of the American Chemical Society 106 (1984) 1676-1681. Copyright (1984) American Chemical Society. (b) Reprinted with permission from T. E. Westre, P. Kennepohl, J. G. DeWitt, B. Hedman, K. O. Hodgson and E. I. Solomon, A Multiplet Analysis of Fe K-Edge 1s → 3d Pre-Edge Features of Iron Complexes, Journal of the American Chemical Society 119 (1997) 6297-6314. Copyright (1997) American Chemical Society.

1.3.3. HERFD-XANES and V2C-XES

Emerging synchrotron-based hard X-ray photon-in/photon-out techniques have recently demonstrated the ability to shed the light on the local coordination environment of Fe atoms (Lancaster *et al.*, 2011, Chandrasekaran *et al.*, 2013). The 1s core electron is excited into the continuum and the hole is filled from the higher-energy core and valence shells, emitting fluorescence light of specific energy. Along with the more intensive fluorescence transitions Fe Kα (2p → 1s) and the spin-sensitive Fe Kβ'/$K\beta_{1,3}$ (3p → 1s) (Pirngruber *et al.*, 2007, Glatzel *et al.*, 2008), weak emission lines Fe Kβ"/$K\beta_{2,5}$, corresponding to the 3d/4p → 1s valence-to-core (V2C) relaxation, are observed. The measurement of X-ray emission spectra (XES) in the V2C region allows distinguishing between different ligands in the coordination sphere of Fe (Lee *et al.*, 2010, Atkins *et al.*, 2013). For measuring X-ray emission spectra, the photon energy of the incoming beam is set using a monochromator and the emitted radiation is scanned typically using analyser crystals on a Johann-type spectrometer in Rowland geometry (Johann, 1931, Glatzel, Sikora, Smolentsev*, et al.*, 2009, Bauer, 2014). The emitted radiation is monochromatised using the analyser crystals and is detected at a range of Bragg angles to record a spectrum.

Complementarily, the position and intensity of the pre-edge peak in the Fe K-edge X-ray absorption near-edge structure (XANES) spectra can be correlated to the valence and geometry of Fe in the system, respectively, as described in the previous section. The XANES spectra complementary to XES are recorded on the same spectrometer using the high-energy-resolution fluorescence-detected (HERFD)-mode. The Johann spectrometer is fixed to detect a single emission energy (e.g. the Fe $K\beta_{1,3}$ line) and the energy of the incoming photons are scanned with the monochromator.

These complementary techniques can reveal the interaction of the reactive molecules specifically with the metallic centres of the catalyst under *operando* conditions. For example, the direct adsorption of NH_3 was shown to take place on copper sites of the Cu-SSZ-13 zeolite (Giordanino *et al.*, 2014), as the shift of the Cu Kβ" feature to higher energies supported the formation of the Cu-N bond instead of the Cu-O bond, accompanied by the reduction of Cu^{2+} to Cu^{+}. A recent study partly included into this thesis (Boubnov *et al.*, 2014) has indicated the bonding of NH_3 molecules via a hydroxyl group to Fe, which was reduced from Fe^{3+} to Fe^{2+}. Especially in the latter study, the spectral features in the V2C spectra were very vague and their interpretation required DFT-based simulations, solidly supported by the

oxidation state and local coordination numbers obtained using the pre-edge portion of the HERFD-XANES spectra.

1.3.4. Extended X-ray Absorption Fine Structure (EXAFS)

Modulations in the absorption profile with increasing photon energy above the absorption edge are due to interactions of the photoelectron with neighbouring atoms. In the case of isolated atoms (as in a monatomic gas), the ejected photoelectron is completely removed from the atom. On the other hand, if the atom is surrounded by neighbouring atoms, the photoelectron can be scattered back to the absorber atom, causing modulations in the post-edge absorption profile.

These modulations are described by the EXAFS function $\chi(E)$, which shows an oscillatory behaviour as a function of the energy of the photoelectron. Figure 4a shows a normalised X-ray absorption spectrum modulated by the EXAFS, which can extend into a thousand electron volts above the edge. The term "extended" refers to this relatively broad energy range, while the characteristic oscillations are termed "fine structure". The EXAFS function $\chi(E)$ is extracted from the measured absorption spectrum $\mu(E)$ (Figure 4a) by subtracting a background function $\mu_0(E)$ which simulates the absorption by an isolated atom and dividing by the edge jump $\Delta\mu(E_0)$:

$$\chi(E) = \frac{\mu(E) - \mu_0(E)}{\Delta\mu(E_0)}.$$

According to Fermi's golden rule, the absorption (transition) probability μ is proportional to the "overlap" between the initial and final quantum-mechanical states of the electronic transition, ψ_i and ψ_f respectively, where $\hat{H}$ is the perturbation Hamiltonian.

$$\mu \propto \left|\langle \psi_f | \hat{H} | \psi_i \rangle\right|^2$$

In other words, if there is a quantum-mechanical "overlap" between the initial and final electronic orbitals, the absorption is strong; if there is no "overlap", the absorption is weak. In this context, the initial state ψ_i is the absorber atom with its tightly bound core electron and an incoming X-ray photon. The final state ψ_f is the interference pattern of the wave functions of the outgoing and the back-scattered photoelectron due to neighbouring atoms. The EXAFS is essentially an overlap between the initial state and that interference pattern.

The EXAFS phenomenon was discovered and described (Sayers *et al.*, 1971) by comparing crystalline and amorphous Ge, showing that a Fourier-transform of the oscillatory EXAFS function is a pseudo-radial distribution function of atomic neighbours, showing the scattering paths of the photoelectron (Figure 4c).

The EXAFS equation

For analysis, the oscillatory EXAFS function $\chi(E)$ is transformed into k-space (Figure 4b)

$$\chi(k) = \sum_j N_j f_j(k) \frac{\sin\left[2kR_j + \delta_j(k)\right]}{kR_j^2} \mathrm{e}^{-2k^2\sigma_j^2} \mathrm{e}^{-2R_j/\lambda_j(k)} ,$$

expressed as a function of the photoelectron wave number $k = \frac{\sqrt{2m(E-E_0)}}{\hbar}$.

This expression is a sum over all possible neighbouring atoms j located at distances R_j from the central atom. N_j indicates the number of atoms in each coordination shell. The terms $f_j(k)$ and $\delta_j(k)$ describe the amplitude and phase shift in the photoelectron wave function respectively, resulting from the backscattering event. These parameters depend on the type of the neighbouring atom (atomic number) and can be calculated theoretically or obtained from data acquired from known reference samples.

The two exponential functions describe attenuation of the EXAFS oscillations. The Debye-Waller factor $\mathrm{e}^{-2k^2\sigma_j^2}$ describes the damping due to vibrations of neighbouring atoms. The mean square displacement of the neighbour from its equilibrium position is σ^2. With increasing temperatures the vibrations and displacements increase, damping the EXAFS oscillations for high k.

The second exponential term $\mathrm{e}^{-2R_j/\lambda_j(k)}$ describes damping due to the mean free path $\lambda(k)$ of the photoelectron, which is the mean distance an electron with wave number k can travel without being scattered. To contribute to the EXAFS oscillations, the backscattered photoelectron has to reach the atom from which it is ejected before the hole is filled by another electron. In other words the short lifetime of the excited state of the ionised atom limits the distance to the furthest neighbours, which can be probed with EXAFS. Additionally, inelastic scattering decreases the mean free path. The mean free path increases with increasing k. To amplify the damped EXAFS oscillations at high k-values, the EXAFS function can be weighted by k^x (x = 1, 2, 3) during analysis.

During data analysis, the structural parameters R_j, N_j and σ_j^2 are fitted. This allows to derive the type of atoms, coordination number and characteristic distances of the neighbouring atoms.

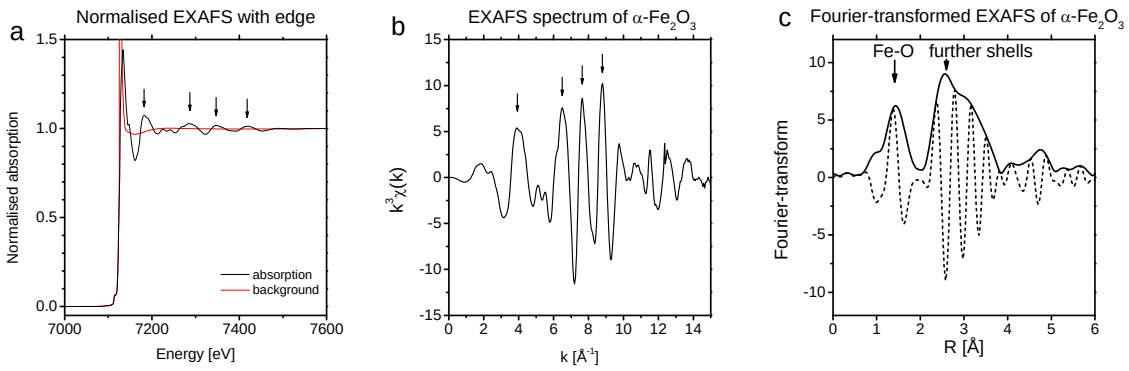

Figure 4 Normalised X-ray absorption spectrum (a) and the extracted and k^3-weighted (b) EXAFS of α-Fe_2O_3. The arrows indicate the same EXAFS features in the two forms of the same dataset. The Fourier-transformed EXAFS spectrum (c), indicating the nearest-neighbour Fe-O scattering paths (up to ca. 2 Å, not phase-corrected) and scattering paths to further atoms.

1.3.5. Measurement of X-ray absorption spectra

Acquisition of high-quality X-ray absorption spectra requires an intense monochromatic X-ray beam of continuously tuneable energy, preferentially from a synchrotron light source. Radiation emitted by electrons in the magnetic fields in storage ring bending magnets is the most common. Higher photon flux and higher photon energy can be provided by insertion devices (undulators, wigglers); e.g. high-brilliance beamlines use energy-tuneable undulators. A schematic of an X-ray absorption experiment at a bending magnet beamline is shown in Figure 5.

The X-ray beam produced using a bending magnet has a certain angular divergence. A system of mechanical slits admits the central portion of the beam to the monochromator (typically a double-crystal monochromator equipped with a Si(111) crystal pair), which selects certain energies according to Bragg-diffraction from the crystals. A subsequent system of slits defines the final beam size used in the experimental setup. The monochromatic beam intensity is measured using ionisation chambers filled with inert gases between two plates with a high voltage applied. Upon absorption of an X-ray photon, the gas molecules are ionised and accelerate towards the electrode, giving rise to an electric current. The incoming intensity and the intensity transmitted by the sample, as well as after a reference sample for energy-

calibration is measured. Additionally, a solid-state fluorescence detector is placed directed at the sample, perpendicular to the incident beam.

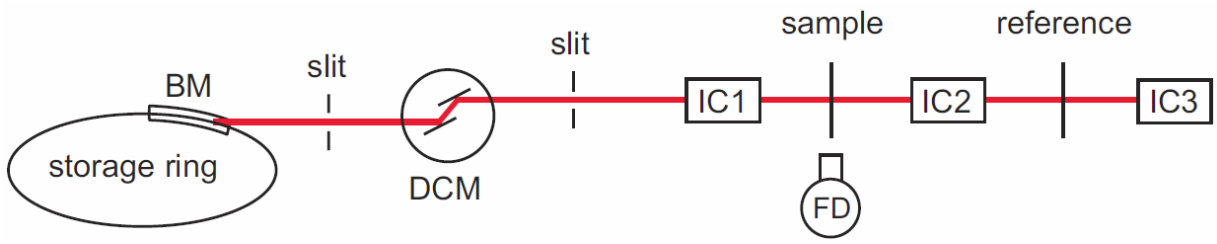

Figure 5 Schematic of a XAS experiment at a synchrotron. The X-ray beam is shown in red. Acronyms: BM, bending magnet; DCM, double-crystal monochromator; IC (1, 2, 3), ionisation chambers; FD, fluorescence detector.

The absorption coefficient μ can be calculated, by measuring the incoming monochromatic X-ray intensity I_0 and transmitted intensity I_T, according to Lambert-Beer's law

$$I_T = I_0 e^{-\mu z}$$

$$\mu = \frac{1}{z} \ln \frac{I_0}{I_T}.$$

z is the sample thickness. The absorption coefficient of the specimen is related to the atomic cross-section by

$$\mu = \frac{\rho_m N_A}{A} \sigma_a = \rho_a \sigma_a,$$

with ρ_m the mass density, N_A Avogadro's number and A the atomic mass. The fraction is simply an expression for ρ_a, the atomic density of a given element in the specimen.

As a result of photon absorption, several secondary electronic processes take place. X-ray fluorescence is a process where holes in a core shell created by absorption are filled by electrons from higher shells, leading to emission of a photon of corresponding energy. Absorption spectra can be measured indirectly by detecting the fluorescence, because to a good approximation, the fluorescence yield is proportional to the absorption coefficient, so that

$$\mu \propto \frac{I_f}{I_o},$$

where I_f is the fluorescence intensity of a specific fluorescence line, e.g. Fe Kα or Fe Kβ.

For data quality (signal-to-noise, etc.), the transmission mode edge jump must be pronounced compared to the total absorption by the sample, meaning that a high content of the element of

interest in the sample is desired. In this case, the sample must be optically thin in order to avoid thickness effects, resulting in very high absorption or almost complete absorption of the beam by the sample. On the other hand, fluorescence-mode measurements are optimised with sufficient dilution of the element of interest, where the effect of incident-beam self-absorption can be minimised. This effect causes distortion of the data (especially in the XANES region), in that the oscillations are damped (Bianchini & Glatzel, 2012); this concerns standard fluorescence-mode and HERFD-mode. Fluorescence-mode is especially suited for samples containing the element of interest in low concentrations. A comparison of two Fe K-edge X-ray absorption spectra of a 1% Fe/Al_2O_3 catalyst acquired simultaneously in transmission-mode and fluorescence-mode is shown in Figure 6a. The shape of the raw data is different: the transmission-mode spectrum shows a negative slope following a $1/E^3$-trend as mentioned earlier, while the fluorescence-mode spectrum exhibits a horizontal (almost constant) background, slightly increasing due to higher scattering efficiency with higher energies. This sample is at the boundary of suitability of the two techniques. On one hand the concentration of Fe is high enough to gain a decent signal-to-noise ratio in transmission-mode although the sample was prepared as a thin pellet, and on the other hand low enough to neglect incident-beam self-absorption. The XANES spectra shown in Figure 6b show no distortions due to incident-beam self-absorption; the difference in normalised intensity over the whole range is due to the normalisation procedure. In most other cases, the sample and measuring conditions must be optimised either for transmission-mode or fluorescence-mode.

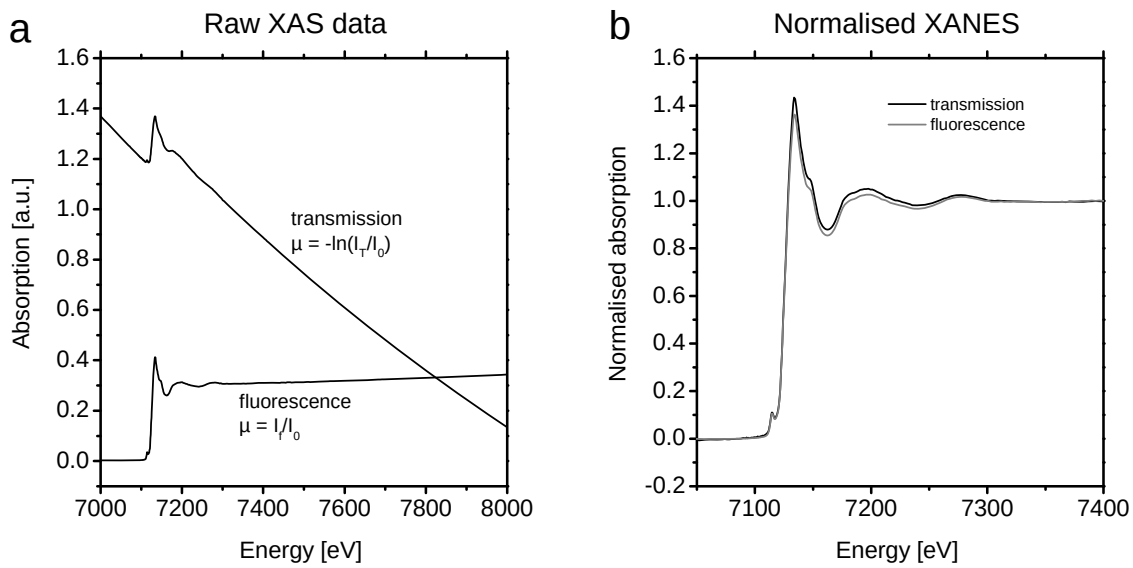

Figure 6 Spectra acquired in transmission and fluorescence mode simultaneously on a 1% Fe/Al_2O_3 catalyst sample. Raw data (a) and normalised XANES (b).

1.4. Advanced tools for *in situ* XAS

Characterisation of heterogeneous catalysts is an essential part of rational catalyst design, as it is needed to derive structure-activity relationships which lead to a better understanding of the catalyst function. Besides the *ex situ* techniques (e.g. TEM, XRD, chemisorption) for probing the catalysts' overall composition and functionality (Boubnov *et al.*, 2012, Tepluchin *et al.*, 2014), *in situ* and *operando* spectroscopic methods allow identification of the chemical species during the reaction, and thus lead to correlation of the catalytic performance and catalyst structure (Boubnov, Gänzler*, et al.*, 2013, Boubnov *et al.*, 2014).

Additionally, experimental results of high quality and reproducibility play a critical role (Meunier, 2010). To achieve this, spectroscopic micro-reactors and infrastructure designed for catalysis studies at synchrotron radiation sources must be modular and robust (if not permanently installed) so that the experimental setup can be built up flawlessly and quickly. Furthermore, the setups must be mobile and flexible to adapt to different laboratories and user-groups. Finally, the experiments need to be user-friendly and programmable, allowing an overview of the whole experiment (van Beek *et al.*, 2011). In the following sections, the functionality of several micro-reactor designs as well as technical options for catalysis research at beamlines is outlined.

1.4.1. Compromise between catalysis and spectroscopy

Reactive centres of catalysts are often studied *in situ* while interacting with probe molecules. This is typically done by treating the catalyst in reactive gases that bind specifically to the sites of interest. For example, Raman spectroscopy of pyridine adsorbed on Co/Mo-based catalysts (Schrader & Cheng, 1983), EXAFS and FTIR spectroscopy of Pt/SiO_2 (Gracia *et al.*, 2003) and FeO_x-based catalysts (Battiston *et al.*, 2000, Galvita *et al.*, 2008) exposed to CO and O_2 illustrate this approach. These methods can predict the role of the catalytic site in relevant reactions and a high spectral quality is prioritised over realistic reaction conditions. One further step required to observe and understand the active site in a catalytic reaction under realistic working conditions in *operando* spectroscopy.

Realistic operating conditions (*operando*) are often industrially-relevant, including elevated reaction temperatures, high-pressure and liquid-phase reactions. The challenge is to make special catalytic reactors which mimic these conditions, suitable for spectroscopic studies. Materials must be found that transmit the radiation used for the spectroscopic characterisation, but at the same time withstand reactive gas atmospheres, high temperatures and high pressure.

In order to carry out catalytic experiments and acquire high-quality spectroscopic data simultaneously, a compromise between reactor technology and spectroscopy must be found: it has been well demonstrated that samples well suited for XAS (e.g. pellets) might not be a good model system ideal for catalysis (e.g. powder) and vice-versa (Grunwaldt *et al.*, 2004, Grunwaldt, 2009). This is e.g. due to the fact that X-ray absorption spectroscopy in transmission mode requires homogeneous samples, which is often a challenge when working with heterogeneous catalysis as porous solid substances. On the other hand, it is desired that the catalyst is in a working state during spectroscopic studies, which requires that it is in a form accessible to the reactants, which in turn should easily flow through the catalyst; a powder sieve fraction is well-suited for this application. A number of compromises between catalysis and spectroscopy conditions will be discussed herein.

1.4.2. Construction materials for in situ XAS sample cells

In order to mimic technically relevant reaction conditions during *in situ* investigations, the size of the catalytic reactor must be scaled to adapt to the small amount of catalyst sample to be probed by the X-ray beam. Besides that, the windows of the reactor should be transparent to the X-ray beam so that the sample can be probed. The construction materials for the windows must be mechanically, thermally and chemically stable to withstand the reaction conditions (Grunwaldt & Baiker, 2005, Bare *et al.*, 2007).

Preferably, these materials consist of light elements to minimise the absorption of X-rays. The attenuation length of some commonly used materials in the operation range of the Si(111) monochromator covering the energies of several catalysis-relevant elements (2-20 keV) is presented in Figure 7. The attenuation length is the optical length (thickness) of a sample transmitting $1/e \approx 37\%$ of the incoming photons.

Mechanically stable materials able to withstand high pressure and high temperature include metals such as beryllium and aluminium, ceramics (Al_2O_3 and SiO_2) as well as diamond and boron nitride (BN) occurring in graphite and diamond crystal structure. Beryllium ($Z = 4$) is favoured for X-ray-based applications due to its low weight and chemical stability. However, due to its toxicity when oxidised, the use of this element is limited to permanent installations and where it is absolutely indispensible. According to Figure 7, to maintain the same absorption, a 1 mm thick Be foil can be replaced by a 100 µm diamond window or a 10 µm Al foil, depending on the requirements.

When diluting samples with chemically inert material to optimise the absorption, Figure 7 suggests that the use of BN is preferable, as it absorbs 10 times less than Al_2O_3 or SiO_2, but its use can cause diffusion limitations in the catalytic experiments since it is not porous. On the other hand, for *ex situ* measurements, BN, cellulose and polyethylene (PE) are common dilution materials.

The measurements described in this thesis are carried out at the Fe K-edge (7112 eV). For experiments in this energy range, the absorption by air (attenuation length for N_2 is less than 1 m), quartz (SiO_2) as reactor material and cellulose as dilution and binding agent for sample pellets are all factors that have a direct influence on the spectral quality. The quartz capillary micro-reactor with a wall thickness of 20 µm used for these studies constitutes half an attenuation length, making its use unproblematic for *in situ* studies of Fe. However, around ten attenuation lengths can be expected for a sample of a Fe/Al_2O_3 catalyst when filled in a micro-reactor of 1 mm diameter, due to absorption by Al_2O_3. High background-absorption can thus be expected, and fluorescence-mode measurements should be considered. The use of cellulose-pellets of ca. 1 mm thickness as samples for *ex situ* measurements should not be problematic, since less than one attenuation length is achieved by cellulose.

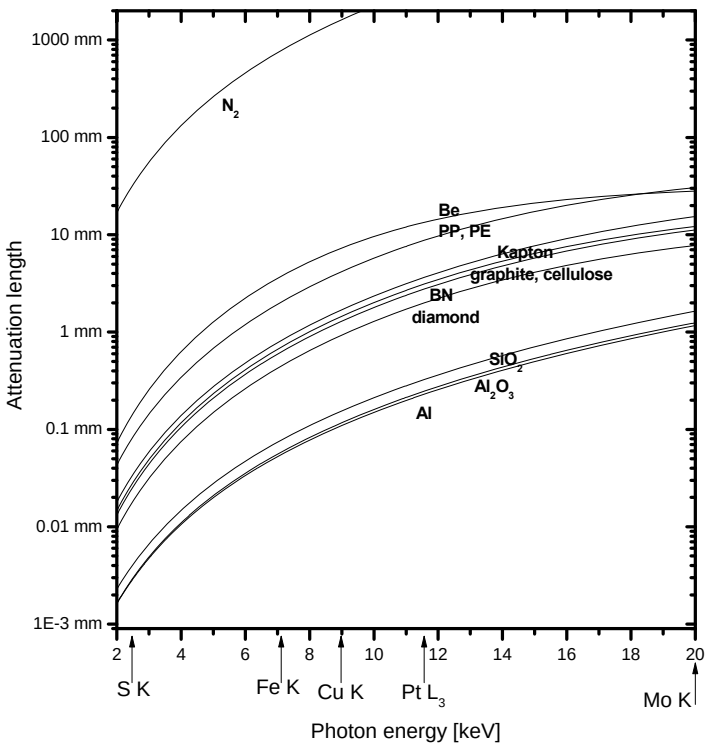

Figure 7 The attenuation length of common materials used for windows in sample environment construction and to dilute samples for X-ray absorption spectroscopic measurements. Below ca. 9 keV, the attenuation length in air (approximated by N_2) is below 1 m.

1.4.3. The capillary micro-reactor

The capillary micro-reactor used for this study (schematic drawing in Figure 8) suited to withstand temperatures up to 700°C was originally developed for *in situ* powder X-ray diffraction (XRD) measurements at synchrotron light sources, combining the quartz capillary tubes conventionally used for XRD with a gas flow (Clausen *et al.*, 1991). In this way, a catalytic experiment with online gas analysis could be carried out and structural information of the catalyst acquired. A combination of (quasi-)simultaneous XAS/XRD on the same sample under identical conditions was introduced (Couves *et al.*, 1991) and realised using the capillary micro-reactor to study dynamic structural changes of Cu/ZnO-based catalysts during calcination and reduction (Clausen *et al.*, 1993, Grunwaldt *et al.*, 2000). Using a dedicated high-temperature furnace (Gas Blower, Cyberstar), the setup was extended to temperatures above 900°C (Grunwaldt *et al.*, 2007, van Beek *et al.*, 2011).

The micro-reactor consists of a quartz capillary loaded with catalyst powder between two quartz wool plugs and connected to a gas inlet and outlet, making it an ideal plug flow reactor. Heating is provided by a gas blower placed below the capillary. Due to the open construction of the setup, XAS measurements are possible both in transmission and fluorescence geometry (Grunwaldt *et al.*, 2005, Høj *et al.*, 2009, Klukowski *et al.*, 2009). The combination of *in situ* techniques such as XAS and XRD, e.g. (Kiebach *et al.*, 2008), with Raman spectroscopy (Grunwaldt *et al.*, 2009, van Beek *et al.*, 2011) and infrared thermography (Kimmerle, Grunwaldt, *et al.*, 2009) were also facilitated, exploiting the open geometry of the reactor. The use of beryllium capillaries, which are additionally stable for high-pressure applications, has been reported (Bare *et al.*, 2007) for XAS at low photon energies. Sealing a thin quartz capillary in the holder with two-component epoxy glue allows the operation of this reactor at pressures up to 20 bar (Karaca *et al.*, 2011).

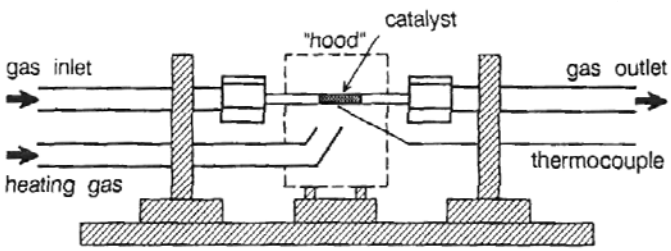

Figure 8 Quartz capillary micro-reactor used for in situ XRD while carrying out a catalytic experiment. Reprinted from (Clausen et al., 1991). Reprinted from Journal of Catalysis, Vol. 132, B.S. Clausen, G. Steffensen, B. Fabius, J. Villadsen, R. Feidenhans'l, H. Topsøe, In situ cell for combined XRD and on-line catalysis tests: Studies of Cu-based water gas shift and methanol catalysts, Pages 524-535, Copyright (1991), with permission from Elsevier.

1.4.4. High-pressure transmission-XAS cell

An important step towards challenging industrially-relevant experimental conditions was the development of a stainless steel reactor used for XAS studies of Cu/ZnO catalysts for methanol synthesis at 220°C and 48 bar, shown in Figure 9 (Clausen & Topsøe, 1991). Several high-pressure cells have been developed (Grunwaldt *et al.*, 2003), but only a few allow measuring real catalysts. The reactor contains a small volume that is completely filled with catalyst powder, with a gas inlet and outlet, creating conditions similar to those in a plug-flow reactor. The catalyst is located between two beryllium X-ray windows sealed with graphite film. For ambient pressure applications, the beryllium windows can be replaced by graphite-sealed Kapton windows or only graphite. This design allows one to study the structure of catalysts in gas-phase reactions, perform *in situ* pre-treatments and conduct on-line analysis of the gas composition at the reactor outlet. Prototypes of this reactor have been developed that can be used at a pressure of up to 200 bar (Grunwaldt *et al.*, 2004, Grunwaldt & Baiker, 2005) and for parallel simultaneous studies of several catalysts (Kimmerle, Haider, *et al.*, 2009). The core of the reactor containing the catalyst sample is sealed using flanges with small X-ray windows on both sides. Due to the massive construction of this reactor, XAS measurements are limited to transmission geometry.

Modified designs of high-pressure reactors, optimised for easier sample-handling, exist (Rochet *et al.*, 2011). Further models of *in situ* XAS reactors designed for studies of automotive catalysis research have also been reported (Schneider *et al.*, 1998, Matam *et al.*, 2011).

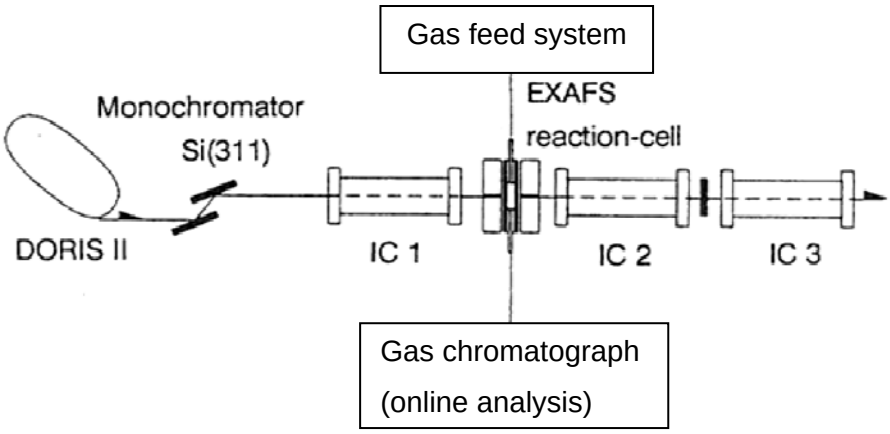

Figure 9 High-pressure *in situ* XAS reactor at the beamline. Reprinted from (Clausen & Topsøe, 1991). Reprinted from Catalysis Today, Vol. 9, B.S. Clausen, H. Topsøe, In Situ high pressure, high temperature XAFS studies of Cu-based catalysts during methanol synthesis, Pages 189-196, Copyright (1991), with permission from Elsevier.

1.5. Structure of this thesis

The following chapters present two inseparable facets of X-ray absorption spectroscopy applied to heterogeneous catalysts: the instrumentation for conducting *in situ* experiments and tools for data analysis.

Chapter 2 presents *in situ* spectroscopic cells for providing the sample environment involving reactions of gases on solid catalysts, used for the present work and projects in collaboration with other research groups. Examples of application as well as technical advantages and drawbacks of the setups are pointed out. The improvement of standard equipment for gas dosing and online gas analysis is likewise presented.

Chapter 3 deals with detailed analysis of the structure of Fe sites in a Fe/Al_2O_3 catalyst, based on the information about the local atomic environment uniquely accessible by EXAFS. For probing the unknown molecular structure, the structural models best matching the experimental data are systematically selected from a library of possible models.

Chapter 4 extends the application of pre-edge spectroscopy at the Fe K-edge to time-resolved XAS data acquired at reaction conditions, where the data quality and resolution are insufficient for resolving the electronic transitions contributing to the pre-edge feature. It is shown using the *in situ* temperature-programmed reduction of Fe/Al_2O_3, that the local coordination and oxidation state of the Fe sites can be probed even with these difficulties. Strengths and limitations of this analysis are presented. The importance of pre-edge analysis is also demonstrated for high-resolution XANES in combination with XES of Fe/ZSM-5, for modelling the complex and understanding the SCR reaction mechanism.

Chapter 5 summarises and concludes on the findings and developments presented in this thesis. An outlook to further developments that are needed and planned in the near future is given.

2. Materials and methods

This chapter describes the technical details of all experiments built up in this thesis work and then carried out within several studies. Firstly, the technical specifications of the capillary micro-reactor and the high-pressure transmission-XAS reactor are given. This is followed by a description of the experimental infrastructure to perform *in situ* XAS experiments: equipment for gas dosing and online gas analysis systems, experiment control, etc. This infrastructure is a new concept built up at ANKA, implemented at the XAS and PDIFF beamlines and planned at the CATACT beamline presently being built, which is a new dedicated EXAFS station for catalysis research. The technical infrastructure for catalysis research is primarily inspired by the recently shut down X1 beamline (DESY, Hamburg), supporting a wide user community conducting catalysis research, e.g. (Grunwaldt & Clausen, 2002, Maier *et al.*, 2011, Ressler *et al.*, 2010). The X1 beamline offered excellent possibilities for the adaptation of equipment brought by users, having an infrastructure for e.g. gas connections including high-pressure lines as well as sufficient space for installing large complex setups. The concept presented herein offers *in situ* equipment on-site, such as that at the Swiss-Norwegian beamlines at ESRF (Grenoble, France), serving primarily the combination of *in situ* characterisation methods (van Beek *et al.*, 2011).

Finally, examples of *in situ* experiments carried out within diploma projects (Sabrina Conrad, Andreas Gänzler) at KIT on Pt/Al_2O_3 catalysts, in collaborations with DTU on V/Al_2O_3 catalysts (Martin Høj), Co/MoS_2 (Jakob Munkholt Christensen) and molybdenum carbides (Qiongxiao Wu), using the presented apparatus are given.

The work on the XAS characterisation of the Fe/Al_2O_3 automotive catalysts has been carried out in collaboration with TU Bergakademie Freiberg (Andreas Pacher and Sven Kureti), who were involved in the synthesis, testing and *ex situ* characterisation (Chapters 3 and 4). The combined HERFD-XANES and V2C-XES on Fe/ZSM-5 (Chapter 4) were carried out in collaboration with Christoph Jacob and Andrew Atkins (KIT) with respect to DFT calculations, as well as Erik Gallo (ESRF) and Hudson Carvalho (KIT), with strong emphasis on the interpretation of the V2C-spectra. Dmitry Doronkin and Maria Casapu (KIT) have dealt with understanding the mechanism of the reaction steps.

2.1. Capillary micro-reactor setup with Gas Blower

A hot-air furnace designed to heating small samples to temperatures up to 900°C and temperature-programmed experiments (Gas Blower, FMB Oxford) (Grunwaldt *et al.*, 2007) was used in this work. It provides effective heat transfer within several millimetres from the nozzle and was used for heating up the capillary micro-reactor. This furnace requires temperature-calibration for every application, and at maximum temperature, a difference of around 100°C is observed between the nominal furnace temperature and that of the sample. To reduce the risk of heat transfer to the surrounding instruments, the metal housing of the Gas Blower is water-cooled.

Figure 10 shows the capillary micro-reactor setup using the Gas Blower, installed for measurements in fluorescence-mode at the XAS beamline at ANKA, oriented at an angle of 45° with respect to the incident beam (first ionisation chamber in the image in the upper left corner) and the solid state fluorescence detector. Due to the plug-flow geometry of the capillary micro-reactor, it is especially useful for studying fast reactions requiring high space-velocities as well as spatially-resolved studies of reactions, where concentration gradients in educts and products occur along the catalyst bed. Capillaries made of quartz, Kapton (polyimide) and sapphire, with outer diameters between 0.5 mm and 3 mm and wall thickness in the range 10-200 μm can be used as reactors.

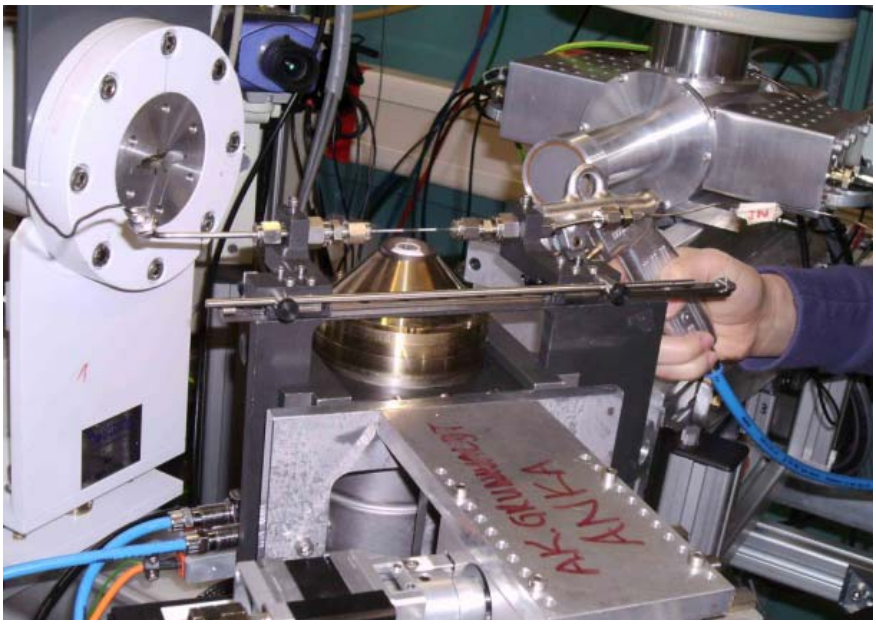

Figure 10 Capillary micro-reactor with Gas Blower, first ionisation chamber (upper left corner) and the fluorescence detector (upper right), at the ANKA XAS beamline. The capillary is placed in the holder above the high-temperature oven, which provides heating by blowing a stream of hot air. The oven is oriented at a 45° angle for fluorescence-mode measurement.

2.2. High-pressure transmission-XAS setup

The high-pressure reactor consists of a stainless steel body with inlet and outlet lines for connecting the reactor to the gas supply. In the centre is a compartment for the powder sample measuring 2 x 10 mm^2 in cross-section and 1, 2 and 5 mm deep for different reactor sizes. On both sides, the reactor is closed with flanges and attached with bolts to seal the vessel and withstand a pressure of 200 bar.

For heating up to 600°C, the high-pressure reactor is enclosed between two shells of an oven with small windows for the X-ray beam. The oven body is thermally isolated, which ensures that heat is well-distributed and not lost. Temperature is monitored by K-type thermocouples inserted into the body of the cell. At the end of the heating program, cooling of the cell can be accelerated with an air flow through channels in the oven. The installation of this setup at the ANKA XAS beamline is shown in Figure 11.

Compared to the capillary micro-reactor, the transmission cell has a different geometry of the catalyst bed. As a result, the plug-flow conditions which can be assumed in the case of the capillary reactor are not as realistic. For this reason, the high-pressure reactor is less suited for studying fast reactions or reactions which require high space velocities to correlate the catalytic activity with the spectroscopic data, as it is important to have well-defined gas concentration gradients or no gradients. On the other hand, this cell has advantages for “slow” reactions, such as temperature-programmed reduction, studied to investigate the transformation of the catalyst during specific treatments rather than the dynamics during a catalytic reaction.

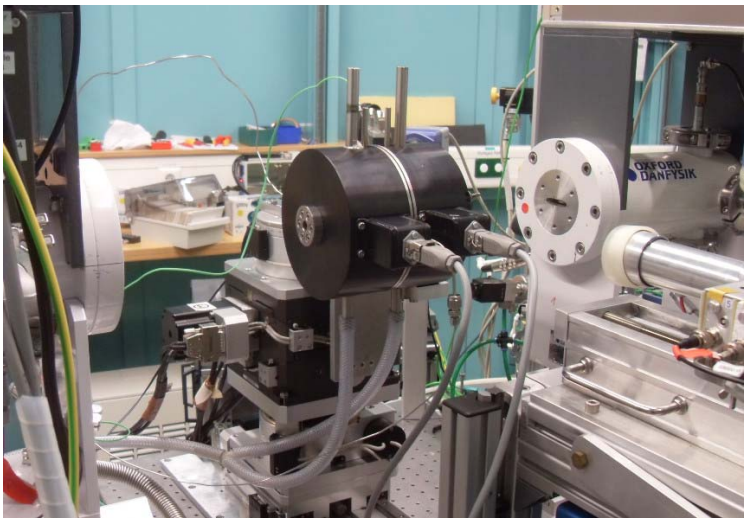

Figure 11 Transmission cell setup installed at the ANKA XAS beamline. The black oven consisting of two shells enclosing the cell is shown along with gas lines, thermocouples and air cooling tubes.

2.3. Pre-requisites for catalysis research at synchrotron beamlines

Catalytic experiments at a synchrotron beamline require sufficient space for the setup and a technical infrastructure for using reactive gases and other media such as pressurised air, cooling water and a user power supply. For safety reasons, the amount of hazardous substances used during the experiments should be kept to a low level. This particularly concerns any gases used; while inert gases or synthetic air are generally harmless (exceptions are large volumes of inert gases due to the danger of asphyxiation), flammable and/or toxic gases (e.g. CO, H_2, NO_x, H_2S, hydrocarbons) constitute a danger and should preferably be used as mixtures diluted with inert gases, typically helium. Exceptions can be made when high concentrations of gases or pure gases are required for the experiments. Access to an exhaust/vent as well as a suitable gas sensors are required.

For experiments involving reactions in of gases over solid catalysts, the setup consists of the catalytic micro-reactor, a gas dosing unit and an online gas analysis system. Figure 12 shows a typical flow scheme for the gas connections, used to study the ammonia-SCR reaction over iron oxide-based catalysts. This gas supply unit is designed for experiments at ambient pressure and can be modified according to the individual experimental requirements. Up to 4 gases can simultaneously be connected to the gas dosing system: the gases are taken from gas cylinders equipped with pressure reduction valves with back pressures typically set to 4 bar. Gases are fed through Teflon or stainless steel gas lines to mass flow controllers (MFCs), which control the flow of each gas. Further downstream, the gases are mixed according to the experimental requirements and fed to the reactor. The total flow rate applied to the reactor is 20-50 mL/min. Vapours of liquids (e.g. water) can be added to the gas flow using a saturator (25 mL) supported on a temperature-controlled stage.

The reactor can be bypassed by directing the gas flow through a tube connected parallel to the reactor in order to either purge the gas lines until the desired gas composition is stabilised and ready to be passed through the reactor or to measure a reference gas flow to be compared with the flow through the reactor to ensure leak-free assembly.

To measure the catalytic activity or monitor the gas composition at the outlet of the reactor, a quadrupole mass spectrometer (QMS, Thermostar, Pfeifer Vacuum) and/or an infrared gas analyser (FTIR, Multigas 2030, MKS) are used. The QMS is connected via a T-piece and continuously takes a negligible sample of the gas (~1 mL/min) from the outlet stream for analysis. QMS gas analysis is well-suited for detection of small stable molecules up to a

molecular mass of ~50 amu (H_2, O_2, N_2, CO, H_2O, CO_2). Molecules with oxo-groups (e.g. NO_x, CO and CO_2) and organic molecules can be well-distinguished by FTIR; this technique is advantageous as it avoids complex fragmentation patterns observed during QMS analysis of reactive molecules. The entire gas sample (flow e.g. 50 mL/min) must pass through the FTIR optical gas cell (volume 250 mL), diluted with a well-defined flow of N_2 (e.g. 200 mL/min, total 250 mL/min) prior to analysis in order to increase the gas exchange rate (e.g. once per minute) for increasing the analysis rate. After analysis, the gas is vented to the exhaust.

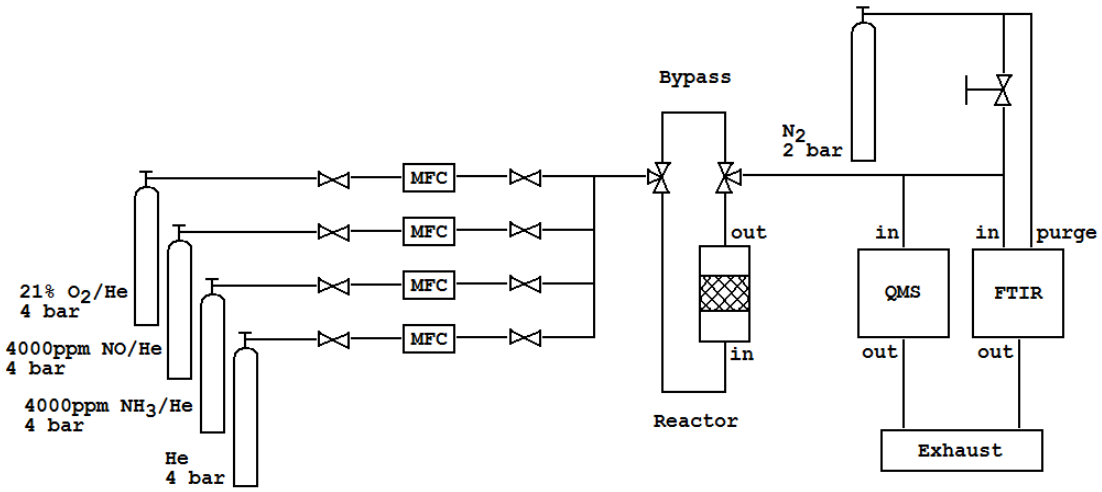

Figure 12 A typical flow diagram for a gas supply and online gas analysis unit used at a synchrotron. Four diluted gases are mixed in appropriate proportions using mass flow controllers (MFC) and fed to the flow reactor. At the exit, the gas composition is analysed by a quadrupole mass spectrometer (QMS) and an infrared gas analyser (FTIR); for the latter the gas flow is diluted with nitrogen, and directed to the vent.

2.4. Mobile integral setup for experimental control

To make the installation of the gas dosing and analysis system at the beamline less time-consuming and more reliable, an integral setup was designed, combining the gas dosing, online gas analysis with high flexibility for studying gas-phase reactions over solid catalysts, at both ambient and elevated pressures. This setup allows experiments related to exhaust-gas after-treatment (CO oxidation, SCR), temperature-programmed reduction and synthesis gas-related reactions at high pressure. The apparatus is mounted on a mobile rack with a pre-installed gas supply system and space for sample environment and gas analysis instruments, shown in Figure 13.

The gas dosing system includes six MFCs (EL-flow, Bronkhorst): two for non-corrosive gases (e.g. O_2, H_2 and inert), two for corrosive gases (e.g. NO_x) with Kalrez gaskets and two for high-pressure experiments with synthesis gas (CO, H_2) up to 50 bar. For this purpose, a

pressure controller is included. The rack is built as a table, with the table plate serving as a panel with gas connections and valves (e.g. bypass/reactor, high/ambient pressure, and QMS connection) and flexibility to modify the gas connections according to the experimental requirements.

The space within the rack accommodates instruments to control the sample environment (Gas Blower regulator, other temperature and pressure regulators) and the gas analysis systems (QMS and FTIR), with all gas and power connections for these instruments preliminarily installed. Additional instruments can easily be added.

A single panel equipped with quick-connect gas fittings allows connection of the required gases, as well as compressed air and cooling water for the Gas Blower and nitrogen for the FTIR. The gas flow rate after the reactor or the FTIR cell can be measured using a flow meter, e.g. Bios Definer DryCal. Finally, all gas lines are directed to a single vent. All electronic devices are connected with a network switch (Cisco) and serial device server (Moxa) via LAN-cables to the network, allowing remote control of the experiment.

This allows many types of experiments to be conducted (different gases and ways of mixing them, different pressure ranges, different forms of gas analysis, etc.), with the additional advantage that the construction of the setup gives the user a clear overview of the connections. This user-friendly experimentation setup is attractive for external research groups and has been successfully applied in several collaboration projects, as outlined in Section 2.7.

2.5. XAS measurements and data analysis

XAS measurements for the present work were carried out at the XAS beamline at the ANKA synchrotron light source (Karlsruhe, Germany) and at the ID26 beamline at ESRF (Grenoble, France).

2.5.1. XANES and EXAFS data acquisition

The XAS beamline at ANKA is a bending magnet beamline with a double-crystal monochromator equipped with Si(111) crystals, providing hard X-rays in the energy range of 2.4 keV - 27 keV with an energy resolution of $\Delta E/E = 2 \times 10^{-4}$. The ANKA storage ring is operated at an electron energy of 2.5 GeV and electron currents of 80-160 mA. At 100 mA ring current, the XAS beamline provides a flux of ca. 5×10^{9} photons/(s·mm^2) at the Fe K-edge.

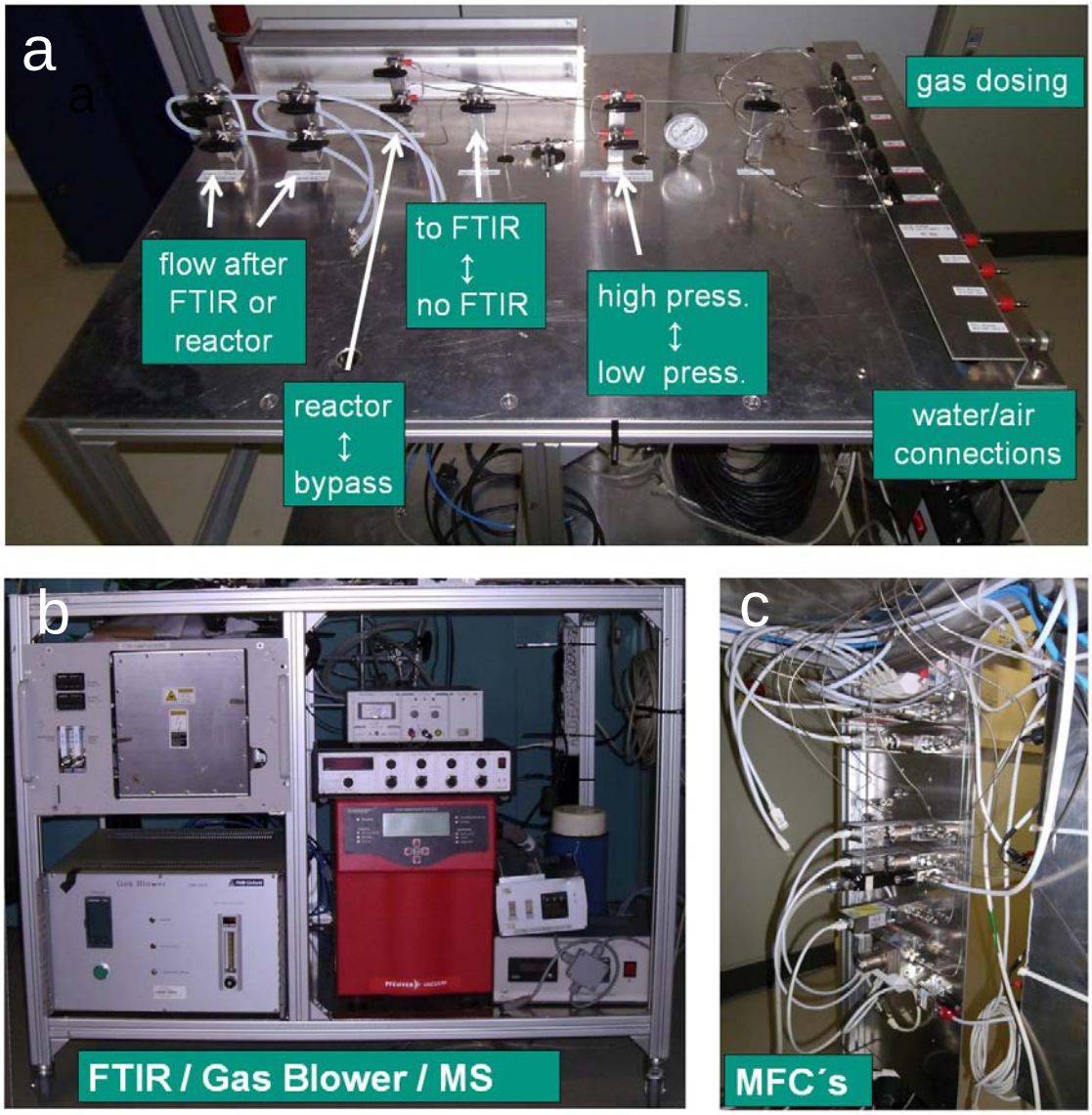

Figure 13 View of the top panel (a), front view (b) and detailed view of the mass-flow controllers (c) installed on the mobile modular setup for experiment control.

The instrumental resolution and the beam profile at the sample position is defined by a system of mechanical slits: for standard resolution measurements, the vertical beamsize is limited to 1.2 mm in front of the monochromator and 1 mm downstream. Under these conditions, the instrumental line broadening is approximately 1.2 eV, determined by radiography (Mangold *et al.*, 2013). The monochromator was operated in continuous scanning mode with data point acquisition in 0.5 eV increments. These energy increments are sufficient to account for the shape of the spectral features, which are influenced by the line broadening due to instrumental resolution and the core-hole lifetime.

For measurements with higher resolution the vertical beamsize was set to 0.3 mm in front of the monochromator and 0.15 mm downstream to decrease the beam divergence. This reduced the instrumental line width to approximately 0.8 eV. These high-resolution spectra were acquired in a step-scanning mode in 0.25 eV energy increments. The horizontal beam dimension was adjusted to the size of the sample: for measuring pellet samples, it was set to 8 mm, and for *in situ* experiments it was adjusted to the smaller sample area with slits downstream the monochromator.

The monochromator was detuned to 70% of the maximum intensity for rejection of higher harmonics. For X-ray absorption measurements in transmission mode, the incoming and transmitted monochromatic intensity was measured using ionisation chambers (Oxford) filled with appropriate mixtures of Ar, N_2 and He to achieve absorption of 15% in the first, 40% in the second and 60% in the third ionisation chamber at 7500 eV, close to the centre of an Fe K-edge EXAFS scan interval. The sample was placed between the first and second ionisation chamber and a Fe foil between the second and the third. The absorption coefficient was calculated according to the Lambert-Beer law. Measurements in fluorescence mode were carried out using an energy-dispersive 5-element solid-state Ge detector (Canberra, line width of 300 eV, peaking time of 500 ns) or a Si-drift detector (Vortex). The Fe Kα fluorescence (6400 eV) was selected as region of interest (window 6100-6700 eV). For full EXAFS scans, the energy-range of 6962-8112 eV was scanned continuously in 5 minute sweeps; data points around the absorption edge (7092-7132 eV) were sampled in 0.5 eV increments and points outside of this range in 1 eV increments. The signal-to-noise ratio was improved by averaging approximately 150 scans. The energy calibration was stable during all scans; statistical uncertainties in energy position were below 1 eV. Alternatively, step-scanning data sets with long integration times were recorded. For time-resolved XANES measurements, shorter energy-ranges were continuously scanned with a higher frequency (ca. 4 min per spectrum including time between scanning).

Higher-resolution *in situ* measurements were conducted at the MAX-lab synchrotron radiation facility (Lund, Sweden) at the I811 beamline, using wiggler radiation and beam collimation, thus avoiding the effect of instrumental broadening due to angular divergence. The beam was focused at the sample to a spot of 0.5 x 0.5 mm^2 with an intensity of 10^{11}-10^{12} photons/second. The instrumental line width was ca. 0.7 eV. The photon energy was scanned in continuous mode using a double-crystal monochromator equipped with Si(111) crystals, recording data points in 0.1 eV increments. Acquisition of one spectrum took ca. 5 minutes.

2.5.2. HERFD-XAS and V2C-XES data acquisition

High-energy-resolution fluorescence-detection (HERFD)-XANES and valence-to-core (V2C)-XES measurements were carried out at the European Synchrotron Radiation Facility (ESRF, Grenoble, France) at the high-resolution X-ray spectroscopy beamline ID26. This beamline is equipped with three mechanically independent undulators providing a flux of 10^{13} photons per second at the sample position. A Si(111) double-crystal monochromator was used to select the photon energy. The Johann-type spectrometer was equipped with five spherically bent (r = 1 m) Ge(620) analyser crystals in Rowland geometry with respect to the sample and the detector. The counts detected by the avalanche photo-diode detector were normalised by the count rate of the incident beam measured with a photodiode between the slits and the sample. The beam size was 1 mm x 4 mm.

The HERFD-XANES spectra at the Fe K-edge (7112 eV) were measured by scanning the incident energy in the range 7080-7200 eV and detecting the fluorescence at the maximum of the Fe $K\beta_{1,3}$ emission line (e.g. at 7058.81 eV). The instrumental energy bandwidth for HERFD-XANES (scanning the incident energy and detecting the emission of a single energy) was FWHM = 1.4 eV, determined from the shape of the elastic scattering peak at 7113 eV. This is higher than the Fe K-edge spectral broadening (ca. 1.25 eV (Krause & Oliver, 1979), but is nevertheless no obstacle for clearly resolving the pre-edge features. Due to the high-resolution detection, these transitions are well-separated from the main edge onset and require minimal or hardly any extraction (Heijboer *et al.*, 2004). Prior to analysis of the pre-edge feature (Chapter 4), the spectra were normalised using a straight line fitted in the EXAFS region (7500-7900 eV) of a subsequently measured long energy scan with a coarse step size, and corrected for incident-beam self-absorption (see next section).

The XES spectra were recorded by setting the excitation (incident) energy of 7145 eV, far above the Fe K-edge, and scanning the emission energy in the range 7010-7140 eV, covering the Fe $K\beta'/K\beta_{1,3}$ emission lines and the Fe $K\beta''/K\beta_{2,5}$ (V2C) lines. The processing and interpretation of the V2C-XES data is outside the scope of this thesis, but is complementary to the HERFD-XANES spectroscopy, as outlined in Chapter 4 and (Boubnov *et al.*, 2014).

2.5.3. Correction of incident-beam self-absorption for higher loading of Fe

Incident beam self-absorption (IBSA) effects distort fluorescence-mode spectra (in this case HERFD-XANES) of samples containing the element of interest, in this case Fe, in relatively high amounts. The IBSA-effects were corrected by factors determined for α-Fe_2O_3 with

varying concentration. This method is empirical and requires knowledge of the edge jump at the Fe K-edge (in transmission mode) of the samples studied in fluorescence mode. It is assumed that the IBSA-distortion found in optically thin and dilute reference samples can be transferred to similar samples. XANES spectra of a series of cellulose pellets (ca. 1 mm thickness) containing α-Fe_2O_3 adjusted for edge jumps at the Fe K-edge of 0.1, 0.3, 0.5, 0.9 and 1.1 were measured in simultaneous transmission/fluorescence mode (installed at 45° with respect to the incident beam) at the XAS beamline of the ANKA synchrotron light source (Karlsruhe, Germany). The IBSA-correction functions were expressed in terms of the absorption coefficient in normalised transmission spectra $\mu_T(E)$ and the IBSA-distorted fluorescence spectra $\mu_F(E)$. IBSA-distortion depends on the value of μ_F and is independent of the incident energy E. The correction of the IBSA-distorted μ_F can thus be achieved by scaling every point by the difference function μ_T-μ_F. For $0 < \mu_F < 1$, μ_T-μ_F is negative (the IBSA-distorted absorption coefficient seems larger and must be corrected by a negative value) and for $\mu_F > 1$, μ_T-μ_F is positive, meaning that the IBSA-distorted absorption coefficient is under-estimated and must be corrected by a positive value. The weight of the correction function was found to be linearly proportional to the edge jump in the given interval. A HERFD-XANES spectrum was measured of one of the α-Fe_2O_3 pellets and the IBSA-correction terms were calculated using this linear relationship for the other samples and the catalyst in the capillary, as their edge jump was known in advance.

2.5.4. Issues with fluorescence-mode measurements

Measurements were carried out in fluorescence-mode since the absorption by Fe was significantly lower than the total absorption of the sample. Measuring Fe-specific fluorescence is particularly challenging due to the fact that iron is highly abundant in stainless steel, which is one of the main constituents of the setup. In order to decrease the amount of fluorescence excited by the X-ray beam scattered from the setup materials, the stainless steel components of the capillary setup (Swagelok tubes, etc.) were covered with Al foil. This can further be improved by replacing the stainless steel parts with corresponding Teflon components.

2.5.5. Pre-edge, XANES and EXAFS analysis

The raw XAS data were processed using the Athena interface of the IFEFFIT software package (Ravel & Newville, 2005). All Fe K-edge spectra were calibrated to the first inflection point in a simultaneously measured Fe foil spectrum set at 7112.0 eV. Note that this

value varies from study to study, e.g. 7111.08 eV (Wilke *et al.*, 2001) and 7111.2 eV (Westre *et al.*, 1997)). Subsequently, the XAS spectra were normalised using a first-degree polynomial fitted below the edge and a second-degree polynomial fitted above the edge.

Analysis of the XANES spectra was carried out using linear combination analysis (LCA). LCA was used to determine the stoichiometric ratios of the Fe species in the binary mixtures of reference compounds and to determine the oxidation state of iron during the *in situ* XANES/TPR experiments, using the first and last spectrum of the TPR series as reference spectra. LCA was carried out in the energy range between below the pre-edge region (e.g. 7102 eV for the 1% Fe/Al_2O_3 catalyst) and the first isosbestic point above the first maximum beyond the edge (e.g. 7155 eV for the 1% Fe/Al_2O_3 catalyst).

Pre-edge spectra were extracted from the near-edge structure (XANES) and the HERFD-XANES spectra by using an arctangent function and a first-degree polynomial, modelling the onset of the absorption edge. The extracted pre-edge peak was de-convolved by a variable number of pseudo-Voigt peak functions, allowing the FWHM to float at around 2-3 eV. The contributions centred above 7115 eV were omitted (Wilke *et al.*, 2001).

The extended fine structure (EXAFS) was extracted, transformed into k-space of the photoelectron and scaled by k^3 to amplify the oscillations at high k-values. EXAFS refinement was carried out using the Artemis interface of the IFEFFIT software. The spectra were Fourier-transformed between 2.0-12.0 $Å^{-1}$ and analysed in R-space in a range of 1.0-3.5 Å. According to the Nyquist criterion, a maximum of 15 parameters can be extracted from the EXAFS data in these ranges. Back-scattering phase shifts and amplitudes for relevant scattering paths were calculated by FEFF6.

2.6. Catalyst synthesis and characterisation

2.6.1. Fe/Al_2O_3 catalyst synthesis

The Fe/Al_2O_3 catalysts were prepared by Marina Tepluchin and Andreas Pacher (as part of their Ph.D. projects) by incipient wetness impregnation of γ-Al_2O_3 (Sasol, calcined at 600°C; BET surface area 184 m^2/g) with an aqueous solution of ferric nitrate nonahydrate (Sigma-Aldrich) aiming at total Fe loadings of 0.1-1 wt.%. The powder samples were dried and calcined at 500°C. Catalytic performance of the materials for CO oxidation is assessed elsewhere (Tepluchin *et al.*, 2014). Catalytic data for NH_3-SCR over Fe/BEA catalysts is

taken from (Balle *et al.*, 2009) and same procedures are used for assessing the catalytic performance for NH_3-SCR over Fe/Al_2O_3.

The Fe/BEA catalyst was prepared by incipient wetness impregnation of the BEA zeolite to obtain a Fe-loading of 0.5% by weight (Høj *et al.*, 2009)

2.6.2. Sample preparation for XAS

For *in situ* TPR measurements, a sieve fraction of 100-200 µm catalyst powder was exposed to a flow of 5% H_2 in balance He in a quartz capillary micro-reactor, similar to setup in (Grunwaldt *et al.*, 2005, Høj *et al.*, 2009, Klukowski *et al.*, 2009).

For *ex situ* measurements, the samples were mixed with cellulose and pressed into pellets. The amount of catalyst for each sample was chosen to achieve a total absorption of 1, i.e. to constitute one absorption length (see Section 1.4.2). Under these conditions, the absorption step at the Fe K-edge is around 1% of the total absorption for a 0.1% Fe/Al_2O_3 catalyst, which makes transmission-mode measurements unsuitable due to the low signal-to-noise ratio. Fluorescence-mode measurement is on the other hand well-suited. Due to the low content of iron, incident-beam self-absorption effects did not influence the XAS spectra, which was confirmed by comparing XANES spectra acquired in fluorescence yield-mode and transmission-mode.

Sample preparation was considered to be a crucial issue for spectroscopy, as the preparation tools can contaminate the iron-containing samples. Mössbauer spectroscopy has confirmed that the Fe/Al_2O_3 catalysts under consideration exclusively contain trivalent iron species, but detection of metallic iron by XAFS in some of the samples suggested that they were contaminated. It is therefore very important to take prevent iron-contamination during mortaring, pressing and sieving the samples e.g. by placing circles of paper on top and underneath the sample inside the pressing tool in order to avoid contact with the stainless steel parts.

2.6.3. X-ray powder diffraction

X-ray powder diffraction (XRD) patterns were acquired using a Bruker D8 Advance lab diffractometer and CuKα radiation (λ = 1.54 Å) over a 2θ-range of 20-80°. The electrons were accelerated by a potential difference of 40 kV, yielding an anode current of 35 mA. The (440) reflection was fitted with a Lorentzian-shape peak function for determining the lattice spacings d_{hkl} and the average crystallite sizes D_{ave} according to Bragg's law $d_{hkl} = \lambda/(2\cdot\sin\theta)$

and the Scherrer equation $D_{ave} = 0.9 \cdot \lambda/(\beta \cdot \cos\theta)$ respectively, where λ is the wavelength of the X-rays, 2θ the scattering angle, and β is the FWHM of the reflection in radians. The scattering angle and FWHM of the 5 other reflections were calculated from the parameters obtained using the (400) reflection. The shape of the reflections was approximated as pure Lorentzian due to the fact that the diffractometer is able to resolve peaks much narrower than those characteristic for γ-Al_2O_3.

2.6.4. Transmission electron microscopy

The structure and morphology of the γ-Al_2O_3 support was studied by transmission electron microscopy (TEM) using a Philips CM200 FEG microscope operated at 200 kV acceleration voltage (done by Winfried Send at the Laboratory for Electron Microscopy, KIT). The sample was dispersed in acetone in an ultrasonic bath and deposited on a lacy carbon copper TEM grid. High-resolution TEM (HRTEM) images were recorded with a CCD camera at a magnification corresponding to pixel resolution of 10 pixels per Å. The images were processed using ImageJ (*ImageJ software at National Institutes of Health*). Several well-resolved particles were selected and a fast Fourier transform was applied to analyse the periodicity and direction of the lattice planes visible in the image. From the lattice spacing determined in Fourier-space the lattice planes were identified in terms of their Miller indices.

2.6.5. ^{57}Fe Mössbauer spectroscopy

Mössbauer spectra were recorded under ambient conditions using a conventional spectrometer equipped with a ^{57}Co source (3.7 GBq) in a Rh matrix. In order to produce a sample for Mössbauer spectroscopy with a sufficient amount of the active isotope, the synthesis protocol decribed earlier was repeated with an iron nitrate precursor prepared by dissolving ^{57}Fe (Campro Scientific) in nitric acid. The sample was inserted inside an Oxford Instruments Mössbauer-Spectromag 4000 Cryostat, where temperatures as low as 3 K could be achieved by pumping the sample space. The spectra were recorded in constant-acceleration mode in the velocity range between -11 mm/s and +11.0 mm/s at 3 K, 200 K and 300 K. Isomer shifts are given relative to α-Fe at room temperature.

2.7. Experiments with *in situ* XAS micro-reactors

The setups for *in situ* spectroscopy were applied in projects with diploma students (Boubnov, Gänzler*, et al.*, 2013, Gänzler *et al.*, in preparation) and several internal and external collaborations (Christensen *et al.*, 2010, Høj *et al.*, 2013, Wu *et al.*, in preparation). In the

following sections a few representative examples of *in situ* XAS experiments conducted with the capillary setup and the high-pressure cell are given.

2.7.1. Oscillatory CO oxidation over Pt/Al_2O_3 catalysts

To gain a deeper insight into the oscillatory kinetics of catalytic CO oxidation over supported Pt/Al_2O_3 catalysts in an excess of oxygen, temporally and spatially resolved XAS and IR-thermography studies were carried out using the capillary reactor, described in (Boubnov, Gänzler*, et al.*, 2013, Gänzler *et al.*, in preparation).

The oscillatory conversion of CO to CO_2 was observed over a catalyst with 1 nm Pt particles at temperatures in the range 100-150°C, corresponding to conversion light-off from ca. 10% to 100%. In this regime, an unstable catalytic phase was assumed to periodically evolve and vanish. Filming the capillary micro-reactor during the reaction using an IR-camera (FLIR) uncovered that during the increase in CO_2-production, a hot-spot (temperature difference of 1-2 K) appeared at the reactor outlet, moved towards the inlet and extinguished (Figure 14a-b). Complementarily, time-resolved XANES measurements at the Pt L_3-edge using a focused X-ray beam (at the SuperXAS beamline at SLS, Villigen, Switzerland) were conducted at several positions of the capillary (Figure 14c-d). Simultaneous with the increase of CO_2-production, the Pt became periodically oxidised and then again reduced. The duration of the oxidised state was longest at the reactor outlet, shorter towards the middle and no oxidation was observed at the inlet.

These results revealed an interesting reaction mechanism: the CO-molecules adsorbed on a reduced Pt surface suddenly became oxidised by oxygen at the outlet, leaving the catalyst in an oxidised state and producing heat detectable by an IR-camera. This exothermic reaction front progressed towards the reactor inlet, oxidising the adsorbed CO-molecules and the Pt surface. Subsequently, the reaction front extinguished, the Pt surface became reduced by CO molecules re-adsorbing on it and the CO-conversion returned to the initial level. The extinguishing was possibly favoured due to re-adsorption of CO closer to the reactor inlet where its concentration is higher and due to the cooling of the hot spot by the flowing gas.

The high space velocity and plug-flow dynamics in the capillary reactor allowed a good observation and understanding of this phenomenon. For IR-thermography, an IR-transparent sapphire capillary was used, while XAS was conducted using a quartz capillary. The two techniques excellently illustrated the versatility of the capillary micro-reactor setup.

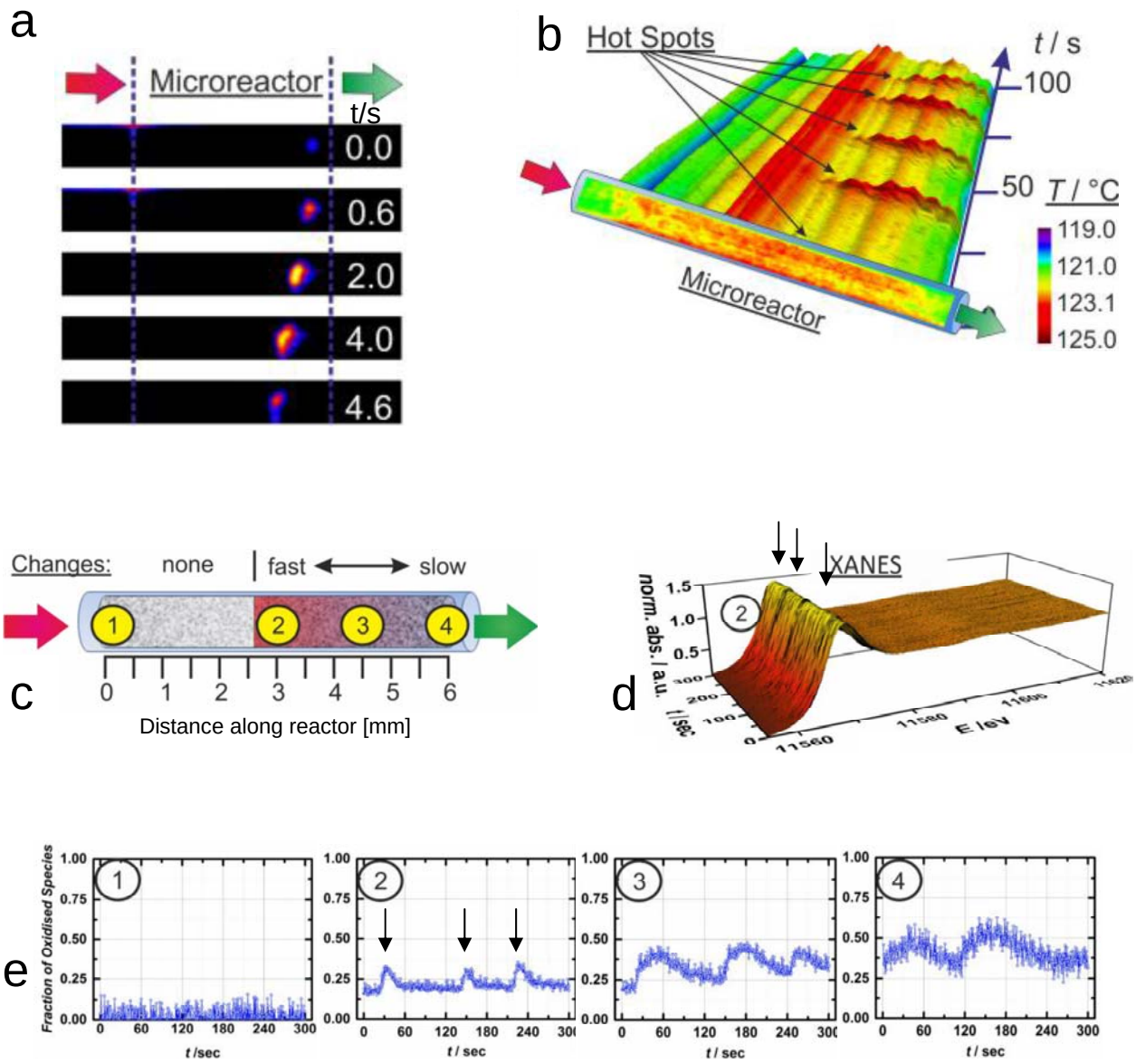

Figure 14 Temporally and spatially resolved oscillatory CO oxidation over 4% Pt/Al_2O_3 studied in the capillary micro-reactor. Hot-spot evolution observed using IR-thermography while applying a temperature of 120°C (a-b). The micro-reactor was filmed with an IR-camera; differential images at indicated time in seconds since the initiation of the hot spot at the outlet (a) and a line profile along the micro-reactor versus time (b). Oxidation state of Pt determined using XAS at 110°C (c-e), indicating the probed positions in the catalyst bed (1-4), an example of Pt L_3-edge XANES spectra acquired at position 2 (d) and the extent of oxidation of the Pt at the four positions (e). The three jumps in oxidation state captured at position 2 are indicated by arrows in (d) and (e). Gas composition 1000 ppm CO + 10% O_2 in balance He, total flow 50 mL/min. The gas flow direction is indicated with thick arrows (red at inlet, green at outlet).

2.7.2. Oxidative dehydrogenation reactions over flame-made V/Al_2O_3 catalyst

A series of V_2O_5/Al_2O_3 catalysts with varying V-loading prepared by flame-spray pyrolysis was studied *in situ* during oxidative dehydrogenation of propane to propene under hydrocarbon-lean and -rich conditions (Høj *et al.*, 2013), see Figure 15. In order to optimise the X-ray absorption by V, a very small amount of sample was required. At the V K-edge, the Al_2O_3 in the sample absorbed most of the X-rays. The fact that the catalyst was flame-made was highly advantageous, as the material was of a very low density and a sieve fraction could be loaded directly into the reactor, providing high-quality XAFS spectra.

The choice of the reactor for these studies was based on the fact that the absorption of photons with a specific energy by graphite (used as window material on the transmission-XAS cell (Bazin et al., 1996)) is ca. a factor of 10 lower than quartz (in the case of the capillary reactor). This means that a capillary micro-reactor with a 20 µm wall thickness would be equally suited for the XAS studies of this catalyst as the transmission-XAS cell with 200 µm thick graphite foil windows. For this reason, both reactors were used for the measurements. By choosing a transmission-XAS cell with an appropriate sample compartment, the sample thickness required for an optimal edge jump could be varied between 1, 2 and 5 mm.

It was noted, however, that under some conditions, the propane was fully combusted to CO_2 and H_2O, indicating that the gas tubes of the transmission cell were contaminated (possibly with noble metal catalyst material) and were combusting the propane when the temperature was sufficiently high. The problem of contamination was solved by using the quartz capillary setup, where only the catalyst bed and the surrounding quartz was heated and a new capillary was used for each experiment.

To monitor the gas composition at the reactor outlet, FTIR gas analysis was used. The high sensitivity was advantageous for detecting the low product yields due to the very small amount of catalyst material used.

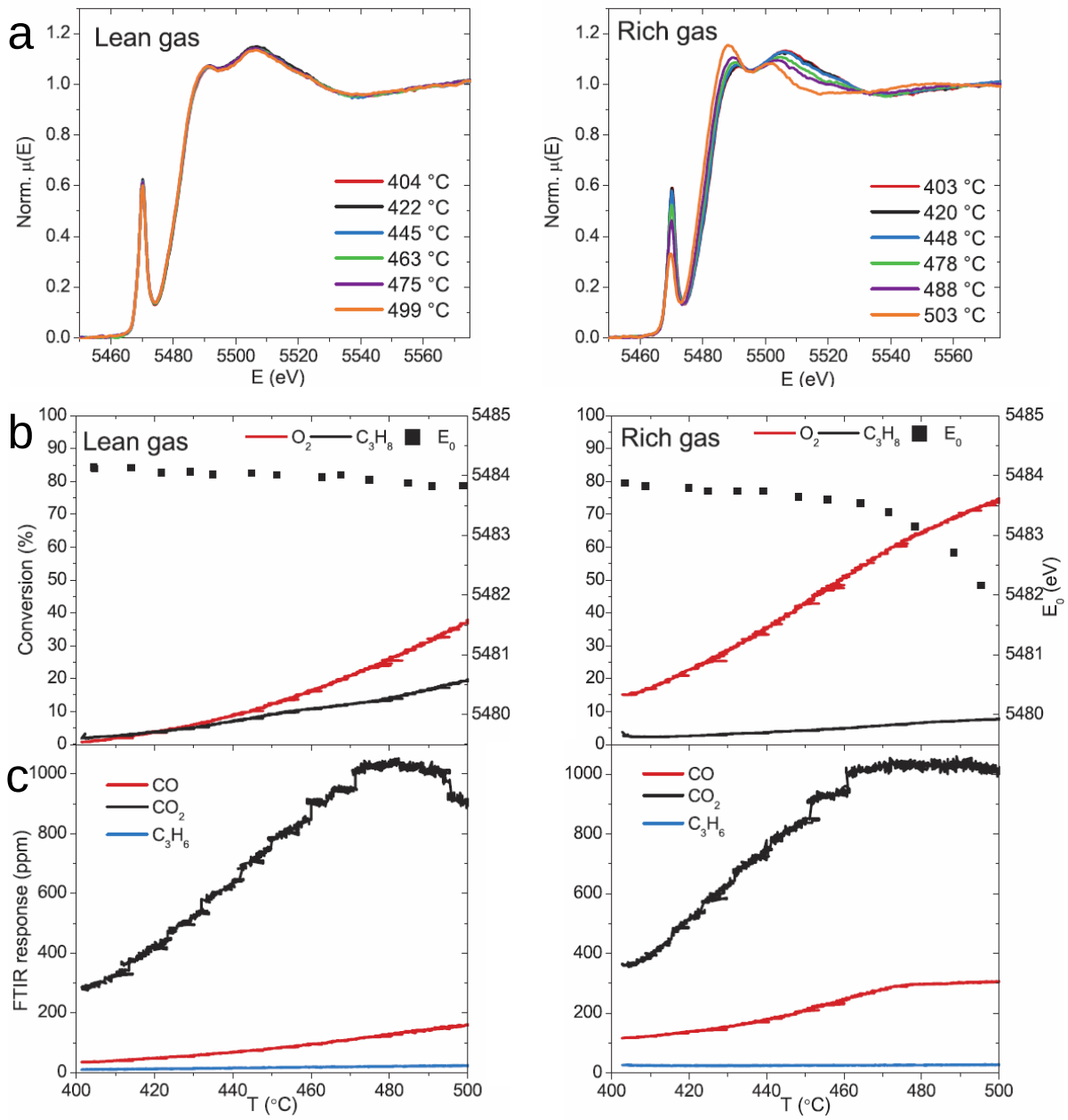

Figure 15 *In situ* XANES at the V K-edge (a) of a 7.5% V/Al_2O_3 catalyst during oxidative dehydrogenation of propane to propene in a lean gas (6.7% O_2 + 2.5% C_3H_8 in He) and a rich gas (3.3% O_2 + 5.0% C_3H_8 in He). The conversion of the gas components (b) and evolution of the products CO_2, CO and propene (c) can be correlated to the absorption edge position (b). The shift in energy and the changes in the XANES spectra especially seen during exposure of the catalyst to the rich gas correspond to the reduction of V^{5+} to $V^{3+/4+}$ (Høj *et al.*, 2013) Reprinted from Applied Catalysis A: General, Vol. 451, M. Høj, A. D. Jensen and J.-D. Grunwaldt, Structure of alumina supported vanadia catalysts for oxidative dehydrogenation of propane prepared by flame spray pyrolysis, p. 207-215, Copyright (2013), with permission from Elsevier.

2.7.3. Synthesis gas ageing of Co/MoS_2 alcohol synthesis catalyst

The *in situ* reduction and ageing of alkali-promoted Co/MoS_2 catalysts in synthesis gas for higher alcohol synthesis (Christensen *et al.*, 2010) were studied at the Co K and the Mo K absorption edges using the transmission-XAS cell. In order to optimise the absorption of the sample, a thin layer of granulated catalyst was filled into the cell and covered with a layer of boron nitride. Care must be taken at this point, as the layers must be very homogeneous to avoid an impact on the spectral quality. For the ageing experiment, 2% CO + 2% H_2 in balance He was used as a model for synthesis gas. In order to make sure that the cell was leak-tight, aluminium foils sandwiched between graphite foils were used as X-ray windows.

During heating in synthesis gas, an increasing Ni K-edge (8333 eV) absorption was observed at the high-energy end of the EXAFS spectra at the Co K-edge (7709 eV). It was assumed that Ni-contamination was due to volatile nickel carbonyls originating from the reaction of CO with nickel parts of a pressure-reduction valve. In succeeding experiments, the carbonyl species were removed from the gas flow by using an active carbon filter at the inlet of the reactor.

2.7.4. The carburisation of molybdenum oxide: a combined XAS/XRD study

In situ XAS and XRD measurements were combined to study the carburisation of molybdenum trioxide to molybdenum carbide with methane (Wu *et al.*, in preparation). The experiments were carried out at the Swiss-Norwegian beamlines at ESRF using a high-pressure capillary setup available at that beamline (Karaca *et al.*, 2011). The XAS and XRD measurements were carried out interchangeably (quasi-simultaneously) one after the other by running a procedure that repeatedly exchanges dedicated monochromators for the two techniques. XAFS spectra were recorded at the Mo K-edge in transmission geometry by measuring the intensities of the ionisation chambers, while powder XRD patterns were acquired with a high-resolution diffractometer on a goniometer at a constant X-ray wavelength of 0.503 Å. A sieve fraction of MoO_3 was loaded into a quartz capillary of 0.5 mm diameter. The sample was exposed to a flow of pure methane and heated at 5°C/min up to 750°C.

Figure 16 shows the temperature-dependent XRD patterns and the XANES spectra side by side. These results revealed that the transformation of MoO_3 to MoO_2 took place at around 390°C and from MoO_2 to Mo_2C at around 530°C. Complementary *in situ* XAS/XRD data proved that the phase transformations of the material and of the electronic structure of Mo occured at the same temperature, at the same time. An *in situ* XAS/XRD study also revealed the mechanism of a CuNi alloy formation depending on the ratio of the two metals (Wu *et al.*, 2014).

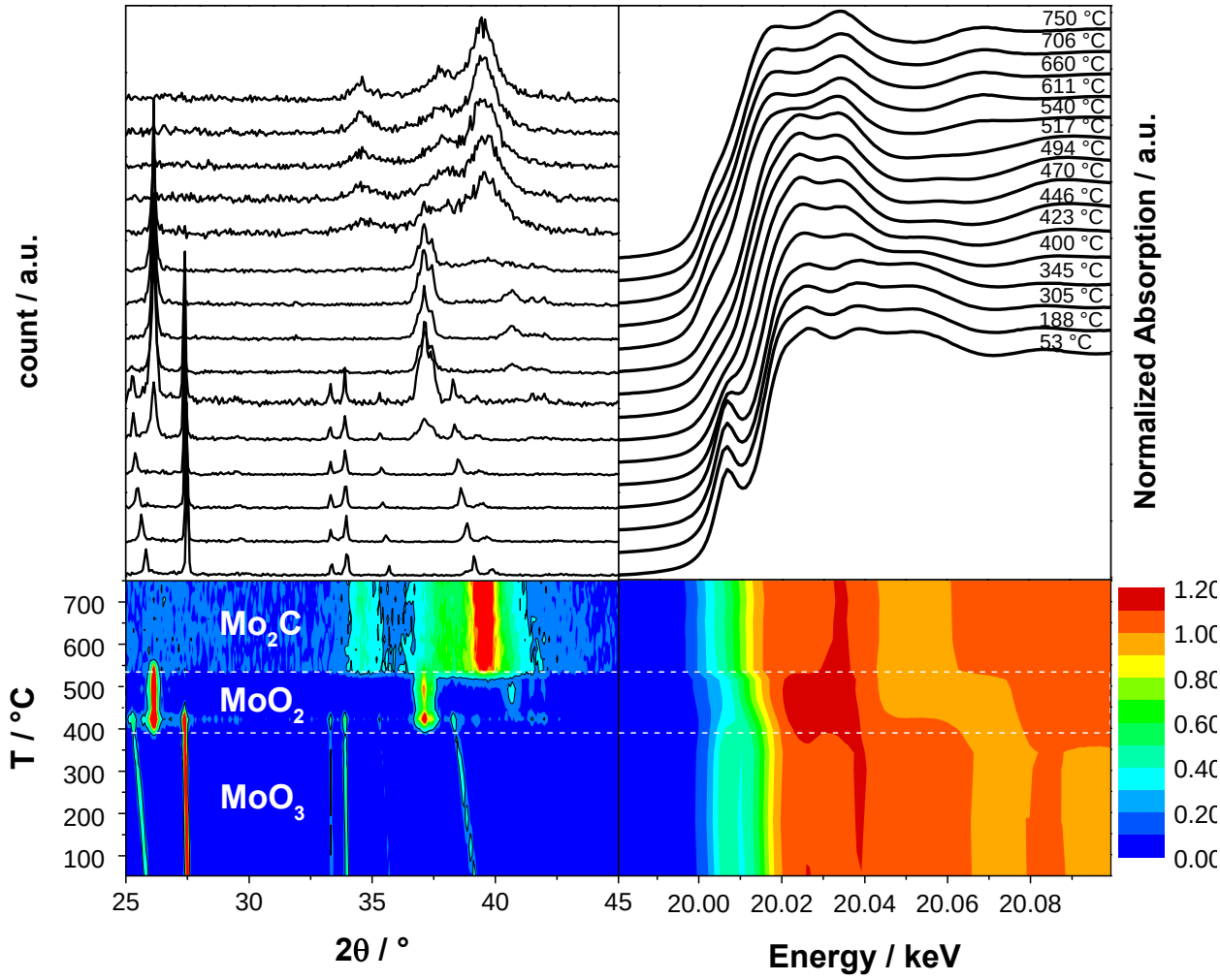

Figure 16 Combined quasi-simultaneous *in situ* XRD (left) and XANES spectra (right) during methane-carburisation of molybdenum trioxide, showing phase transformations $MoO_3 \rightarrow MoO_2 \rightarrow Mo_2C$ (Wu et al., in preparation).

3. Structure of Fe centres in Fe/Al_2O_3-based catalysts for automotive application

This chapter addresses the reactivity and structure of recently studied Fe/Al_2O_3 catalysts, which were found active for CO oxidation (Tepluchin *et al.*, 2014) and for NH_3-SCR. Firstly, the catalytic performance in NH_3-SCR is compared between Fe catalysts supported on BEA-zeolite and on γ-Al_2O_3. Next, the reducibility of the Fe sites is studied by *in situ* XANES spectroscopy at the Fe K-edge, while conducting a temperature-programmed reduction. Finally, the structure of the Fe centres on γ-Al_2O_3 is addressed by EXAFS. For analysing the EXAFS spectra, a library of possible structures of Fe on γ-Al_2O_3 is created, since the exact structure is not known. Suitable structures for a detailed EXAFS analysis are pre-selected using a procedure developed in this work. The identified structure of Fe/Al_2O_3 is discussed with respect to that of Fe on zeolites, attempting to explain the inferior activity of the former.

This work is a part of a larger project in collaboration with Sven Kureti, Andreas Pacher and Marina Tepluchin, involving catalyst preparation, characterisation and testing from their side. TEM work was done at the Laboratory for Electron Microscopy (KIT) with Winfried Send and Mössbauer spectroscopy was done at the Institute for Inorganic Chemistry (KIT) by Valeriu Mereacre. DFT-based structure optimisation was carried out by Matthew Kundrat and Christoph Jacob (KIT). The XAS study presented as part of this thesis was done at ANKA with Stefan Mangold. Catalytic data for the Fe/BEA catalyst is taken from (Balle *et al.*, 2009) and raw XAS data of the Fe/BEA catalyst was obtained from the authors of (Høj *et al.*, 2009).

3.1. Catalytic performance of Fe supported on BEA zeolite and γ-Al_2O_3

The catalytic performance for standard NH_3-SCR under oxygen-rich conditions was studied in terms of the conversion of the pollutant NO and the reductant NH_3 (Figure 17), which were dosed in equal concentrations. Compared to the two Fe/Al_2O_3 catalysts, the performance of Fe/BEA for NO-removal was superior, lower amounts of catalyst material were required (200 mg and 1000 mg respectively), and conversion started at lower temperatures. For all three catalysts, NO reacted with NH_3 to selectively yield N_2 up to a conversion of ca. 20%, after which the oxidation of NH_3 counteracted the selective removal of NO. Thus, the role of the support has a large impact on the catalytic activity along with the type and nuclearity of the Fe sites, arising from different Fe loadings applied during synthesis.

In the following sections, the reducibility and structure of the Fe centres is examined using XAS in order to investigate the role of γ-Al_2O_3 as a support.

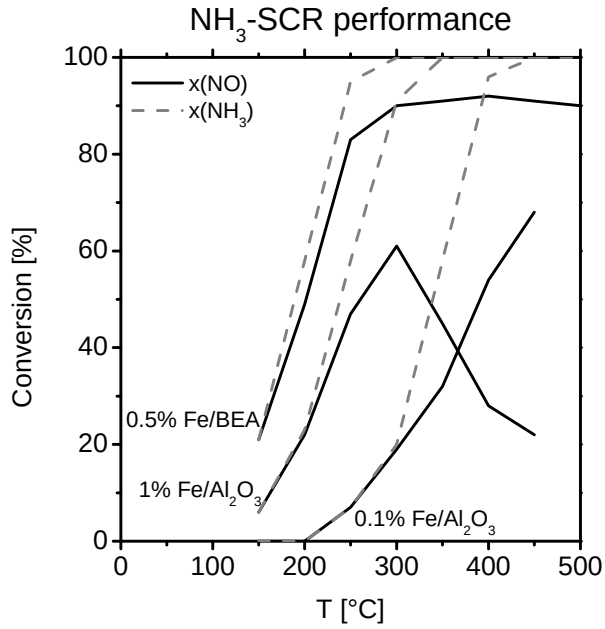

Figure 17 Conversion of NO and NH_3 during NH_3-SCR testing. Inlet gas composition: 500 ppm NO + 500 ppm NH_3 + 5% O_2, balance N_2. Total flow 500 mL/min. The amount of catalyst used was 200 mg for the 0.5% Fe/BEA and 1000 mg for the 0.1% and 1% Fe/Al_2O_3. Data for the Fe/BEA catalyst was taken from (Balle *et al.*, 2009) and for 0.1% and 1% Fe/Al_2O_3 catalysts measured by Andreas Pacher.

3.2. Reducibility of Fe sites on BEA zeolite and γ-Al_2O_3

Evidence exists that zeolite-supported Fe^{3+} sites are partially reduced to Fe^{2+} during the NH_3-SCR process (Klukowski *et al.*, 2009, Høj *et al.*, 2009), suggesting that the reduction of NO by NH_3 occurs through intermediate reactions with the Fe centres. During *in situ* XAS studies of Fe/Al_2O_3 catalysts (not shown) this reduction was not observed, indicating that the reducibility of the Fe sites is important for the catalytic reaction.

The reducibility of the Fe sites was probed by temperature-programmed reduction (TPR) of the catalyst in a flow of 5% H_2/He, while following the oxidation state of the Fe centres by recording Fe K-edge XANES spectra. The *in situ* XANES spectra acquired during TPR of the 1% Fe/Al_2O_3 catalyst are shown in Figure 18a. The shift of the pre-edge peak (inset of Figure 18A) from 7114 eV to 7112 eV and the shift of the absorption edge by 5 eV to lower energies are evidence of the reduction of Fe^{3+} to Fe^{2+}. Isosbestic points at e.g. 7130 eV and 7155 eV indicate that only two types of species are involved in this transformation. The metallic state

of Fe was not observed in this experiment, supporting the observation of well-dispersed Fe oxo-clusters which are stabilised against sintering and therefore avoiding full reduction.

The oxidation state of Fe was estimated by linear combination analysis (Figure 18b), using the first and last spectrum of each series as reference spectra for Fe^{3+} and Fe^{2+} species respectively. The results reflect the reduction profile, with the onset of significant structural changes above ca. 350°C for the Fe/Al_2O_3 catalyst, while the reduction of Fe in the Fe/BEA catalyst is complete at ca. 300°C. This discrepancy in reduction temperatures can be correlated to the significantly lower NH_3-SCR performance of the Fe/Al_2O_3 system compared to Fe on BEA-zeolite.

The necessity of high reduction temperatures in case of the Fe/Al_2O_3 system is possibly due to the tight attachment of the Fe sites to the γ-Al_2O_3 matrix. As a next step, the structure of the Fe sites was revealed by EXAFS spectroscopy.

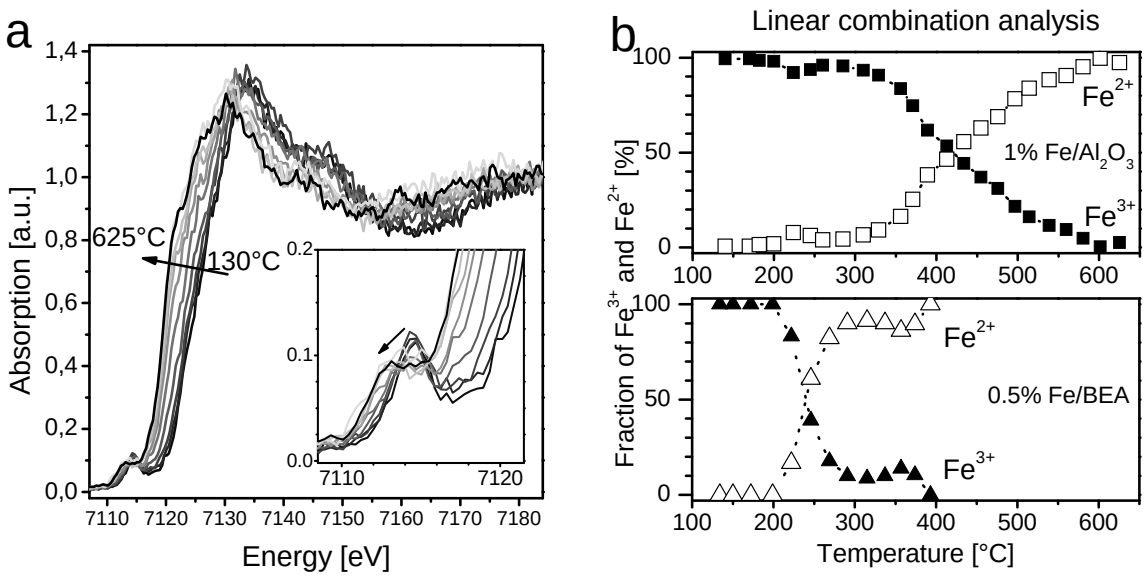

Figure 18 (a) Continuous-scanning *in situ* XANES spectra of the 1% Fe/Al_2O_3 catalyst during hydrogen-TPR: selected spectra recorded in the temperature range 130°C-625°C. Inset shows details of the pre-edge features from the same series of spectra (not extracted). (b) Results of linear combination fitting (1% Fe/Al_2O_3 and 0.5% Fe/BEA zeolite for comparison) using the initial and final XANES spectra in the series as reference spectra (cf. text). Reprinted from Journal of Physics: Conference Series 430, A. Boubnov, H. Lichtenberg, S. Mangold and J.-D. Grunwaldt, Structure and reducibility of a Fe/Al_2O_3 catalyst for selective catalytic reduction studied by Fe K-edge XAFS spectroscopy, Journal of Physics: Conference Series 430 (2013) 012054, Copyright (2013), with permission from IOP Science.

3.3. Identification of the structure of Fe on γ-Al_2O_3 by EXAFS

3.3.1. EXAFS models for supported dispersed Fe catalytic sites

Bond distances and coordination numbers of the atomic environment of the Fe absorber were determined by extended X-ray absorption fine structure (EXAFS). The results were refined using scattering paths of the photoelectron to the neighbouring atoms. These atoms must be placed with respect to the absorber atom in a way, which is identical to or resembles the atomic arrangent present in the chemical compound being studied. For identification of bulk substances, a direct comparison with EXAFS spectra of reference compounds is possible (Changela *et al.*, 2012). In the case of single-molecule coordination compounds the scattering paths are well-known in advance and can be readily used as fitting models (Bauer *et al.*, 2005, Kelly *et al.*, 2007).

The matter becomes more complex as the metal ions are immobilised on a solid matrix, which is the case for supported heterogeneous catalysts. This state of the metal ion differs significantly from crystalline forms such as metal oxides and from well-defined ligand environments such as those in coordination compounds. Suitable models with relevant local atomic structures for heterogeneous catalysts must be specially designed.

Commonly for simplicity, the EXAFS scattering paths used for decribing the structure of heterogeneous catalysts are based on bulk materials. In many studies of the structure of highly-dispersed Fe sites in Fe/ZSM-5 catalysts, the atomic order up to ca. 4 Å in α-Fe_2O_3 was used (Battiston *et al.*, 2000, Battiston, Bitter, de Groot*, et al.*, 2003, Battiston, Bitter, Heijboer*, et al.*, 2003, Battiston, Bitter & Koningsberger, 2003, Pirngruber *et al.*, 2004, Schwidder *et al.*, 2005). Often, large and strongly varying correction terms (such as the ΔE_0) were applied in order to obtain a statistically reliable EXAFS fit. Recent structure refinements based on EXAFS analysis on the Fe/Al_2O_3 system in our group also included constrained coordination numbers and thermal deviation terms in order to achieve reasonable results (Boubnov, Lichtenberg*, et al.*, 2013). This is due to the strong structural deviation of molecular surface structures from the chemically similar bulk crystalline analogues. A problem is that the obtained Fe-Fe coordination numbers are small (around 1) and no attention is given to e.g. the Fe-Si or Fe-Al contributions, which can be significant and should be detectable within the 4 Å probed with EXAFS.

Several different iron oxide models, including spinel phases, were used for fitting the EXAFS of dispersed Fe in Fe/MCM-41 catalysts (Wong *et al.*, 2000) and Fe/ZSM-5 (Schwidder *et al.*,

2005), where a match of characteristic bond distances in the fit with that in the bulk oxides as well as physically realistic coordination numbers and Debye-Waller factors was an important criterion for a good model. The use of α-Fe_2O_3 as reference can be well-justified in a study of the Fe/BEA zeolite (Høj *et al.*, 2009), where only the two nearest-neighbour Fe-O coordination shells are observed in the spectra and fitted for dispersed Fe species at low Fe loadings. At higher loadings, where α-Fe_2O_3-phases were formed in the catalyst, their contribution was accounted for by applying further Fe-Fe paths to the EXAFS fit.

Realistic models for the Fe sites in Fe/ZSM-5 catalysts were built as DFT-optimised clusters of Fe connected to a small section of the zeolite network (Choi *et al.*, 2003, 2005). These authors have conducted EXAFS fits, identifying monomeric and dimeric Fe clusters connected to the zeolite, as Fe-O, Fe-Al, Fe-Fe and Fe-Si scattering paths were taken into account.

EXAFS analysis of Fe/γ-Al_2O_3 catalysts (Kou *et al.*, 1996) and Pt/Fe/γ-Al_2O_3 (Lin *et al.*, 2001) with low Fe loadings in both cases acquired very similar EXAFS spectra and both proposed a two-dimensional iron oxide layer on top of an alumina surface. In the latter case, the Pt atoms were located above, but were not identified in the Fe K-edge EXAFS. Nevertheless, the α-Fe_2O_3 model was used for generating EXAFS scattering paths, obtaining a good fit with nearest-neighbour Fe-O shells and three further Fe-Fe shells with low coordination numbers and high errors. The scattering EXAFS contributions from e.g. Fe-Al interactions were not considered.

To lay a stronger focus on the role of the catalyst support, molecular models of Fe in oxidic form attached to a γ-Al_2O_3 surface can be applied to simulate the theoretical structural EXAFS input. Fitting the coordination shells of already pre-defined structures only requires a few free parameters and minimises correction measures. Comparing data fits using several independent models can help to justify the structures obtained. At the same time, unrealistic models can be excluded if they lead to unrealistic fit results.

A accessible sites on γ-Al_2O_3 surfaces can be assumed to be sites on the exposed crystallographic planes. To determine which crystallographic planes are exposed, high-resolution TEM can be used as a local probe for selected crystallites. The overall crystal structure can be obtained from powder XRD data, from which the average size of the γ-Al_2O_3 crystallites can be determined. This is on one hand a complementary method to TEM, but also probes the average structure of the sample (in contrast to TEM as a local probe) and can

provide an estimate on the preferential crystal growth direction, as described in the following sections. The oxidation state and local coordination geometry of the Fe ions can be extracted from the X-ray absorption near-edge structure (XANES) spectral features. Mössbauer spectroscopy can be used to analyse the long-range order of the Fe oxide species and to distinguish between different crystallographic phases and particle sizes by probing the properties.

3.3.2. The structure of γ-Al_2O_3

Figure 19 shows the XRD pattern of γ-Al_2O_3 along with a fit of the 6 identified reflections, indexed in the diagram. The fit results excellently match the structure of γ-Al_2O_3 with cubic spinel structure, lattice parameter A = 7.90 Å and an average crystallite size D_{ave} = 7.2 nm, assuming isotropic crystallites, consistent with previously reported results (Lee *et al.*, 1997, Rozita *et al.*, 2010) and TEM (Figure 20). A misfit occurred in the FWHM of the (220) reflection (32.0°), being significantly broader than the (440) reflection (66.9°), not obeying the Scherrer relation. The reflection broadening is obviously not primarily caused by the size effect, but also the micro-structure, which is not taken into account by the Scherrer equation.

The TEM micrographs shown in Figure 20 reveal a certain degree of structural hierarchy in γ-Al_2O_3: on the sub-micrometre scale plates and curved rods are observed along with globular agglomerates (Figure 20a). At slightly higher magnification (Figure 20b), the images show platelets consisting of small, almost identical structures of the order of 10 nm. High-resolution micrographs (Figure 20c-e) show that these structures are nanometre-sized crystals with clearly visible lattice planes. The lattice planes are already visible in the *a priori* randomly positioned sample, confirming the high symmetry present in the cubic crystals.

The images of 4 particles located on the edge of the agglomerates (Figure 20c-e) were analysed for periodicity with fast Fourier-transforms (FFT, Figure 20f). The lattice distances were determined in Fourier-space and matched with Miller indices in accordance with the XRD results. The corresponding lattice spacings were identified in the HRTEM images to examine whether the crystal terminates in a specific direction. A total of 5 occurrences of crystal termination were observed in the (222) direction (2.3 Å) and 2 occurrences of termination in the (400) direction (2.0 Å). Furthermore, (311) and (220) lattice spacings (2.4 Å and 2.8 Å respectively) were identified, but no crystal termination was observed in these directions. Termination of γ-Al_2O_3 crystallites with the (222) and (400) planes (Rozita *et al.*, 2010), and restructuring of (220) planes into stair-like surfaces exposing (222) planes on the

order of 1 nm (Kovarik *et al.*, 2012, Pinto *et al.*, 2004) was observed, which indicates that the (220) lattice planes are energetically unfavourable. The (222) and (400) lattice planes are the main terminating crystal planes to be used in the model construction of surface-supported Fe-species and the (220) facets can be omitted. It is still important to bear in mind that TEM images as a local probe might not represent the whole sample as far as selection of images (normally only the best-resolved and thinnest areas of the sample are imaged and analysed) and sampling (only the smallest particles of the initial material stay on the TEM-grid) is concerned.

In contrast to the crystalline and well-characterised corundum (α-Al_2O_3), the so-called transitional forms of alumina, such as γ-Al_2O_3, are less dense and have less regular structures. These structures depend on the conditions under which they were synthesised. However, the disordered structure of these transitional forms of alumina is also a hindrance to their characterisation. Therefore, no well-determined γ-Al_2O_3 crystal structure is available, see e.g. (Sun *et al.*, 2006, Digne *et al.*, 2006, Nelson *et al.*, 2006, Paglia *et al.*, 2006).

Vacancy distribution in the structure

It is frequently stated that γ-Al_2O_3 has a defect spinel structure with a unit cell structure $Al_{64/3}\square_{8/3}O_{32}$, where the Al cations are distributed among the octahedral and tetrahedral lattice sites and □ are vacancies. A part of the octahedral and tetrahedral cation sites are vacant (defect sites) to maintain a charge balance, resulting in the empirical formula Al_2O_3. The stoichiometry of octahedral to tetrahedral sites is 2:1 according to the spinel structure, and the stoichiometry of Al cations to vacancies is 8:1.

The exact distribution of the vacancies in γ-Al_2O_3 is a matter of dabate: Verwey (Verwey, 1935) states that 70% of the Al cations occupy the octahedral sites and 30% the tetrahedral, corresponding to an even distribution of octahedral and tetrahedral vacancies, a result confirmed by means of ^{27}Al MAS-NMR and Monte Carlo simulations by Lee and co-workers (Lee et al., 1997). The Monte Carlo simulations were run for a periodic Al_2O_3 structure constructed of approximately 2 nm supercell building blocks with a fixed oxygen lattice and initially randomly distributed vacancies. The Al cations were allowed to occupy the most geometrically favourable positions, taking into account realistic Al-O bond lengths.

Rietveld-refinement of synchrotron-based XRD data of γ-Al_2O_3, Sun (Sun et al., 2006) has shown that γ-Al_2O_3 is definitely a spinel-related structure, but several structural models including varying distributions of hydroxyl groups used for charge balance and vacancies

were consistent with the experimental data and could thus not be ruled out. A refined structure was in this case 3-9 nm crystallites with 72% of the Al cations in the octahedral sites.

Electronic band structure (density of states) calculations (Mo *et al.*, 1997, Gutiérrez *et al.*, 2001) have shown that only vacant octahedral sites yield the most energetically favourable crystal structure. These studies as well as the work of Lee (Lee et al., 1997) rely on the assumption that all vacancies are homogeneously distributed within the bulk crystal structure, and the effects of the crystal surfaces were neglected. The model crystals were constructed of spinel-type supercells with periodic boundary conditions.

Surface structure

Concerning γ-Al_2O_3 crystal surfaces, the following studies provide a good overview of the terminating crystal planes to be considered: high-resolution TEM has facilitated the observation that the individual crystallites are surface-terminated by (100) and (111) lattice planes (Rozita *et al.*, 2010). Further high-resolution TEM work by (Kovarik et al., 2012) shows a dominant (110) surface, which is locally restructured into (111) facets of 2-3 nm dimensions; no (100) facets were observed in this case.

The (100) surface was used as a catalyst support for DFT-calculations (Loviat et al., 2009): the surface contains 5-fold coordinated Al atoms, corresponding to octahedral Al with one oxygen missing. This specific form of Al in the surface lattice is considered in the publication as a good model of the fivefold coordinated Al, which was furthermore confirmed experimentally and assigned an especially high reactivity with oxygen. Attention was dedicated to 5-fold coordinated Al on the (100) surface (Kwak et al., 2011), which are interesting as active sites for catalytic alcohol dehydration.

The role of crystal surfaces in γ-Al_2O_3 was further explored (Dyan et al., 2008) using quantum-mechanical surface simulations, coming to the conclusion that the vacancies placed close to the crystal surfaces experience distortions in the atomic arrangement on relaxation of the structure. To minimise the surface charge, an Al cation excess was compensated by a decrease in the Al coordination; an oxygen excess led to the formation of $O_2^{\delta-}$-groups. Interestingly, the latter case was demonstrated for a (100) surface containing the surface-exposed 5-fold coordinated Al, as in the study by (Loviat et al., 2009) mentioned above. The rearrangement behaviour was similar for surfaces terminated by the lattice planes (100), (110) and (111). The models were constructed of 2 nm x 2 nm x 1 nm parallelepipeds with 2D periodic boundary conditions for modelling a more realistic structure.

Crystallite size

A structural aspect of γ-Al_2O_3 is the limited crystallite size that it exhibits, as is briefly reviewed in the following section.

The formation of α-Al_2O_3 from γ-Al_2O_3 in a thin film using TEM was studied (Chou & Nieh, 1991), analysing the structure after treatment at different temperatures. After treatment at 800°C, the aluminium oxide was present as a mixture of amorphous species and γ-Al_2O_3 crystallites of ca. 10 nm; after treatment at 1200°C, a transition to α-Al_2O_3 is initiated. At this stage the γ-Al_2O_3 crystallites increased in size to 50 nm. This irreversible phase transformation yields micrometre-large α-Al_2O_3 crystals.

From the studies mentioned in the previous paragraphs, particle sizes in the range 3-9 nm were obtained from XRD data (Sun et al., 2006). Several commercial γ-Al_2O_3 samples were studied by TEM and XRD (Rozita et al., 2010) and two forms were identified: 10-15 nm globular crystallites and platelets of about 5 x 50 x 50 nm^3 dimension. In both cases, small particle sise and high aspect ratios of the crystals resulted in high surface areas. Platelets of 10 x 100 x 100 nm^3 dimensions were observed by (Kovarik *et al.*, 2012), again verifying that at least one of the crystal dimensions must not exceed around 10 nm.

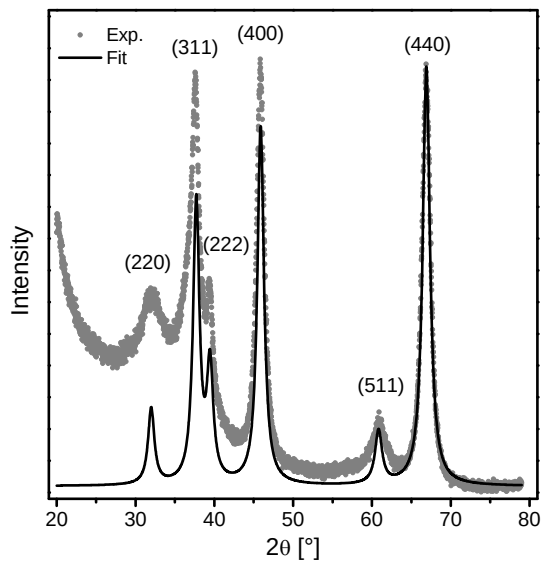

Figure 19 XRD pattern of γ-Al_2O_3 (grey dots) and fit with Lorentzian-shape profiles (solid line) constrained to satisfy Bragg's law and the Scherrer relation, based on the position and width of the (440) reflection. The fit corresponds to a spinel structure with lattice constant A = 7.90 Å and average crystallite size D_{ave} = 7.2 nm.

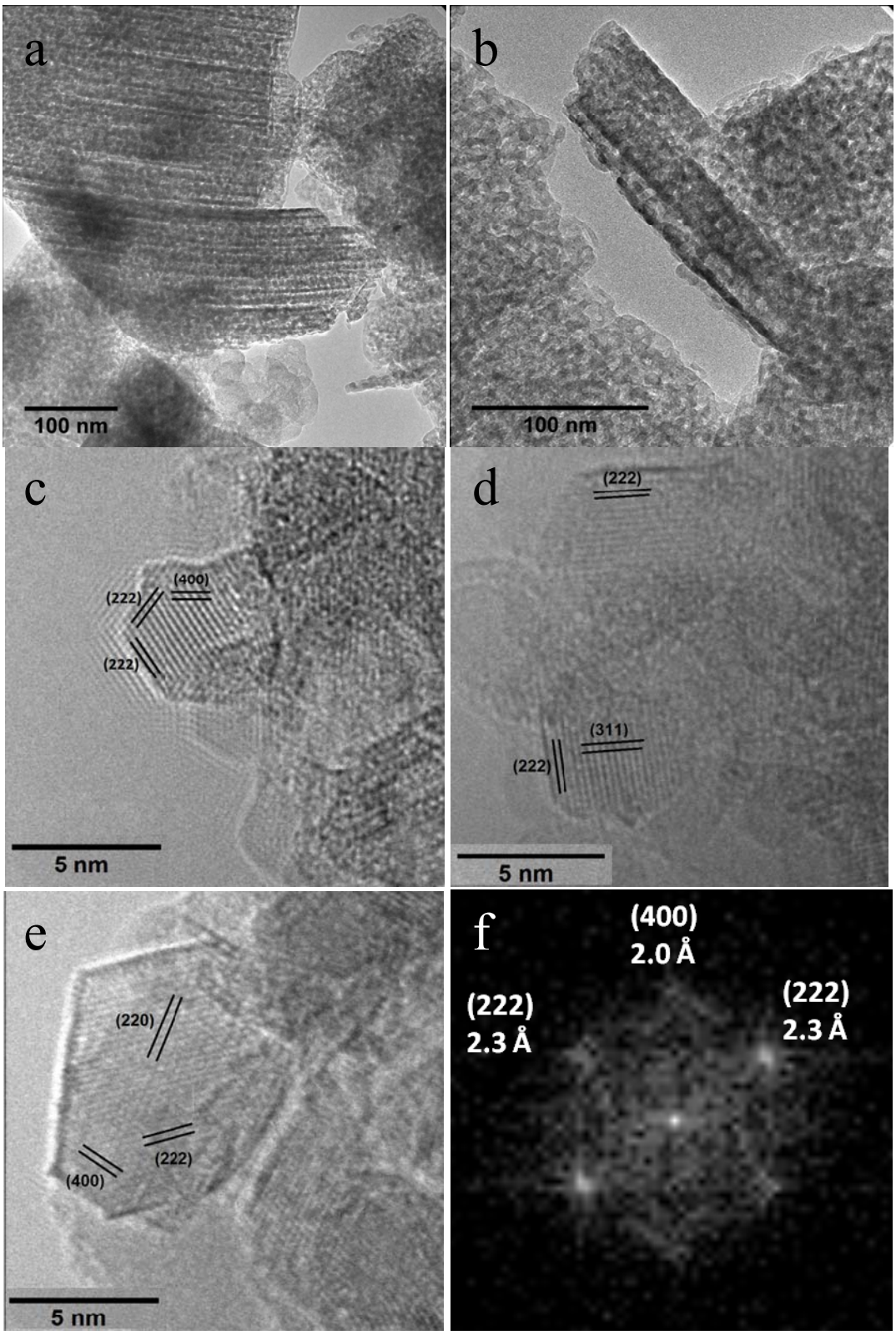

Figure 20 Transmission electron micrographs (TEM) of γ-Al_2O_3: low-magnification images (a, b) of the agglomerate structure and high-resolution (HRTEM) images of the individual nanometre-sized crystallites (c-e). FFT plot (f), identifying lattice spacings in (c).

3.3.3. The structure of Fe sites in 0.1% Fe/Al_2O_3 catalysts

The Mössbauer spectra of the 0.1% $^{57}Fe/Al_2O_3$ sample at 3, 200 and 300 K (Figure 21a) show a wide distribution of relaxation times, which is most pronounced at 3 K. Due to this distribution, part of the Fe in the sample relaxes quickly in terms of the Mössbauer time scale, giving rise to a doublet (paramagnetic character), and part of the sample relaxes slowly, giving rise to a broad magnetic sextet (magnetic ordering). This sextet reflects a distribution of hyperfine magnetic field, with a mean value of about 50 T at low temperature (Figure 21b). Even at 3 K, where relaxation is expected to be completely suppressed, the spectrum still shows a significant contribution of a paramagnetic doublet, indicating highly dispersed Fe sites. On the other hand, the magnetic ordering shows that the Fe species are present as small clusters. With decreasing temperature from 300 to 3 K, the contribution of the paramagnetic part (doublet) decreases and the magnetic part (sextet) increases (Table 1). This temperature dependence is typically observed for nanoparticles with a broad size distribution (Kündig *et al.*, 1966). The isomer shifts correspond to the sole presence of trivalent Fe.

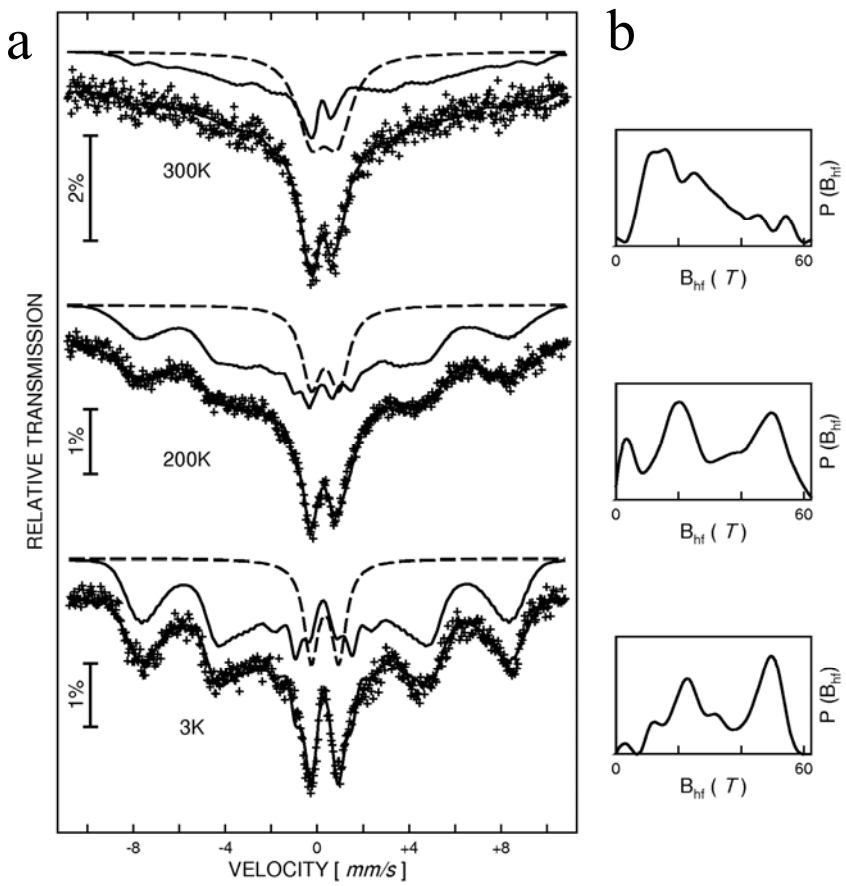

Figure 21 ^{57}Fe Mössbauer spectra of 0.1% $^{57}Fe/Al_2O_3$ at 3 K, 200 K and 300 K (a). The probability distribution of the magnetic hyperfine field (B_{hf}) at each temperature extracted from the sextet (magnetically ordered Fe^{3+}) is shown in (b).

Table 1 Refined parameters of Mössbauer spectroscopy of 0.1% $^{57}Fe/Al_2O_3$: isomer shifts (δ) relative to α-Fe at 295 K, quadrupole splitting (ΔE_Q) and line FWHM (Γ) of the doublet (high-spin Fe^{3+}). Area ratios between the doublet and sextet contributions are given.

T [K]	δ [mm/s]	ΔE_Q [mm/s]	Γ [mm/s]	Area doublet/sextet [%]
300	0.40	1.15	1.04	38/62
200	0.42	1.20	1.02	20/80
3	0.44	1.20	0.77	17/83

The XANES spectra of 0.1% Fe/Al_2O_3 and 0.1% $^{57}Fe/Al_2O_3$ as well as sanidine and α-Fe_2O_3, including the enlarged pre-edge peak region, are shown in Figure 22. The edge energy in the XANES spectra (Figure 22a) and the position of the pre-edge peak (Figure 22b) of the 0.1% Fe/Al_2O_3 and 0.1% $^{57}Fe/Al_2O_3$ sample are consistent with trivalent iron, when comparing with the reference spectra and literature (Wilke *et al.*, 2001). The intensity of the pre-edge peak for both catalyst samples is approximately halfway between that for sanidine with Fe in tetrahedral (T_d) sites and for α-Fe_2O_3 with Fe in octahedral (O_h) sites. Since the intensity is inversely related to the coordination geometry (Westre *et al.*, 1997), it can be concluded that the Fe centres in the catalysts are bonded to approximately 5 oxygen atoms.

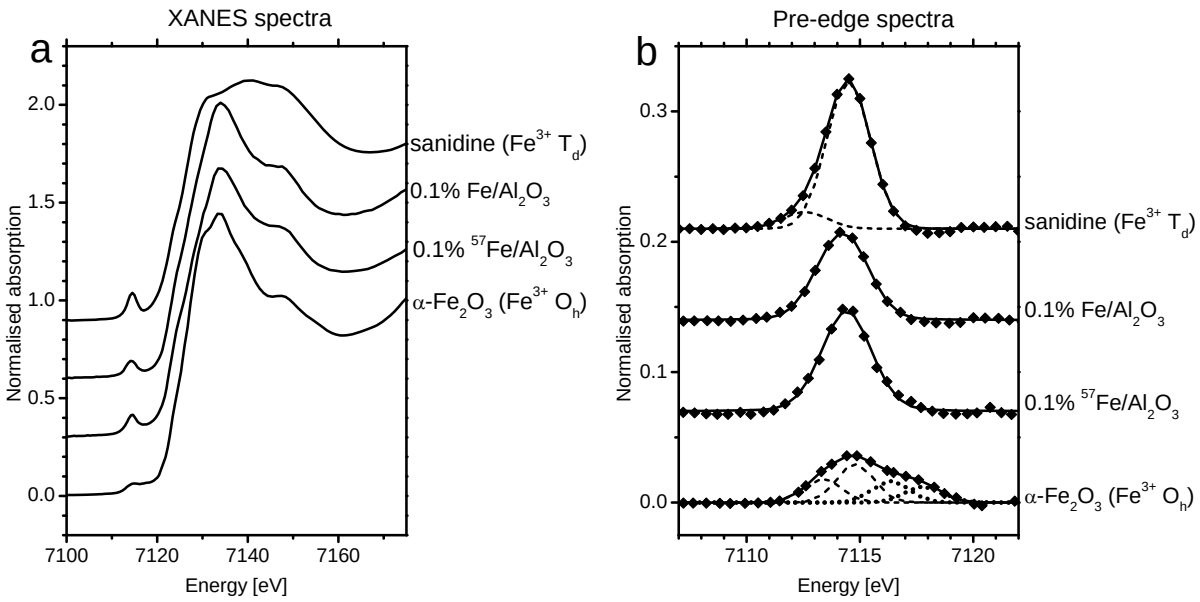

Figure 22 XANES spectra (a) and pre-edge spectra (b) of the 0.1% Fe/Al_2O_3 catalysts together with α-Fe_2O_3 (Fe^{3+} at O_h sites) and sanidine (Fe^{3+} at T_d sites). The pre-edge spectra are fitted with pseudo-Voigt peak functions: the dashed lines indicate the 1s → 3d transitions specific for probing the local coordination and the dotted lines indicate non-local transitions found in α-Fe_2O_3.

In order to further elucidate the structure of iron, the magnitude and imaginary part of the Fourier-transformed EXAFS spectra of the 0.1% Fe/Al_2O_3 and 0.1% $^{57}Fe/Al_2O_3$ (Figure 23) was considered. Qualitatively, both spectra have similar local Fe-O coordination shells (1-2 Å) as the EXAFS spectrum of α-Fe_2O_3, indicating the oxidic state of Fe. The further coordination shells (2-4 Å) in α-Fe_2O_3 indicate a high degree of order in the crystal structure. In the 0.1% Fe/Al_2O_3 catalysts, the further contributions are much weaker, which can either be due to a high fraction of disordered structures, or the fact that the Fe centre is located on a surface, i.e. is not surrounded by a crystalline matrix on all sides. Furthermore, the EXAFS spectra of the catalysts resemble the previously reported spectra of a Fe_2O_3/Al_2O_3 catalyst (Kou *et al.*, 1996), which were analysed using the structure of α-Fe_2O_3 as an input model and concluding on two-dimensional chains of Fe atoms on the surface of γ-Al_2O_3. The present study takes the characterisation of this chemical system one step further, in that Fe-Al coordination shells are accounted for in the structural refinement. The EXAFS spectrum of 0.1% Fe/Al_2O_3, which was collected with a high signal-to-noise ratio, will be analysed quantitatively in the following sections.

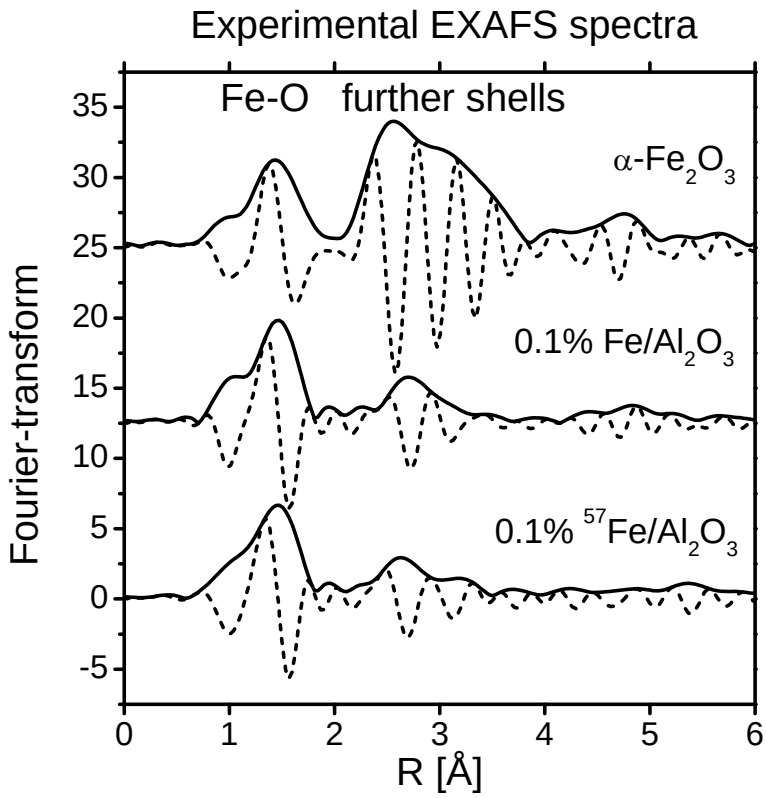

Figure 23 Fourier-transformed EXAFS data (imaginary part and magnitude) of the 0.1% Fe/Al_2O_3 catalysts (standard and ^{57}Fe) compared to α-Fe_2O_3. The local Fe-O shells (1-2 Å) are similar in the catalysts and α-Fe_2O_3, but the further shells (2-4 Å) are different.

3.3.4. Structural models of Fe/Al_2O_3 for EXAFS fitting

Rather than seeking a "true structure" of Fe/Al_2O_3, structural models that are in agreement with experimental data can be devised, which serve as a starting point for understanding the catalytic activity. To this end, two complementary approaches were followed: first, models of surface-supported Fe oxide were considered. Second, models in which bulk γ-Al_2O_3 is doped with Fe were set up. This second type of models was also suitable for further optimisation with density-functional theory (DFT) calculations.

Surface-supported Fe oxide models

As a basis for the structure of Fe/Al_2O_3 with monomeric Fe species on the Al_2O_3 surface, a spinel structure ($MgAl_2O_4$, space group *Fd-3m*) was selected and modified accordingly: the Mg atoms were replaced by Al, and the lattice constant (A = 7.90 Å) was adjusted to match the Al-O distance of the octahedral Al atoms to that in α-Al_2O_3. At this point, there are two types of lattice sites for the metal ion: an octahedrally coordinated (O_h) and a tetrahedrally coordinated (T_d), both types occupied by Al. Fe atoms were included by replacing Al at either of these sites. This resulted in $FeAl_xO_y$ clusters with Fe atoms at an O_h or a T_d site. It is important to note that in this model no vacancies were considered for simplicity; furthermore, the vacancy distribution in γ-Al_2O_3 is subject to debate (Mo *et al.*, 1997, Gutiérrez *et al.*, 2001, Dyan *et al.*, 2008). To place an oxidic Fe atom on the alumina surface, the Al and O atoms constituting one half of the sphere were manually removed from the structure, assisted by the programs Avogadro (*Avogadro software, version 1.1.0*) and Mercury (*Mercury software (CCDC), version 3.0*).

A total of 24 molecular structures of Fe on and in the surface of γ-Al_2O_3 were developed to model the atomic environment of the iron centres in the Fe/Al_2O_3 catalyst. The sextet observed below 200 K in the Mössbauer spectra suggested that the Fe oxide species are present as nanoparticles rather than monomeric species. Nevertheless, in the first step, the models developed herein involve single oxidised Fe atoms replacing Al atoms at different sites in γ-Al_2O_3. Clusters of several Fe ions are investigated in a second step.

Starting with Fe merely replacing Al at the O_h and T_d positions of the original structure, the first two models are obtained, referred to as bulk O_h and bulk T_d respectively. A further 16 models of Fe were placed in various ways on the (222) and (400) planes of γ-Al_2O_3, which according to the TEM results are the most probably exposed. The γ-Al_2O_3 crystal can be cleaved along the (222) planes in two ways, resulting in two surfaces, which are distinguished

in the following by subscripts. The $(222)_1$ surface (Figure 24a) exposes a "triple layer" of Al atoms arranged in the order T_d-O_h-T_d from the surface, referring to the type of crystallographic sites they occupy. One Fe atom placed in each of these layers gave rise to structures 9, 3 and 8, and an Fe placed at an O_h site defined structure 1. Since all metal atoms are in oxidised state, also those at the surface are to be terminated by oxygen. The $(222)_2$ surface (Figure 24b) exposed a layer of Al atoms at the O_h sites only. Fe located at one of these sites served as model 2 and Fe atoms placed at two T_d sites and an O_h site on the surface resulted in models 10, 11 and 4.

The γ-Al_2O_3 crystal was also cleaved to expose the (400) surface, which in turn can be defined in two different ways. The $(400)_1$ surface (Figure 24c) was created with the aforementioned condition in mind, that all surface metal ions are saturated by oxygen atoms. Models 16, 6, 15 and 7 describe Fe supported on this surface. The $(400)_2$ surface (Figure 24d) was generated by cleaving the crystal directly, while leaving 5-fold coordinated octahedral Al atoms in O_h-like sites directly at the surface. Previously reported results support the existence of such a surface (Loviat *et al.*, 2009), explicitly outlining the role of 5-fold coordinated Al atoms on the surface as catalytically active centres (Kwak *et al.*, 2011, Pinto *et al.*, 2004). Placement of Fe on this surface resulted in models 14, 5, 13 and 12.

Surface-based models of the Fe centres in O_h sites were labelled 1-7, and those based on Fe in T_d sites 8-16. The O_h sites (as well as the T_d sites) in the bulk of the spinel structure are geometrically equivalent. The surface-based structural models were generated by removing part of the atoms surrounding the Fe centre in the bulk structure, which simply means modifying the coordination numbers for each EXAFS path. The coordination numbers for the neighbouring atoms within 3.5 Å from the Fe centre in the mentioned models are listed in Table 2 (surface-based O_h models), Table 3 (relaxed O_h models), Table 4 (surface-based T_d models) and Table 5 (relaxed T_d models). The first Fe-O coordination shell of surface-supported Fe might not have the same bond distance and number of neighbours as compared to those in the bulk structure. The further coordination shells (Fe-Al and Fe-O) are on the other hand expected to depend specifically on whether the Fe atom is located at an O_h or T_d site. Therefore the first coordination shell will be treated separately from the further shells.

Fe-doped γ-Al_2O_3 models

Another set of models was created starting from a model structure of bulk γ-Al_2O_3. As a basis for this we have chosen the bulk structure of (Krokidis *et al.*, 2001) in a symmetrised form

(Mercuri, 2011), which was subsequently optimized using DFT with three-dimensional periodic boundary conditions. This γ-Al_2O_3 bulk structure is a defect spinel structure with an $Al_{16}O_{24}$ unit cell, in which the oxygen atoms are arranged in a distorted face-centered cubic lattice, while the aluminum atoms occupy some of the octahedral and tetrahedral sites in this lattice. In this particular structure, 3/4 of the Al atoms occupy octahedral sites, while the other 1/4 occupy tetrahedral sites. This is consistent with the accepted ratios found in γ-Al_2O_3 samples (Krokidis *et al.*, 2001, Digne *et al.*, 2004).

The 16 aluminum atoms in the unit cell are each possible candidates for substitution with an iron atom. Symmetry in the structure however means that only six unique substitution locations need be investigated, as all of these locations are either two-fold or four-fold degenerate. For each of these cases, one iron atom was substituted for one aluminium atom, and the structure was re-optimised with DFT. These models will be referred to as relaxed models.

All calculations were performed with the BAND program (te Velde & Baerends, 1991, *BAND2013, SCM*) using the Becke-Perdew exchange-correlation functional (Becke, 1988, Perdew, 1986) and a TZP Slater type basis set (van Lenthe & Baerends, 2003). A large frozen core was used for the heavy atoms, and scalar relativistic effects were included using the zeroth-order regular approximation (ZORA) (van Lenthe *et al.*, 1994). In all geometry optimisations, the unit cell was kept fixed.

The unit cell of γ-Al_2O_3 used for generating relaxed models of Fe replacing Al at different sites is shown in Figure 24e. This unit cell has the formula $Al_{16}O_{24}$ and is rotationally symmetric. The 16 Al sites are not entirely unique, being 2 sets of quadruplets and 4 sets of twins, giving at most 6 unique sites for Fe-substitution. Of these, 2 sets of twins (4 total sites, labelled R5 and R6) are approximately tetrahedrally (T_d) coordinated to the surrounding oxygen atoms, and the rest (12 total sites, labelled R1 to R4) are approximately octahedral (O_h), with some being more distorted than others. The variation within the O_h sites and also between the two types of T_d sites arises due to the different placement of the vacancies. When the structures are perturbed by substituting an Al atom with an Fe atom at a specific site and re-optimised, the oxygen atoms move further from the Fe than they were from the Al, but not drastically. The changes in bond lengths are less than 0.1 Å.

The relaxed models differ from the surface-supported molecular models in that they are based on a bulk defect-spinel structure. The distribution of the oxygen atoms is exactly as in the

spinel lattice, but the location of the O_h sites and the T_d sites is modified in order to account for the stoichiometry and the vacancy locations. The local Fe-O(1) coordination numbers (6 for O_h and 4 for T_d) and further Fe-O(2) coordination numbers (8 for O_h and 12 for T_d) are therefore the same as those in ideal bulk spinel, but the Fe-Al coordination numbers vary from site to site. In most cases, the Fe-Al coordination number is lower or equal to the bulk value as expected, but in model R4 there are 8 Al atoms at 2.73-2.91 Å, being 2 atoms in excess of the expected. The ranges of the bond distances are consistent with those used for the surface-supported structures.

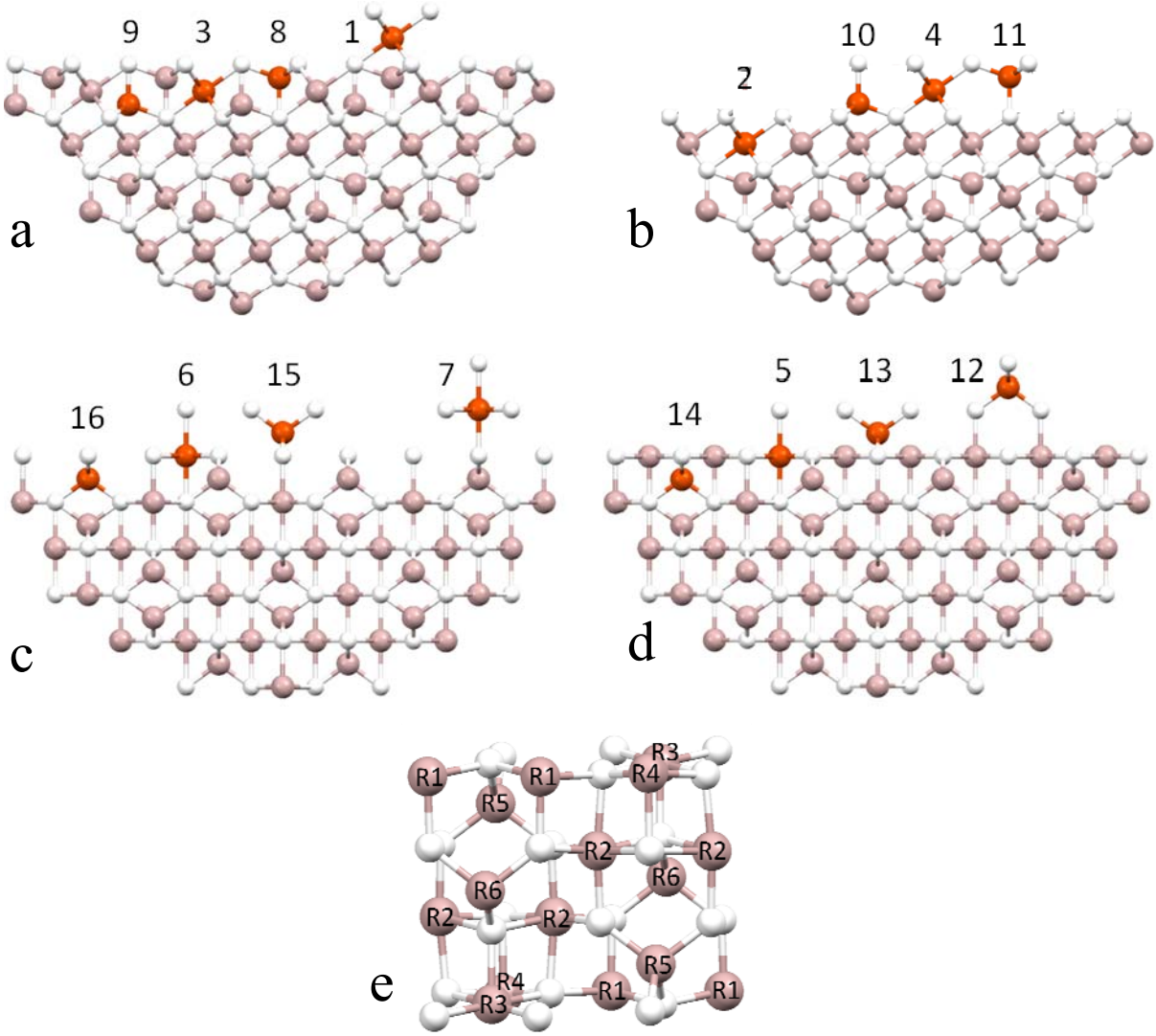

Figure 24 Location of the Fe atoms replacing Al at different sites on the $(222)_1$ surface (a), $(222)_2$ surface (b), $(400)_1$ surface (c) and $(400)_2$ surface (d) of γ-Al_2O_3, as described in the text. Al sites within the γ-Al_2O_3 unit cell replaced by Fe according to (Krokidis *et al.*, 2001) to optimise the geometry based on DFT calculations (e). Symmetry-equivalent sites are labelled in the same way. Models with Fe atoms at O_h sites are labelled 1-7 and R1-R4; Fe atoms at T_d sites are labelled 8-16 and R5-R6. All models are viewed from the (220) direction. The orange-coloured atoms are Fe, the grey atoms are Al and the white atoms are O.

Table 2 Coordination numbers and bond distances obtained from bulk and surface-based models (1-7) of Fe species at O_h sites of alumina in the 0.1% Fe/Al_2O_3 catalyst, used as starting parameters in EXAFS analysis.

Model	Path	Fe-O(1)	Fe-Al_{Oh}(1)	Fe-Al_{Td}(2)	Fe-O(2)
	d [Å]	1.98	2.79	3.28	3.42
Bulk	CN	6	6	6	8
1			1	2	4
2			5	3	7
3			3	6	7
4			3	0	4
5			4	3	4
6			2	3	4
7			0	0	4

Table 3 Coordination numbers and bond distances obtained from relaxed models (R1-R4) of Fe species at O_h sites of alumina in the 0.1% Fe/Al_2O_3 catalyst, used as starting parameters in EXAFS analysis.

Model	Path	Fe-O(1)	Fe-Al_{Oh}(1)	Fe-Al_{Td}(2)	Fe-O(2)
R1	CN	6	6	3	8
	d [Å]	1.87-2.09	2.73-2.98	3.22-3.27	3.27-3.72
R2		6	5	5	8
		1.83-1.99	2.66-2.91	3.13-3.27	3.37-3.64
R3		6	6	2	8
		1.97-2.04	2.74-2.93	3.34-3.35	3.30-3.59
R4		6	8[a]	2	8
		1.91-2.11	2.73-2.91	3.32-3.36	3.30-3.41

[a] Over-saturation of the Fe-Al_{Oh}(1) coordination shell by 2 atoms is proposed in this model, compared to the bulk value of 6.

Table 4 Coordination numbers and bond distances obtained from bulk and surface-based models (8-16) of Fe species at T_d sites of alumina in the 0.1% Fe/Al_2O_3 catalyst, used as starting parameters in EXAFS analysis.

Model	Path	Fe-O(1)	Fe-Al_{Oh}(1)	Fe-O(2)	Fe-Al_{Td}(2)
	d [Å]	1.71	3.28	3.28	3.42
Bulk	CN	4	12	12	4
8			6	9	3
9			9	12	4
10			6	6	1
11			3	6	0
12			2	2	0
13			6	6	2
14			10	10	2
15			2	6	2
16			6	10	2

Table 5 Coordination numbers and bond distances obtained from the relaxed models (R5 and R6) of Fe species at T_d sites of alumina in the 0.1% Fe/Al_2O_3 catalyst, used as starting parameters in the EXAFS analysis.

Model	Path	Fe-O(1)	Fe-Al_{Oh}(1)	Fe-O(2)	Fe- Al_{Td} (2)
R5	CN	4	10	12	2
	d [Å]	1.83-1.89	3.23-3.34	3.12-3.45	3.30-3.48
R6		4	10	12	2
		1.77-1.82	3.13-3.31	3.10-3.44	3.30-3.48

3.3.5. Simulated EXAFS spectra of the molecular models and qualitative evaluation

For all models, scattering paths for the EXAFS refinement were simulated using FEFF6. Initial EXAFS spectra of the coordination shells excluding the local Fe-O shell were calculated based on the coordination numbers as defined in Table 2 (surface-based O_h models), Table 3 (relaxed O_h models), Table 4 (surface-based T_d models) and Table 5 (relaxed T_d models). The mean square thermal displacement was fixed to $\sigma^2 = 0.005$ Å^2, but no corrections in bond distances and E-shifts were applied. For the relaxed models, all non-local coordination shells within a radius of ca. 3.5 Å from the Fe centre were used with the bond distances as calculated. Figure 25 shows the simulated Fourier-transformed EXAFS spectra in an R-interval of 2.0-3.5 Å as well as the coordination shells shown separately, with coordination numbers corresponding to those in the bulk models. The model EXAFS data for Fe in O_h sites (Figure 25a) have common characteristics, such as the three local minima in the imaginary part of the Fourier-transform. The Fe-Al(2) and the Fe-O(2) coordination shells exhibit close similarity, potentially making them indistinguishable when they are added. Here, they are clearly defined, which is essential for a correct interpretation of the subsequent EXAFS refinement. The Fourier-transformed EXAFS spectra of Fe atoms at T_d sites (Figure 25b) exhibit two characteristic local minima in the imaginary part, which are clearly distinguishable from the spectra of Fe at O_h sites. Also note that the imaginary part of the Fe-Al(1), Fe-O(2) and Fe-Al(2) shells add up destructively, causing the amplitude in the EXAFS spectrum of the bulk T_d model to appear smaller than the Fe-O(2) shell. Again, by appropriately choosing input models, the misinterpretation of such artefacts can be avoided.

The simulated EXAFS spectra of the 24 structures were systematically evaluated in order to find realistic models for EXAFS refinement. This selection was based on a least-square fitting of the imaginary part of the Fourier-transform. The imaginary part of the experimental spectrum was fitted in the R-range of 2.0-3.5 Å with the corresponding imaginary part of each

simulated spectrum scaled by a factor. The results were sorted according to the goodness of fit (coefficient of determination R^2, Figure 26a), which is positively correlated to the scaling factor (Figure 26b). The best models (R^2 between ca. 10-60%) were scaled by 0.1-1, whereas the worst models (R^2 = 0) were scaled by zero. This preliminary evaluation showed a clear superiority of the O_h models compared to the T_d models, with two exceptions (models 15 and 4). Eight best-fitting models R2, R3, 7, 15, R4, 1, 3 and 6 were selected for further structural refinement.

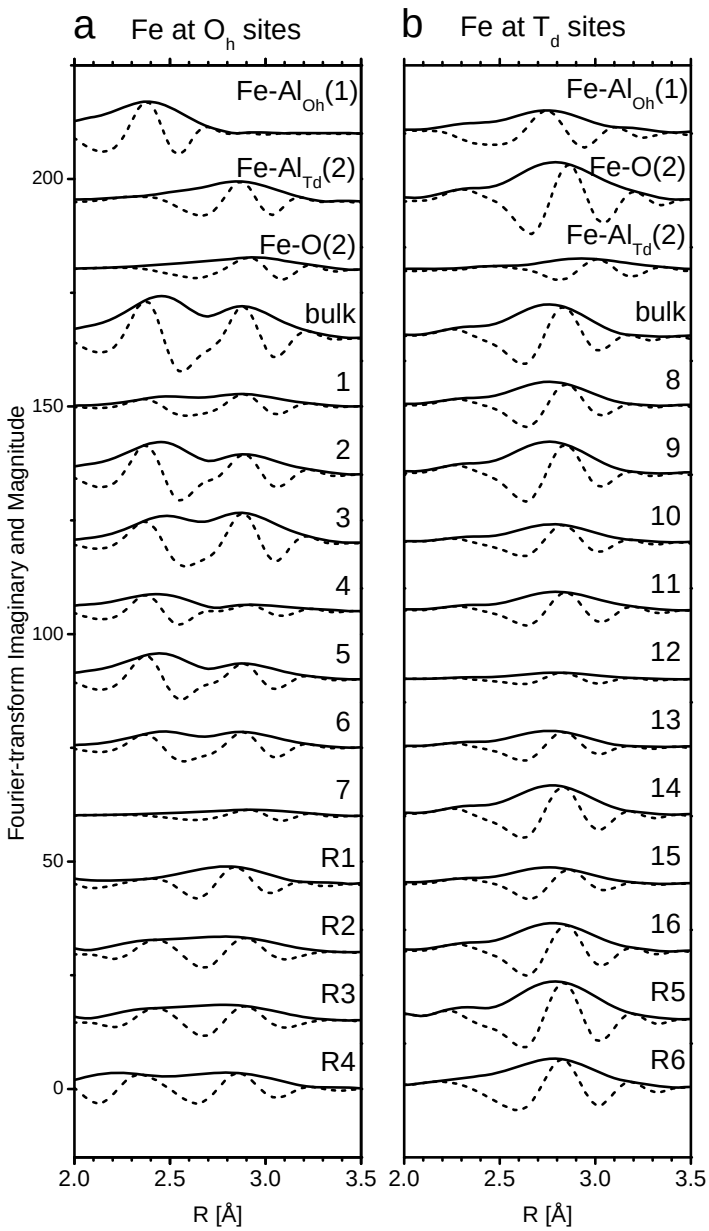

Figure 25 Simulated Fourier-transformed EXAFS spectra (imaginary part and magnitude) in the R-range 2.0-3.5 Å, corresponding to the further coordination shells in the spectrum of 0.1% Fe/Al_2O_3 (Figure 23). These spectra are basis for preliminary evaluation of Fe-models to describe the sites in the Fe/Al_2O_3 catalyst. A fixed value of σ^2 = 0.005 $Å^2$ was used in the simulation.

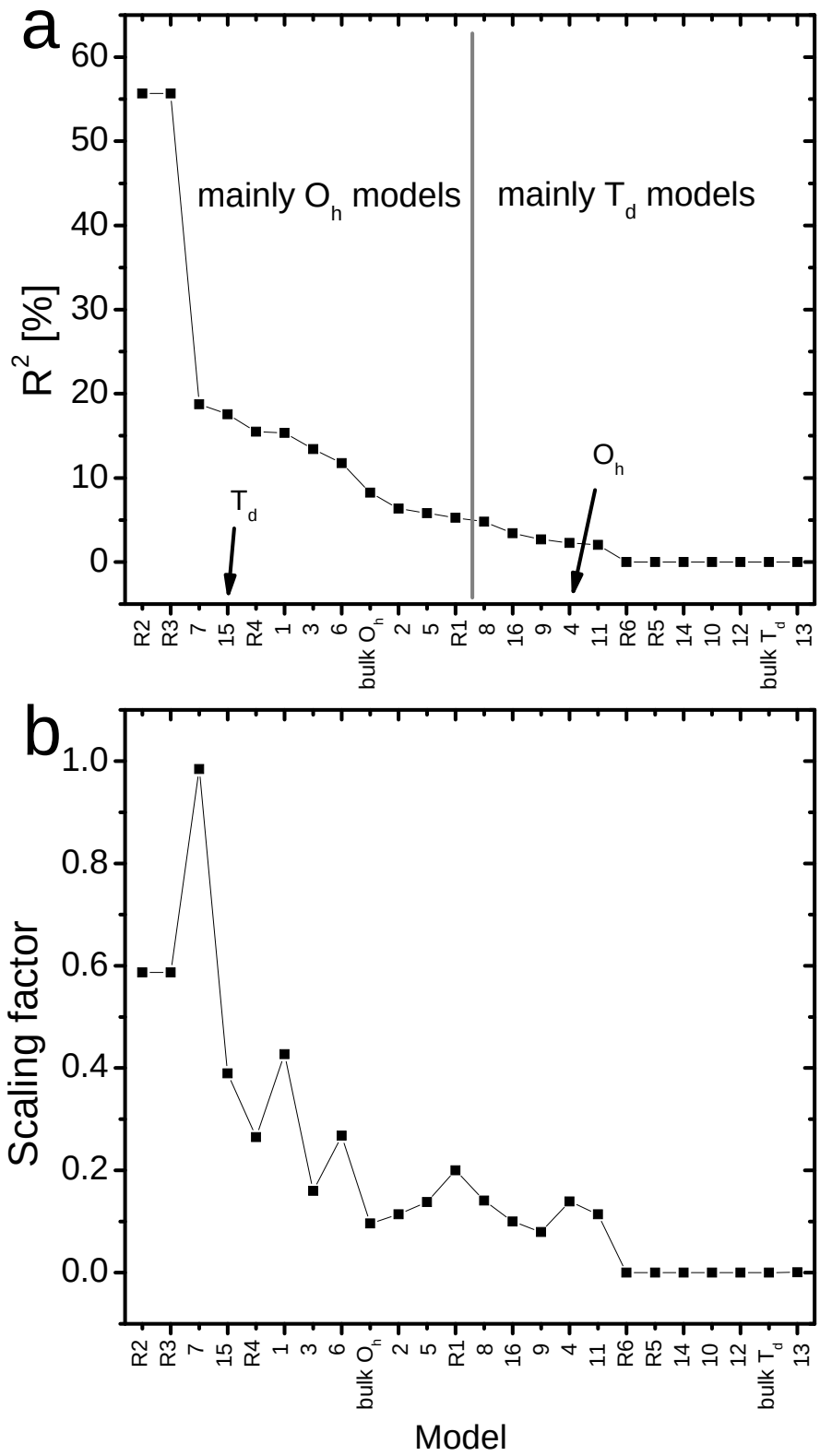

Figure 26 Coefficient of determination R^2 (a) and the scaling factor (b) obtained from the preliminary evaluation of the of Fe/Al_2O_3 models based on linear fit of the simulated EXAFS spectra (Figure 25) to the experimental EXAFS spectrum of the 0.1% Fe/Al_2O_3 catalyst (Figure 23). The models were sorted according to R^2.

3.3.6. Refinement of EXAFS data of α-Fe_2O_3 as reference and 0.1% Fe/Al_2O_3

Prior to the refinement of the spectrum of the 0.1% Fe/Al_2O_3 catalyst, the spectrum of α-Fe_2O_3 was refined (Figure 27) in order to optimise the procedure. A total of 9 single-scattering paths (Table 6) and 8 multi-scattering paths (not shown) were defined using crystallographic data, with a maximum effective scattering distance of 3.77 Å. Including the multiple-scattering paths leads only to a minor improvement of the already good fit, at the cost of additional parameters with low structural significance. Multiple-scattering can be calculated correctly when the structure of the compound is well-known. This is not the case for the 0.1% Fe/Al_2O_3 catalyst. This justifies neglecting the multiple-scattering paths.

For refining the EXAFS spectrum of α-Fe_2O_3, the bond distances were adjusted by correction terms, one for the local Fe-O shells and one for all further coordination shells, with maximum values of ±0.02 Å. The mean square thermal displacement (σ^2) as a variable in the Debye-Waller factor was in a reasonable range between 0.004 and 0.009 $Å^2$, however under the condition that these values were shared between coordination shells of the same back-scattering atom. The electronic amplitude reduction factor (S_0^2 = 0.80) was determined, and the low value of the total phase shift (ΔE_0 = -2.4 eV) indicated that subtraction and fitting of the EXAFS data was successful. From this perspective, this approach was validated for EXAFS refinement of the 0.1% Fe/Al_2O_3 catalyst with an unknown structure.

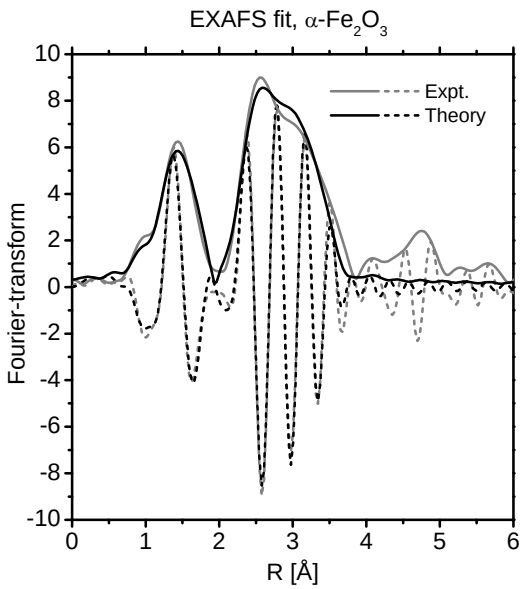

Figure 27 Experimental and fitted Fourier-transformed EXAFS spectrum (imaginary part and magnitude) of α-Fe_2O_3 using crystallographic data.

Table 6 Refined structural parameters of the EXAFS spectrum of α-Fe_2O_3. The electronic amplitude reduction factor S_0^2 was determined to be 0.80.

Path	d [Å]	CN	σ^2 [Å^2]	ΔE_0 [eV]	R-factor [%]
Fe-O	1.92	3	0.004[a]	-2.4	1.1
Fe-O	2.08	3	0.004[a]		
Fe-Fe	2.89	1	0.004[b]		
Fe-Fe	2.97	3	0.004[b]		
Fe-Fe	3.36	3	0.004[b]		
Fe-O	3.39	3	0.004[a]		
Fe-O	3.59	3	0.004[a]		
Fe-Fe	3.70	6	0.009		
Fe-O	3.79	3	0.004[a]		

[a] Shared σ^2-values among all Fe-O shells.
[b] Shared σ^2-values among the 3 nearer Fe-Fe shells (2.89-3.36 Å).

The EXAFS refinement of the 0.1% Fe/Al_2O_3 sample was carried out using all single-scattering paths up to an effective scattering distance of typically 3.4-3.7 Å, corresponding to four coordination shells: the local Fe-O shell representing the FeO_x moiety and further two Fe-Al and one Fe-O shells, specific for the location of the Fe site on the γ-Al_2O_3 surface in the models.

The reliability of the structural model was retained by refining as few structural parameters as reasonably possible. The bond distance of the local Fe-O shell was set as a floating parameter independently of the further shells. For the further shells, the initially defined bond distances were adjusted by a common correction term. A fixed electronic amplitude reduction factor (S_0^2 = 0.80) and mean square thermal displacement (σ^2) values shared among the same back-scattering atoms in different shells were applied. The local Fe-O coordination numbers were allowed to float freely, as these were not *a priori* known and the coordination numbers of the further shells were allowed to float, conserving the proportions of their coordination numbers as those defined in the models. The total phase shift was expected to have negative values of a few eV.

Among the eight best models selected for EXAFS refinement, seven represent Fe at O_h sites of γ-Al_2O_3, and one (model 15) represents of Fe at a T_d site. The bond distances and coordination numbers in each model were used as starting guesses. Figure 28a shows EXAFS fits using all eight models (black curves) and the corresponding experimental spectrum (grey curves); the results are presented in Table 7 and Table 8.

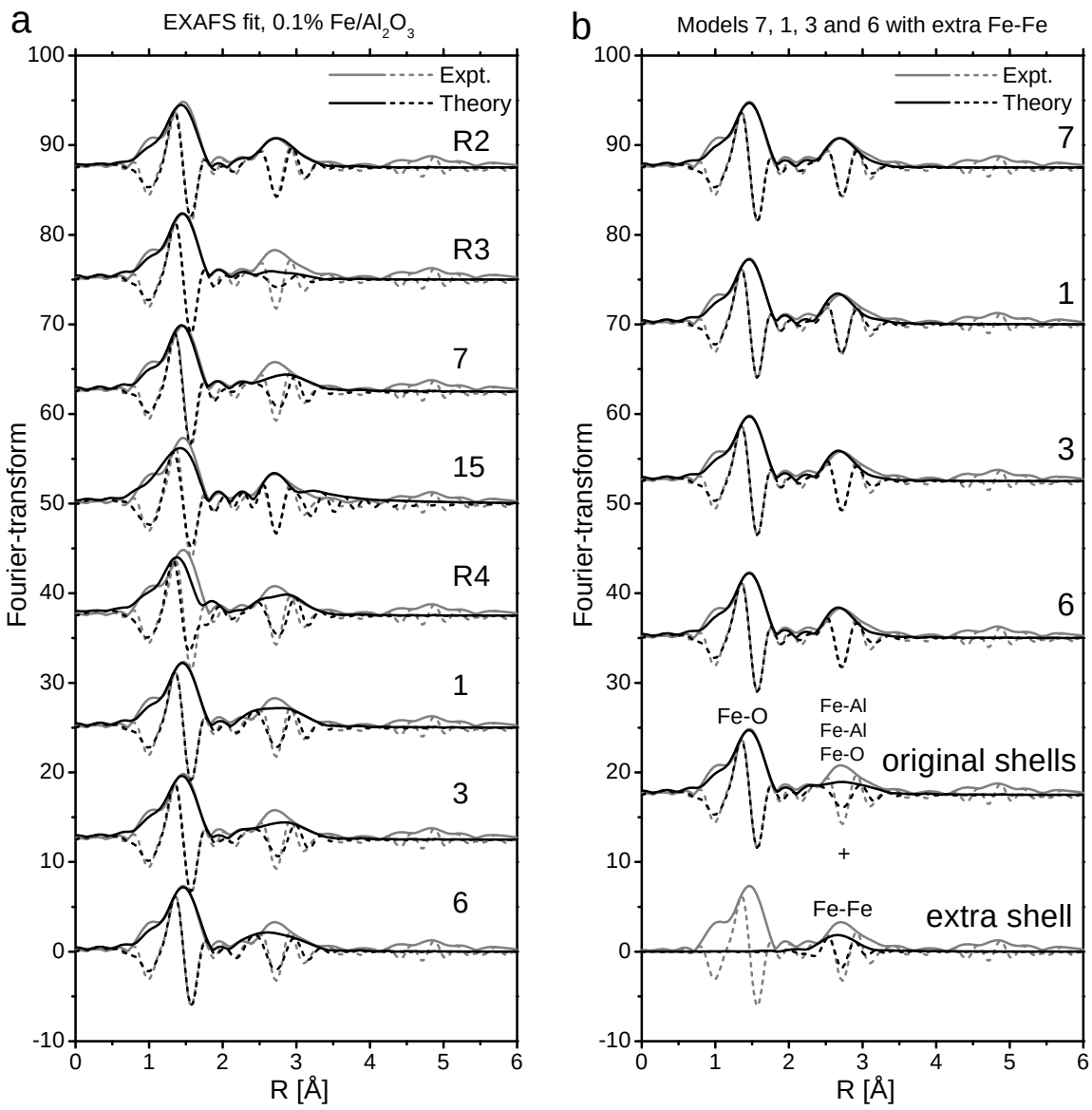

Figure 28 Experimental and fitted Fourier-transformed EXAFS spectrum of the 0.1% Fe/Al_2O_3 catalyst using the best 8 models from the preliminary evaluation (a) and an improvement of the fit using models 7, 1, 3 and 6 by including an additional Fe-Fe shell (b).

The EXAFS fit of model R2 matched the experimental data very well, and this model was also superior in the preliminary selection. It describes a strongly distorted atomic coordination environment of the Fe ion with 4-5 oxygen atoms bonded at Fe-O distances at 1.84-2.00 Å. This is typical for a distorted structure such as in surface species. However, a slight misfit in the Fe-O shells (Figure 28a) indicates an inaccuracy in the initial description of the local Fe-O coordination. Further shells are, on the other hand, excellently represented by this model, which suggests 3-4 Al back-scatterers at neighbouring O_h sites (2.72-2.97 Å) and the same number of Al in T_d sites (3.19-3.32 Å), as well as approximately 6 O-atoms in the further shells. Assuming that the Fe species are surface-supported and not embedded in the bulk

structure, as suggested by this model, such a structure is in terms of the coordination numbers hypothetically similar to models 2, 3, 5 and 6 (Figure 24a-d and Table 2), where Fe is immobilised in close contact with either of the four surface types of γ-Al_2O_3 described earlier.

Table 7 Refined structural parameters of the EXAFS spectrum of the 0.1% Fe/Al_2O_3 catalyst, based on best 7 structural models of Fe at O_h sites. Corresponding fits are shown in Figure 28a.

Path	Model	d [Å][a]	CN	σ^2 [Å^2][b]	ΔE_0 [eV]	R-factor [%]
Fe-O(1)	R2	1.84-2.00	4.4	0.0026	-5.7	2.3
	R3	1.87-1.94	4.4	0.0054	-7.4	8.3
	7	1.91	4.3	0.0057	-6.6	5.6
	R4	1.88-2.08	7.5	0.0068	-5.9	10.2
	1	1.92	4.6	0.0067	-4.8	3.0
	3	1.93	4.6	0.0067	-4.3	3.0
	6	1.93	4.8	0.0069	-4.3	3.4
Fe-Al_{Oh}(1)	R2	2.72-2.97	3.7	0.0071		
	R3	2.79-2.98	4.4	0.70		
	7	-	0	-		
	R4	2.82-3.00	10	0.0287		
	1	2.84	0.9	0.0050		
	3	2.85	1.3	0.0074		
	6	2.85	1.8	0.0103		
Fe-Al_{Td}(2)	R2	3.19-3.32	3.7	0.0071		
	R3	3.39-3.40	1.5	0.70		
	7	-	0	-		
	R4	3.42-3.46	2.5	0.0287		
	1	3.33	1.9	0.0050		
	3	3.33	2.6	0.0074		
	6	3.33	2.7	0.0103		
Fe-O(2)	R2	3.43-3.70	5.9	0.0026		
	R3	3.20-3.49	5.8	0.0054		
	7	3.42	6.4	0.0057		
	R4	3.39-3.50	10	0.0068		
	1	3.47	3.8	0.0067		
	3	3.48	3.0	0.0067		
	6	3.48	3.6	0.0069		

[a] Single bond distances are given for the surface-based models, where single shells were refined. An interval of bond distances is given for the relaxed models, where all bonds can vary in length.

[b] Shared σ^2-values were used for Fe-O and Fe-Al shells.

Table 8 Refined structural parameters of the EXAFS spectrum of the 0.1% Fe/Al_2O_3 catalyst, based on model 15 of Fe at a T_d site. The corresponding fit is shown in Figure 28a.

Path	Model	d [Å]	CN	σ^2 [Å^2][a]	ΔE_0 [eV]	R-factor [%]
Fe-O(1)	15	1.91	5.8	0.0097	-7.5	5.9
Fe-Al_{Oh}(1)		3.27	2.3	-0.0054		
Fe-O(2)		3.27	6.8	0.0097		
Fe-Al_{Td}(2)		3.41	2.3	-0.0054		

[a] Shared σ^2-values were used for Fe-O and Fe-Al shells.

The next statistically best fits was based using models 1 and 3, representing oxidic Fe species supported on top and incorporated into the γ-Al_2O_3 $(222)_1$ surface, respectively (Figure 24a). Following these were the fits based on models 6 and 7 (Figure 24c), representing Fe on the γ-Al_2O_3 $(400)_1$ surface. In all four cases, the local Fe-O(1) coordination number of 4.3-4.8 can be interpreted as a mixture of FeO_4 and FeO_5 moieties, which is confirmed by the pre-edge analysis results.

The coordination numbers in the Fe-Al_{Oh}(1), Fe-Al_{Td}(2) and Fe-O(2) shells of 0-1.8, 0-2.7 and 3.0-6.4, respectively, best reproduce the original values of model 1 (Table 2). These relatively low values indicate, on one hand, that the FeO_x moieties are bonded on top of the γ-Al_2O_3 surface rather than being incorporated into it, but on the other hand, that they are placed near vacancies, which are not taken into accound herein for the surface-based models.

The strong preference by iron atoms of the O_h-sites over T_d-sites can be explained by several effects. Firstly, it is possible that during catalyst synthesis, the Fe ions occupy the vacant O_h-sites because all T_d-sites are already preferentially occupied by Al ions in the surface-near regions of γ-Al_2O_3. In this case, the defect chemistry of γ-Al_2O_3 seems to have an influence on the catalytic behaviour of the Fe/γ-Al_2O_3 system. From energetic considerations on structures R1 to R6 (not shown), the lattice expansion required to accomodate a Fe^{3+} ion at a T_d-site is not strictly greater than that required for an O_h-site, making sterical limitations of accomodation of Fe ions at T_d-sites a less influencial factor. Nevertheless, sterical limitations cannot be completely ignored since the ionic radius of Fe^{3+} is larger than that of Al^{3+}. In opposite cases where the Fe atoms substitute larger lattice atoms (e.g. indium in In_2O_3 films (An *et al.*, 2013, 2014)), sterical limitations do not appear to play a role.

During the fitting, the coordination numbers in the further shells were scaled, changing the coordination numbers for models 3, 6 and 7, but conserving the ratio between them. Interestingly, the ratio of coordination numbers seems to be decisive for a correct model description, which is observed when comparing the coordination numbers in these four

models with those in models 2, 4 and 5 (Table 2a), which were filtered out in the preliminary evaluation. Thus, the coordination number of the Fe-Al_{Td}(2) shell should be equal to or greater than the coordination number of the Fe-Al_{Oh}(1). At the same time, the coordination number of the Fe-O(2) should be at least twice the coordination number of the Fe-Al_{Oh}(1). This means that the preferential locations of the Fe atoms are in the vicinity of several Al atoms at T_d sites. However, such an interpretation must be investigated carefully as it does not apply strictly to all models. For example, model 7 does not have Fe-Al coordination and is bonded via a single oxygen atom to the surface (Figure 24c). The Fe-O(2) shell can be thought to compensate for the Fe-Al_{Td}(2) shell due to its graphical resemblance (Figure 25a).

As a further step, the EXAFS refinement using models 1, 3, 6 and 7 was extended by including an extra Fe-Fe coordination shell at around 3.1 Å (Figure 28b and Table 9) to account for oligomeric clusters of FeO_x moieties rather than monomeric species. This distance is typically found between Fe ions in an oxide (cf. results for α-Fe_2O_3 in Table 6). In all cases, the fit was improved, uncovering a Fe-Fe coordination number of 1.0-1.3, which supports the presence of clusters composed of several (on average two) Fe ions, consistent with the results of Mössbauer spectroscopy. The inclusion of the Fe-Fe shell, however, alters the structural parameters of the other coordination shells. Most obvious is the increase of σ^2 for the Fe-Al shells to very high values of 0.016-0.043 $Å^2$ and the necessity to fix σ^2 for the Fe-Fe shell to 0.005 $Å^2$ to obtain a stable fit, which compromises the reliability of this analysis.

Model R4 suggests 8 Al neighbours in the neighbouring Oh sites (Table 3), which is an over-saturation compared to the spinel structure with only 6. The poor fit quality and very high coordination numbers for the local Fe-O shells and the further shells supports this interpretation. Model R3 describes the local Fe-O shell very well, but a strong misfit for the further shells with an unrealistically high σ^2-value (0.7 $Å^2$) also disqualifies this model.

It is important to note that the decrease in coordination numbers in the Fe-Al shells due to vacancies is analogous to the decrease due to the surface-immobilisation of the Fe centres. The further Fe-O shell (3.3-3.7 Å) is also decreased accordingly in surface-models, but in the relaxed models the bulk value (CN = 8) is retained (cf. Table 2 and Table 3). The similarity between the Fe-Al(2) and Fe-O(2) shells (Figure 25a) can thus lead to false refinement results.

Model 15 returned a negative value of the mean square thermal displacement (Table 8), which is physically unrealistic, although for the further shells the fit was statistically satisfactory (Figure 28a). The possibility of Fe at T_d sites was finally disqualified.

Table 9 Extended analysis of models 7, 1, 3 and 6 with an additional Fe-Fe contribution.

Path	Model	d [Å]	CN	σ^2 [Å^2][a]	ΔE_0 [eV]	R-factor [%]
Fe-O(1)	7 (mod.)	1.92	4.5	0.0064	-5.3	1.7
	1 (mod.)	1.92	4.6	0.0067	-4.8	1.4
	3 (mod.)	1.92	4.4	0.0065	-4.8	1.5
	6 (mod.)	1.92	4.6	0.0066	-4.8	1.6
Fe-Al_{Oh}(1)	7 (mod.)	2.84	0	-		
	1 (mod.)	2.84	0.9	0.016		
	3 (mod.)	2.84	1.6	0.036		
	6 (mod.)	2.84	2.1	0.043		
Fe-Al_{Td}(1)	7 (mod.)	3.33	0	-		
	1 (mod.)	3.32	1.9	0.016		
	3 (mod.)	3.32	3.2	0.036		
	6 (mod.)	3.33	3.1	0.043		
Fe-O(2)	7 (mod.)	3.47	4.7	0.0064		
	1 (mod.)	3.47	3.7	0.0067		
	3 (mod.)	3.47	3.8	0.0065		
	6 (mod.)	3.47	4.1	0.0066		
Fe-Fe	7 (mod.)	3.07	1.3	0.005		
	1 (mod.)	3.08	1.0	0.005		
	3 (mod.)	3.07	1.2	0.005		
	6 (mod.)	3.07	1.2	0.005		

[a] Shared σ^2-values were used for Fe-O and Fe-Al shells. For the Fe-Fe shells, fixed values of σ^2 = 0.005 Å^2 were used.

To summarise, the suitability of models 1, 3, 6 and 7 suggests that in the 0.1% Fe/Al_2O_3 catalyst, small clusters of FeO_4 and FeO_5 moieties are located at octahedral sites on top of the (222) and (400) planes of γ-Al_2O_3, close to tetrahedrally-coordinated lattice Al atoms. The Fe sites can possibly be located on any exposed plane, including also surface defects and edges between the facets.

The low-nuclearity character of the Fe sites was previously also noted for Fe/ZSM-5 (Battiston, Bitter, de Groot*, et al.*, 2003) and Fe/Al_2O_3 (Kou *et al.*, 1996). The interaction of the mononuclear and binuclear Fe sites with the support was considered by (Choi *et al.*, 2003), with a clear suggestion that the Fe sites are standing out on the support, being more exposed to the reactants and therefore more catalytically reactive. The Fe sites on γ-Al_2O_3 presented here are in close interaction with ca. 4 Al atoms (total at O_h and T_d sites) (Table 7 and Table 9), which probably has a strong negative influence on the reactivity of the Fe.

3.4. Conclusion

It was shown in this work that the identification using EXAFS of an unknown structure, such as that of highly dispersed supported Fe species can be approached by using a library of theoretical structure models. This was an alternative approach for to commonly applied EXAFS analysis methods, which partly use bulk α-Fe_2O_3, e.g. (Battiston, Bitter, de Groot*, et al.*, 2003) or spinel-phase oxides (Schwidder *et al.*, 2005, Wong *et al.*, 2000) as input models. Since the present work aimed at uncovering the interaction of the Fe atoms with the γ-Al_2O_3 support, exact models of this chemical system were essential.

In pursuing the goals, first, a set of the most suitable models was selected and afterwards, these models were refined and further improved. The advantage of this approach is that in the first step, unsuitable models can be filtered out, such as the models describing the Fe ions in T_d sites. The subsequent refinement of the EXAFS spectra yielded a complete picture of the local-range order, including the local Fe-O shell and the further shells, which probed the location of the Fe ion on the γ-Al_2O_3 substrate. At the same time, invalid models were rejected. The structural analysis could be further extended to probe the number of Fe ions forming a catalytic site, by including a Fe-Fe shell to the best models.

This three-step refinement method of EXAFS spectra (preliminary selection, refinement, extended refinement) can be generally useful for studying doped materials to locate the preferred sites of the dopant. The use of theoretical models for predicting the structure and location of Fe species on catalyst supports (and generally the location of dopants within a matrix) is sensible since it takes into account the interactions of the dopant atom with the matrix, which a bulk oxide model does not. During fitting, the use of robust input models has been an advantage, because the integrity of the hypothetical model was thus retained. A robust model is a set of scattering paths where the distances are not allowed to float individually, but a common correction term was applied to them. In the opposite case, there is a risk that the fitting fails and large shifts are introduced only to satisfy the fit statistics.

Structure-realistic EXAFS models should be considered more often when addressing the structure of highly dispersed oxidic catalytic sites. The present study has showed that the Fe sites are interacting with several Al atoms of the γ-Al_2O_3 support, possibly binding it tightly and inhibiting reactivity.

4. Fe K-pre-edge analysis for application in heterogeneous catalysis

This chapter deals with a simplified and yet powerful method for extracting the oxidation state and local coordination geometry of Fe ions from the pre-edge peak observed in Fe K-edge XANES spectra. The aim was to adapt the generally known variogram-based method for pre-edge analysis to catalysis research, and to describe its advantages and limitations.

Firstly, the procedure of pre-edge extraction was studied and adapted for XANES spectra of different resolution and quality. Variograms were established for different spectral resolution, for qualitative and quantitative chemical analysis of the Fe species, using reference compounds with known chemical state. It was shown that this analysis can probe the Fe species on a 1% Fe/Al_2O_3 catalyst during temperature-programmed reduction, where the spectra exhibited high noise levels and were not suitable for EXAFS analysis.

Secondly, the pre-edge analysis method was shown to be valuable for analysing high-quality HERFD-XANES spectra as complementary data to V2C-XES. The study was a close collaboration of *operando* catalysis studies with online gas analysis. An active, carefully characterised Fe/ZSM-5 catalyst with well-defined single Fe sites was investigated using this novel spectroscopic method during NH_3-SCR, while measuring NO_x conversion. The V2C spectra were interpreted using simulated V2C spectra using DFT based on theoretical structural models. HERFD-XAS provided necessary information for building these models and finally for understanding the reaction mechanism.

The standard XAS measurements took place at ANKA XAS with support from Stefan Mangold, especially with regard to the dedicated measurements with high-resolution mode with reduced beam slits and fluorescence-mode. The HERFD-XANES and V2C/XES measurements took place at ESRF ID26 with support, motivation and help with data analysis from Pieter Glatzel and Erik Gallo. Mineral samples as reference compounds were kindly provided by Farahnaz Daliran, Kirsten Drüppel (KIT), N. E. Nikol'skaya, T. A. Burova and V. I. Yashina (Russia).

4.1. Challenges in analysis of iron species by pre-edge XAS

It was previously shown (Westre *et al.*, 1997, Wilke *et al.*, 2001) that the pre-edge peak in Fe K-edge absorption spectra directly reflects the oxidation state and coordination geometry of iron in oxidic environment (Fe-O coordination), which allow retrieval of chemical information from the pre-edge spectra, even if the knowledge of the chemical state and

geometry is limited. Typically the intensity and energy position of the pre-edge peak are graphically correlated using a scatter plot (variogram), in which the plot points corresponding to the pre-edge spectra of compounds with different oxidation states and coordination geometries have unique coordinates. A pre-edge variogram based on reference spectra of well-defined iron species can thus be used as a grid for qualitative and quantitative characterisation of iron species in unknown compounds.

The pre-edge peak about 10 eV below the Fe-K absorption edge corresponds to a 1s → 3d electronic transition. For an unambiguous analysis, the main absorption edge overlapping with the pre-edge peak must be subtracted in a well-defined manner and the electronic transitions must be clearly identified, both of which requires high spectral resolution. High-resolution instruments, such as monochromator crystals with small d-spacing (e.g. Si(220) (Waychunas *et al.*, 1983, Westre *et al.*, 1997, Wilke *et al.*, 2001), Si(311) (Dräger *et al.*, 1988, Quartieri *et al.*, 2005) and Si(400) (Galoisy *et al.*, 2001)) have taken instrumental resolution close to the natural line broadening, and HERFD-XAS/XES spectrometers (Battiston, Bitter, de Groot*, et al.*, 2003, Heijboer *et al.*, 2004, Pirngruber *et al.*, 2007, Boubnov *et al.*, 2014) even beyond, giving potential to improve the acquisition and careful analysis of pre-edge data.

The variogram-based approach is simple and shows a high potential to elucidate the local environment of Fe species in complex chemical systems such as minerals, glasses and catalysts, but to the best of our knowledge, its application is limited to studies employing high-resolution techniques (see above). Of high interest remains the extension of the variogram-based approach for pre-edge analysis to catalysis-related XAS studies using standard resolution data, especially under operating conditions. XAS experiments for catalysis research are often carried out at conventional EXAFS beamlines, e.g. SNBL (Grunwaldt *et al.*, 2007, Doronkin, Fogel*, et al.*, 2014) and DUBBLE (Agostini *et al.*, 2013) at ESRF, Grenoble, and ANKA XAS, Karlsruhe (Grunwaldt *et al.*, 2005), using bending magnet radiation without beam collimation or focusing, where energy-resolution is limited by the angular divergence of the beam and by the diffraction-broadening on the monochromators, which are typically equipped with Si(111) crystals. Furthermore, a compromise between the high quality data acquisition and catalysis-relevant measuring conditions must be found (Grunwaldt *et al.*, 2004, Bare & Ressler, 2009, Meunier, 2010, Grunwaldt, 2009). *In situ* XAS studies of highly dynamic catalytic reactions require rapid data acquisition and many catalysts contain the element of interest in low concentrations. Both effects have a direct impact on the signal-to-noise ratio. Sample inhomogeneities are also an important challenge. Dynamic

changes in the catalyst structure are most clearly observable when the catalyst is a powder sample and in close contact with reactant molecules (Grunwaldt *et al.*, 2004). On the other hand, samples prepared as self-supporting wafers can provide high quality spectra, but diffusion limitations limit the relevance of these studies for catalytic reactions.

The objective of this chapter is to investigate whether procedures described in literature to extract chemical information from pre-edge data acquired with high resolution can also be used under challenging reaction conditions at conventional XAS beamlines. For this purpose, the effect of the spectral resolution and data quality (in terms of energy increments) is systematically studied at different steps of the pre-edge analysis. Firstly, the edge subtraction from XANES spectra of a reference compound acquired in HERFD-mode and transmission-mode with high and standard resolution and different quality is tested with several model functions. It is shown that resolution and quality of the measured spectra are less critical than the choice of the model function. After successful edge subtraction, the pre-edge spectra are deconvoluted, which is useful for arbitrarily separating local from non-local transitions (e.g. in α-Fe_2O_3) and works for both high and standard resolution. However, this is less suitable for multiplet analysis, since not all transitions can be identified. The subsequent variogram-based chemical analysis is verified using binary mixtures of reference compounds and a library of compounds containing pure and mixed Fe species, showing that the analysis of standard-resolution pre-edge spectra leads to the same results as those obtained from high-resolution spectra. Finally, structural changes in a 1% Fe/Al_2O_3 catalyst during reduction in 5% H_2/He are studied to verify the applicability of pre-edge spectroscopy for chemical analysis in the field of catalysis research.

An independent *operando* HERFD-XAS/V2C-XES study of a Fe/ZSM-5 catalyst is also presented, highlighting the importance and usefulness of pre-edge analysis also to high-resolution XANES spectra.

4.2. Pre-edge treatment for structural analysis – a historical overview

4.2.1. Studies of Fe in crystalline compounds

The Fe K-pre-edge peak is observed some 10 eV before the shoulder of the main edge and overlaps with the edge tail. Hence, in order to obtain quantitative information about the pre-edge peak, it must be isolated from the “background” of the main edge.

One of the first well-recognised papers dealing with the Fe K-pre-edge characteristics (Waychunas *et al.*, 1983) together with other features of the XANES spectra, examined the energy position of the overall pre-edge feature in the normalised XANES spectrum using the zero-crossing of the first derivative, i.e. the maximum of the pre-edge feature and its relative intensity is determined graphically. This has allowed derivation of trends in the pre-edge features in relation to the Fe ion structure, as described in the previous section. It is furthermore important that the XANES spectra were measured with a high-energy-resolution incident beam, using a Si(220) channel-cut monochromator with an estimated overall resolution (FWHM) of 1.2 eV, close to the calculated core-hole lifetime broadening at the Fe K-edge (Krause & Oliver, 1979). High-resolution conditions allow semi-quantitative evaluation of the XANES data, as the features (to a high degree, the pre-edge features) can then be well-separated from the main edge onset.

The dependence of the alignment of the single-crystal samples to the polarised beam have been examined (Dräger *et al.*, 1988) in order to extract information about the contribution of the dipole and quadrupole transitions to the pre-edge features. For this, a high-resolution Si(311) double-crystal monochromator with a resolution of ca. 1 eV was used. The pre-edge peaks were extracted from the edge onset, although no description was provided to explain the procedure. Based on the resulting isolated pre-edge peaks, is was shown that in the anisotropic crystals of α-Fe_2O_3 and $FeCO_3$, a dipole transition in the former originating from a significant 3d-4p mixing was observed due to a distortion of the coordination octahedron, while in the latter, no dipole contributions were observed due to a perfect octahedral (centrosymmetric) geometry. The anisotropy has facilitated the isolation of the very weak quadrupole transitions in both crystals. Additionally, a speculation is made about long-range (non-local) effects contributing to the pre-edge of α-Fe_2O_3, which is cited in later papers (Battiston, Bitter, de Groot*, et al.*, 2003, Battiston, Bitter, Heijboer*, et al.*, 2003, Petit *et al.*, 2001, Wilke *et al.*, 2001, Heijboer *et al.*, 2004) as transitions typically several eV higher than the others arising due to electronic interactions with neighbouring Fe ions in the oxide crystal.

An early recognised paper specifically using Fe K-pre-edge information to quantify the Fe oxidation state (Bajt *et al.*, 1994) in oxides and silicates of Fe used an approach which is close to the aim of the present work: the use of a conventional-resolution spectrum to isolate and analyse pre-edge information. In this case, a Si(111) channel-cut monochromator (intrinsic resolution ca. 1.4 eV at the Fe K-edge) was used. For extraction of the pre-edge feature, a second-degree polynomial was fitted to the edge onset excluding the pre-edge region and the

latter was fitted with a Gaussian function (a peak-function modelling the experimental broadening), which gave a better result than using a Lorentzian function (a peak function modelling the natural core-hole line broadening). The Fe oxidation state in the standard samples was independently determined by Mössbauer spectroscopy and a linear correlation was derived between the pre-edge position and the fraction of Fe^{3+}. From this calibration, the Fe^{3+}-fraction in several unknown minerals was determined. However, non-local transitions observed in the high-energy tail of the pre-edge of α-Fe_2O_3 mentioned above were not covered in this paper, possibly leading to the overestimation of the pre-edge energy position of α-Fe_2O_3 used as a calibration standard and thus an underestimation of the Fe^{3+}-fraction in unknown samples.

In a detailed study (Westre *et al.*, 1997), the pre-edge features of a large collection of iron complexes with several oxidation states and various coordination geometries were investigated experimentally and theoretically. The high-resolution spectra (overall resolution of 1.4 eV) measured using Si(220) monochromators were analysed using the EDG_FIT software (written by George at SSRL) by fitting the near-edge region using empirically-chosen functions, including pseudo-Voigt peaks for shoulders and crests. The pre-edge peaks were fitted using pseudo-Voigt functions with a 50% Gaussian fraction, which was empirically determined.

Using standard-resolution spectra measured using the Si(111) double-crystal monochromator, pre-edge information was allowed to clearly distinguish between oxidation state and coordination of Fe dopant atoms in mixed oxides (Hilbrandt & Martin, 1998). Later, a systematic quantification of the oxidation state and geometry in Fe-bearing minerals and glasses by using pre-edge information was reported (Galoisy *et al.*, 2001). Quantitative analysis requires highly-resolved spectra, which in this case were obtained using the Si(400) channel-cut monochromator; the overall resolution was evaluated as 1.5 eV. The main edge onset was modelled with the arctangent function and the pre-edge features with 3-4 pseudo-Voigt peaks of 1.5 eV widths. The pre-edge features of minerals with well-defined structure were de-convoluted with the model peak functions and then the pre-edge features in the less-defined glass structures were quantified using varied proportions of the model fits of the well-defined minerals.

A further developed and more general approach to pre-edge analysis for structure analysis of unknown structures (Wilke *et al.*, 2001) was based on reference compounds. Here, a trend was derived of the variation of the pre-edge parameters with the Fe structure. Exploiting the

dependence of the pre-edge peak position on the oxidation state (1.4 eV to differentiate between Fe^{2+} and Fe^{3+}) and the intensity on the coordination number (Figure 29a), a general trend plot with four reference compounds for the extreme chemical states (variogram, Figure 29b) was constructed for characterising other compounds. The pre-edge parameters of binary mixtures of these four reference compounds were employed as a grid for the trend. This method is robust because it uses the overall pre-edge information for describing an average chemical state and is therefore indifferent to small variations, unresolved transitions and other sources of error which must be taken into account when modelling electronic transitions, such as in (Westre *et al.*, 1997). High-resolution measurements with e.g. a Si(220) double crystal monochromator (intrinsic resolution 0.8 eV at the Fe K-edge) are however a pre-requisite for this type of analysis. The main edge was subtracted using spline interpolation of points several eV below and above the pre-edge feature. Spline interpolation connects defined data points with piecewise polynomials (typically cubic), which at the joints must be continuous and differentiable. This, however, requires high-quality data and has the potential weakness that the curve is not defined by a single function and can become subject of subjective data treatment and irreproducibility, leading to high errors (Berry *et al.*, 2003, Heijboer *et al.*, 2004). The extracted pre-edge feature was modelled by an adequate number of pseudo-Voigt peak functions, supported by the results of (Westre *et al.*, 1997). The FWHM and Gaussian fraction of the pseudo-Voigt functions (shared parameters for all peaks used for the same pre-edge feature) were determined empirically: in a first step, both the FWHM and Gaussian fraction were allowed to vary and resulted in Gaussian fractions in the interval 20-60%, with an average of 49% for all the tested minerals of known structure. In a second step, the Gaussian fraction was set to 50%, allowing only the FWHM to vary. In some cases, additional peaks with independently varying parameters were introduced to fit non-local transitions. The integrated intensity and centroid position of the pseudo-Voigt functions representing the local transitions were considered.

Because the average pre-edge parameters are used in the variogram, the interpretation of the local structure of the Fe sites is not always unambiguous, as e.g. sample 8 in Figure 29b at the crossing of the trend lines representing the $^{[6]}Fe^{2+}$-$^{[4]}Fe^{3+}$ and $^{[4]}Fe^{2+}$-$^{[6]}Fe^{3+}$ mixtures. In this case, the shape of the pre-edge feature must be examined separately and complementary structural information about the mineral from other sources must be used to elucidate the structure. Additionally, the number of nearest-neighbour atoms around the Fe absorber (the coordination number of Fe) determined using this variogram-based approach is an average

value. Hence, a pre-edge intensity about halfway between those belonging to 4-fold and 6-fold coordinated Fe can be interpreted as a mixture of the two, or as a pure 5-fold coordinated Fe centre. The trends in the variogram, i.e. the relationships between the centroid position and the oxidation state of Fe, are not linear and that the curvature of the trend line is strongly dependent on the coordination geometries in the binary mixture. For mixtures of Fe^{2+} and Fe^{3+} sites with equal coordination geometry, the trend is close to linear and independent of the coordination geometry. However, for mixtures where both the oxidation state and the geometry of Fe changes ($^{[6]}Fe^{2+}$-$^{[4]}Fe^{3+}$ and $^{[4]}Fe^{2+}$-$^{[6]}Fe^{3+}$ mixtures), specific non-linearity exists (Figure 29c). If the average Fe oxidation state is known, such a relationship can be potentially used to identify whether and how the coordination geometry varies in the respective Fe^{2+} and Fe^{3+} compound in the mixture.

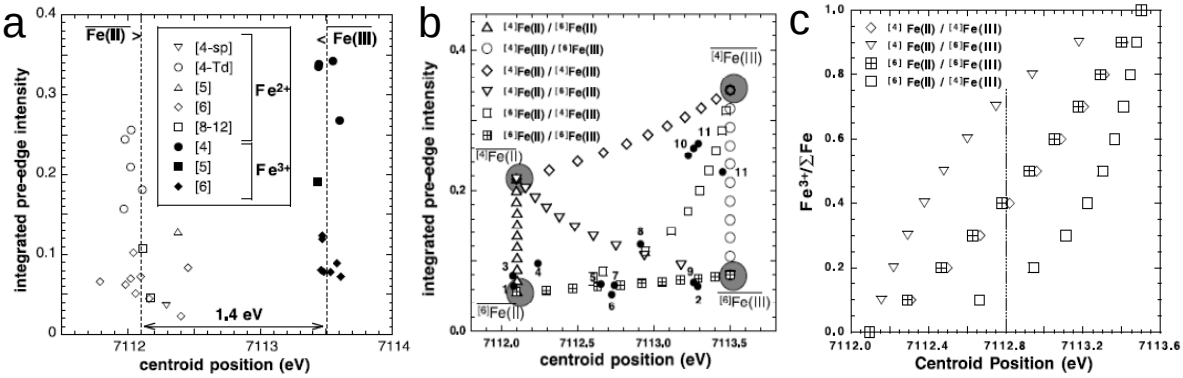

Figure 29 The dependence of the pre-edge intensity and position on the oxidation state and coordination geometry in known Fe-bearing minerals (a). The trend based on the dependence in (a), using pre-edge parameters from spectra of 4 representative substances and the variation of the pre-edge parameters when treating mixtures of the 4 species (b). Numbered black dots are the pre-edge parameters of minerals with unknown structure. Variogram showing the dependence of the fraction of Fe^{3+} on the pre-edge position, considering different combinations of coordination geometry (c). Reprinted from American Mineralogist, Vol. 86, M. Wilke, F. Farges, P. E. Petit, G. E. Brown Jr., F. Martin, Oxidation state and coordination of Fe in minerals: An Fe K-XANES spectroscopic study, p. 714-730, Copyright (2001) Mineralogical Society of America.

4.2.2. Extending to Fe in glasses and non-crystalline materials

As shown, the Fe K-pre-edge information is of high interest in mineralogy for identifying the local Fe structure of minerals with a mixture of species and/or of unknown structure. Another research field is the study of Fe-containing glasses, as this is related to geological processes under the Earth's crust and also to the production of industrial glass (Wilke *et al.*, 2005). An important difference of the structure of Fe in glass with respect to that in crystalline compounds is the poorly defined coordination geometry due to distortion variations from site to site (Wilke *et al.*, 2005). This effect must be considered in the case of Mössbauer

spectroscopy for quantifying the Fe^{3+} and Fe^{2+} species (Alberto *et al.*, 1996, Rossano *et al.*, 1999) and also in the case of pre-edge analysis, as discussed below. The Mössbauer spectral features in these studies were relatively broad due to the site-to-site distortions. As mentioned, the Fe oxidation state and geometry in glasses were quantified using pre-edge analysis (Galoisy *et al.*, 2001); pre-edge features representative for specific Fe species (Fe^{2+}, $^{[4]}Fe^{3+}$, $^{[6]}Fe^{3+}$) in selected standard crystalline compounds were used as a basis for quantification of the respective Fe species in unknown glass compounds, which resulted in reasonably good fits.

An attempt to establish a robust procedure for XANES-based quantification of oxidised Fe species in glass materials was made by drawing relationships between the spectral quantities and the structure (Berry *et al.*, 2003). The spectra were measured at standard resolution conditions (Si(111) channel-cut monochromator with an overall resolution of 2.2 eV). In a way, this work resembles previously reported results (Waychunas *et al.*, 1983) in that numerical dependencies of the different parts of the XANES on the Fe site structure are studied. Well-defined relationships were drawn between the Fe^{3+}-fraction and the pre-edge peak position (linear relationship, Figure 30c), edge position and also the contributions of the 1s → 4s and 1s → 4p features determined by their areas in the spectrum derivative. The samples were a series of Fe-containing glasses synthesised under varying O_2-fugacity in order to tune the Fe^{3+}-fraction, which was subsequently determined by Mössbauer spectroscopy. A clear difference is seen between the variation of the pre-edge energy with Fe^{3+}-fraction in the series of glasses compared to several minerals, suggesting that a calibration based on minerals is not suitable to characterise Fe in glasses and a different approach is needed.

It is pointed out (Berry *et al.*, 2003), that for empirical pre-edge data treatment aimed at charactering and comparing unknown samples based on trends from known samples, the beamline resolution is not critical. This statement defends the use of a relatively low energy-resolution compared to that in numerous other studies. Likewise, model functions used to fit the edge onset and the pre-edge peak are claimed to not be crucial for the individual studies of the pre-edge when used consistently, unless the values hereby obtained should be compared with work of other authors. The authors are aware of the fitting criteria and different model functions used by e.g. (Wilke *et al.*, 2001, Galoisy *et al.*, 2001, Bajt *et al.*, 1994, Westre *et al.*, 1997), but find the spline interpolation method to give reasonable results, being however a somewhat sensitive method. For pre-edge fitting, 2-3 pseudo-Voigt functions are used, which converge to Gaussians accounting for the relatively poor resolution. The widths of the peak

functions are not constrained to be equal within each pre-edge feature, although this is common practice in the abovementioned studies. The main goal is a good fit, from which the area-based average (centroid) energy position can be obtained.

Independent, but complementary works of (Wilke *et al.*, 2005) and (Farges *et al.*, 2004) on basaltic and silicate glasses follow these studies. Wilke makes a re-assessment of the type of calibration done by Berry for synthetic glasses, but using a high-resolution Si(111) four-crystal monochromator with an intrinsic resolution of ca. 1.1 eV. This is claimed to be necessary to increase precision and thus decrease errors in Fe oxidation state determination (Wilke *et al.*, 2005), where the pre-edge extraction and analysis has been changed and adapted for glasses. The edge onset is modelled by the left side of two Gaussians: one broad and low to account for the initial rise of absorption before the edge and one narrow and high to account for the steep rise of the edge. The pre-edge peak is also modelled by two Gaussian functions. This is justified by the continuous site-to-site variations of the Fe coordination geometry and thus cannot be treated as a binary combination of well-defined geometries (modelled by pseudo-Voigt peaks), as is possible with crystalline compounds. Unlike the result of Berry (Figure 30c), the relationship between the Fe^{3+}-fraction and the pre-edge peak position in the work of Wilke is not linear (Figure 30f). Similar to the case of crystalline materials, the oxidation state variograms should be viewed together with the centroid position-integrated area variogram (Figure 30g and h respectively), in order to understand the origin of non-linearity of the oxidation state variogram. In the case of both Berry and Wilke, the coordination geometry (i.e. the distribution of coordination geometries) is the same for the whole range of Fe oxidation states in the sample series: the linear trend in Figure 30g spanning between the data point for fayalite and haematite (crystalline standards for 6-fold Fe^{2+} and Fe^{3+} respectively, Figure 30g) suggests to the reader that the glasses mostly contain 6-fold coordinated Fe sites. Note that in this case, the position and intensity of the haematite data point may be over-estimated due to the high-energy non-local transitions in the pre-edge peak, which are otherwise systematically omitted in analysis of high-resolution spectra (Wilke *et al.*, 2001, Battiston, Bitter, de Groot*, et al.*, 2003, Battiston, Bitter, Heijboer*, et al.*, 2003, Heijboer *et al.*, 2004). In the case of Wilke (Figure 30h), the data points of the glasses span between data points of 5-fold coordinated Fe^{2+} and Fe^{3+}-species (pre-edge intensities between that of 4- and 6-fold coordination), indicating on average 5-fold coordinated Fe in this set of glasses. However, true 5-fold coordination could not be distinguished here from a mixture of 4- and 6-fold coordination (Wilke *et al.*, 2005).

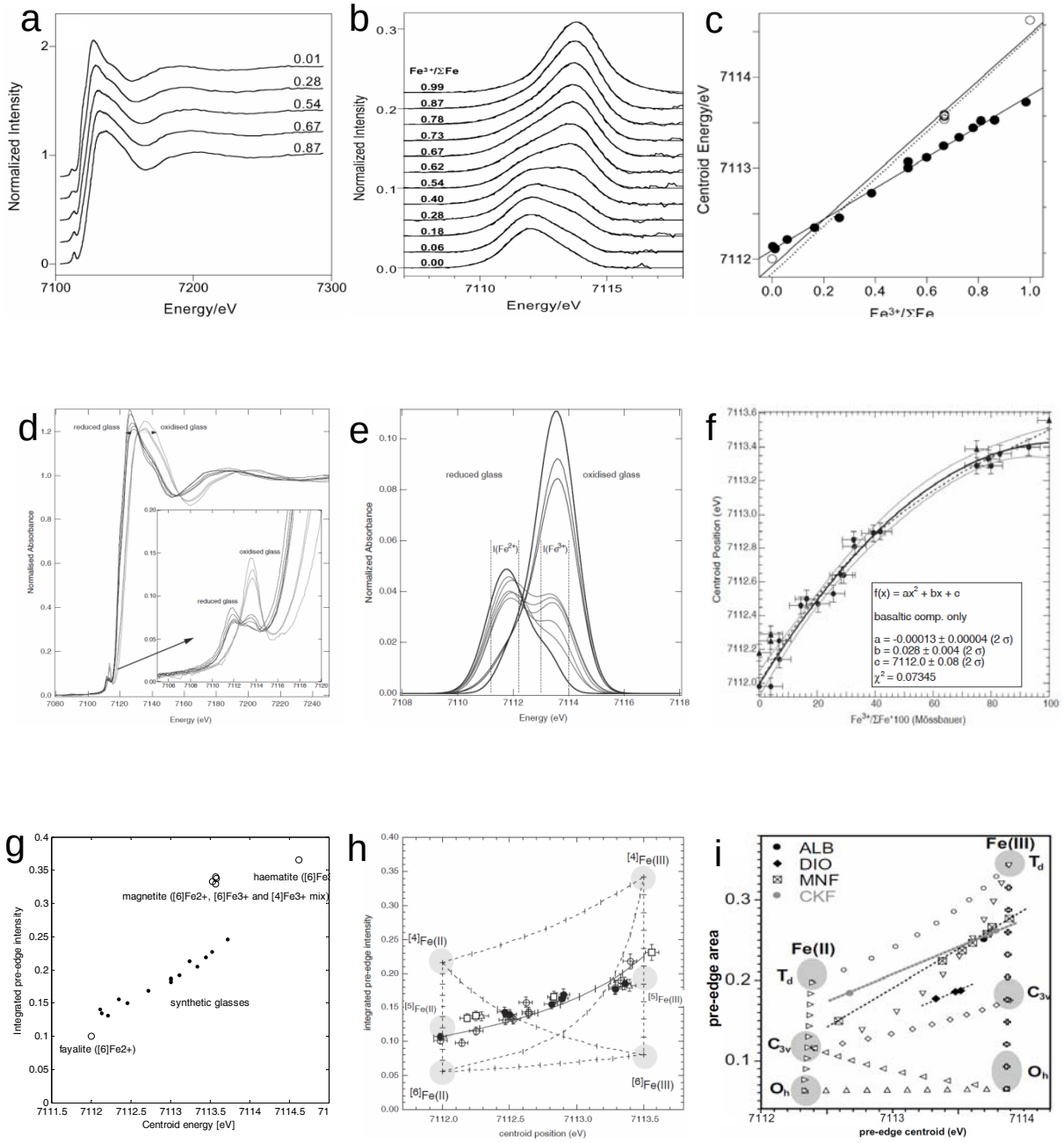

Figure 30 The normalised XANES spectra (a, d), extracted pre-edge peaks (b, e) and the relationships between the Fe^{3+}-fraction determined by Mössbauer spectroscopy in synthetic glasses and the average pre-edge position (c, f), compared between (Berry *et al.*, 2003) using standard-resolution spectra (a, b, c) and (Wilke *et al.*, 2005), using high-resolution spectra. A comparison of pre-edge parameter variograms showing the trends in silicate glasses: plot made using data provided by (Berry et al., 2003) (g), variogram by (Wilke et al., 2005) (h) and (Farges et al., 2004) (i). (a-c and data in g) Reprinted from American Mineralogist, Vol. 88, A. J. Berry, H. St.C. O'Neill, K. D. Jayasuriya, S. J. Campbell, G. J. Foran, XANES calibrations for the oxidation state of iron in a silicate glass, p. 967-977, Copyright (2003) Mineralogical Society of America. (d-f and h) Reprinted from Chemical Geology, Vol. 220, M. Wilke, G. M. Partzsch, R. Bernhardt, D. Lattard, Determination of the iron oxidation state in basaltic glasses using XANES at the K-edge, p. 143-161, Copyright (2005), with permission from Elsevier. (i) Reprinted from Journal of Non-Crystalline Solids, Vol. 344, F. Farges, Y. Lefrère, S. Rossano, A. Berthereau, G. Calas, G. E. Brown Jr., The effect of redox state on the local structural environment of iron in silicate glasses: a combined XAFS spectroscopy, molecular dynamics, and bond valence study, p. 176-188, Copyright (2004), with permission from Elsevier.

An intensity-ratio method is also introduced by the same authors as an alternative for quantifying the Fe^{3+}-fraction from the pre-edge (Wilke *et al.*, 2005). It correlates the ratio $I(Fe^{3+})/[I(Fe^{2+}) + I(Fe^{3+})]$ of the integrated intensities $I(Fe^{2+})$ and $I(Fe^{3+})$ around the maximum of the respective oxidation state-specific peaks (marked in Figure 30e) to the Mössbauer-determined Fe^{3+}-fraction. This method is more sensitive than the use of the centroid position, since the peak intensities depend more strongly on the average oxidation state in the whole Fe^{3+}-fraction interval. However, the intensity-ratio method requires calibrations for every type of Fe-bearing system with its specific Fe coordination geometry (in this case, basaltic and sodium silicate-glasses), as this strongly affects the intensities in the pre-edge region (Wilke *et al.*, 2005).

In parallel, a study focusing on Fe-containing silicate glasses was done (Farges *et al.*, 2004) and though variograms supported by numerical analyses and simulations came to the conclusion that the series of glass samples possibly exhibit 5-fold coordinated Fe, as can be seen in the linear trends in the variogram used in that work in Figure 30i. The observation that the Fe site-coordination is constant with the Fe oxidation state is considered here as a great simplification in the structural analysis where mixtures of oxidation states are involved. This type of simplification can also be made valid for other Fe-based systems in other studies (Wilke *et al.*, 2005, Berry *et al.*, 2003), as the linear span in the position-intensity variogram (Figure 30g, h and i) is also observed there.

The paper makes a comparison of several known pre-edge extraction procedures: cubic spline interpolation, several procedures integrated in the XANDA package, the arctangent and a two-Lorentzian model for processing data collected under high-resolution conditions, using a Si(220) double-crystal monochromator. The two-Lorentzian method was preferred because it required less empirical input and was least sensitive to noise in the data (Farges *et al.*, 2004). The arctangent method was considered the least suitable as it did not smoothly converge to zero outside the pre-edge region. It is also worth remembering that interpolation techniques can be very sensitive to noise. The pre-edge features were modelled by two pseudo-Voigt peaks of 1 eV width and 45% Gaussian fraction, which was calculated (not determined empirically) by convoluting a Lorentzian of width 1.1 eV (Fe K-edge core-hole line width, incorrectly cited from (Krause & Oliver, 1979)) with a Gaussian of width 0.7 eV (intrinsic beamline resolution) to obtain a Voigt peak function, which could be approximated with a pseudo-Voigt peak function with the abovementioned parameters. The authors also provide a general calculation of pseudo-Voigt parameters to model convolutions (Voigt) of a wide

range of Lorentzian and Gaussian functions, similar to (Thompson *et al.*, 1987) who described this kind of peak-modelling for use with powder X-ray diffraction.

These studies can be well-accompanied by pre-edge-based quantification of Fe-species in ancient coloured glassware in order to understand the processes used for glass working in the past (Quartieri *et al.*, 2005), using an adapted modification of the methods used by (Arrio *et al.*, 2000, Galoisy *et al.*, 2001, Wilke *et al.*, 2001) to model the pre-edge features. Another example of historical studies (Wilke *et al.*, 2009) investigates iron gall ink in historical manuscripts with a long-term aim of conservation of these manuscripts from deterioration. Previously developed methods (Wilke *et al.*, 2001, Wilke *et al.*, 2005) for subtracting the main edge onset were used and the pre-edge position and intensity were determined numerically and compared with the variogram for determining the Fe^{3+}-fraction (Wilke *et al.*, 2005). The method for determining the Fe^{3+}-fraction was claimed to be valid, given that the energy-resolution conditions and pre-edge treatment is similar to this and previous studies.

4.2.3. The use of pre-edge information for characterisation of Fe-based catalysts

A large part of the use of XAFS for characterisation of Fe-based catalysts belongs to the last decade. The Fe-species in heterogeneous catalysts are known to be present in a large variety of oxo- and hydroxo-phases on the catalyst support (monomers, dimers, oligomers, bulk oxide and hydroxide phases, e.g. (Battiston, Bitter, de Groot*, et al.*, 2003)), which makes the problem of structure determination especially difficult as X-ray absorption spectroscopy probes and averages all of the atoms of the specific element. This section will highlight some of the applications of Fe K-edge XANES for structural determination, focusing on the pre-edge information, and will possibly emphasise the need for utilisation and further development of this analytical method for heterogeneous catalysis.

Structural investigations involving analysis of XANES features of Fe/Al_2O_3-catalysts with pre-defined Fe^{2+} and Fe^{3+} species for CO-hydrogenation were reported (Kou *et al.*, 1996). Along with detailed EXAFS analysis, the XANES have been analysed in that the energy-difference between the 3d and 4p levels (assigned to the pre-edge peak and edge crest, respectively) was determined and claimed to reflect the stability of the 3d-band. The relative pre-edge intensity (presumably the height in the normalised XANES spectrum) was reported and higher values were interpreted as contributions from tetrahedrally-coordinated Fe species. The energy-axis for each spectrum was re-defined with the first inflection point (onset of the

pre-edge peak) as the zero-point. Therefore, the evaluation of the Fe oxidation state based on the pre-edge position as described in the previous section is not applicable, but an alternative method of XANES analysis is presented.

A multi-component Pt-Fe/γ-Al_2O_3 catalyst was studied by (Lin *et al.*, 2001). EXAFS analysis was done at the Pt L_3 and Fe K-edges and additionally complemented by the semi-quantitative analysis of the XANES in the same way as (Kou *et al.*, 1996), in that the stability of the 3d-orbital was correlated to a low ionisation threshold E_0 (difference between the pre-edge peak and the main edge position) and a high 3d-4p difference, as described above. The relative pre-edge intensity was correlated to the Fe coordination geometry. In short, as-prepared catalyst exhibited E_0 and 3d-4p values typical for the very stable α-Fe_2O_3 and the Fe^{3+}/Al_2O_3 cited from (Kou *et al.*, 1996), but pre-edge intensities similar to that of the spinel-structured magnetite (Fe_3O_4), containing a portion of tetrahedrally-coordinated Fe ions. After reduction, the E_0 increased and the 3d-4p energy difference increased, tending towards values for Fe_3O_4 and FeO, followed by a decrease of the pre-edge intensity. This semi-quantitative method, complemented by EXAFS analysis has provided information for constructing models and predicting the location and surrounding of the transition metal atoms in the catalyst.

A paper on the Fe/MCM-41 zeolite system (Wong *et al.*, 2000) has reported on the transformations of iron oxide under conditions of the ethylbenzene dehydrogenation reaction. Nano-scale Fe_2O_3 species (crystalline phase not detected by XRD) were reduced at increasing temperatures into structures exhibiting XANES features characteristic of Fe_3O_4, FeO and finally, metallic Fe. Accompanied by structure refinement from EXAFS measured at elevated temperatures (which should be treated with caution), XANES spectra show the shift of the edge position and of the pre-edge peak to lower energies. However, as not covered in the paper, the pre-edge peak (as it appears in the normalised XANES spectrum) is relatively sharp and intense in the initial state and maintains its intensity or slightly decreases during reduction, indicating that in all steps of the experiment, Fe is present in a non-centrosymmetric geometry, which for instance can be the tetrahedral geometry present in spinel structures. Therefore, the initial oxidation state of the catalyst, as can be evaluated from the XANES spectrum, possibly Fe^{3+}, but the phase is most probably a spinel-like phase (e.g. γ-Fe_2O_3) or the Fe species constitute small disordered oxidised clusters with the Fe^{3+} ions in a non-centrosymmetric environment.

4.2.4. XAFS studies of the Fe/ZSM-5 system with focus on the pre-edge

A series of papers employing the methods of Wilke deal with Fe K-edge XAS investigations of Fe/ZSM-5 zeolite catalysts for selective catalytic reduction of nitrogen oxides by hydrocarbons (HC-SCR) (Battiston *et al.*, 2000, Battiston, Bitter, de Groot*, et al.*, 2003, Battiston, Bitter, Heijboer*, et al.*, 2003, Bitter *et al.*, 2003, Battiston, Bitter & Koningsberger, 2003). The over-exchanged (Si/Al = 17, Fe/Al ~ 1) catalysts prepared by chemical vapour deposition of $FeCl_3$ followed by washing exhibit Fe as binuclear complexes, which is shown by EXAFS. The EXAFS results must be treated cautiously because many coordination shells were fitted for each spectrum. The ΔE_0-values varied individually for each shell were very different, showing that the Fe-O shells were very different to those of the reference compound α-Fe_2O_3. The Fe^{3+} (concluded from the similarity to α-Fe_2O_3 in the XANES spectrum) in the binuclear complex is reversibly reduced by CO as seen by a -2.5 eV shift of the edge position (Battiston *et al.*, 2000). The pre-edge peak visible in the figure seems unaffected, but is not discussed or analysed. The EXAFS spectra were measured under standard resolution conditions (Si(111) double-crystal monochromator).

In later extended studies, these authors have determined the structure of the Fe sites at different steps of the catalyst synthesis (Battiston, Bitter, de Groot*, et al.*, 2003, Bitter *et al.*, 2003) i.a. by means of high-resolution transmission electron microscopy (HRTEM) with elemental mapping, Mössbauer spectroscopy and specific surface measurements (Battiston, Bitter, de Groot*, et al.*, 2003) as well as reactant molecule uptake measurements and catalytic tests (Bitter *et al.*, 2003). The accessibility of the binuclear Fe complexes inside of the zeolite pores by probe molecules was shown to be limited by Fe species located in the micropores of the zeolite. Calcination led to the removal of these species from the micropores and agglomeration as nanoparticles of α-FeOOH and α-Fe_2O_3 on the surface of the zeolite crystals outside of the micropore structure. Severe calcination caused an especially high degree of agglomeration compared to mild calcination. However, the catalytic activity and the probe molecule uptake kinetics were not affected by the extent of calcination, suggesting that the less accessible binuclear Fe complexes deep inside the zeolite channels do not contribute significantly to the catalytic performance (Bitter *et al.*, 2003). On the other hand, the mildly calcined catalysts were preferred as representative samples of the Fe/ZSM-5 systems for the EXAFS studies by this group, as the number of agglomerated nanoparticles (contributing to EXAFS, but not a catalytic species of interest) was lowered (Battiston, Bitter, Heijboer*, et al.*, 2003, Battiston, Bitter & Koningsberger, 2003).

These studies report that the Mössbauer spectral features related to the binuclear Fe sites were well-resolved, whereas those reflecting the bulk agglomerates were relatively broad (Battiston, Bitter, de Groot*, et al.*, 2003) due to structural disorder. A similar situation was already discussed for the case of Fe-containing glasses (Alberto *et al.*, 1996, Rossano *et al.*, 1999, Wilke *et al.*, 2005). The fact that the Mössbauer features for the Fe binuclear sites are well-resolved (Battiston, Bitter, de Groot*, et al.*, 2003) suggests that their Fe coordination geometry is well-defined as in crystalline materials, in contrast to the poorly defined geometry in glasses. Thus, if the presence of nano-scale agglomerates can be avoided, the structure of the Fe centres present in the catalysts can be treated in the same way as mixtures of different Fe sites in minerals. In fact, following examples from literature will show the comparison of pre-edge data of catalysts with that of minerals and crystalline materials presented by Wilke (Wilke *et al.*, 2001).

In addition to EXAFS analysis, high-energy-resolution fluorescence-detected XANES (HERFD-XANES) spectra were used for extraction of pre-edge information. The incident radiation energy was scanned using a Si(111) double-crystal monochromator and the emitted Fe Kβ-fluorescence was detected using a Rowland circle spectrometer equipped with spherically bent Si(531) analyser crystals, resulting in an intrinsic resolution of 0.4 eV, which is below the natural linewidth. The pre-edge peak was extracted using cubic splines to interpolate the regions before and after the pre-edge region, as done by e.g. (Wilke *et al.*, 2001). The pre-edge of the reference compound procedure α-Fe_2O_3 was modelled by 4 pseudo-Voigt peaks of 50% Gaussian fraction, where peaks centred above 7115 eV attributed to non-local transitions were omitted in the further analysis. The pre-edge features of the catalysts were analysed numerically and graphically without peak-fitting. The pre-edge feature of the catalyst after washing, mild and severe calcination is in all cases representative of Fe^{3+} in octahedral geometry, compared with the reference compound and literature (Wilke *et al.*, 2001). After calcination treatments favouring the formation of bulk iron oxide species, the pre-edge feature showed a slight high-energy tail, which is typical for α-Fe_2O_3.

The continuation of this study is reported in two further papers, where the redox and structural properties of the binuclear Fe complex are probed by XANES and EXAFS under relevant chemical environments: heat treatment in inert He and oxidising O_2 atmosphere (Battiston, Bitter, Heijboer*, et al.*, 2003) and under HC-SCR conditions (Battiston, Bitter & Koningsberger, 2003). The HERFD-XANES pre-edge peak analysis in the former study shows that under inert atmosphere at room temperature, the Fe^{3+} in the binuclear complex is

in a slightly distorted octahedral coordination. At higher temperatures, the complex is dehydrated, which causes the pre-edge peak to increase due to the decreasing Fe-O coordination number from 6-fold to 5-fold, thus losing symmetry but retaining the oxidation state Fe^{3+}. At further elevated temperatures, one of the bridging oxygen atoms is released, resulting in reduction (shift of the pre-edge to lower energy) and further decrease in Fe-O coordination, evaluated by using the variogram of (Wilke *et al.*, 2001). Exposure to the O_2 atmosphere at higher temperatures inhibits the reduction (release of the bridging oxygen atom), but does not affect the dehydration – the pre-edge peak is relatively intense but centred at ca. 7113.5 eV characteristic of Fe^{3+}. On the other hand, exposure to H_2 at high temperatures reduces Fe^{3+} to Fe^{2+} and decreases the Fe-O coordination.

Under the HC-SCR-relevant experimental conditions (Battiston, Bitter & Koningsberger, 2003), pre-edge peak information extracted from XANES spectra recorded with standard resolution using a Si(111) double crystal monochromator and analysed according to (Wilke *et al.*, 2001), showed that heat treatment with He or butane causes a reduction of a major fraction of Fe to Fe^{2+}, whereas treatments with O_2, a NO+O_2 mixture or butane+NO+O_2 mixture leave Fe in the Fe^{3+}-state. Exposure to NO causes a partial reduction of Fe to Fe^{2+}. Furthermore, the average Fe coordination geometry of the Fe species in the catalyst was 5-fold in all cases except for the catalyst exposed to the butane+NO+O_2 mixture, where the pre-edge intensity corresponds to a coordination between 5- and 6-fold or a distorted octahedral.

In the two abovementioned studies on the same chemical system but using pre-edge information from XANES acquired under different energy-resolution conditions, there are several differences. The study using HERFD-XANES (Battiston, Bitter, Heijboer*, et al.*, 2003) detects a larger overall variation in the Fe coordination geometry, whereas using standard resolution (Battiston, Bitter & Koningsberger, 2003), Fe is in most cases (except for the butane+NO+O_2 mixture) in a constant 5-fold-coordinated state.

Regarding the resolution conditions, it is important that the intensity (and to some degree, the position) of the pre-edge feature varies slightly depending on the overall resolution of the spectra, which for a most accurate analysis should be compared with spectra of standards acquired under identical conditions. This was not accomplished in either case, as both the HERFD-XANES (Battiston, Bitter, Heijboer*, et al.*, 2003) and the standard-resolution XANES (Battiston, Bitter & Koningsberger, 2003) were compared with standard data of Wilke (Wilke *et al.*, 2001), who used a high-resolution monochromator. Although these differences are not crucial for a qualitative analysis, as Battiston and co-workers argue

(Battiston, Bitter, Heijboer, *et al.*, 2003), they must still be considered when assessing the application of pre-edge information. Figure 31 illustrates this effect: extracted Fe K-pre-edge features in Fe/ZSM-5 under flows of He and O_2 at 350°C and the data points plotted with the variogram of Wilke. The differences are not large: mainly the pre-edge intensity from HERFD-XANES is lower for both points than the standard XANES), which can justify the direct comparison of data. Hypothetically, the integrated intensity and average position of a specific set of transitions should not depend on the resolution, because the resolution only determines the shape of these transitions. The resolution-dependent differences may, however, arise from the pre-edge extraction procedure, which is purely mathematical and uses model functions, which may not always have a physical meaning.

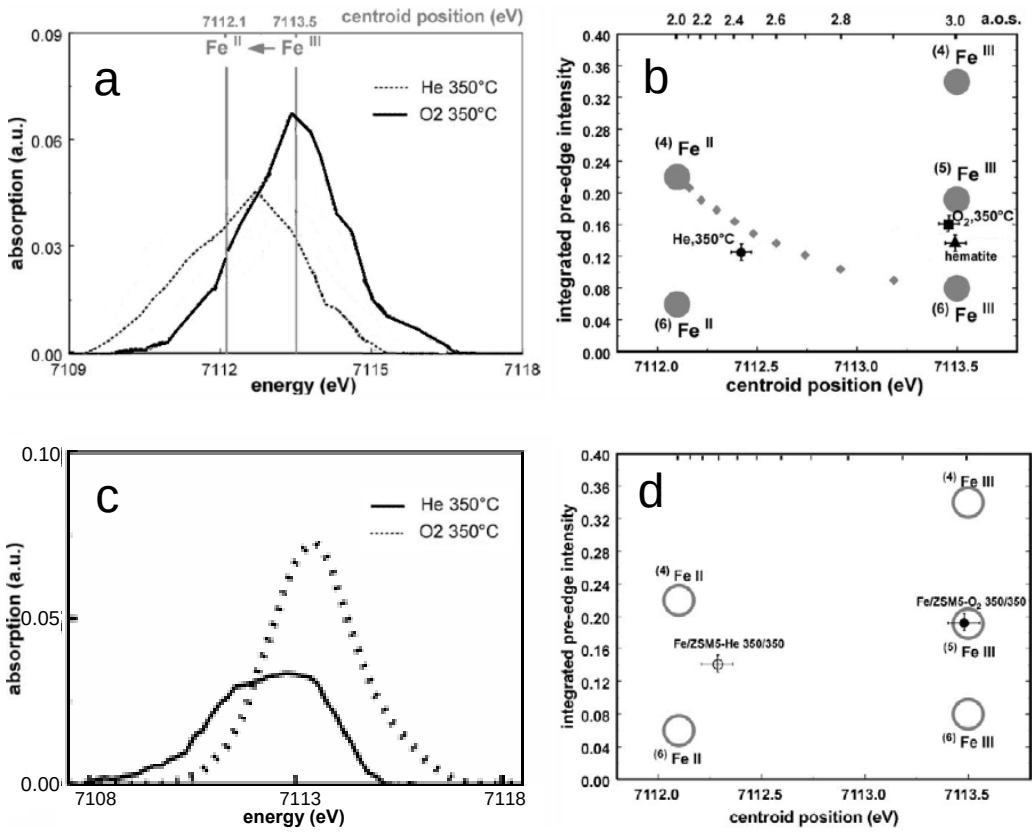

Figure 31 Extracted pre-edge features for Fe/ZSM-5 at 350°C under He and O_2 atmospheres measured with high-resolution Fe Kβ-fluorescence detected XAS (a) (Battiston, Bitter, Heijboer, *et al.*, 2003) and the same conditions measured using a standard-resolution XAS setup (c) (Battiston, Bitter & Koningsberger, 2003). The centroid position and integrated intensity (numerically determined) are plotted in both cases (b and d respectively) by the authors in the variogram from (Wilke *et al.*, 2001). (a-b) Reprinted (modified) from Journal of Catalysis, Vol. 215, A. A. Battiston, J. H. Bitter, W. M. Heijboer, F. M. F. De Groot, D. C. Koningsberger, Reactivity of Fe-binuclear complexes in over-exchanged Fe/ZSM-5, studied by in situ XAFS spectroscopy. Part 1: Heat treatment in He and O_2, p. 279-293, Copyright (2003), with permission from Elsevier. (c-d) Reprinted from Journal of Catalysis, Vol. 218, A. A. Battiston, J. H. Bitter, D. C. Koningsberger, Reactivity of binuclear Fe complexes in over-exchanged Fe/ZSM-5, studied by in situ XAFS spectroscopy. 2. Selective catalytic reduction of NO with isobutane, p. 163-177, Copyright (2003), with permission from Elsevier.

Concerning the pre-edge centroid position, known to reflect the Fe oxidation state, the resolution also has an effect, as already seen in the case of synthetic glasses presented in the previous section (Berry *et al.*, 2003, Wilke *et al.*, 2005). The linear relationship between the Fe oxidation state and the pre-edge position for the conventional resolution spectra (Figure 30c) and the non-linear relationship for the high-resolution spectra (Figure 30f) cross at approximately $Fe^{3+}/\Sigma Fe = 0.5$ and centroid position of ca. 7113 eV, so that in high-resolution pre-edge features, the centroid position would be over-estimated for more reduced samples and under-estimated for the more oxidised samples. This was also observed in the Fe/ZSM-5 samples under He and O_2 at 350°C (Figure 31d and d), although the effect is very slight and the error bars overlap for the data points collected under O_2 at 350°C.

Regarding the correlation of the Fe oxidation state to the Fe coordination geometry, a change of the coordination geometry of the Fe centres along with the oxidation state in the Fe/ZSM-5 system is reported (Battiston, Bitter, Heijboer*, et al.*, 2003). The variogram shows a trend of less-than-5-fold coordinated Fe^{2+} and higher-than-5-fold coordinated Fe^{3+}, which is logical as more oxidised Fe atoms should be coordinated by more oxygen atoms than the reduced Fe atoms. However, as seen in the examples of synthetic glasses (Berry *et al.*, 2003, Farges *et al.*, 2004, Wilke *et al.*, 2005) where the average Fe coordination geometry is constant and independent of the Fe oxidation state, this trend is not typical for all chemical systems. Again, the exact values depend on the spectral resolution as demonstrated above.

Other forms of the Fe/ZSM-5 catalyst system such as the framework-substituted (Si/Al = 36, Si/Fe = 175 meaning Fe/Al = 0.2) with potential application for selective hydrocarbon oxidation and nitrogen oxide conversion have been studied with *in situ* XAS (Heijboer *et al.*, 2004), exploiting pre-edge information from Fe Kβ-detected HERFD-XANES. The beamline setup uses a Rowland circle spectrometer equipped with six spherically bent Ge(620) analyser crystals. The resolution of the spectrometer is 1 eV and the HERFD-XANES spectra were collected by integrating over 1 eV at the maximum of the Fe $K\beta_{1,3}$ line, which was possibly not done by Battiston and co-authors in their HERFD-XANES work reported above (Battiston, Bitter, Heijboer*, et al.*, 2003). The spectroscopic features in the resulting high-resolution XANES spectra are not only much better resolved than in conventional XANES, but also significantly (2-3 times) more intense. "Conventional" XANES spectra used for comparison to HERFD-XANES were calculated by integrating over 25 eV at the Fe $K\beta_{1,3}$ line. As estimated (Heijboer *et al.*, 2004), the reproducibility of the pre-edge extraction using cubic splines, as e.g. by Wilke, was estimated to be limited by a 20% variation, depending on

the points before and after the pre-edge feature to be interpolated. HERFD-XANES was argued to overcome this problem with the extraction procedure, due to the good separation of the pre-edge feature from the main edge onset. A non-zero background contribution however exists between the pre-edge and the main edge in the presented spectrum plots, and an individual decision of the person performing data analysis is generally required to evaluate whether this contribution should be modelled or avoided. The pre-edge features in the HERFD-XANES were modelled by 1-4 possible pseudo-Voigt peak functions and contributions centred above 7115.0 eV were omitted. For direct comparison with the results of Wilke, the determined centroid positions were shifted to lower energies by 0.77 eV.

One of the focuses of the HERFD-XANES study (Heijboer *et al.*, 2004) is the determination of the Fe^{3+} coordination geometry in the Fe/ZSM-5 catalyst at different synthesis steps under an O_2 flow. Accurate quantitative information about the fraction of tetrahedral Fe sites (inside the micropores) and octahedral sites (located outside the pores as inactive agglomerated species) was provided, similar to (Battiston, Bitter, de Groot*, et al.*, 2003).

Many contemporary publications show the use of the Fe K-pre-edge feature as a fingerprint of the Fe coordination geometry without carrying out quantitative analysis of the pre-edge peak. For example, in a study of the Fe sites in a FAPO-36 zeolite catalyst (Ristić *et al.*, 2003), the pre-edge peak of the "as-synthesised" zeolite and the "template-free" zeolite indicated that in Fe is present in tetrahedral and octahedral sites respectively in these samples, by comparing the data with pre-edge peaks of α-Fe_2O_3 and $FePO_4$. In a similar way, a Fe/ZSM-5 catalyst for N_2O decomposition was studied (Jia *et al.*, 2002) and well-resolved pre-edge features in the XANES spectra provide valuable information about the structure of the Fe sites, complemented by EXAFS refinement and reactivity experiments.

At the same time, Fe/ZSM-5 catalysts gain interest for application in N_2O-decomposition (Choi *et al.*, 2003, Pirngruber *et al.*, 2004, Pirngruber, Grunwaldt*, et al.*, 2006, Pirngruber *et al.*, 2007). The structure of monomeric tetrahedral Fe sites in the Fe/ZSM-5 system (Si/Al = 25), which are formed by chemical vapour deposition of $FeCl_3$ into the zeolite, was studied (Choi *et al.*, 2003). Exposure of the catalyst to oxidising gases (O_2, N_2O) and reductive pre-treatments (H_2) is followed *in situ* by EXAFS and XANES, where the pre-edge peak shows the changes in the Fe oxidation state. Similar to (Battiston, Bitter, de Groot*, et al.*, 2003), qualitative analysis of the pre-edge peak is conducted of the Fe/ZSM-5 system (Si/Al = 20) with a large fraction of binuclear Fe centres (Marturano *et al.*, 2001), comparing it with that of known Fe-containing substances with known geometry and oxidation state.

A dedicated *in situ* XAS paper on this catalyst under N_2O decomposition reaction conditions is presented (Pirngruber *et al.*, 2004), where EXAFS analysis and linear combination analysis (LCA) of the XANES spectra provide structural information on the Fe centres. For XANES analysis, the most oxidised (in O_2) and the most reduced (in H_2) form of the catalyst at 400°C was used as standards for the Fe^{3+} and Fe^{2+} states respectively. The changes in the pre-edge peak are shortly mentioned, but not analysed quantitatively.

To briefly address the nuclearity of the Fe sites, the probability of formation of oxygen-bridged binuclear sites (Feng & Hall, 1997) was calculated to be especially high for Si/Al ratios between 11 and 25, strongly decreasing for higher ratios, as the Fe atoms are probably bonded to the Al-sites of the zeolite. The Fe/ZSM-5 system with a Si/Al ratio of 17 (Battiston *et al.*, 2000, Battiston, Bitter, de Groot*, et al.*, 2003, Battiston, Bitter, Heijboer*, et al.*, 2003, Battiston, Bitter & Koningsberger, 2003) hence favours the formation of binuclear Fe sites, whereas the system with a Si/Al ratio of 25 (Choi *et al.*, 2003) is at the border of favouring the formation of mononuclear Fe sites. Further work (Pirngruber, Roy*, et al.*, 2006) addresses the nuclearity of the Fe sites in Fe/ZSM-5 catalysts by experimental methods.

Also, in the field of Fe/ZSM-5 catalysts, DFT calculations predicted the occurrence of Fe^{4+} species (Jia *et al.*, 2002). A technique which can specifically probe the existence of high-spin Fe^{4+}-species is resonant inelastic X-ray scattering (RIXS), which is practically a combination of HERFD-XANES with X-ray emission spectroscopy (XES) used herein. In RIXS, both the incident energy and the emitted energy is analysed; high resolution conditions are needed for this: for example, a Si(220) double crystal monochromator and a Rowland circle detector with spherically bent Si(531) analyser crystals (Pirngruber, Grunwaldt*, et al.*, 2006, Pirngruber *et al.*, 2007). The main Fe Kβ-fluorescence lines are the Fe $K\beta_{1,3}$ (most intense, used for HERFD-XANES) and the Fe Kβ'. According to the selection rules for different electronic configurations of Fe (not covered in the present work), the characteristic 1s → 3d transition responsible for the pre-edge features are only observed in the Fe $K\beta_{1,3}$ fluorescence for Fe^{2+} and Fe^{3+}. This transition can however be seen in both the Fe $K\beta_{1,3}$ and the Fe Kβ' fluorescence lines for Fe^{4+}. Hence, the presence or absence of pre-edge features in the Fe Kβ' emission unequivocally proves the presence or absence of Fe^{4+} with the high-spin $3d^4$-state (Pirngruber, Grunwaldt*, et al.*, 2006, Pirngruber *et al.*, 2007). In both works by Pirngruber dedicated to RIXS, Fe^{4+} species were not detected in the Fe/ZSM-5 system on exposure to N_2O. It is worth mentioning that for RIXS and HERFD-XANES measurements, a very high X-ray photon flux is required and care must be taken to avoid and/or determine beam damage,

which can result in probing structural changes induced by the beam, rather than the reaction conditions (Pirngruber et al., 2007).

Another catalyst system, the Fe/BEA zeolites, are of high interest for selective catalytic reduction of nitrogen oxides by ammonia (NH_3-SCR) and have recently been studied by a series of techniques including *in situ* XAS (Høj et al., 2009, Klukowski et al., 2009, Maier et al., 2012, Maier et al., 2011). The Fe oxidation state is correlated with the NH_3-SCR activity of the catalyst (Høj et al., 2009) by means of LCA of the XANES spectra under reaction conditions. The starting and final spectrum of the Fe sites in a temperature-programmed reduction (TPR) experiment were used as Fe^{3+} and Fe^{2+} standards, similar to (Pirngruber et al., 2004). Pre-edge information is not used. This work demonstrates that a high NH_3-SCR activity is correlated with the presence of monomeric Fe^{2+} sites.

A qualitative analysis of the pre-edge region is presented (Klukowski et al., 2009) under different reaction conditions: appearance of the maxima and shoulders in the pre-edge region at characteristic energies (7112 eV and 7113.5 eV) serve as evidence of Fe^{2+} and Fe^{3+} species respectively. The work derives a mechanism for the NH_3-SCR reaction over Fe/BEA catalysts based on data about adsorbed molecular species (using DRIFTS) and the chemical state of Fe (based on XANES).

These studies have employed standard-resolution XANES data routine procedures for pre-edge data treatment should be introduced for these applications in order to strengthen the conclusions made about the nature of the Fe centres when high-resolution spectra are not available.

4.3. Pre-edge analysis procedures for catalytic studies

The pre-edge peaks of normalised XANES spectra were analysed using MATLAB codes based on procedures described in literature (Roe *et al.*, 1984, Galoisy *et al.*, 2001, Wilke *et al.*, 2001, Quartieri *et al.*, 2005, Wilke *et al.*, 2005). The absorption edge onset was modelled by fitting the energy regions below and above the pre-edge feature (see Section 4.2.1) and subsequently subtracted to extract the pre-edge peak. Four methods for extraction of the pre-edge peak were initially examined: interpolation by a cubic spline, fitting with an arctangent, an inclined arctangent (arctangent with a first degree polynomial) and 2 Gaussian functions with a shared centre. One of these Gaussian functions was broad and flat to account for the increase in absorption before the pre-edge region; the other function was narrow and intense

to account for the edge onset. The inclined arctangent, used throughout all successive analysis, has the form

$$y(x) = A_1 \arctan\frac{x-\mu_1}{\sigma_1} + c_1 + c_2(x-\mu_1),$$

with amplitude A_1, width σ_1 and gradient of the straight line c_2, centred around μ_1 and vertically offset by c_1.

The spline interpolation with not-a-knot end conditions was applied to the XANES data. When the model functions were fitted to the XANES spectra, all parameters were allowed to float within limits set far from the target values; the function converged to the data points with standard deviations in the order of 1% of the normalised pre-edge peak height (ca. 0.1). The values of the model function should preferentially not exceed the values of the experimental data above the edge (e.g. the arctangent should tend to a value below 1). A crucial step was the individual selection of fitting intervals for each spectrum. The fitting range in the edge onset area was extended as far as it could be modelled with the appropriate functions.

As a further step, electronic transitions in the extracted pre-edge features (in the following referred to as pre-edge spectra) were fitted with peak functions (Wilke *et al.*, 2001). The MATLAB-procedure for this step automatically fitted 1-5 pseudo-Voigt functions of the form

$$psV(x) = A_2\left[nG(x) + (1-n)L(x)\right]$$

with $G(x) = \frac{2\sqrt{\ln 2}}{FWHM\sqrt{\pi}}\exp\left[-4\ln 2\left(\frac{x-\mu_2}{FWHM}\right)^2\right]$ and $L(x) = \frac{2}{\pi FWHM}\frac{1}{1+4\left(\frac{x-\mu_2}{FWHM}\right)^2}$.

The pseudo-Voigt function is a linear superposition of a Gaussian and a Voigt profile with respective fractions n and $1 - n$ ($0 \le n \le 1$), serving as an approximation for a true Voigt profile, which is a convolution of the two functions. Both functions are centred about μ_2 and their width is described in terms of the full width at half maximum (FWHM) of the pseudo-Voigt profile.

During the fit, the FWHM and Gaussian fraction n were allowed to float. The first fit of the pre-edge feature was carried out with a single pseudo-Voigt peak function. The starting guess values for the further four fits (2-5 peaks) were obtained from the results of the first fit. The starting situation for a 2 peak fit was the use of two peaks of half the area of the single peak

separated by half the FWHM of the single peak. Accordingly, for a three peak fit, three peaks of a third of the area of the single peak separated by one-third the FHWM of the single peak are used as initial guesses, etc. The result of fitting 1-5 peaks to a pre-edge spectrum of α-Fe_2O_3 is shown in Figure 32. The FWHM and Gaussian fraction were constrained to be shared by all peaks within one fit, but their values were not fixed. Further analysis of the pre-edge spectra with respect to the oxidation state and local geometry of Fe was carried out graphically according to (Wilke *et al.*, 2001) by correlating the integrated intensity and the centroid position (i.e. the area-based average energy position) of the pre-edge peak.

Similar curve-fitting procedures are used in X-ray absorption data processing packages (SixPACK (Webb, 2005) and Athena (Ravel & Newville, 2005), both based on IFEFFIT), but have some constraints because they are not easy to change or adapt for users. For example, sharing fitting parameters for several model functions is not possible and automatic assignment of the starting guesses as described above cannot be programmed. Alternatively, commercial software such as PeakFit (Systat Software Inc.) can be used for pre-edge analysis (Quartieri *et al.*, 2005), but with limited access to several different fits. On the contrary, the MATLAB-based procedure used in this study allows quick examination of fits with a different number of peaks and selection of the most suitable one. The optimum number of pseudo-Voigt peaks for modelling the pre-edge feature was chosen based on the quality of fit, preliminary knowledge of the expected number of electronic transitions as well as the peak width and a Gaussian fraction consistent with the instrumental resolution. Moreover, several possibilities, such as wider peaks accounting for overlapping transitions, can be taken into account. Multiple data sets can be analysed in parallel, starting parameters can be stored and manipulated in input text files, and output data files are generated after each analysis.

4.3.1. Fe-bearing reference compounds

For analysis using the variogram-based approach, reference compounds, minerals and oxides representing different chemical states of iron were used, presented in Table 10. The minerals olivine, siderite, aegirine, ceylonite and bronzite were received from Federal State Unitary Enterprise “All-Russian Research Institute of Mineral Resources” (FGUP “VIMS”, Moscow, Russia) and Moscow Geological Prospecting Institute - Russian State Geological Prospecting University (MGRI-RSGPU, Moscow, Russia). Staurolite, magnetite and sanidine were provided by the Institute of Applied Geosciences (KIT, Karlsruhe, Germany). The minerals have been analysed by the groups. Additionally, high-purity iron nitrate, rodolicoite, wustite,

maghemite and iron phthalocyanine were purchased from indicated manufacturers. Previously characterised haematite, amorphous hydrated iron phosphate, iron (III) acetylacetonate and iron (II) oxalate were kindly provided by Jan-Dierk Grunwaldt.

Table 10 Chemical composition of the reference compounds used in this study and the mode of measurement used for acquiring the XANES spectra. The list is sorted according to valence (Fe^{2+} and Fe^{3+}) and coordination symmetry of the Fe ions (tetrahedral T_d, octahedral O_h, square planar and mixed).

	Samples	Measurement modes
Fe^{3+} O_h	Haematite α-Fe_2O_3	transmission (standard and high res.), HERFD
	$FePO_4 \cdot xH_2O$	transmission (standard res.)
	Fe(III)acac	transmission (standard res.)
	$Fe(NO_3)_3 \cdot 9H_2O$ (Prolabo)	transmission (standard res.)
	Aegirine $NaFeSi_2O_6$ (Russia)	transmission (standard res.)
Fe^{3+} T_d	Rodolicoite $FePO_4$ (Merck)	transmission (standard and high res.), HERFD
	Sanidine $(K,Na)(Si,Al,Fe)_4O_8$ (Eifel, Germany) (Ginibre *et al.*, 2004)	fluorescence (standard res.)
Fe^{2+} O_h	Wustite FeO (Aldrich)	transmission (standard and high res.)
	Fe(II)oxalate	transmission (standard res.)
	Siderite $FeCO_3$ (Russia)	transmission (standard res.)
	Olivine $(Mg,Fe)_2SiO_4$ (Sakha Rep., "Mir" diamond mine)	transmission (standard res.), HERFD
	Bronzite $(Mg,Fe)_2Si_2O_6$ (polar Ural, Russia)	transmission (standard res.)
Fe^{2+} T_d	Staurolite $Fe_2Al_9O_6(SiO_4)_4(O,OH)_2$	transmission (standard and high res.), HERFD
	Ceylonite $(Mg,Fe)Al_2O_4$ (Russia)	transmission (standard res.)
Others		
Fe^{+3}, T_d and O_h	Maghemite γ-Fe_2O_3 (Alfa Aesar)	transmission (standard res.)
Fe^{+2}, Fe^{+3}, T_d and O_h	Magnetite Fe_3O_4	transmission (standard res.)
Fe^{+2}, square planar	Fe(II) phthalocyanine (Alfa Aesar)	transmission (standard res.)

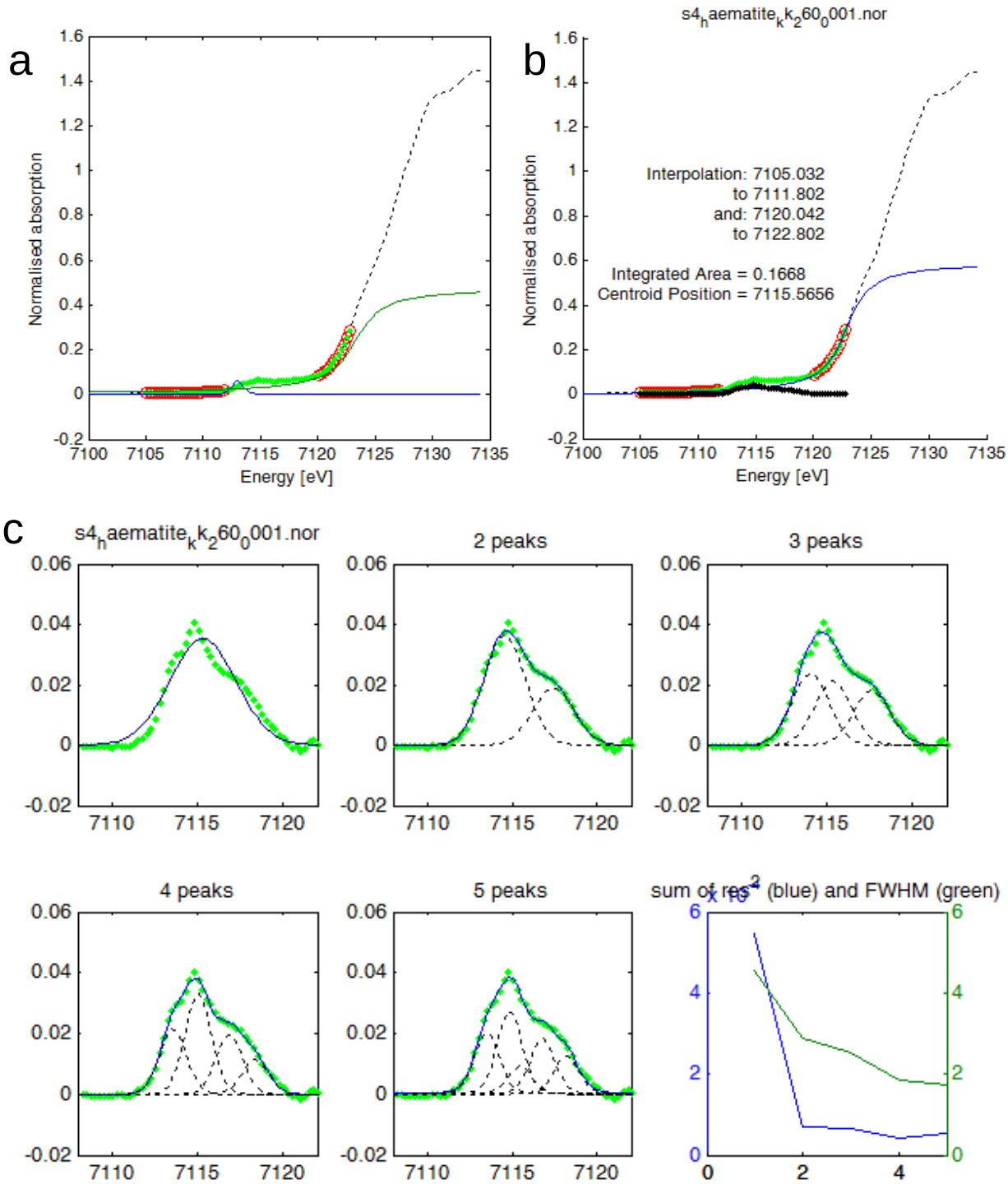

Figure 32 Screenshots from the MATLAB-based program, automatically performing background subtraction (starting guess in (a) and best fit of inclined arctangent in (b)) and fitting of 1, 2, 3, 4 and 5 pseudo-Voigt peaks (c) to a pre-edge spectrum of α-Fe_2O_3. The sum of squared residuals (blue curve) and the FWHM in eV (green curve) as a function of the number of peaks accompany the fit results.

The samples were prepared as pellets (pressed with cellulose). The Fe content was adjusted to an absorption length resulting in an edge jump between 0.3 and 0.9. Six mechanical binary mixtures of the compounds staurolite, FeO, $FePO_4$ and α-Fe_2O_3 were prepared with Fe stoichiometric ratios close to 50:50 and their exact ratios were determined using linear combination analysis of the normalised XANES spectra. To generate spectra of mixtures, normalised XANES spectra of reference compounds measured with standard resolution were merged in the required ratios. *In situ* XANES data of the TPR experiment was recorded and treated as described in the Materials and Methods section, in addition to pre-edge analysis.

4.4. Comparison of pre-edge extraction models

To find the most suitable model functions for pre-edge extraction in an empirical way, several functions were tested. For modelling the absorption edge onset, steeply increasing functions have been used in several studies, such as a second-degree polynomial (Bajt *et al.*, 1994), arctangent (Galoisy *et al.*, 2001, Quartieri *et al.*, 2005), arctangent with a first degree polynomial (Roe *et al.*, 1984), damped harmonic oscillator function (Cottrell *et al.*, 2009) or several peak functions (Westre *et al.*, 1997, Farges *et al.*, 2004, Farges, 2005, Wilke *et al.*, 2005). Therefore we investigated here how the background model functions (inclined arctangent, arctangent, 2 Gaussians and the cubic spline) converged to the XANES spectra of staurolite acquired with different energy resolution and scan parameters: transmission-mode with standard resolution (0.5 eV and 1 eV increments), high resolution (0.25 eV increments) and, for comparison, HERFD-XANES (0.05 eV increments). Pre-edge extraction and fitting were carried out not simultaneously but subsequently. Hence, they were optimised individually.

The HERFD-XANES spectrum of staurolite in Figure 33a shows a pre-edge feature well-separated from the edge onset, which is due to the specific detection of the Fe $K\beta_{1,3}$ fluorescence line with high resolution, excluding all other transitions. All model functions subtract the small contribution of the edge onset from the pre-edge feature in a similar manner (Figure 33b) and with high quality (low residuals and standard deviation σ).

The transmission-mode XANES spectrum of staurolite measured with high resolution (Figure 33c) differs from the HERFD-XANES spectrum with a strong background consisting of the edge onset tail, comparing Figure 33b and d. This is caused by a continuum of electronic transitions resulting from photo-absorption, which all contribute to the transmission spectrum. Like in the HERFD-XANES spectrum measured at ID26 (ESRF), the double-feature in the

pre-edge region can be identified in the transmission-mode spectrum measured at ANKA XAS, due to the enhanced energy-resolution of this beamline with reduced slit widths.

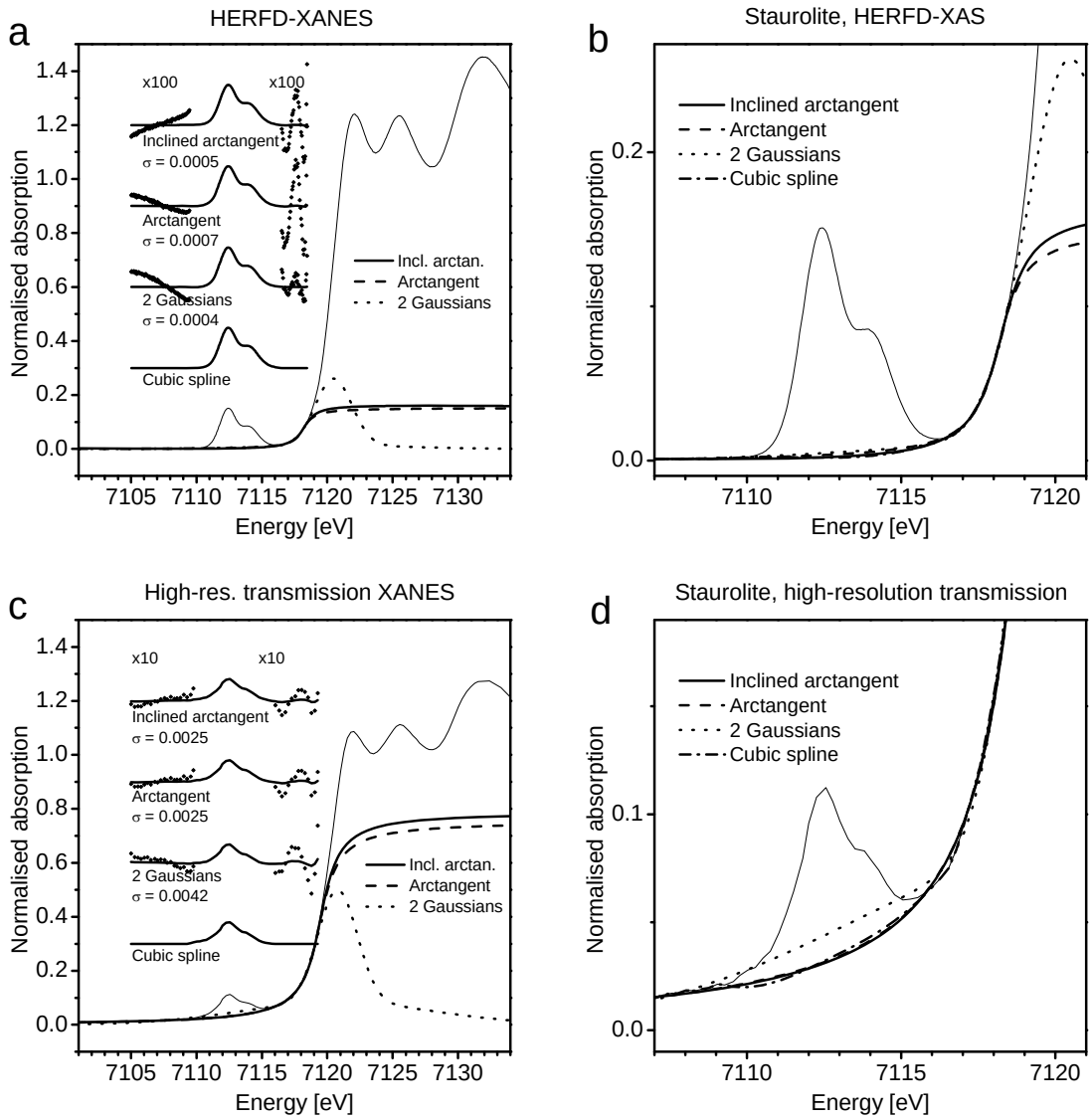

Figure 33 XANES spectra of staurolite and pre-edge extraction models for HERFD-XANES data recorded in 0.05 eV increments (a) and high-resolution transmission-mode XANES data recorded in 0.25 eV increments (c). The functions for modelling the edge onset – the inclined arctangent, arctangent, 2 Gaussian functions and cubic spline – are displayed with the XANES spectra they are applied to. The resulting extracted pre-edge peaks are shown offset for clarity. The fitting residuals are magnified by a factor of 100 (HERFD) and 10 (high-resolution transmission) to show the misfit and the standard deviation (σ) is given. Details in the pre-edge region of plots (a) and (c) are shown in plots (b) and (d) respectively.

For subtraction of the pre-edge peak from the edge onset, the model functions were fitted to the high-resolution transmission spectrum to about 0.5 (normalised absorption) (Figure 33c), whereas a portion up to only ca. 0.1 in the HERFD-XANES data (Figure 33a) is necessary. The standard deviations (σ) are an order of magnitude higher in the high-resolution

transmission XANES, including significant fit residuals in the regions below and above the pre-edge peak. They are shown along with the extracted pre-edge spectra in Figure 33 (a and c), magnified by factors of 100 and 10, respectively. Although the misfit was quite small, the model functions could not perfectly reproduce the shape of the spectra.

The best-converging functions for modelling the edge onset in the transmission-mode spectra acquired with high resolution (Figure 33c and zoom in d) are the inclined arctangent function and the arctangent. The curvature of the edge onset is modelled very well. The inclined arctangent is potentially more flexible as it can correct any constant gradient component at the expense of including the inclination slope as one extra parameter.

The edge onset could also be modelled by 2 Gaussians, but with a larger standard deviation. Only the low-energy side of this peak function was used in the fit. This feature is characterised by two slopes joined by a smooth kink, which can indeed be a good model for the shape of the transmission XANES spectrum in Figure 33c. On the other hand, in the pre-edge region this function is more rigid than the arctangent functions and tends to "cut" through the pre-edge feature (clearly visible in Figure 33d), truncating it in intensity and distorting the width and shape of the peak. It is possible that this effect can be eliminated by letting the two Gaussian peaks centre at individual positions (Wilke *et al*., 2005).

The quality of the background subtraction by cubic spline interpolation cannot be evaluated statistically, since the spline passes exactly through the points below and above the pre-edge region, leaving no residuals. Interpolation of points below and above the pre-edge feature using a cubic spline has been reported previously (Battiston, Bitter, de Groot*, et al.*, 2003, Battiston, Bitter, Heijboer*, et al.*, 2003, Wilke *et al.*, 2001). Cubic spline interpolation is well-suited for high-quality data but very sensitive to noise, as slight displacement of data points can cause the spline to deviate from a reasonable trajectory. Even pre-edge data measured with standard resolution can be extracted using cubic splines, but requires a low noise level and densely sampled data points (Berry *et al.*, 2003). To maintain a stable trajectory of the spline across this rather large gap in the present work, an additional knot was manually included in the pre-edge region. However, this is not acceptable for a reproducible and objective approach, therefore interpolation by cubic splines was not pursued further in this work.

In case of the XANES spectrum measured with standard resolution in 0.5 eV energy increments (Figure 34a and zoom in b), the fit quality followed a similar trend as for the high-

resolution transmission spectrum: the inclined arctangent and the arctangent are superior. The standard-resolution spectrum measured in 1 eV energy increments (Figure 34c and zoom d) was generated by removing every second data point from the spectrum acquired in 0.5 eV increments. Surprisingly, the inclined arctangent fitted the spectrum with this low data point density significantly better than the arctangent function. A slope as one additional degree of freedom to the function can thus improve the least-squares fit significantly, if only a few data points are fitted. However, such an effect is less relevant for low-quality data or when only a few data points are available.

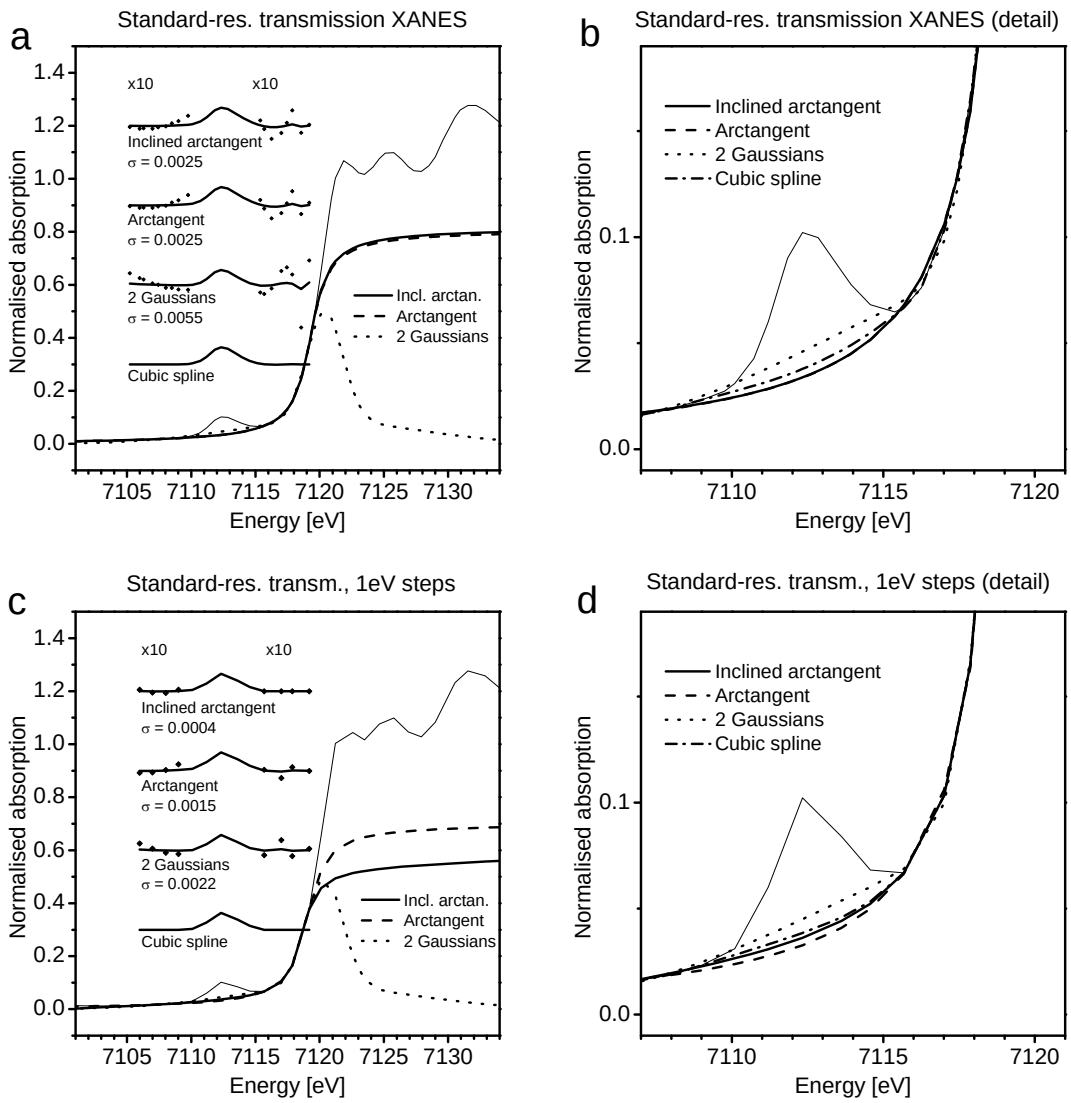

Figure 34 XANES spectra of staurolite and pre-edge extraction models for standard-resolution transmission-mode XANES data recorded in 0.5 eV increments (a) and the same data set with quality degraded by removing every second data point, resulting in 1 eV energy increments (c). The functions for modelling the edge onset – the inclined arctangent, arctangent, 2 Gaussian functions and cubic spline – are displayed with the XANES spectra they are applied to. The resulting extracted pre-edge peaks are shown offset for clarity. The fitting residuals are magnified by a factor of 10 to show the misfit and the standard deviation (σ) is given. Details in the pre-edge region of plots (a) and (c) are shown in plots (b) and (d) respectively.

To address the challenge of data quality in terms of the data point sampling density, the transmission-mode XANES spectra shown in Figure 33c and Figure 34 (a and c) were recorded with varying increments (0.25, 0.5 and 1 eV).However, the background subtraction by the three functions remains the same and does not depend on the data point density. From this observation it can be concluded that a high data point density has hardly any influence on the quality of the background subtraction. On the other hand, the data point density should be sufficient for resolving the spectral features, otherwise spectral information is lost, as for example shown in Figure 34c (1 eV energy increments).

The inclined arctangent and the arctangent function turned out to be well-suited candidates for subtraction of the main edge onset contribution in transmission-mode XANES data acquired with standard and high resolution. As the slope in the inclined arctangent provides additional adjustments for improving the quality of fitting in the background-subtracting step, this function is used in the following sections.

4.5. Structural trends derived from pre-edge information

In the next step, the chemical structure of iron was analysed by evaluating pre-edge data recorded with both standard-and high-resolution. The chemical state of iron can be extracted from pre-edge structures, cf. pioneering work (Wilke *et al.*, 2001) and other studies (Battiston, Bitter, Heijboer*, et al.*, 2003, Heijboer *et al.*, 2004). Graphical correlations between integrated intensities and the centroid positions of pre-edge features in a variogram allow differentiating between different oxidation states and coordination geometries of iron. The applicability of this method can be verified by applying it to pre-edge spectra of reference compounds containing known Fe species as well as to binary mixtures of these compounds. This approach is first tested using pre-edge spectra acquired with high resolution. Subsequently, to complement the above-mentioned studies, the variogram-based method is applied to pre-edge spectra measured with standard resolution, which is important for *operando* studies on catalysts, the main objective of this study.

Figure 35 shows pre-edge spectra of the reference compounds staurolite, FeO, $FePO_4$ and α-Fe_2O_3 and their mechanical mixtures acquired with high resolution in transmission mode (the parent XANES spectra from which those pre-edge spectra were extracted are shown in Figure 36). The pre-edge spectra of the reference compounds, extracted from XANES spectra measured with standard resolution in 0.5 eV energy increments, are shown in Figure 39 along with pre-edge spectra of binary mixtures extracted from XANES spectra generated by

merging absorption data of the reference compounds in various ratios. For each mixture series, one XANES spectrum was generated in precisely the same ratio as in the mixture measured with high resolution for direct comparison of the analysis as will be shown later. The parent XANES spectra (measured and merged) are shown in Figure 40.

The pre-edge spectra were empirically deconvoluted using pseudo-Voigt peak functions and then compared with theoretically predicted electronic transitions (Table 11). The peak-fitting procedure must also be applicable when theoretical information of the electronic structure is not available. For this reason, peak fitting was applied to pre-edge spectra of the mixtures of reference compounds. This is especially useful for identification and isolation of non-local transitions, as shown in the following sections.

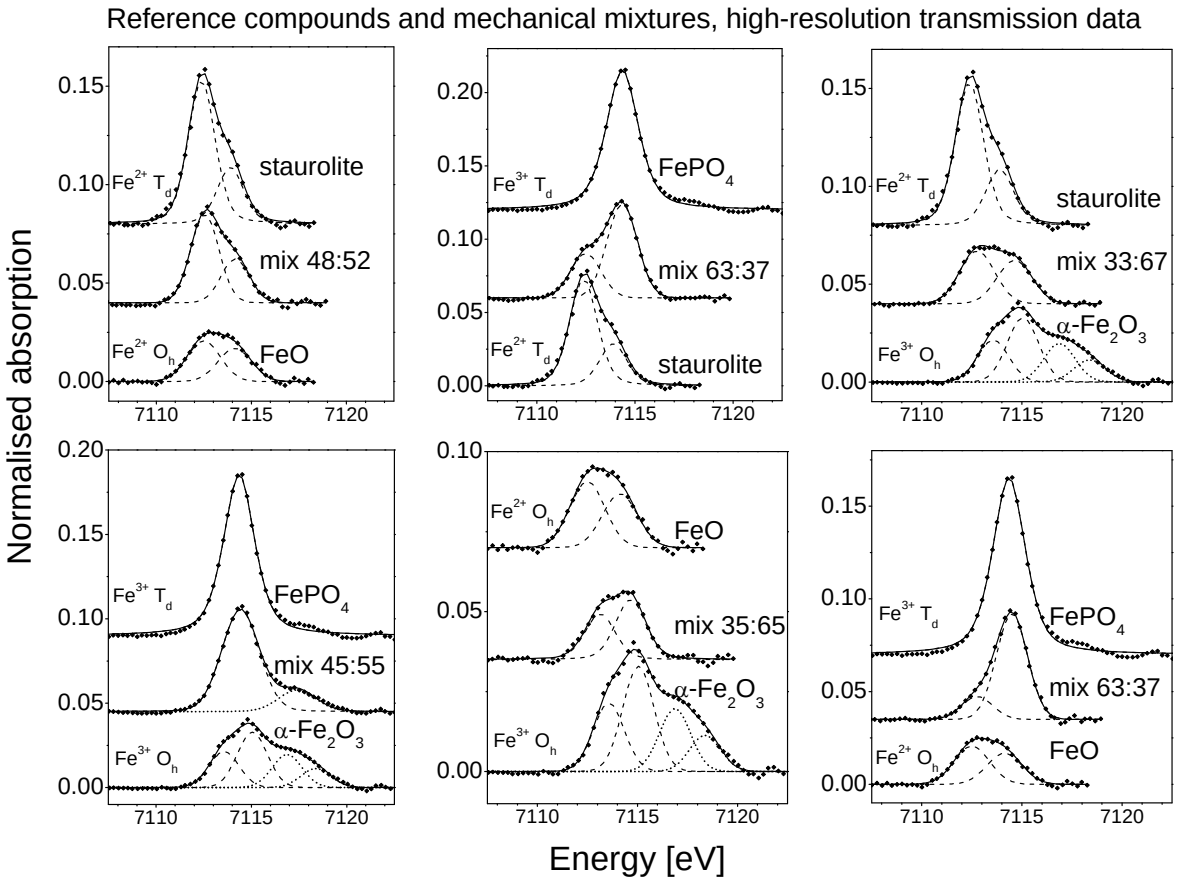

Figure 35 Pre-edge spectra of the of the reference compounds staurolite, FeO, $FePO_4$ and α-Fe_2O_3 and their binary mechanical mixtures from high-resolution transmission-mode XANES data, extracted using the inclined arctangent model function and fit with pseudo-Voigt peak functions. Transitions centred above 7115 eV (plotted in dotted lines) were omitted in the analysis. The parent XANES spectra are given in Figure 36. The mixing ratios were determined using linear combination analysis of the normalised XANES spectra.

Applying the high-energy-resolution fluorescence-detection (HERFD) mode, the electronic transitions in the pre-edge were studied in detail. The HERFD-pre-edge spectra (Figure 37a) extracted from HERFD-XANES spectra (Figure 37b) further improve the high resolution achieved in transmission-mode measurements with narrow beam slits. The high data quality in terms of the very small energy increments (0.05 eV), the good separation from the edge crest and the higher intensity of the pre-edge peak due to specific Fe Kβ-detection facilitates the analysis.

The pre-edge spectra of the reference compounds staurolite (Fe^{2+} T_d), FeO (Fe^{2+} O_h) and $FePO_4$ (Fe^{3+} T_d) acquired with both high and standard resolution were fitted with two (staurolite, FeO) and one ($FePO_4$) pseudo-Voigt peaks respectively (cf. Figure 35 and Figure 39), but with broader peak functions for the standard resolution spectra (cf. Table 11 and Table 12). The pre-edge spectrum of α-Fe_2O_3 was on the other hand deconvoluted into 4 peaks in the high-resolution spectrum and 2 peaks (2.9 eV FWHM, broader than the typical curve) in the standard-resolution spectrum. The use of 4 peaks (not shown) to fit the standard-resolution pre-edge spectrum of α-Fe_2O_3 had no positive effect on the quality of fit and led to identical numerical results. Deconvolution of the standard-resolution spectra required peaks with an average FWHM of 2.2 eV, in contrast to an average of 1.9 eV for the high-resolution spectra.

For comparison, pre-edge spectra acquired in HERFD-mode could be deconvoluted with a larger number of narrower pseudo-Voigt functions. Note that for the Fe^{2+} O_h species, olivine was used as reference instead of FeO. The FWHM-values of 1.5-1.7 eV are a significant improvement compared to transmission-mode measurements due to the high instrumental resolution (elastically scattered peak of 1.4 eV). However, this instrumental broadening with respect to the incident beam is higher than the lifetime broadening predicted at the Fe K-edge (1.25 eV) (Krause & Oliver, 1979), resulting in Gaussian fractions over 90%.

A distinctive feature of the pre-edge spectrum of α-Fe_2O_3 was the contribution above 7115 eV (plotted in dotted lines), which was attributed to transitions into the orbitals of the nearest-neighbour Fe atoms (non-local transitions), having mainly dipole character (Caliebe *et al.*, 1998, Glatzel, Sikora & Fernández-García, 2009). These are irrelevant for probing the first Fe-O coordination shell. An important reason for fitting the pre-edge spectra was to eliminate these contributions prior to further analysis (Battiston, Bitter, de Groot*, et al.*, 2003, Wilke *et al.*, 2001). The two-peak fit provided the same proportion of local and non-local contributions (1 and 1) as the four-peak fit (2 and 2) (cf. Figure 35 and Figure 39).

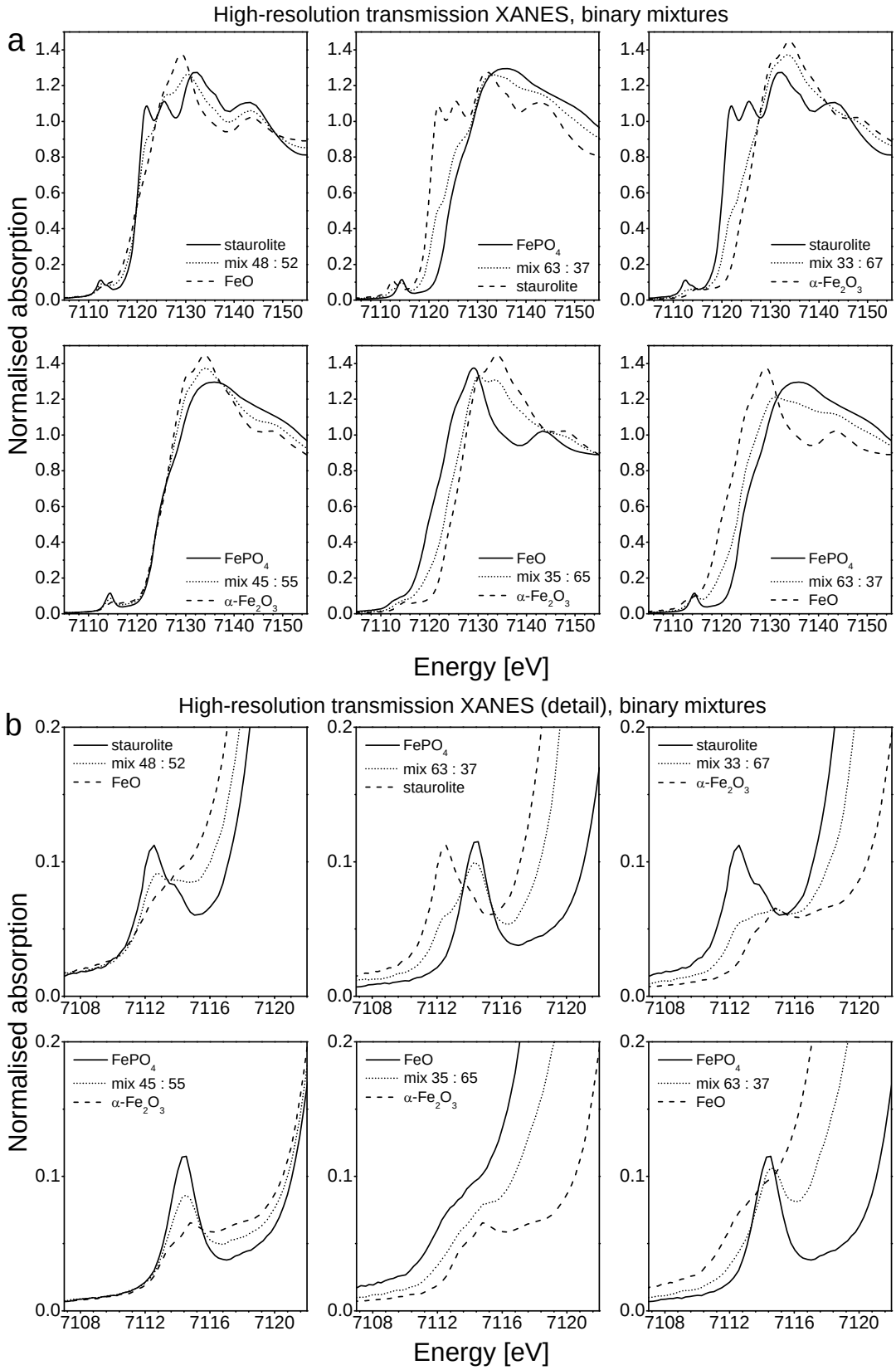

Figure 36 High-resolution transmission XANES spectra (a) and detail of pre-edge peak (b) of the reference compounds and their binary mechanical mixtures. The stoichiometric Fe proportions in the binary mixtures were determined by linear combination analysis.

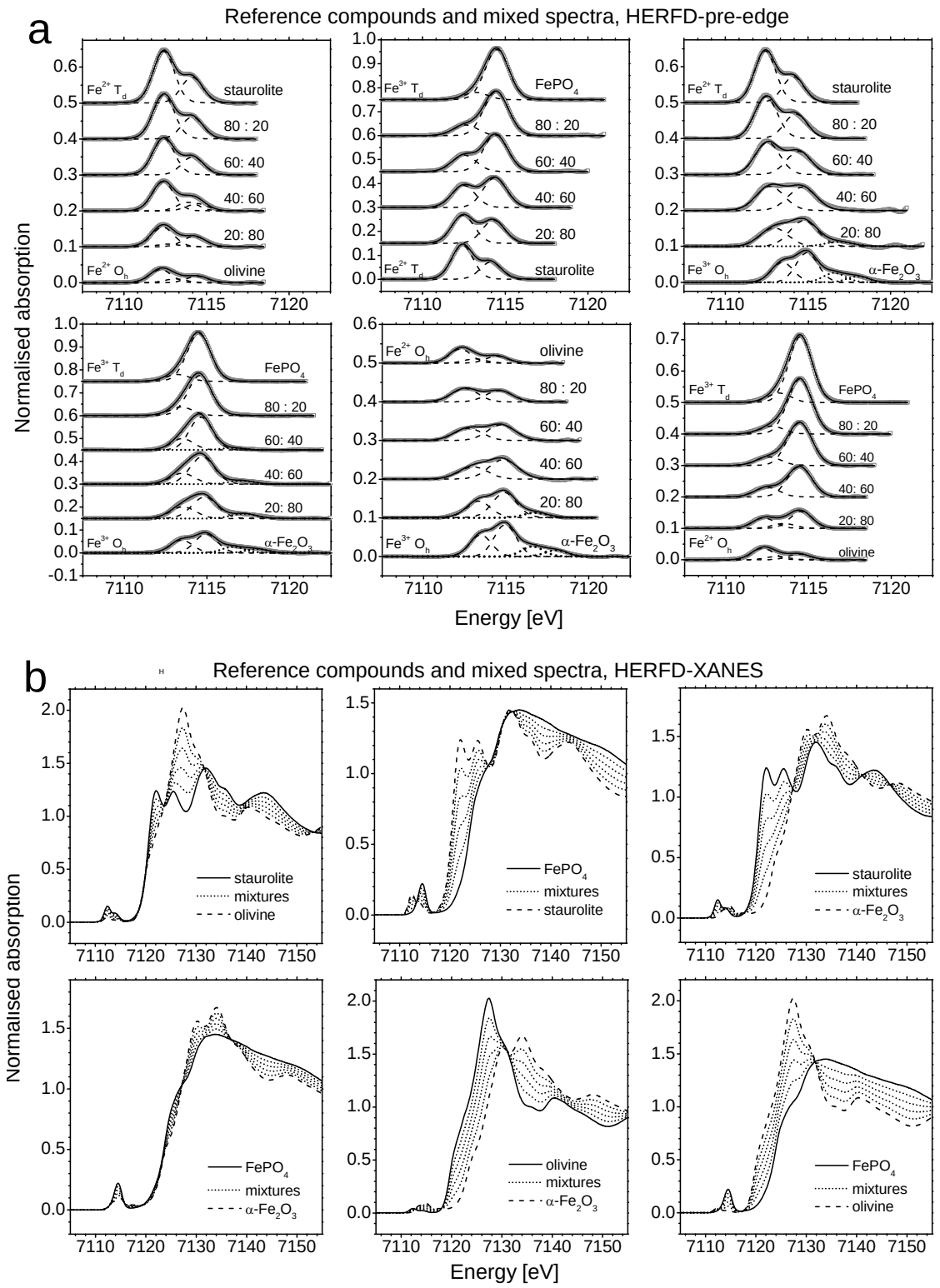

Figure 37 Pre-edge spectra (a) and the parent HERFD-XANES spectra (b) of the reference compounds staurolite, olivine, $FePO_4$ and α-Fe_2O_3 and their binary mixtures. The pre-edge spectra were extracted using the inclined arctangent and fit with pseudo-Voigt peak functions. Transitions centred above 7115 eV (plotted in dotted lines) were omitted in the analysis. The mixture spectra were generated by merging normalised XANES spectra of the pure reference compounds in the specified ratios.

Table 11 The number, width (FWHM) and Gaussian fraction of the pseudo-Voigt peak functions used for fitting the pre-edge spectra of the reference compounds and their mechanical binary mixtures acquired in high-resolution transmission-mode as well as HERFD-mode (indicated in parentheses). For the pure compounds, the electronic states resulting from crystal-field splitting of the free ion states are given. Final states marked bold dominate in terms of intensity according to theory (Figure 38) and are well-identified most pre-edge spectra.

Samples	No. of peaks	free ion state→[Final states]	FWHM [eV]	$x_{Gaussian}$ [%]
Staurolite (Fe^{2+} T_d)	2 (2)	^4F→[$^4A_2$ $\mathbf{^4T_2}$ $^4T_1$], ^4P→[$\mathbf{^4T_1}$]	1.7 (1.5)	69 (89)
FeO (Fe^{2+} O_h)	2	^4F→[$\mathbf{^4T_{1g}}$ $^4T_{2g}$], ^4P→[$\mathbf{^4T_{1g}}$]	2.1	100
Olivine (Fe^{2+} O_h)	(3)		(1.5)	(95)
$FePO_4$ (Fe^{3+} T_d)	1 (2)	^5D→[^5E $\mathbf{^5T_2}$]	1.9 (1.7)	44 (94)
α-Fe_2O_3 (Fe^{3+} O_h)	2+2* (2+2*)	^5D→[$\mathbf{^5T_{2g}}$ $\mathbf{^5E_g}$]	1.8 (1.6)	97 (95)

Mechanical mixtures	Ratio	No. of peaks	FWHM [eV]	$x_{Gaussian}$ [%]
Staurolite-FeO	48:52	2	1.8	100
$FePO_4$-staurolite	63:37	2	1.8	99
Staurolite-α-Fe_2O_3	33:67	2+0*	2.0	100
$FePO_4$-α-Fe_2O_3	45:55	1+1*	2.3	89
FeO-α-Fe_2O_3	35:65	2+0*	1.8	72
$FePO_4$-FeO	63:37	2	1.8	100

* The second number is the number of peaks centred above 7115 eV, being non-local transitions observed in the spectrum of α-Fe_2O_3 and mixtures containing α-Fe_2O_3, which are omitted in the analysis of the chemical state of Fe.

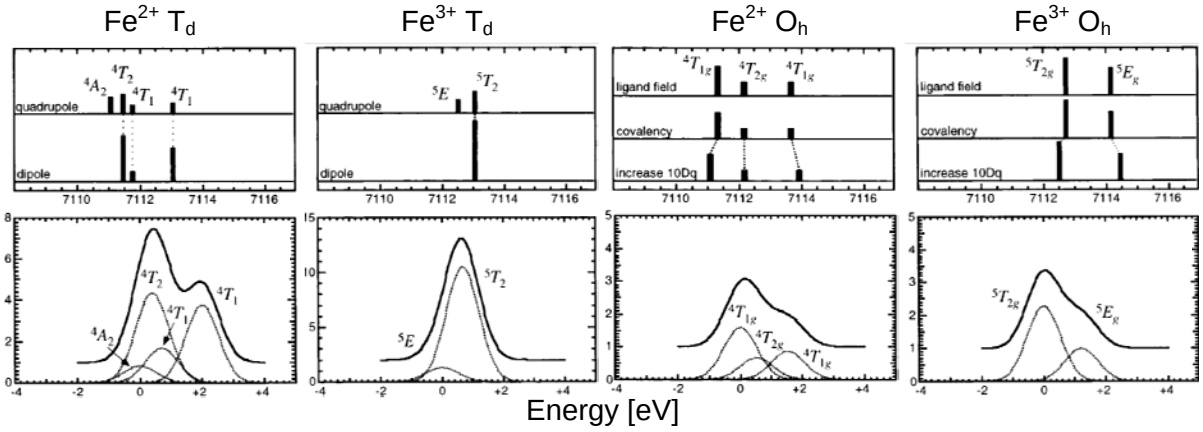

Figure 38 Theoretically predicted final electronic states of the 3d-electrons due to crystal-field splitting in different ligand geometries around Fe (top) and their contributions to the pre-edge spectra (bottom). Reprinted from (Westre *et al.*, 1997). Reprinted with permission from T. E. Westre, P. Kennepohl, J. G. DeWitt, B. Hedman, K. O. Hodgson and E. I. Solomon, A Multiplet Analysis of Fe K-Edge 1s → 3d Pre-Edge Features of Iron Complexes, Journal of the American Chemical Society 119 (1997) 6297-6314. Copyright (1997) American Chemical Society.

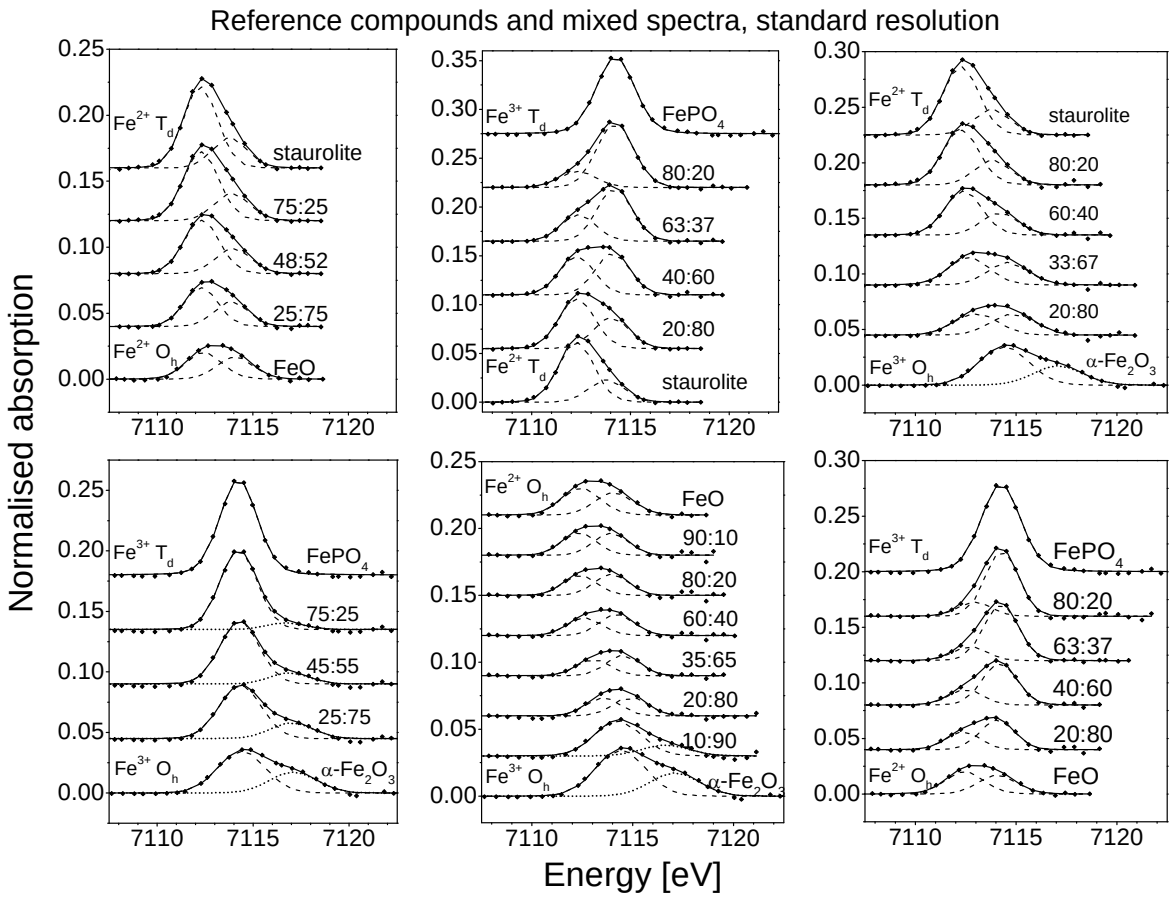

Figure 39 Pre-edge spectra of the of the reference compounds staurolite, FeO, $FePO_4$ and α-Fe_2O_3 and their binary mixtures from standard-resolution transmission-mode XANES data, extracted using the inclined arctangent model function and fit with pseudo-Voigt peak functions. Transitions centred above 7115 eV (plotted in dotted lines) were omitted in the analysis. The parent XANES spectra can be viewed in Figure 40; the mixture spectra were generated by merging normalised XANES spectra of the pure reference compounds in the specified ratios.

Crystal-field theory predicts final electronic states of the Fe ion in different oxidation states and coordination geometries, which are probed by transitions corresponding to pre-edge features. For the Fe species in the reference compounds the final states of these transitions are given in Table 11, but typically fewer peaks were sufficient to deconvolute the spectra. Statistically, the fits could not be improved significantly by using more peaks. The HERFD-pre-edge spectra empirically deconvoluted closely approach an accurate resemblance to the theory (Figure 37), as most predicted transitions are reproduced for the four Fe species studied (numbers in parentheses in Table 11), but a complete theoretical analysis was still not possible. For example, a total of 4 final states ([$^4A_2$ $^4T_2$ $^4T_1$] and [$^4T_1$]) was found in the spectrum of staurolite, but only 2 were clearly identified, probably, the $^4T_2$ and $^4T_1$ states marked bold in Table 11, as transitions to these states are the most intense (Figure 38) (Westre *et al.*, 1997).

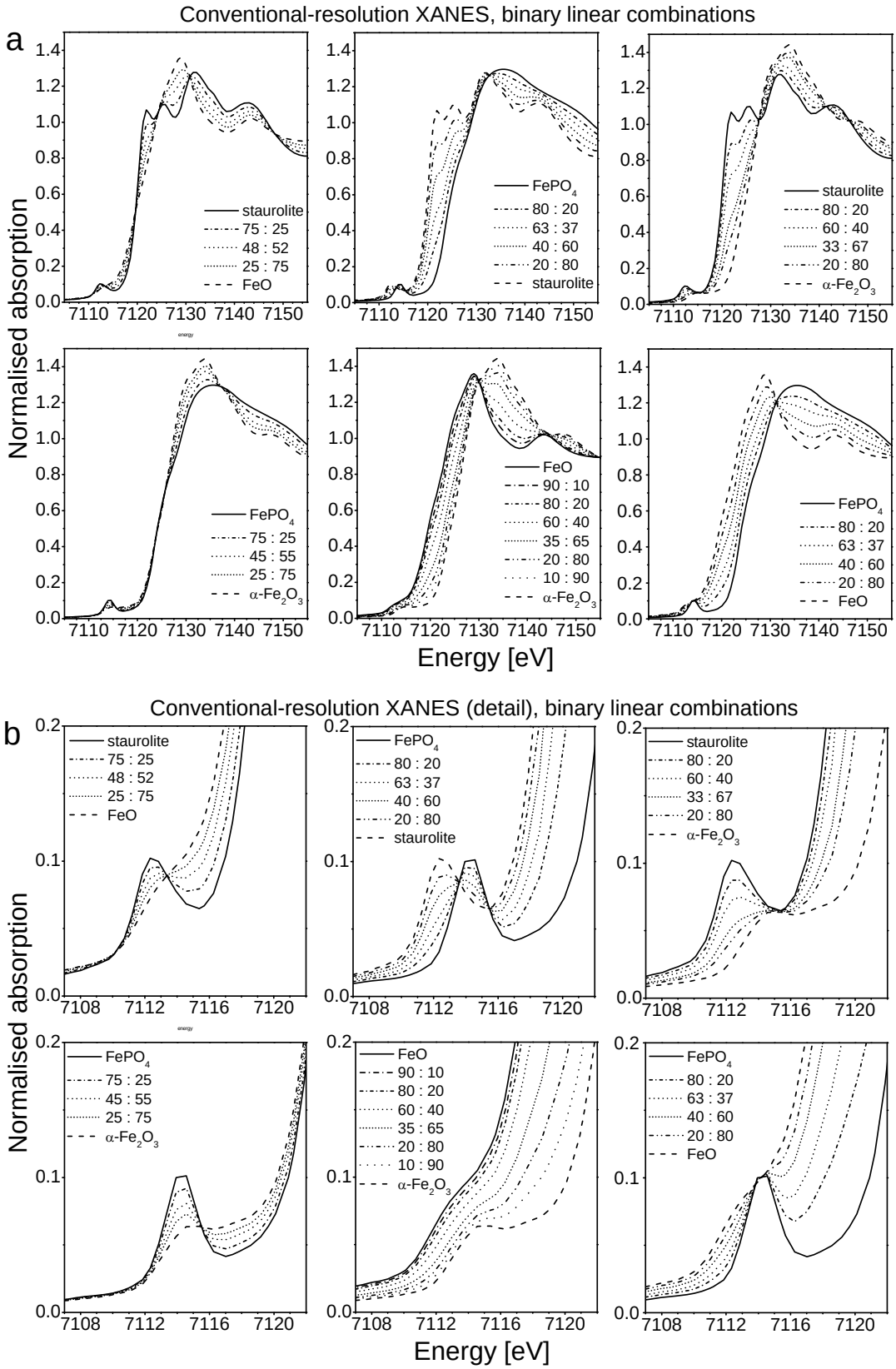

Figure 40 Standard-resolution XANES (a) and detail of pre-edge peak (b) of the reference compounds and binary mixtures. The spectra of the binary mixtures are linear combinations of the normalised XANES spectra of the reference compounds with indicated stoichiometric proportions.

Table 12 The number, width (FWHM) and Gaussian fraction of the pseudo-Voigt peak functions used for fitting the pre-edge spectra of the reference compounds acquired in transmission mode with standard resolution.

	Samples	Number of peaks	FWHM [eV]	$x_{Gaussian}$ [%]
Fe^{2+} T_d	Staurolite	2	2.1	95
	Ceylonite $(Mg,Fe)Al_2O_4$	2	2.5	87
Fe^{2+} O_h	FeO	2	2.2	89
	Fe(II)oxalate	2	2.2	51
	$FeCO_3$	2	2.4	75
	Olivine $(Mg,Fe)_2SiO_4$	2	2.4	67
	Bronzite $(Mg,Fe)_2Si_2O_6$	2	2.3	50
Fe^{3+} T_d	$FePO_4$	1	2.3	83
	Sanidine	2	2.3	99
Fe^{3+} O_h	α-Fe_2O_3	1+1*	2.9	100
	$FePO_4 \cdot xH_2O$	2	2.3	93
	Fe(III)acac	2	2.1	97
	$Fe(NO_3)_3 \cdot 9H_2O$	2+1*	2.1	67
	Aegirine $NaFeSi_2O_6$	2	2.2	78
Others	γ-Fe_2O_3 (Fe^{+3}, T_d and O_h)	1+1*	2.6	99
	Fe_3O_4 (Fe^{+2}, Fe^{+3}, T_d and O_h)	2+1*	2.3	100
	Fe(II) phthalocyanine	1+1*	2.6	87

* The second number is the number of peaks centred above 7115 eV, being non-local transitions observed in the spectrum of α-Fe_2O_3 and mixtures containing α-Fe_2O_3, which are omitted in the analysis of the chemical state of Fe.

In any case, the number of peaks should not play a role in the variogram-based pre-edge analysis (shown later), since this does not have an influence on the complete integrated area and average position of the pre-edge peak. Also, the Gaussian fraction in the pseudo-Voigt profiles was allowed to float during the deconvolution in order to achieve a statistically reasonable fit and ended with rather high values due to the instrumental broadening. Due to the uncertainties introduced with this empirical approach, the Gaussian fraction was not correlated to the peak width (FWHM), as predicted (Farges *et al.*, 2004).

The pre-edge spectra of binary mixtures of the reference compounds acquired with high and standard resolution were all adequately deconvoluted using 2 peak functions (Figure 35 and Figure 39), with larger broadening (FWHM) for standard resolution (cf. Table 11 and Table 12). In pre-edge spectra of mixtures containing α-Fe_2O_3, one peak was assigned to local

transitions. A second peak was attributed to non-local transitions when these were identified as e.g. in mixtures of $FePO_4$ and α-Fe_2O_3.In some cases both peaks were assigned to local transitions, as e.g. in mixtures of FeO and α-Fe_2O_3.

Table 13 The number, width (FWHM) and Gaussian fraction of the pseudo-Voigt peak functions used for fitting the standard-resolution pre-edge spectra of the binary mixtures of selected reference spectra.

Mixed XANES spectra	Ratio	No. of peaks	FWHM [eV]	$x_{Gaussian}$ [%]
Staurolite-FeO	75:25	2	2.2	92
	48:52	2	2.2	97
	25:75	2	2.1	100
$FePO_4$-staurolite	80:20	2	2.2	97
	63:37	2	2.1	100
	40:60	2	2.1	98
	20:80	2	2.1	97
Staurolite-α-Fe_2O_3	80:20	2+0*	2.1	91
	60:40	2+0*	2.2	100
	33:67	2+0*	2.4	89
	20:80	2+0*	2.6	100
$FePO_4$-α-Fe_2O_3	75:25	1+1*	2.3	99
	45:55	1+1*	2.4	97
	25:75	1+1*	2.6	100
FeO-α-Fe_2O_3	90:10	2+0*	2.1	99
	80:20	2+0*	2.0	99
	60:40	2+0*	2.0	97
	35:65	2+0*	1.9	98
	20:80	2+0*	2.0	100
	10:90	1+1*	2.7	96
$FePO_4$-FeO	80:20	2	1.9	96
	63:37	2	2.0	93
	40:60	2	2.0	90
	20:80	2	2.0	100

* The second number is the number of peaks centred above 7115 eV, being non-local transitions observed in the spectrum of α-Fe_2O_3 and mixtures containing α-Fe_2O_3, omitted in the analysis of the chemical state of Fe.

In the pre-edge variogram in Figure 41a, the points corresponding to Fe^{2+} and Fe^{3+} were easily distinguished by their centroid energy-positions. Pre-edge spectra of $FePO_4$ and α-Fe_2O_3 (Fe^{3+} in T_d and O_h geometries respectively) exhibited centroid positions at ca. 7114.4 eV, clearly separated from staurolite (Fe^{2+} in T_d), by 1.5 eV as reported previously (Wilke *et al.*, 2001). The centroid position in the pre-edge spectrum of FeO was at higher energies compared to

staurolite, possibly due to a certain Fe^{3+} impurity. The integrated intensities of the pre-edge spectra, approximately 0.1 for the compounds with O_h geometry and higher than 0.2 for T_d geometry are in agreement with previously reported values (Wilke *et al.*, 2001). In the variogram for standard-resolution pre-edge spectra (Figure 42a), the data points corresponding to the reference compounds were very well reproduced compared to those obtained from high-resolution spectra.

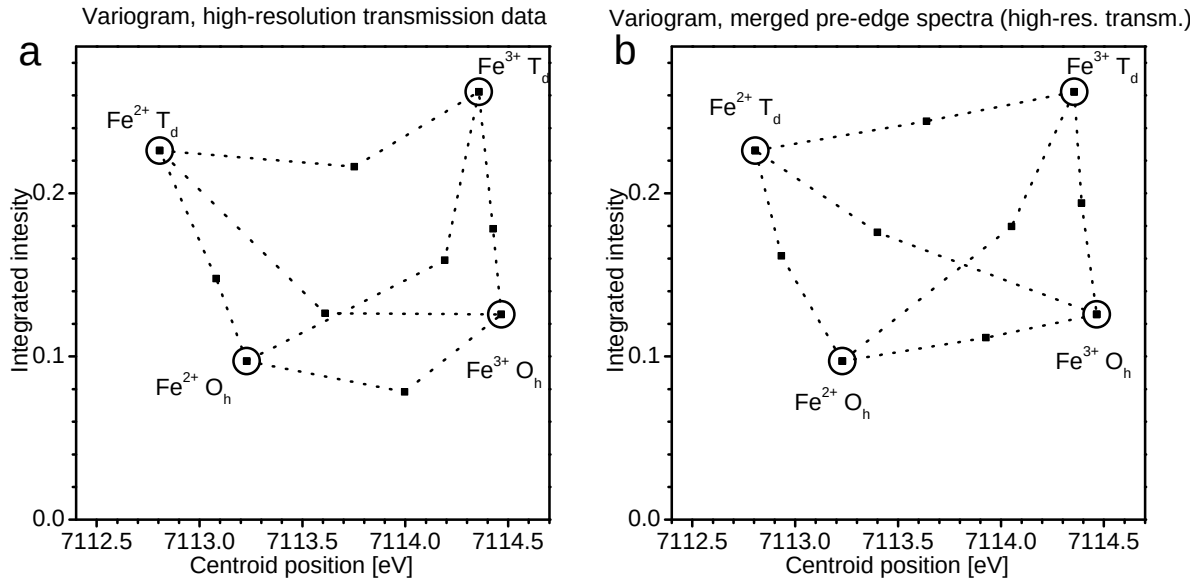

Figure 41 Pre-edge variogram of the integrated intensity and centroid position for the reference compounds staurolite, FeO, $FePO_4$ and α-Fe_2O_3 and their binary mechanical mixtures shown in Figure 35. The points for the binary mixtures in the variogram in (a) originate from the extracted pre-edge spectra of the mixed compounds. The corresponding points in the variogram in (b) are based on the 50:50 linear combinations of the already extracted pre-edge spectra of the pure reference compounds. The peak width (FWHM) and Gaussian fraction ($x_{Gaussian}$) of the pseudo-Voigt functions used for peak fitting are presented in Table 11.

The points in the variogram based on the six experimental spectra acquired from mixtures of the reference compounds were located in between the points corresponding to the pure reference compounds, but with significantly lower intensity. This was observed for both high and standard resolution data (Figure 41a and Figure 42a respectively). A reason for this decrease in intensity could be the steep edge onset which overlaps closely with the pre-edge peak. This can clearly be seen in the XANES spectra of FeO - α-Fe_2O_3 mixtures in Figure 40b. The portion of the pre-edge peak that overlaps with the edge and is subtracted can be a significant fraction of the pre-edge peak intensity, but is negligible in comparison to the value of the main edge. The strong decrease in intensity can directly be observed in the pre-edge spectra of e.g. the 35:65 and 20:80 mixtures of FeO and α-Fe_2O_3 in Figure 39 and shows the limitation of the approach. This effect is minimised when the pre-edge peak is well-separated

from the edge onset, such as in HERFD-XANES spectra (see Figure 50 in Section 4.7). When analysing pre-edge spectra from HERFD-XANES, a separate variogram is necessary, as the pre-edge peaks are approximately a factor 2 more intense than those in conventional XANES, also see (Heijboer *et al.*, 2004) for comparison.

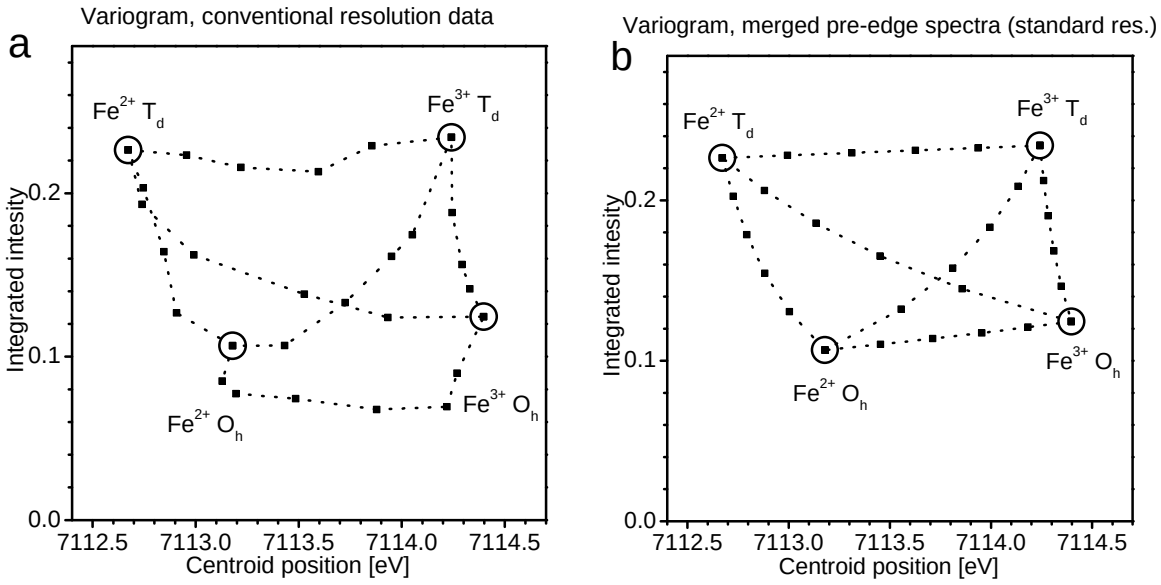

Figure 42 Pre-edge variogram of the integrated intensity and centroid position for the reference compounds staurolite, FeO, $FePO_4$ and α-Fe_2O_3 and their binary mixtures shown in Figure 39. The points for the binary mixtures in the variogram in (a) originate from the extracted experimental pre-edge spectra of the mixed compounds. The corresponding points in the variogram in (b) are based on the linear combinations (ratios 20:80, 40:60, 60:40 and 80:20) of the already extracted pre-edge spectra of the pure reference compounds. The peak width (FWHM) and Gaussian fraction ($x_{Gaussian}$) of the pseudo-Voigt functions used for peak fitting are presented in Table 12 and 0.

The variogram-based analysis of standard-resolution pre-edge spectra does not differ from that of high-resolution spectra, as the same trends are seen in both. Additionally, the total integrated area of the pre-edge peak is also not affected by the difference in resolution, meaning that the results obtained with high and standard resolution can be analysed in a single variogram. The standard deviation in the integrated area was ±0.013, determined statistically by comparing the integrated intensities of pre-edge spectra of both reference compounds and binary mixtures with the same stoichiometric ratios, acquired with both high and standard resolution. The effect of the spectral resolution on the centroid position in the variogram was also investigated: Compared to high resolution spectra, the centroid position of standard-resolution pre-edge spectra was systematically shifted to lower energy by 0.12±0.06 eV, although all spectra were calibrated using the first inflection point in the XANES spectrum of a Fe foil. This shift most probably occurs because the high-energy tail of the pre-edge peak is

very weak compared to the edge onset and is therefore truncated along with the edge during the extraction. The area-based average position of the extracted peak thus shifts to lower energies. This small shift can be noticed by a comparison of the variograms (Figure 41a and Figure 42a), but remains practically undetected when comparing the entire pre-edge spectra (Figure 35 and Figure 39).

4.6. Validation of pre-edge analysis using further reference compounds

Next, the results from the previous sections were applied to reference compounds that partly contain several Fe species. Before applying the pre-edge analysis method to unknown systems, it is important to know how accurately the oxidation state and the coordination geometry can be quantified. Hence, a collection of different Fe-containing reference compounds with specific chemical states of Fe were investigated (Table 10). The varying chemical composition has a large impact on the shape of the parent XANES spectra (Figure 44a) above the absorption edge, which probes multiple-scattering of low-energy photo-electrons. Nevertheless, the pre-edge spectra (Figure 43; detail in the XANES spectra Figure 44b) specifically reflect the already described trend in energy-position and intensity arising from the valence and geometry of the Fe ions, as seen in the variogram in Figure 45. Nevertheless, variations within the same chemical state of Fe are present. The pre-edge spectra of staurolite and ceylonite (Fe^{2+} in T_d symmetry) are well-fitted by two peak functions in the same intensity ratio, but the pre-edge peak in the ceylonite spectrum is slightly wider and shifted to higher energies.

The pre-edge spectra of the compounds with Fe^{2+} in Oh geometry are also described by two peak functions with similar intensity ratios. The centroid position varies between 7112.7 eV and 7113.2 eV (Figure 45), where the one at highest energy belongs to FeO (circled) and is separated from the others, indicating that FeO contains traces of Fe^{3+} (Hazen & Jeanloz, 1984). The samples with pre-edge centroid positions at energies closer to 7112.5 eV can therefore be considered as more suitable as references for Fe^{2+}. The integrated area also varies, which is in part influenced by the subtraction of the edge onset. Errors can be introduced for the pre-edge spectrum of FeO, since the pre-edge peak overlaps with the edge onset (Figure 44).

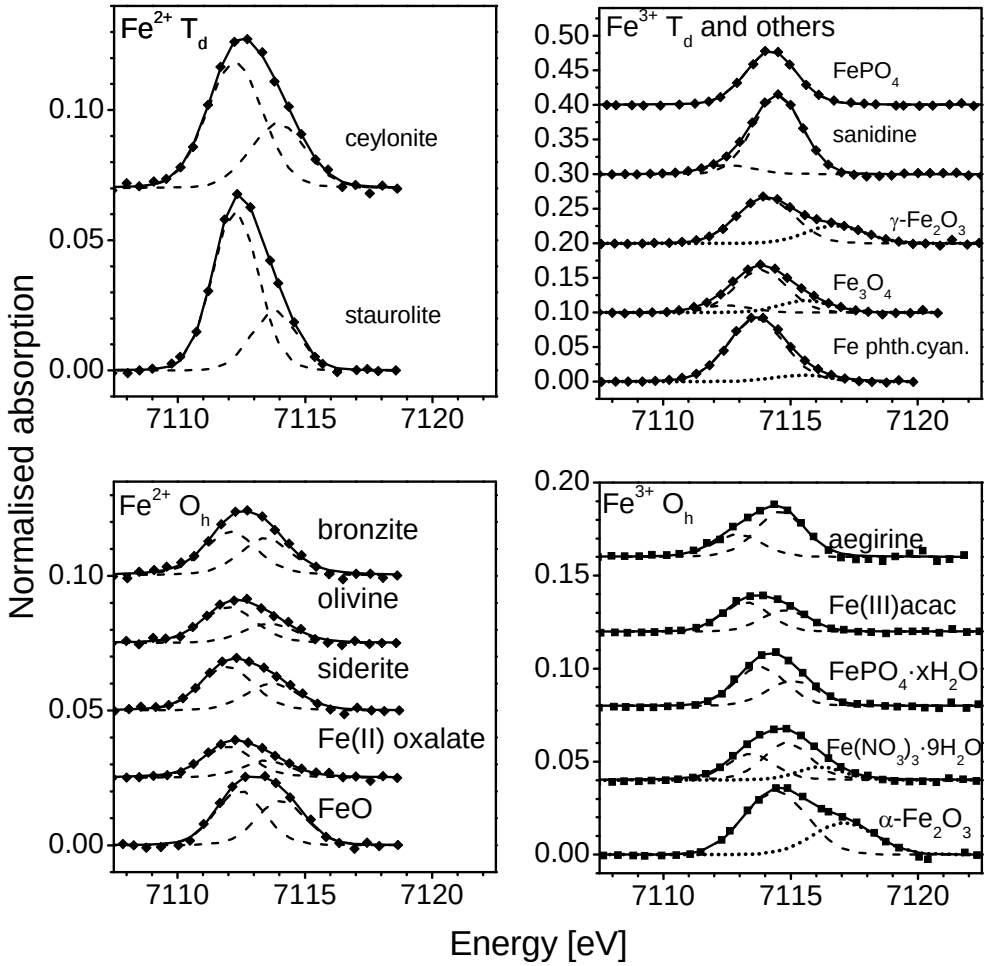

Figure 43 Pre-edge spectra of reference compounds extracted from standard-resolution transmission-mode XANES data, summarised in Table 12. Extraction was carried out using the inclined arctangent model function and the pre-edge spectra were fit with pseudo-Voigt peak functions. Transitions centred above 7115 eV (plotted in dotted lines) were omitted in the analysis. The parent XANES spectra can be viewed in Figure 44.

The pre-edge spectra of $FePO_4$ and sanidine (reference compounds for Fe^{3+} in T_d symmetry) are of high intensity and centred at 7114.3 eV. The pre-edge spectrum of sanidine exhibits a main peak and a weak shoulder at ca. 7112 eV, which is consistent with the two transitions characteristic for trivalent tetrahedral iron (see Table 11 and (Westre *et al.*, 1997)). The high integrated intensity of the sanidine spectrum is consistent with previously reported values for this Fe species (Wilke *et al.*, 2001), while it can be admitted that the intensity found for $FePO_4$ might be lower than expected. The coordination geometry of dehydrated $FePO_4$ is tetrahedral, but becomes octahedral when H_2O molecules are included in the lattice. In this case, a partial contamination with hydrated species cannot be excluded.

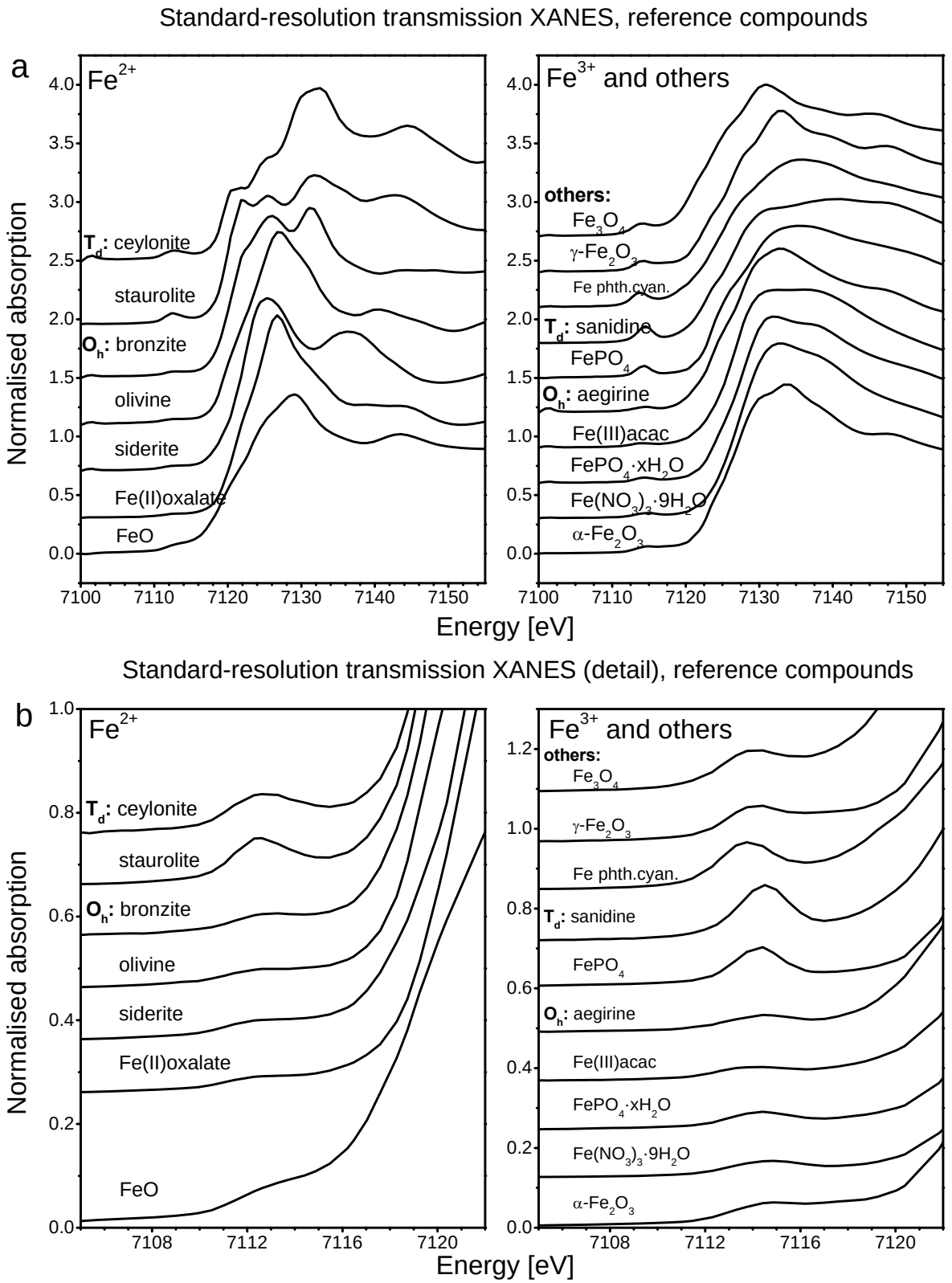

Figure 44 XANES spectra (a) and the detail of pre-edge peak (b) of all reference compounds measured with standard resolution. The Fe site specification in the compounds labelled "others" is presented in Table 10.

A large variation is observed in the pre-edge spectra of Fe^{3+} O_h compounds. The spectra of aegirine, Fe(III)acac and $FePO_4 \cdot xH_2O$ are fitted with two peak functions with of varying intensity ratios. A third high-energy peak is found in the pre-edge spectrum of $Fe(NO_3)_3 \cdot 9H_2O$, which is omitted in the analysis as a non-specific transition as it is placed above 7115 eV, outside the energy-range typical for local transitions. The spectrum of α-Fe_2O_3 is fitted with two peaks as discussed in the previous sections – one for local and one for non-local transitions.

The data points in the variogram in Figure 45 originating from the reference compounds representing the four end-member states of Fe ions (Fe^{2+} and Fe^{3+} in T_d and O_h geometries) are distributed in four groups, each related to its specific type of Fe species. Thus, the variogram can be used to distinguish between Fe^{2+} and Fe^{3+} as well as between the geometries, independent of the total chemical composition, which is in line with (Wilke *et al.*, 2001). Based on the pre-edge spectra of the compounds with Fe^{2+} and Fe^{3+} in O_h symmetry, an uncertainty of ±0.2 eV in the centroid position and ±0.03 for the intensity is estimated. The encircled points represent the four reference compounds staurolite, FeO, $FePO_4$ and α-Fe_2O_3 which were presented in the previous sections to illustrate the principles of pre-edge analysis. These data points suffer from the already mentioned uncertainties (e.g. FeO due to presumed contamination by Fe^{3+}), but are representative of the different chemical states of Fe.

Using the established correlations, three compounds of other chemical states of Fe (Table 10) were analysed for the valence and geometry of Fe. Maghemite (γ-Fe_2O_3) formally has a defect spinel structure and Fe^{3+} distributed among T_d and O_h sites. This compound exhibits a XANES spectrum similar to that of α-Fe_2O_3 as both are pure oxides of Fe^{3+} (Figure 44), but with higher pre-edge peak intensity due to the presence of tetrahedrally coordinated Fe ions. The pre-edge peak (Figure 43) is fitted with a main contribution centred at 7114.2 eV and a shoulder above 7115 eV. The main peak contains overlapping features corresponding to the transitions observable for Fe^{3+} species in T_d and O_h sites. The high-energy shoulder can be attributed to non-local transitions observed in pre-edge spectra of trivalent metal ions due to metal-metal interactions (de Groot *et al.*, 2009), but was omitted in the analysis. In the variogram (Figure 45), maghemite is placed at 7114.2 eV as expected for compounds containing pure Fe^{3+}, with intensity slightly below that of the $FePO_4$ reference, clearly pointing at a mixture of mentioned lattice sites – predominantly the T_d sites.

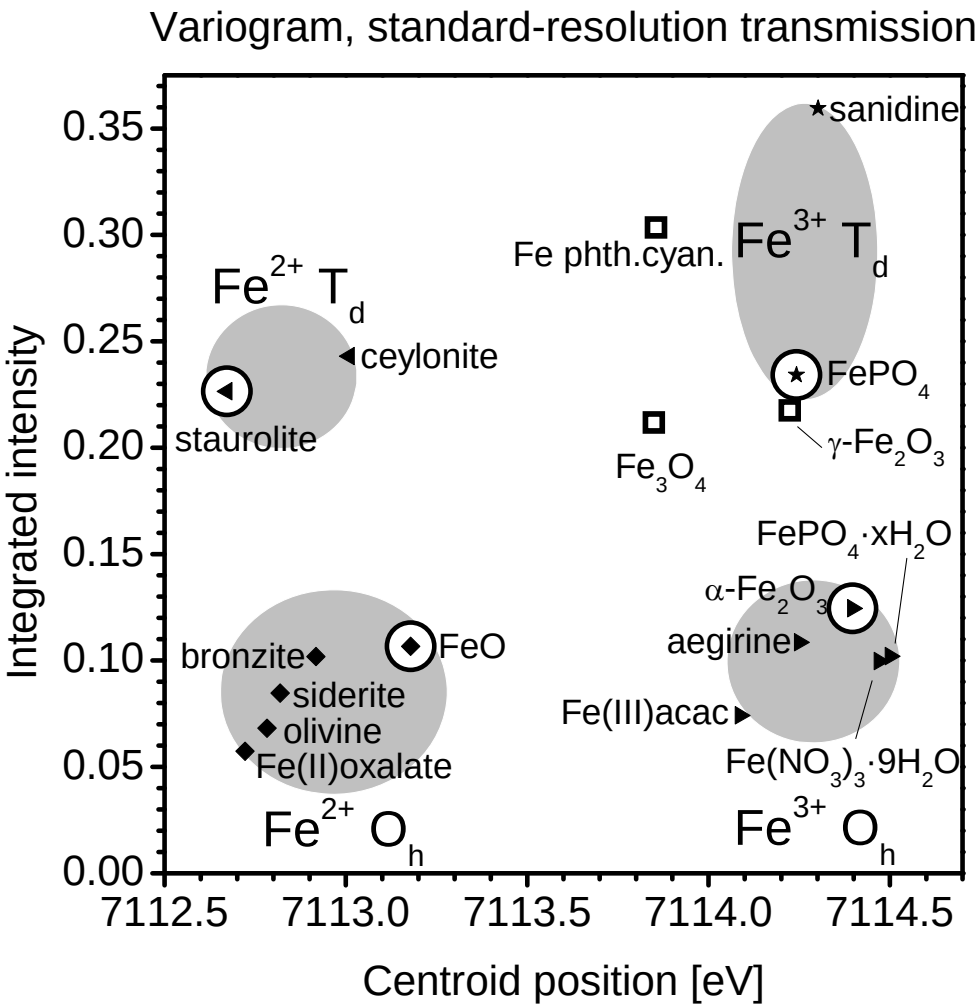

Figure 45 Pre-edge variogram for spectra of reference compounds, which are shown in Figure 43. Circled data points correspond to the four references samples covered in detail in the previous sections. Grey areas highlight the groups of points corresponding to the four types of Fe species. The uncertainties determined graphically from this plot are ±0.2 eV in centroid position and ±0.03 in integrated intensity. The peak width (FWHM) and Gaussian fraction ($x_{Gaussian}$) of the pseudo-Voigt functions used for peak fitting are presented in Table 12.

The structure of magnetite (Fe_3O_4) is an inverse spinel similar to that of maghemite, formally with the Fe atoms equally distributed as Fe^{2+} at O_h sites, Fe^{3+} at O_h sites and Fe^{3+} at T_d sites. In fact, the mixture of oxidation states is consistent with the position of the edge at lower energies than that typical for Fe^{3+}, but higher than that for Fe^{2+} (Figure 44). Regarding the pre-edge spectrum, three peaks satisfactorily fit this spectrum (Figure 43). The first weak peak at ca. 7112 eV is a contribution from the Fe^{2+} species at O_h sites (presumably due to the $^4T_{1g}(^4F)$ state), the second peak mainly contains contributions from the intense $^5T_2(^5D)$ state of the Fe^{3+} at T_d sites and a third peak above 7115 eV, which can possibly be assigned to non-local transitions and omitted. The position of magnetite in the variogram (Figure 45) is

consistent with the electronic speciation of the Fe ions, but exact quantification is difficult, considering the high errors within the analysis.

The coordination compound iron phthalocyanine formally contains a divalent Fe ion coordinated in square planar geometry by four N-atoms of the tetradentate phthalocyanine ligand. The position of the absorption edge (Figure 44) and the pre-edge spectrum (Figure 43) strongly suggest a large fraction of Fe^{3+} in the compound, reflecting that the formally assumed valence of the Fe ion is inaccurate. Oxidation from Fe^{2+} to Fe^{3+} could have occurred during the preparation of the sample, and the pre-edge spectrum confirms this. The high intensity of the pre-edge peak is due to the strong 3d-4p hybridisation, which for square planar geometry is known to be as high as for tetrahedral geometry, giving rise to an intensive pre-edge peak.

Having characterised three test compounds using the method presented in this work, it is possible to conclude that the chemical state and the distribution of site geometries can be extracted from pre-edge spectra, even if data was acquired with standard resolution. The precision of this method is, however, limited due to relatively high uncertainties. Therefore, pre-edge analysis is well-suited as a complementary technique for confirming the nature of Fe species, but preliminary knowledge of the structure determined by other techniques is advantageous.

4.7. Evolution of Fe in 1% Fe/Al_2O_3 and 0.5% Fe/BEA during reduction

Finally, pre-edge analysis was applied to a typical *in situ* study of a 1% Fe/Al_2O_3 catalyst during temperature-programmed reduction in 5% H_2/He (Figure 46). A high degree of noise in the XANES spectra was partly due to statistical noise caused by the rapid data acquisition, to the low Fe content and to fluctuations in the edge jump caused by mechanical instabilities of the setup. The latter effect can be seen above the edge, as the spectra tend to group instead of being evenly spaced in the stacked plot in Figure 46a.

At first, linear combination analysis (LCA) of the XANES spectra was performed. For this purpose, XANES spectra of the initial and the final state of the Fe/Al_2O_3 catalyst were used, each one merged of several data sets in order to increase the signal-to-noise ratio (Figure 46a, bottom). The LCA results (Figure 47c) indicate a transformation between two states, assumed to be Fe^{3+} and Fe^{2+}, respectively. All spectra could be well fit as linear combinations of the initial and final spectrum. Isosbestic points indicate that the structural transformation of the Fe sites occurs in one-step.

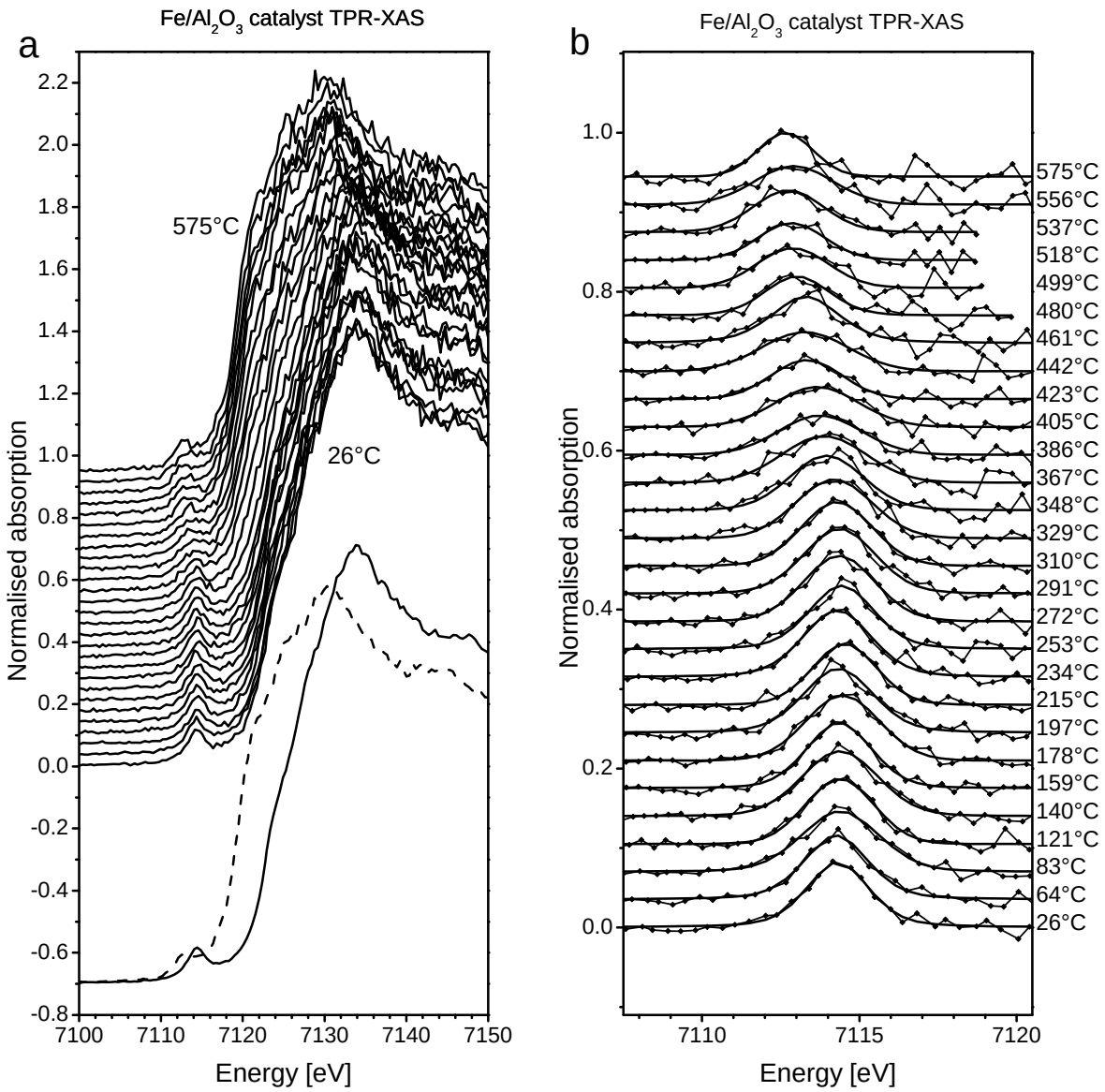

Figure 46 *In situ* Fe K-edge XANES spectra (a) and the pre-edge spectra (b) of a 1% Fe/Al_2O_3 catalyst acquired during a TPR experiment with standard resolution in fluorescence mode. The spectra were acquired using continuous energy scans with a period of approximately 4 minutes per spectrum. The catalyst powder was exposed to a flow of 5% H_2/He (50 mL/min) in a quartz capillary micro-reactor and heated from room temperature to 575°C at a linear rate of 5°C/min. The spectra of the starting state (solid line) and final state (dashed line) are shown together in (a); these were used as basis for linear combination analysis of the whole series of the XANES spectra. The pre-edge spectra in (b) were extracted using the inclined arctangent function and fit with a single pseudo-Voigt peak function. The peak width (FWHM) and Gaussian fraction ($x_{Gaussian}$) of the pseudo-Voigt functions are presented graphically in Figure 47b.

The corresponding pre-edge spectra are shown in Figure 46b. Although the pre-edge region was affected by a certain level of noise, it could be successfully extracted and fitted with a single pseudo-Voigt function. The pre-edge spectra measured between 26-310°C are almost identical and are modelled by a pseudo-Voigt peak of 2.5 eV width positioned at 7114.4 eV which is characteristic for Fe^{3+}. The high intensity of this peak indicates non-centrosymmetric

geometry, as the pre-edge variogram in Figure 47a shows. The integrated intensity is between that of pre-edge spectra of $FePO_4$ and sanidine, which were used as Fe^{3+} references for the T_d geometry, and the peak is similar or slightly wider (2.3 eV, Table 12). The Fe^{3+} ions in the Fe/Al_2O_3 catalyst can thus be assumed to be mainly in a tetrahedral or similar geometry, but most probably in a mixture of 4- and 5-fold coordination. In this case, the single peak accounts for all transitions which are present but not individually resolved within the pre-edge feature. The surface species of Fe in the catalyst can be rather disordered (Boubnov, Lichtenberg*, et al.*, 2013) and the Fe ion site can probably not be described by a single well-defined structure model.

Upon the structural transformation between 300-500°C, the pre-edge peak shifts to lower energies (Figure 47 (b and c), marked by grey lines). Around 400°C, halfway in the $Fe^{3+} \rightarrow Fe^{2+}$ transformation, the pre-edge peak centred at 7113.7 eV increased in width to 3.2 eV, and the Gaussian fraction of the pseudo-Voigt peak function increased to 100%.

The Gaussian/Lorentzian character of the peak functions was, however, subject to large errors, as described previously. Once the chemical transformation was complete, the peak width again decreased to 2.5 eV and was located at ca. 7112.8 eV, characteristic for Fe^{2+} species. The broadening of the pre-edge peak during the transformation was attributed to overlapping pre-edge spectra of the initial and final state. The final state of the Fe sites could be described as 4- to 5-fold coordinated Fe^{2+}, (between the 4-fold and 6-fold coordinated Fe^{2+} reference points in the variogram). In fact, during the entire transformation, the coordination was conserved as 4- to 5-fold.

For comparison, an analogous TPR-study of a 0.5% Fe/BEA catalyst is presented in studied in Figure 48. In contrast to the study of the Fe/Al_2O_3 catalyst, the XANES spectra (Figure 48a) were acquired with higher resolution and better quality (0.1 eV energy increments). The pre-edge spectra extracted using the inclined arctangent function could be fitted with 1-2 pseudo-Voigt peaks: a double feature fitted with two peaks of 2.9 eV FWHM was easily distinguished after Fe was reduced to Fe^{2+} (Figure 48 b and d), but the pre-edge of the initial oxidised Fe^{3+} species was best fitted with a single peak of 2.0-2.5 eV FWHM. Attempts to apply a two-peak fit resulted in the overlap of the two peaks. At all times, the pseudo-Voigt functions took on a highly (>90%) Gaussian character (Figure 48d).

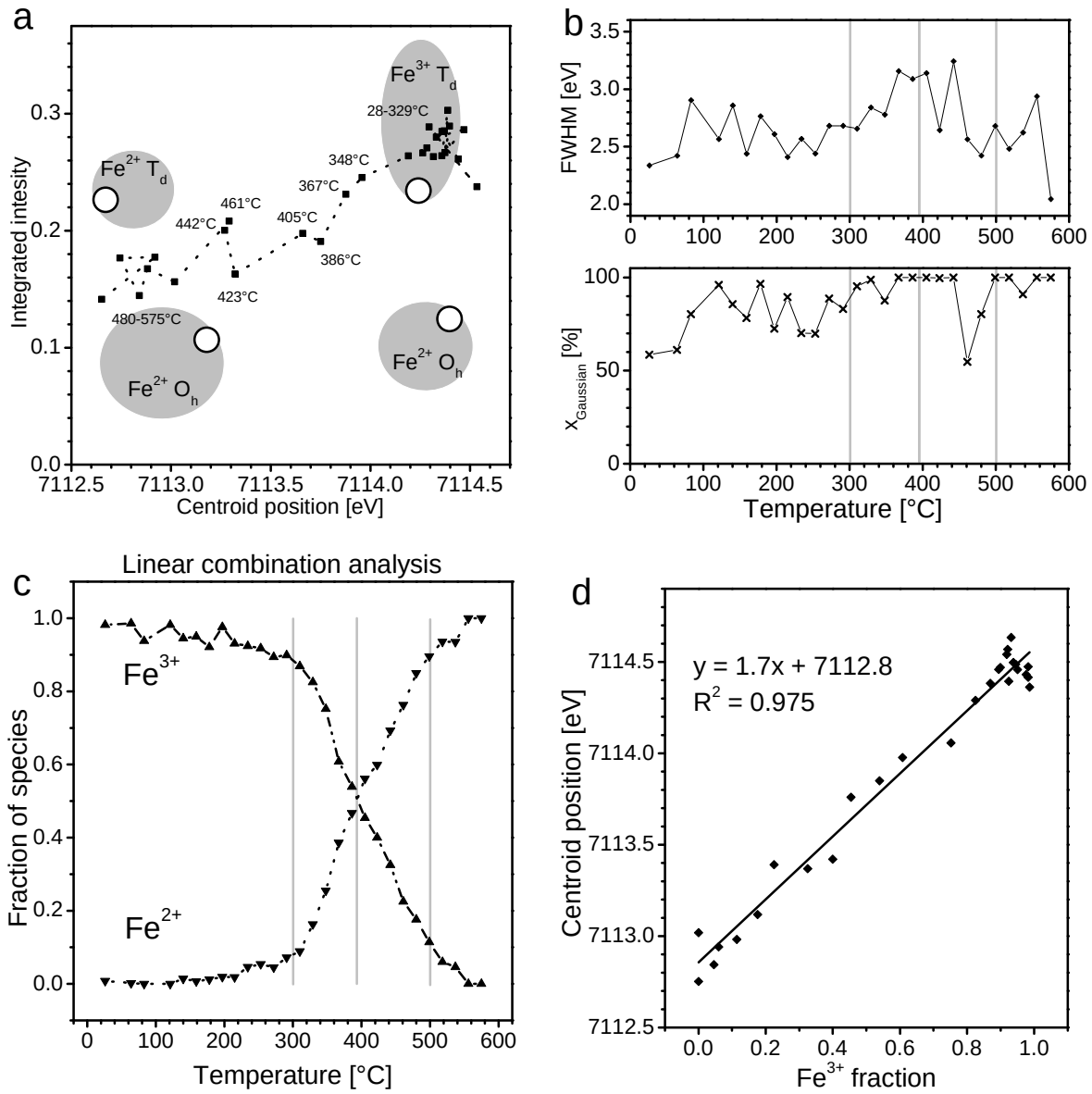

Figure 47 Analysis of the *in situ* pre-edge spectra of the 1% Fe/Al_2O_3 catalyst, shown in Figure 46b. Variogram of the total integrated intensity and centroid position of the pre-edge peak at different temperatures of the TPR experiment, compared with data points of the reference compounds staurolite, FeO, $FePO_4$ and α-Fe_2O_3 from spectra measured with standard resolution, marked with circles (a). The grey fields indicate the expected positions for the data points which are specific for the four types of Fe species: Fe^{2+} in T_d and O_h geometry and Fe^{3+} in T_d and O_h geometry, reproduced from Figure 45. The evolution with temperature of the peak width (FWHM) and Gaussian fraction ($x_{Gaussian}$) of pseudo-Voigt functions (b). Fraction of Fe^{3+} and Fe^{2+} species with temperature, calculated as a linear combination of the first XANES spectrum assumed to be Fe^{3+} and the last XANES spectrum assumed to be Fe^{2+} (c). Linear combination fitting was carried out between 7105 eV and the isosbestic point at 7132 eV seen in Figure 46a and the sum of the components was not forced to add to 1. The linear relationship between the fraction of Fe^{3+} species calculated by LCA and the pre-edge centroid position (d). The grey lines in (b) and (c) indicate the temperatures where the transformation of Fe^{3+} to Fe^{2+} has advanced ca. 10%, 50% and 90% to guide the eye.

The variogram in Figure 48c is very similar to the one for Fe/Al_2O_3, showing a reduction of Fe^{3+} to Fe^{2+}, maintaining a local coordination number of ca. 5. The transition was halfway through at about 315°C and when the experiment is finished at 393°C, the reduction is only about 80% complete, because the pre-edge centroid did not reach 7112.6 eV, characteristic for pure Fe^{2+}. The good reducibility at low temperature of the Fe/BEA catalyst with respect to the Fe/Al_2O_3 has shown to be correlated to a high catalytic activity for NOx-removal by selective catalytic reduction with ammonia (NH_3-SCR) (Boubnov, Lichtenberg*, et al.*, 2013).

The simultaneous analysis of the oxidation state and local coordination number embraces also valuable information in HERFD-XANES data. In fact, the pre-edge analysis procedure in the present work was recently applied to study a Fe/ZSM-5 catalyst during NH_3-SCR and under relevant reaction conditions, acquiring combined HERFD-XANES and valence-to-core X-ray emission spectra (Boubnov *et al.*, 2014). Under the series of oxidising and reducing atmospheres applied to the catalyst sample, the Fe sites took on average oxidation states between Fe^{2+} and Fe^{3+}, maintaining a local coordination number of ca. 4-5. The intensity of the pre-edge peak in HERFD-XANES spectra, detecting the fluorescence with high resolution at the Fe $K\beta_{1,3}$-line, was approximately twice as high as that reported herein for transmission and standard-resolution fluorescence XANES data. For establishing a variogram, the XAS spectra of reference samples must be acquired in the HERFD-mode, but the study demonstrate in general the advantageous approach also in catalysis.

Variogram-based pre-edge analysis will be in general a valuable approach in XAS studies e.g. those reported in refs. (Høj *et al.*, 2009, Klukowski *et al.*, 2009, Maier *et al.*, 2011, Bordiga *et al.*, 2013, Liu *et al.*, 2013, Liu *et al.*, 2014, Tepluchin *et al.*, 2014, Doronkin, Casapu*, et al.*, 2014), providing further information about oxidation state and geometry also under operando conditions.

The LCA results can be correlated with the pre-edge analysis results for quantifying the Fe oxidation state in similar chemical systems. Calibrations of the pre-edge centroid position and the fraction of Fe^{3+} species, especially with application to geology and studies of historical items, are reported for various Fe-containing materials using standard-resolution data (Berry *et al.*, 2003, Schmid *et al.*, 2003) and high-resolution data (Wilke *et al.*, 2005, Wilke *et al.*, 2009, Cottrell *et al.*, 2009). Figure 47d shows a linear relationship between the Fe oxidation state in terms of the Fe^{3+} fraction and the pre-edge centroid position. From this relationship, the fraction of Fe^{3+} species in a mixture of Fe^{2+} and Fe^{3+} can be determined merely from the pre-edge centroid position within an error of ca. 10%. The determination of the oxidation state

of Fe can thus be carried out by both pre-edge analysis and LCA. The latter is a simple and common method in catalysis (Pirngruber *et al.*, 2004, Høj *et al.*, 2009), where the spectra of the fully oxidised and fully reduced catalyst are used as standards. However, a disadvantage of LCA is that XANES spectra of well-defined reference compounds such as bulk oxides cannot adequately reproduce the XANES features of the catalysts, which have unique spectral features for each chemical system. Hence, a full reduction of the each catalyst system must be carried out to reach the final state and use the corresponding spectrum as specific reference. Moreover, the pre-edge spectrum simultaneously probes the geometry of the Fe species, which is important for the identification of the role of the Fe centres for the catalytic reaction (Battiston, Bitter, Heijboer*, et al.*, 2003). On the other hand, reliable reference samples are needed for this analysis and the results are subject to a certain error.

Another established method is the use of the edge position (Berry *et al.*, 2003, Maier *et al.*, 2011), as this is directly affected by the oxidation state. This method has its advantages when pre-edge analysis becomes difficult due to the low intensity of the pre-edge peak occurring for octahedrally coordinated Fe and a high noise level (Maier *et al.*, 2011). In fact, the pre-edge method suffers when analysing low-intensity pre-edge spectra due to distortions in the pre-edge variogram (Figure 42a). For analysis of the edge position, the oxidation state must be calibrated with respect to the edge position. However, since the characteristics of the XANES spectra may vary for different chemical systems, each type of chemical system must be considered individually. In contrast, pre-edge analysis is potentially independent of the chemical system within the oxidation states and coordination geometries discussed in the present work. Further difficulties associated with the use of the edge position are due to the fact that the edge of a Fe K-edge XANES spectrum can have several inflection points, making the definition of the edge position ambiguous. The edge position is commonly determined using the derivative spectrum, which is potentially sensitive to noise in the data.

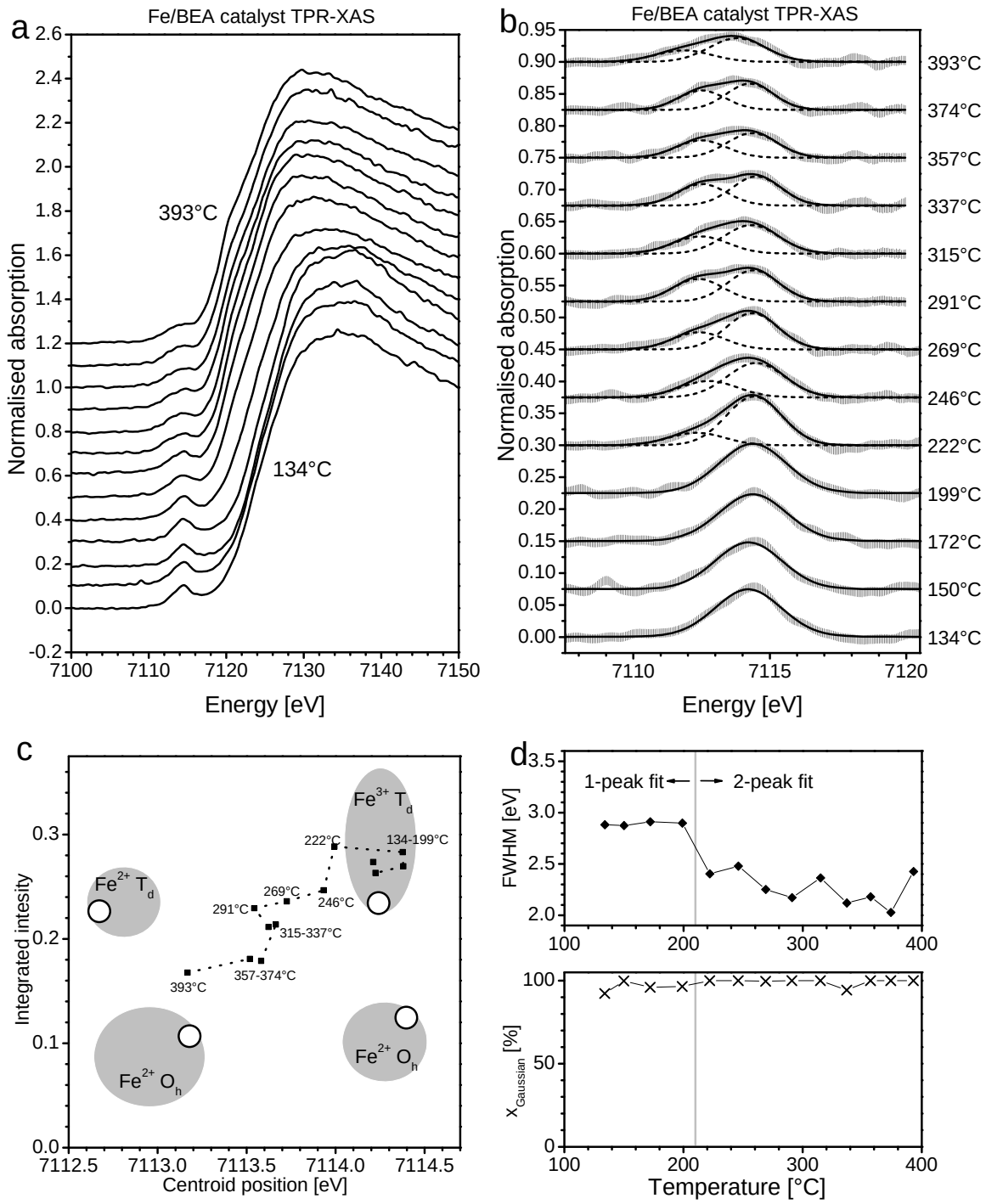

Figure 48 *In situ* Fe K-edge XANES spectra (a) and the pre-edge spectra (b) of a 0.5% Fe/BEA zeolite catalyst acquired during a TPR experiment with high resolution in fluorescence. The spectra were acquired using continuous energy scans with a period of approximately 5 minutes per spectrum with energy increments of 0.1 eV (conditions: 20% H_2/He in a quartz capillary micro-reactor, heated up to 400°C, cf. ref. (Høj *et al.*, 2009)). The pre-edge spectra in (b) were extracted using the inclined arctangent function and fit with 1-2 pseudo-Voigt peak functions. Variogram (c) and evolution with temperature of the peak width (FWHM) and Gaussian fraction ($x_{Gaussian}$) of pseudo-Voigt functions (d), analogous to Figure 47 (a and b). The vertical grey line separates the FWHM and $x_{Gaussian}$ obtained when fitting the pre-edge spectra with 1 and 2 pseudo-Voigt peaks.

4.8. Structure of Fe/ZSM-5 during NH_3-SCR probed by HERFD-XANES and V2C-XES

A detailed study with combined HERFD-XANES and V2C-XES of a Fe/ZSM-5 catalyst with well-defined low-nuclearity Fe sites was studied *in situ* under NH_3-SCR reaction conditions (Boubnov *et al.*, 2014). The analysis of the pre-edge peak in HERFD-XANES spectra (Figure 49a-b) probing the oxidation state and coordination geometry of the Fe centres was complementary to V2C-XES, probing the ligands interacting with Fe.

Similar to the pre-edge trend for the 1% Fe/Al_2O_3 catalyst during TPR, the pre-edge peak as well as the edge position of the XANES spectrum shifted in energy in response to the gas atmosphere. When exposed to NH_3, a shift to lower energies indicated a reduction of Fe^{3+} to Fe^{2+}. The transitions were significantly better resolved than for Fe/Al_2O_3, and could be fitted with two pseudo-Voigt functions instead of one. In their appearance, the pre-edge spectra were qualitatively similar to those on the staurolite-$FePO_4$ trendline (tetrahedral Fe^{2+} and Fe^{3+}) (cf. Figure 37a), suggesting a large fraction of tetrahedrally coordinated Fe sites.

Using a variogram (Figure 50) an almost constant local coordination number of 4-5 was observed, under oxidising as well as under reducing atmospheres. The conservation of a constant coordination number was an important indication for proposing the reaction mechanism (not shown). For example, it was postulated that the inhibition by water of an NH_3 adsorption site occurs as an exchange of an NH_2 group by an OH group. The oxidation state of Fe, used for describing the reaction mechanism, was determined by pre-edge analysis.

The structural information obtained from the pre-edge spectra has assisted the building of molecular models of the active Fe centres for interpreting the V2C spectra and obtaining insight into the reaction mechanism. The Fe Kβ" feature in the V2C spectra recorded in parallel (not shown) revealed the electronic interaction with ligands in three peaks. Peak A at 7088 eV arose when dosing NO, NO_2 or NH_3, due to lone pairs of the triple-coordinated oxygen with a partial positive charge, indicating the bonding of NO_x or NH_3 via a hydroxyl group in the form of a Fe-OH^+-N bond. The dominant peak B at 7092 eV always present was assigned oxygen lone pairs in the hydroxyl ligands and oxygen atoms of the zeolite, to which the Fe atom was bonded. Peak C at 7095 eV was assigned to nitrogen lone pairs of a NH_3 ligand bonding directly to the Fe ion as NH_2-groups. This peak was observed when NH_3 was dosed, alone or in presence of O_2, and NO (but absent when NH_3 and NO_2 were dosed).

Theoretically, the V2C peaks shift depending on if the Fe site is reduced to Fe^{2+} or oxidised to Fe^{3+}. However, the shift was not observed as the peaks were broader than those simulated and very weak in intensity. For identification of the peaks, smoothed second derivatives of the V2C spectra were analysed. Merely the presence or absence of the three peaks was correlated to the one or the other type of ligands. Therefore the complementary pre-edge spectra were relied upon for probing the Fe oxidation state.

In the present work, the signals were weak due to only small contribution of ligands from gas phase compared to the stable bonds linking the Fe site to the zeolite. V2C is known to be sensitive to first-shell neighbouring atoms, but not those in the second-shell (Atkins *et al.*, 2013). In the present study, second-shell coordination of NH_3 and NO_x to Fe via a hydroxyl group was proposed, based on the measured results. The identification of this electron-deficient triple-coordinated oxygen in the hydroxyl group (peak A) was a significant finding of this study, which is hardly accessible by other characterisation techniques.

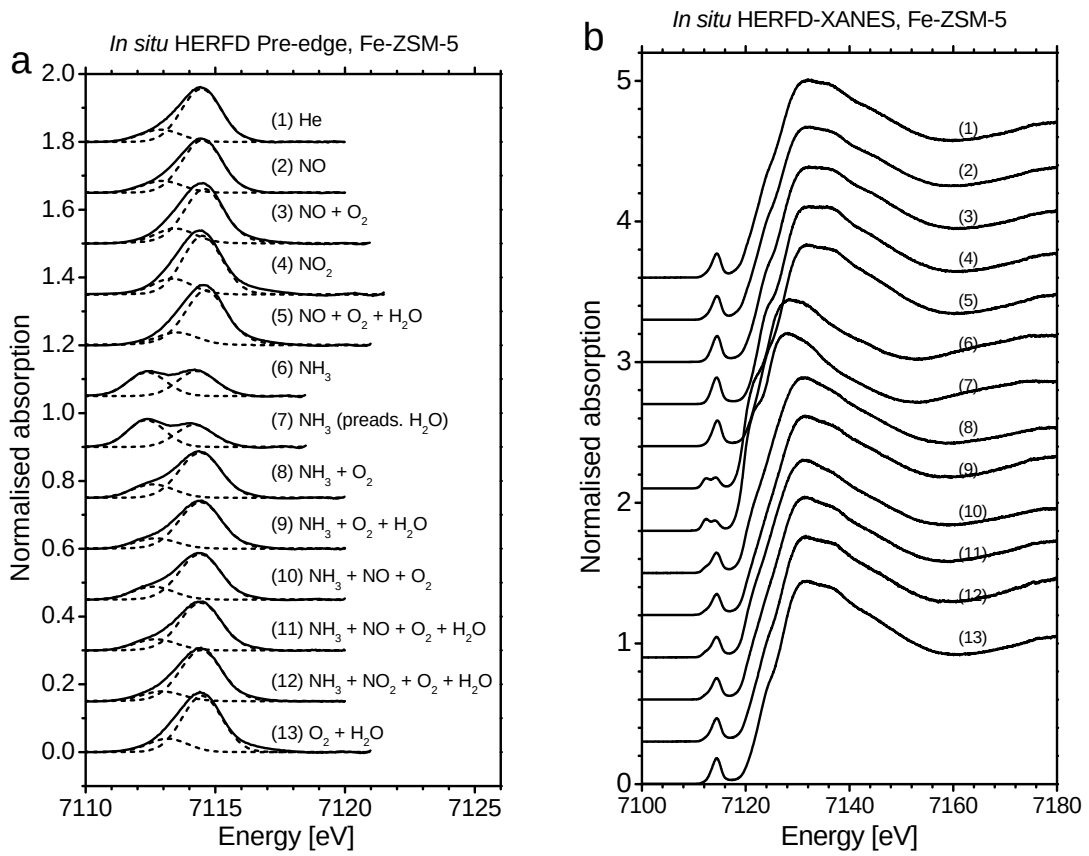

Figure 49 *In situ* pre-edge spectra acquired in HERFD-mode of the Fe-ZSM-5 catalyst under SCR-relevant reaction conditions (a) and the parent HERFD-XANES spectra (b). Reprinted with permission from Journal of the American Chemical Society, A. Boubnov, H. W. P. Carvalho, D. E. Doronkin, T. Günter, E. Gallo, A. J. Atkins, C. R. Jacob, J.-D. Grunwaldt, Selective Catalytic Reduction of NO Over Fe-ZSM-5: Mechanistic Insights by Operando HERFD-XANES and Valence-to-Core X-ray Emission Spectroscopy, Journal of the American Chemical Society 136 (37) (2014) 13006-13015. Copyright (2014) American Chemical Society.

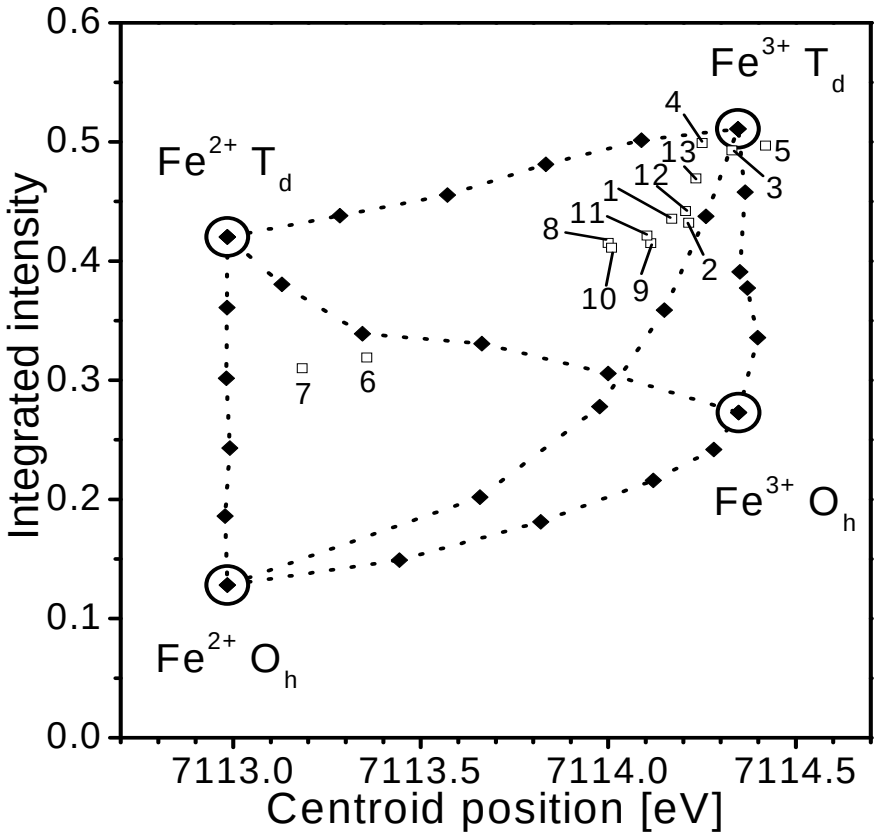

Figure 50 HERFD-pre-edge variogram for analysing the Fe centres of the Fe-ZSM-5 catalyst under SCR-relevant conditions using HERFD-XANES spectra of reference compounds. The numbering of the data points corresponds to the reaction conditions and is analogous to that in Figure 49. Reprinted with permission from Journal of the American Chemical Society, A. Boubnov, H. W. P. Carvalho, D. E. Doronkin, T. Günter, E. Gallo, A. J. Atkins, C. R. Jacob, J.-D. Grunwaldt, Selective Catalytic Reduction of NO Over Fe-ZSM-5: Mechanistic Insights by Operando HERFD-XANES and Valence-to-Core X-ray Emission Spectroscopy, Journal of the American Chemical Society 136 (37) (2014) 13006-13015. Copyright (2014) American Chemical Society.

4.9. Conclusion

Fe K-pre-edge analysis is an attractive method both in materials science and catalysis for unravelling oxidation state and geometry. By extending the original approach by groups like Farges and Wilke, we have shown here that this method can also be a valuable tool to estimate the oxidation state and coordination geometry of Fe centres under reaction conditions where typically data are recorded at conventional EXAFS beamlines. The example of an *in situ* pre-edge study revealed that during reduction of Fe^{3+} to Fe^{2+} in a 1% Fe/Al_2O_3 catalyst, the local coordination of 4-5 O-atoms stays constant, which is useful information for mechanistic studies of this catalyst for automotive applications. Importantly, the variogram-based analysis of the pre-edge peak allows simultaneous access to the local coordination number and oxidation state, circumventing problems due to high noise levels, the temperature-sensitivity of EXAFS as well as related problems with XANES.

Empirical processing of the pre-edge spectra by fitting with robust model functions compensates for the unknown state of iron in the chemical system under investigation, thus maintaining a high degree of objectivity and reproducibility. This is important for studies of heterogeneous catalysts since the structure of the Fe species, mostly in non-crystalline samples, is often unknown. Hence, only the chemical speciation of the Fe sites is important and a chemical similarity of the reference compounds with the compounds under investigation is not a pre-requisite. Similarly, multiple data sets are subject to reliable analysis.

The elegance of using a pre-edge variogram for analysis of Fe lies largely in the fact that the pre-edge peak position is only indicative of the oxidation state, while the intensity is only indicative of the coordination geometry, making it possible to extract these values individually. The number of frequently occurring oxidation states (between Fe^{2+} and Fe^{3+}) and local coordination numbers (between 4 and 6) is low, contributing to a rather accurate analysis. For other first-row transition metals, the position of the K-pre-edge peak depends on both the oxidation state and coordination geometry, and often more oxidation states can be expected (e.g. in the case of Mn), which requires complementary structural information from XANES and EXAFS.

The electronic processes observed using HERFD-XANES and V2C-XES are complementary: the oxidation state and coordination geometry are probed by exciting the 1s electron to the unoccupied states within the 3d/4p orbitals, whereas the electronic interactions with ligands are probed by the relaxation of electrons from occupied states within the 3d/4p orbitals to fill the 1s hole. From an analytical point of view, it was shown here that a quantitative analysis of pre-edge spectra well complements the analysis of weak Fe Kβ”-features in the V2C spectra, which give information on the ligand structure. Hence, both pieces of information were critical for proposing a mechanism.

5. General conclusions and outlook

For the understanding of the structure-function relationships of alternative (inexpensive and environmentally benign) catalysts and subsequent steps to improve their performance, a well-established infrastructure for experimental and theoretical work is needed.

An instrumentation platform for *in situ* XAS studies in catalysis research was built up at ANKA as scope of this work. The improvements of existing concepts were attractive for the study of different catalyst systems, several of which were mentioned in this thesis.

With focus on the area of *in situ* X-ray absorption spectroscopy, challenges and new approaches were demonstrated in the combination of a spectroscopic investigation and the application of reaction conditions to different catalytic systems in collaboration projects. These include the combination of XAS, XRD, Raman, DRIFTS and IR-thermography and demanding conditions, e.g. >900°C or >100 bar. Equally important is data analysis.

The main focus of this thesis was the exploration of the Fe/Al_2O_3 and Fe/ZSM-5 catalyst systems by XAS. Especially demanding was the XAS data acquisition at the Fe K-edge of Fe/Al_2O_3 catalysts with a low iron loading, due to a high absorption of the X-ray beam by air, the capillary reactor and finally by the γ-Al_2O_3 support. This has imposed a necessity to de-couple the time-resolved *in situ* study of structural transformations from the stationary structural studies by EXAFS carried out *ex situ*, for optimising the measurement conditions. The analysis of the recorded X-ray absorption spectra was also subject to challenges.

The first challenge was to obtain structural information on the Fe centres in the 1% Fe/Al_2O_3 catalyst from spectra, which were acquired rapidly at the ANKA XAS beamline, suffering insufficient data quality and resolution compared to contemporary studies. Analysing the pre-edge peak, it was shown that during reduction by hydrogen, the Fe^{3+} species were reduced to Fe^{2+} in a temperature range of 300-500°C with the important additional information that the local Fe-O coordination did not change but remained around 5. Detailed understanding of the strengths and limitations of the variogram-based pre-edge analysis method has circumvented the requirements of high data quality and resolution, which are not always obtained on a standard beamline. Based on literature and adaptation of the pre-edge method, a way was developed, with the aid of which the oxidation state and geometry can be determined independently of the analysis of the full XANES and EXAFS spectra. Using pre-edge analysis, the oxidation state could be determined with high accuracy, and an uncertainty of only 10% between Fe^{2+} and Fe^{3+}. The local coordination number could be acquired at high temperatures, where the use of EXAFS is complex due to the temperature sensitivity and noise during rapid acquisition of *in situ* spectra. Additionally, the high-resolution fluorescence-detection mode or high-resolution transmission-XAS is not a pre-requisite for pre-edge analysis and detailed multiplet analysis is not necessary, since an empiric deconvolution of the pre-edge peak is sufficient for a qualitative and quantitative characterisation of the Fe sites. The dedicated pre-edge data analysis tool developed here allows rapid processing of multiple data sets with a high degree of objectivity, which can

accelerate research involving XANES spectra exhibiting pre-edge features. This is also interesting for other catalytic systems with pronounced pre-edge features (e.g. Mn, V).

In the HERFD-XAS application, the pre-edge data served as a sound complementary technique to the V2C-XES, the analysis of which is elaborate, and the signals are weak but the analytical information unique. Thus, the combination of the two techniques served as a key to give new insight to the mechanistic steps in the NH_3-SCR reaction over Fe/ZSM-5. Generally, the possibility of this emerging hard X-ray spectroscopy technique to give complementary information on the ligands is a perspective extension of *in situ* XAS.

Another analytical challenge was the understanding of the interaction of the FeO_x moieties with the γ-Al_2O_3 support by analysing the Fe K-edge EXAFS spectra of a 0.1% Fe/Al_2O_3 catalyst, where a high dispersion of the Fe species on the support was expected. The choice of a suitable model of the atomic short-range order around the absorber atom is critical for obtaining sufficient and reliable structural information from refining the EXAFS. The application of crystalline compounds for modelling surface-supported chemical species with a complex structure is not always useful or sufficient. The testing of a library of hypothetical structures, on the other hand, has proven to identify the location and structure of the catalytic Fe centres by making several structures plausible and eliminating the others. The library of simulated EXAFS spectra was preliminarily filtered and the best few models were used in the final refinement. The FeO_4 and FeO_5 moieties occupy octahedral lattice sites at the surface of γ-Al_2O_3 and are arranged in oligomeric clusters of several Fe atoms. This analysis approach can generally be applied for solving the structure of dopant atoms in contact with a crystalline matrix, rapidly screening all possibilities and thus increasing the probability of correctly describing the structure. Compared to the structure of known zeolite-supported Fe catalysts, there is evidence for tight bonds between the Fe centres and the γ-Al_2O_3 surface, which possibly decreases the accessibility and decreases the catalytic reactivity of the Fe sites. Additionally, this effect is amplified by the tendency of Fe species to agglomerate into oligomeric clusters. Further work in future must be dedicated to find new or modify the existing support materials for promoting a higher dispersion of the catalytic Fe sites.

So far, a first experimental platform for *in situ* XAS studies of heterogeneous catalysts for gas-phase reactions, in particular over exhaust gas catalysts, was successfully established at ANKA. The collaboration with other research groups, some results of which were briefly shown in Chapter 2, has increased the technical demands to the experimental setups and opened its applicability to other users. The high flexibility of the setups has opened

possibilities to apply *in situ* XAS and online gas analysis to e.g. reactions over V/Al_2O_3 catalysts, where very small amounts of catalyst are used, with the high utility of the setup for specially and temporally resolved XAS and IR-studies on a Pt/Al_2O_3 catalyst. The fluorescence-mode spectroscopy under technically relevant reaction conditions on Fe/Al_2O_3 and Fe/ZSM-5 catalysts was successfully conducted with the capillary setup. Careful conduction of experiments was possible for studying Co/MoS_2 alcohol synthesis catalysts, as well as observing phase changes from MoO_3 to MoC_2 by combined XAS/XRD. Online gas analysis by QMS and FTIR during the measurements was indispensible for drawing structure-activity correlations.

Further development and improvement of this *in situ* platform will be driven in the near future by extending the setup to applications for more demanding catalytic systems. This requires the realisation of a catalysis lab at ANKA. The extension of the transmission cell to high-pressure applications will allow the study of catalysts for high-pressure reactions, such as alcohol synthesis and Fischer-Tropsch synthesis, under realistic reaction conditions. *In situ* reactors for liquid-phase reactions (Grunwaldt *et al.*, 2006) are also implemented and should be routinely used in the near future for current projects such as hydrothermal synthesis of novel materials and biomass conversion catalysis. The implementation of each new possibility is expected to add to the complexity of the setups, therefore it is of high importance to keep the setups simple and robust, for best maintenance and flexibility and to serve a wider user community in future.

The combination of (quasi-)simultaneous *in situ* techniques has gained popularity in the last years. The combination of XAS and XRD has been strongly pursued at conventional EXAFS beamlines using a small position-sensitive detector for scanning the angle range (Clausen *et al.*, 1993), compact wide-angle position-sensitive detectors (e.g. INEL CPS 120) (Grunwaldt & Clausen, 2002, Grunwaldt *et al.*, 2000) and large area-detectors (Ehrlich *et al.*, 2011), moving on to dedicated beamlines for combining XAS with high-resolution XRD, e.g. at SNBL at ESRF (van Beek *et al.*, 2011).

Combined techniques are of great importance for studying heterogeneous catalysts (Grunwaldt *et al.*, 2007, Grunwaldt *et al.*, 2009) and dedicated *in situ* reactors, e.g. for transmission/fluorescence XAS/XRD during liquid-phase reactions (Hannemann *et al.*, 2007) are presently being further designed and implemented. The employment of two monochromators dedicated for combining XAS and XRD, such as at SNBL, is one solution, but the optimisation of the combined setup using a single monochromator and implementing a

position-sensitive detector (e.g. MEDIPIX) at a conventional X-ray absorption beamline is the path pursued at ANKA. As pre-requisites for (quasi-)simultaneous studies, XAS in transmission and fluorescence-mode, XRD and IR-thermography are already possible with the same setup (capillary micro-reactor) to study the same reaction (e.g. CO oxidation). In the near future, these *in situ* EXAFS experimentation combined with other techniques (e.g. XRD, Raman and DRIFTS (Grunwaldt *et al.*, 2009, Marinkovic *et al.*, 2011, Chiarello *et al.*, 2014)) for catalysis research is to be extended to the new CATACT beamline at ANKA.

For advancing structure-activity relationships as a part of rational catalyst design, *in situ* spectroscopy must progress in both the field of instrumentation and data analysis tools as shown in this thesis. In this way, demanding experiments can be conducted in a reproducible manner with maximum information derived from results. By correctly coupling instrumentation and data analysis, a compromise between spectroscopy and technically relevant reaction conditions can thus be achieved.

References

Agostini G., Lamberti C., Pellegrini R., Leofanti G., Giannici F., Longo A. & Groppo E., Effect of Pre-Reduction on the Properties and the Catalytic Activity of Pd/Carbon Catalysts: A Comparison with Pd/Al2O3, *ACS Catalysis* 4 (2013) 187-194.

Alberto H. V., Pinto da Cunha J. L., Mysen B. O., Gil J. M. & Ayres de Campos N., Analysis of Mössbauer spectra of silicate glasses using a two-dimensional Gaussian distribution of hyperfine parameters, *Journal of Non-Crystalline Solids* 194 (1996) 48-57.

Als-Nielsen J. & McMorrow D. (2001). *Elements of Modern X-ray Physics*, p. 203: John Wiley & Sons, Inc.

An Y., Wang S., Feng D., Wu Z. & Liu J., Correlation between oxygen vacancies and magnetism in Fe-doped In_2O_3 films, *Applied Surface Science* 276 (2013) 535-538.

An Y., Wang S., Feng D., Wu Z. & Liu J., Local structure of Fe-doped In_2O_3 films investigated by X-ray absorption fine structure spectroscopy, *Applied Physics A* 115 (2014) 823-828.

Arrio M. A., Rossano S., Ch B., Galoisy L. & Calas G., Calculation of multipole transitions at the Fe K pre-edge through p - d hybridization in the Ligand Field Multiplet model, *EPL (Europhysics Letters)* 51 (2000) 454.

Atkins A. J., Bauer M. & Jacob C. R., The chemical sensitivity of X-ray spectroscopy: high energy resolution XANES versus X-ray emission spectroscopy of substituted ferrocenes, *Physical Chemistry Chemical Physics* 15 (2013) 8095-8105.

Avogadro software, version 1.1.0, http://avogadro.openmolecules.net (01.05.2013).

Bajt S., Sutton S. R. & Delaney J. S., X-ray microprobe analysis of iron oxidation states in silicates and oxides using X-ray absorption near edge structure (XANES), *Geochimica et Cosmochimica Acta* 58 (1994) 5209-5214.

Balle P., Geiger B. & Kureti S., Selective catalytic reduction of NO_x by NH_3 on Fe/HBEA zeolite catalysts in oxygen-rich exhaust, *Applied Catalysis B: Environmental* 85 (2009) 109-119.

Bañares M. A., Operando methodology: combination of in situ spectroscopy and simultaneous activity measurements under catalytic reaction conditions, *Catalysis Today* 100 (2005) 71-77.

BAND2013, SCM, http://www.scm.com (14.07.2014).

Bare S. R. & Ressler T., Chapter 6 Characterization of Catalysts in Reactive Atmospheres by X-ray Absorption Spectroscopy, *Advances in Catalysis* 52 (2009) 339-465.

Bare S. R., Yang N., Kelly S. D., Mickelson G. E. & Modica F. S., Design and operation of a high pressure reaction cell for in situ X-ray absorption spectroscopy, *Catalysis Today* 126 (2007) 18-26.

Battiston A. A., Bitter J. H., de Groot F. M. F., Overweg A. R., Stephan O., van Bokhoven J. A., Kooyman P. J., van der Spek C., Vankó G. & Koningsberger D. C., Evolution of Fe species during the synthesis of over-exchanged Fe/ZSM5 obtained by chemical vapor deposition of $FeCl_3$, *Journal of Catalysis* 213 (2003) 251-271.

Battiston A. A., Bitter J. H., Heijboer W. M., de Groot F. M. F. & Koningsberger D. C., Reactivity of Fe-binuclear complexes in over-exchanged Fe/ZSM5, studied by in situ XAFS spectroscopy - Part 1: Heat treatment in He and O_2, *Journal of Catalysis* 215 (2003) 279-293.

Battiston A. A., Bitter J. H. & Koningsberger D. C., XAFS characterization of the binuclear iron complex in overexchanged Fe/ZSM5 – structure and reactivity, *Catalysis Letters* 66 (2000) 75-79.

Battiston A. A., Bitter J. H. & Koningsberger D. C., Reactivity of binuclear Fe complexes in over-exchanged Fe/ZSM5, studied by in situ XAFS spectroscopy 2. Selective catalytic reduction of NO with isobutane, *Journal of Catalysis* 218 (2003) 163-177.

Bauer M., HERFD-XAS and valence-to-core-XES: new tools to push the limits in research with hard X-rays?, *Physical Chemistry Chemical Physics* 16 (2014) 13827-13837.

Bauer M., Kauf T., Christoffers J. & Bertagnolli H., Investigations into the metal species of the homogeneous iron(III) catalyzed Michael addition reactions, *Physical Chemistry Chemical Physics* 7 (2005) 2664-2670.

Bazin D., Dexpert H. & Lynch J. (1996). *X-Ray Absorption Fine Structure for Catalysts and Surfaces*, pp. 113-129.

Becke A. D., Density-functional exchange-energy approximation with correct asymptotic behavior, *Physical Review A* 38 (1988) 3098-3100.

Benfatto M. & Della Longa S., Geometrical fitting of experimental XANES spectra by a full multiple-scattering procedure, *Journal of Synchrotron Radiation* 8 (2001) 1087-1094.

Berry A. J., O'Neill H. S., Jayasuriya K. D., Campbell S. J. & Foran G. J., XANES calibrations for the oxidation state of iron in a silicate glass, *American Mineralogist* 88 (2003) 967-977.

Bianchini M. & Glatzel P., A tool to plan photon-in/photon-out experiments: count rates, dips and self-absorption, *Journal of Synchrotron Radiation* 19 (2012) 911-919.

Bitter J. H., Battiston A. A., van Donk S., de Jong K. P. & Koningsberger D. C., Accessibility of the Fe-species in Fe/ZSM-5 prepared via $FeCl_3$ sublimation, *Microporous and Mesoporous Materials* 64 (2003) 175-184.

Bordiga S., Groppo E., Agostini G., van Bokhoven J. A. & Lamberti C., Reactivity of Surface Species in Heterogeneous Catalysts Probed by In Situ X-ray Absorption Techniques, *Chemical Reviews* 113 (2013) 1736-1850.

Boubnov A., Carvalho H. W. P., Doronkin D. E., Günter T., Gallo E., Atkins A. J., Jacob C. R. & Grunwaldt J.-D., Selective catalytic reduction of NO over Fe-ZSM-5: Mechanistic insights by operando HERFD-XANES and valence-to-core XES spectroscopy, *Journal of the American Chemical Society* 136 (2014) 13006-13015.

Boubnov A., Dahl S., Johnson E., Molina A. P., Simonsen S. B., Cano F. M., Helveg S., Lemus-Yegres L. J. & Grunwaldt J.-D., Structure–activity relationships of Pt/Al_2O_3 catalysts for CO and NO oxidation at diesel exhaust conditions, *Applied Catalysis B: Environmental* 126 (2012) 315-325.

Boubnov A., Gänzler A., Conrad S., Casapu M. & Grunwaldt J.-D., Oscillatory CO Oxidation Over Pt/Al2O3 Catalysts Studied by In situ XAS and DRIFTS, *Topics in Catalysis* 56 (2013) 333-338.

Boubnov A., Lichtenberg H., Mangold S. & Grunwaldt J.-D., Structure and reducibility of a Fe/Al_2O_3 catalyst for selective catalytic reduction studied by Fe K-edge XAFS spectroscopy, *Journal of Physics: Conference Series* 430 (2013) 012054.

Brandenberger S., Kröcher O., Tissler A. & Althoff R., The State of the Art in Selective Catalytic Reduction of NOx by Ammonia Using Metal-Exchanged Zeolite Catalysts, *Catalysis Reviews* 50 (2008) 492-531.

Brandenberger S., Kröcher O., Tissler A. & Althoff R., The determination of the activities of different iron species in Fe-ZSM-5 for SCR of NO by NH_3, *Applied Catalysis B: Environmental* 95 (2010) 348-357.

Caliebe W. A., Kao C. C., Hastings J. B., Taguchi M., Kotani A., Uozumi T. & de Groot F. M. F., 1*s*2*p* resonant inelastic x-ray scattering in α-Fe_2O_3, *Physical Review B* 58 (1998) 13452-13458.

Chandrasekaran P., Chiang K. P., Nordlund D., Bergmann U., Holland P. L. & DeBeer S., Sensitivity of X-ray Core Spectroscopy to Changes in Metal Ligation: A Systematic Study of Low-Coordinate, High-Spin Ferrous Complexes, *Inorganic Chemistry* 52 (2013) 6286-6298.

Changela H. G., Bridges J. C. & Gurman S. J., Extended X-ray Absorption Fine Structure (EXAFS) in Stardust tracks: Constraining the origin of ferric iron-bearing minerals, *Geochimica et Cosmochimica Acta* 98 (2012) 282-294.

Chiarello G. L., Nachtegaal M., Marchionni V., Quaroni L. & Ferri D., Adding diffuse reflectance infrared Fourier transform spectroscopy capability to extended x-ray-absorption fine structure in a new cell to study solid catalysts in combination with a modulation approach, *Review of Scientific Instruments* 85 (2014) 074102.

Choi S. H., Wood B. R., Ryder J. A. & Bell A. T., X-ray Absorption Fine Structure Characterization of the Local Structure of Fe in Fe−ZSM-5, *The Journal of Physical Chemistry B* 107 (2003) 11843-11851.

Choi S. H., Wood B. R., Ryder J. A. & Bell A. T., EXAFS characterization of the local structure of Fe in Fe-ZSM-5: an experimental and theoretical study, *Physica Scripta* 2005 (2005) 688.

Chou T. C. & Nieh T. G., Nucleation and Concurrent Anomalous Grain Growth of α-Al_2O_3 During γ-α Phase Transformation, *Journal of the American Ceramic Society* 74 (1991) 2270-2279.

Christensen J. M., Jensen P. A., Schiødt N. C., Jensen A. D., Christensen J. M., Jensen P. A., Schiødt N. C. & Jensen A. D., Coupling of Alcohols over Alkali-Promoted Cobalt-Molybdenum Sulfide, *ChemCatChem* 2 (2010) 523-526.

Clausen B. S., Gråbæk L., Steffensen G., Hansen P. L. & Topsøe H., A Combined QEXAFS/XRD Method for Online, *in situ* Studies of Catalysts - Examples of Dynamic Measurements of Cu-Based Methanol Catalysts, *Catalysis Letters* 20 (1993) 23-36.

Clausen B. S., Steffensen G., Fabius B., Villadsen J., Feidenhansl R. & Topsøe H., *In situ* Cell for Combined XRD and Online Catalysis Tests - Studies of Cu-Based Water Gas Shift and Methanol Catalysts, *Journal of Catalysis* 132 (1991) 524-535.

Clausen B. S. & Topsøe H., *In situ* High-Pressure, High-Temperature XAFS Studies of Cu-Based Catalysts During Methanol Synthesis, *Catalysis Today* 9 (1991) 189-196.

Clausen B. S., Topsøe H. & Frahm R. (1998). Vol. 42. *Advances in Catalysis,* edited by D. D. Eley, W. O. Haag, B. Gates & H. Knözinger, pp. 315-344: Academic Press.

Cottrell E., Kelley K. A., Lanzirotti A. & Fischer R. A., High-precision determination of iron oxidation state in silicate glasses using XANES, *Chemical Geology* 268 (2009) 167-179.

Couves J. W., Thomas J. M., Waller D., Jones R. H., Dent A. J., Derbyshire G. E. & Greaves G. N., Tracing the conversion of aurichalcite to a copper catalyst by combined X-ray absorption and diffraction, *Nature* 354 (1991) 465-468.

de Groot F., Vankó G. & Glatzel P., The 1s x-ray absorption pre-edge structures in transition metal oxides, *Journal of Physics: Condensed Matter* 21 (2009) 104207.

Deutschmann O. & Grunwaldt J.-D., Abgasnachbehandlung in mobilen Systemen: Stand der Technik, Herausforderungen und Perspektiven (Exhaust Gas Aftertreatment in Mobile Systems: Status, Challenges, and Perspectives), *Chemie Ingenieur Technik* 85 (2013) 595-617.

Digne M., Raybaud P., Sautet P., Rebours B. & Toulhoat H., Comment on "Examination of Spinel and Nonspinel Structural Models for γ-Al_2O_3 by DFT and Rietveld Refinement Simulations", *The Journal of Physical Chemistry B* 110 (2006) 20719-20720.

Digne M., Sautet P., Raybaud P., Euzen P. & Toulhoat H., Use of DFT to achieve a rational understanding of acid–basic properties of γ-alumina surfaces, *Journal of Catalysis* 226 (2004) 54-68.

Dong H. H., Xie M. J., Xu J., Li M. F., Peng L. M., Guo X. F. & Ding W. P., Iron oxide and alumina nanocomposites applied to Fischer-Tropsch synthesis, *Chemical Communications* 47 (2011) 4019-4021.

Doronkin D. E., Casapu M., Günter T., Müller O., Frahm R. & Grunwaldt J.-D., Operando Spatially and Time Resolved XAS Study on Zeolite Catalysts for Selective Catalytic Reduction of NOx by NH3, *The Journal of Physical Chemistry C* 118 (2014) 10204–10212.

Doronkin D. E., Fogel S., Gabrielsson P., Grunwaldt J.-D. & Dahl S., Ti and Si doping as a way to increase low temperature activity of sulfated Ag/Al_2O_3 in H_2-assisted NH_3-SCR of NO_x, *Applied Catalysis B: Environmental* 148–149 (2014) 62-69.

Dräger G., Frahm R., Materlik G. & Brümmer O., On the Multipole Character of the X-Ray Transitions in the Pre-Edge Structure of Fe K Absorption Spectra. An Experimental Study, *Physica Status Solidi B* 146 (1988) 287-294.

Dyan A., Azevedo C., Cenedese P. & Dubot P., Electronic and atomic structure computation of disordered low index surfaces of γ-alumina, *Applied Surface Science* 254 (2008) 3819-3828.

Ehrlich S. N., Hanson J. C., Lopez Camara A., Barrio L., Estrella M., Zhou G., Si R., Khalid S. & Wang Q., Combined XRD and XAS, *Nuclear Instruments and Methods in Physics Research Section A: Accelerators, Spectrometers, Detectors and Associated Equipment* 649 (2011) 213-215.

Englisch M., Lercher J. A. & Haller G. L. (1996). Vol. 2. *X-ray absorption fine structure for catalysts and surfaces,* edited by Y. Iwasawa, pp. 276-303. Singapore: World Scientific.

Farges F., Ab initio and experimental pre-edge investigations of the Mn K -edge XANES in oxide-type materials, *Physical Review B* 71 (2005) 155109.

Farges F., Lefrère Y., Rossano S., Berthereau A., Calas G. & Brown Jr G. E., The effect of redox state on the local structural environment of iron in silicate glasses: a combined XAFS spectroscopy,

molecular dynamics, and bond valence study, *Journal of Non-Crystalline Solids* 344 (2004) 176-188.

Feng X. & Hall W. K., Limitations on the formation of oxygen-bridged divalent cations in FeZSM-5, *Catalysis Letters* 46 (1997) 11-16.

Galoisy L., Calas G. & Arrio M. A., High-resolution XANES spectra of iron in minerals and glasses: structural information from the pre-edge region, *Chemical Geology* 174 (2001) 307-319.

Galvita V., Rihko-Struckmann L. K. & Sundmacher K., The CO adsorption on a Fe_2O_3–$Ce_{0.5}Zr_{0.5}O_2$ catalyst studied by TPD, isotope exchange and FTIR spectroscopy, *Journal of Molecular Catalysis A: Chemical* 283 (2008) 43-51.

Gänzler A., Casapu M., Boubnov A., Müller O., Conrad S., Lichtenberg H. & Grunwaldt J.-D., Chasing the Active Site during Oscillatory CO Oxidation (in preparation).

Ginibre C., Wörner G. & Kronz A., Structure and Dynamics of the Laacher See Magma Chamber (Eifel, Germany) from Major and Trace Element Zoning in Sanidine: a Cathodoluminescence and Electron Microprobe Study, *Journal of Petrology* 45 (2004) 2197-2223.

Giordanino F., Borfecchia E., Lomachenko K. A., Lazzarini A., Agostini G., Gallo E., Soldatov A. V., Beato P., Bordiga S. & Lamberti C., Interaction of NH_3 with Cu-SSZ-13 Catalyst: A Complementary FTIR, XANES, and XES Study, *The Journal of Physical Chemistry Letters* (2014) 1552-1559.

Glatzel P., Mirone A., Eeckhout S. G., Sikora M. & Giuli G., Orbital hybridization and spin polarization in the resonant 1*s* photoexcitations of α-Fe_2O_3, *Physical Review B* 77 (2008) 115133.

Glatzel P., Sikora M. & Fernández-García M., Resonant X-ray spectroscopy to study K absorption pre-edges in 3d transition metal compounds, *The European Physical Journal Special Topics* 169 (2009) 207-214.

Glatzel P., Sikora M., Smolentsev G. & Fernández-García M., Hard X-ray photon-in photon-out spectroscopy, *Catalysis Today* 145 (2009) 294-299.

Gracia F. J., Bollmann L., Wolf E. E., Miller J. T. & Kropf A. J., *In situ* FTIR, EXAFS and activity studies of the effect of crystallite size on silica-supported Pt oxidation catalysts, *Journal of Catalysis* 220 (2003) 382-391.

Grossale A., Nova I. & Tronconi E., Study of a Fe–zeolite-based system as NH_3-SCR catalyst for diesel exhaust aftertreatment, *Catalysis Today* 136 (2008) 18-27.

Grunwaldt J.-D. & Baiker A., In situ spectroscopic investigation of heterogeneous catalysts and reaction media at high pressure, *Physical Chemistry Chemical Physics* 7 (2005) 3526-3539.

Grunwaldt J.-D., Caravati M. & Baiker A., In Situ Extended X-ray Absorption Fine Structure Study during Selective Alcohol Oxidation over Pd/Al_2O_3 in Supercritical Carbon Dioxide, *The Journal of Physical Chemistry B* 110 (2006) 9916-9922.

Grunwaldt J.-D., Caravati M., Hannemann S. & Baiker A., X-ray absorption spectroscopy under reaction conditions: suitability of different reaction cells for combined catalyst characterization and time-resolved studies, *Physical Chemistry Chemical Physics* 6 (2004) 3037-3047.

Grunwaldt J.-D. & Clausen B. S., Combining XRD and EXAFS with on-Line Catalytic Studies for in situ Characterization of Catalysts, *Topics in Catalysis* 18 (2002) 37-43.

Grunwaldt J.-D. & Frenkel A. I., Synchrotron Studies of Catalysts: From XAFS to QEXAFS and Beyond, *Synchrotron Radiation News* 22 (2009) 2-4.

Grunwaldt J.-D., Hannemann S., Göttlicher J., Mangold S., Denecke M. A. & Baiker A., X-ray absorption spectroscopy on heterogeneous catalysts at the new XAS beamline at ANKA, *Physica Scripta* T115 (2005) 769-772.

Grunwaldt J.-D., Molenbroek A. M., Topsøe N. Y., Topsøe H. & Clausen B. S., In Situ Investigations of Structural Changes in Cu/ZnO Catalysts, *Journal of Catalysis* 194 (2000) 452-460.

Grunwaldt J.-D., van Vegten N., Baiker A. & van Beek W., Insight into the structure of Pd/ZrO_2 during the total oxidation of methane using combined in situ XRD, X-ray absorption and Raman spectroscopy, *Journal of Physics: Conference Series* 190 (2009) 012160.

Grunwaldt J.-D., Vegten N. v. & Baiker A., Insight into the structure of supported palladium catalysts during the total oxidation of methane, *Chemical Communications* (2007) 4635-4637.

Grunwaldt J.-D., Wandeler R. & Baiker A., Supercritical Fluids in Catalysis: Opportunities of In Situ Spectroscopic Studies and Monitoring Phase Behavior, *Catalysis Reviews* 45 (2003) 1-96.

Grunwaldt J. D., Shining X-rays on catalysts at work, *Journal of Physics: Conference Series* 190 (2009) 012151.

Gutiérrez G., Taga A. & Johansson B., Theoretical structure determination of γ-Al_2O_3, *Physical Review B* 65 (2001) 012101.

Hannemann S., Casapu M., Grunwaldt J.-D., Haider P., Trüssel P., Baiker A. & Welter E., A versatile in situ spectroscopic cell for fluorescence/transmission EXAFS and X-ray diffraction of heterogeneous catalysts in gas and liquid phase, *Journal of Synchrotron Radiation* 14 (2007) 345-354.

Hazen R. M. & Jeanloz R., Wüstite ($Fe_{1-x}O$): A review of its defect structure and physical properties, *Reviews of Geophysics* 22 (1984) 37-46.

Heijboer W. M., Glatzel P., Sawant K. R., Lobo R. F., Bergmann U., Barrea R. A., Koningsberger D. C., Weckhuysen B. M. & de Groot F. M. F., Kβ-Detected XANES of Framework-Substituted FeZSM-5 Zeolites, *The Journal of Physical Chemistry B* 108 (2004) 10002-10011.

Hilbrandt N. & Martin M., Site preference of iron ions in α-alumina: An Fe-K XAFS study on specimens prepared by a combined self-propagating chemical combustion and sintering technique, *Journal of the Chemical Society, Faraday Transactions* 94 (1998) 3381-3384.

Høj M., Beier M. J., Grunwaldt J.-D. & Dahl S., The role of monomeric iron during the selective catalytic reduction of NO_x by NH_3 over Fe-BEA zeolite catalysts, *Applied Catalysis B: Environmental* 93 (2009) 166-176.

Høj M., Jensen A. D. & Grunwaldt J.-D., Structure of alumina supported vanadia catalysts for oxidative dehydrogenation of propane prepared by flame spray pyrolysis, *Applied Catalysis A: General* 451 (2013) 207-215.

Homs N., Fierro J. L. G., Guerrero-Ruiz A., Rodriguez-Ramos I. & Ramírez de la Piscina P., Study of the activation process and catalytic behaviour of a supported iron ammonia synthesis catalyst, *Applied Surface Science* 72 (1993) 103-111.

Hunger M. & Weitkamp J., In situ IR, NMR, EPR, and UV/Vis Spectroscopy: Tools for New Insight into the Mechanisms of Heterogeneous Catalysis, *Angewandte Chemie International Edition* 40 (2001) 2954-2971.

ImageJ software at National Institutes of Health, http://rsbweb.nih.gov/ij/ (13.01.2014).

Jacobsen C. J., Dahl S., Clausen B. S., Bahn S., Logadottir A. & Nørskov J. K., Catalyst design by interpolation in the periodic table: bimetallic ammonia synthesis catalysts, *Journal of the American Chemical Society* 123 (2001) 8404-8405.

Jia J., Sun Q., Wen B., Chen L. & Sachtler W. H., Identification of Highly Active Iron Sites in N_2O-Activated Fe/MFI, *Catalysis Letters* 82 (2002) 7-11.

Johann H. H., Die Erzeugung lichtstarker Röntgenspektren mit Hilfe von Konkavkristallen, *Zeitschrift für Physik* 69 (1931) 185-206.

Johnson T., Diesel Engine Emissions and Their Control, *Platinum Metals Review* 52 (2008) 23-37.

Karaca H., Safonova O. V., Chambrey S., Fongarland P., Roussel P., Griboval-Constant A., Lacroix M. & Khodakov A. Y., Structure and catalytic performance of Pt-promoted alumina-supported cobalt catalysts under realistic conditions of Fischer–Tropsch synthesis, *Journal of Catalysis* 277 (2011) 14-26.

Kelly S. D., Kemner K. M. & Brooks S. C., X-ray absorption spectroscopy identifies calcium-uranyl-carbonate complexes at environmental concentrations, *Geochimica et Cosmochimica Acta* 71 (2007) 821-834.

Kiebach R., Pienack N., Bensch W., Grunwaldt J.-D., Michailovski A., Baiker A., Fox T., Zhou Y. & Patzke G. R., Hydrothermal Formation of W/Mo-Oxides: A Multidisciplinary Study of Growth and Shape, *Chemistry of Materials* 20 (2008) 3022-3033.

Kimmerle B., Grunwaldt J.-D., Baiker A., Glatzel P., Boye P., Stephan S. & Schroer C. G., Visualizing a Catalyst at Work during the Ignition of the Catalytic Partial Oxidation of Methane, *The Journal of Physical Chemistry C* 113 (2009) 3037-3040.

Kimmerle B., Haider P., Grunwaldt J.-D., Baiker A., Boye P. & Schroer C. G., High throughput cell for X-ray absorption spectroscopy applied to study the effect of Au on Rh-catalyzed partial oxidation of methane, *Applied Catalysis A: General* 353 (2009) 36-45.

Klukowski D., Balle P., Geiger B., Wagloehner S., Kureti S., Kimmerle B., Baiker A. & Grunwaldt J.-D., On the mechanism of the SCR reaction on Fe/HBEA zeolite, *Applied Catalysis B: Environmental* 93 (2009) 185-193.

Koningsberger D. & Prins R., X-ray absorption: principles, applications, techniques of EXAFS, SEXAFS, and XANES, (1988).

Kou Y., Wang H.-l., Niu J.-z. & Ji W.-j., Surface Coordinate Geometry of Iron Catalysts: Distinctive Behaviors of Fe/Al_2O_3 in CO Hydrogenation, *The Journal of Physical Chemistry* 100 (1996) 2330-2333.

Kovarik L., Genc A., Wang C., Qiu A., Peden C. H. F., Szanyi J. & Kwak J. H., Tomography and High-Resolution Electron Microscopy Study of Surfaces and Porosity in a Plate-like γ-Al2O3, *The Journal of Physical Chemistry C* 117 (2012) 179-186.

Krause M. O. & Oliver J. H., Natural widths of atomic K and L levels, Kα X-ray lines and several KLL Auger lines, *Journal of Physical Chemistry Reference Data* 8 (1979) 329-338.

Krokidis X., Raybaud P., Gobichon A.-E., Rebours B., Euzen P. & Toulhoat H., Theoretical Study of the Dehydration Process of Boehmite to γ-Alumina, *The Journal of Physical Chemistry B* 105 (2001) 5121-5130.

Kündig W., Bömmel H., Constabaris G. & Lindquist R., Some properties of supported small α-Fe_2O_3 particles determined with the Mössbauer effect, *Physical Review* 142 (1966) 327-333.

Kwak J. H., Mei D., Peden C. H., Rousseau R. & Szanyi J., (100) facets of γ-Al_2O_3: The Active Surfaces for Alcohol Dehydration Reactions, *Catalysis Letters* 141 (2011) 649-655.

Lancaster K. M., Roemelt M., Ettenhuber P., Hu Y., Ribbe M. W., Neese F., Bergmann U. & DeBeer S., X-ray Emission Spectroscopy Evidences a Central Carbon in the Nitrogenase Iron-Molybdenum Cofactor, *Science* 334 (2011) 974-977.

Lee M. H., Cheng C.-F., Heine V. & Klinowski J., Distribution of tetrahedral and octahedral A1 sites in gamma alumina, *Chemical Physics Letters* 265 (1997) 673-676.

Lee N., Petrenko T., Bergmann U., Neese F. & DeBeer S., Probing Valence Orbital Composition with Iron Kβ X-ray Emission Spectroscopy, *Journal of the American Chemical Society* 132 (2010) 9715-9727.

Lin L.-w., Kou Y., Zou M. & Yan Z., An amorphous approach to the structure of a Pt-Fe/γ-Al_2O_3 catalyst characterized by XAFS, *Physical Chemistry Chemical Physics* 3 (2001) 1789-1794.

Liu F., He H. & Xie L., XAFS Study on the Specific Deoxidation Behavior of Iron Titanate Catalyst for the Selective Catalytic Reduction of NOx with NH3, *ChemCatChem* 5 (2013) 3760-3769.

Liu H., Wang J., Yu T., Fan S. & Shen M., The role of various iron species in Fe-[small beta] catalysts with low iron loadings for NH3-SCR, *Catalysis Science & Technology* 4 (2014) 1350-1356.

Liu Z., Millington P. J., Bailie J. E., Rajaram R. R. & Anderson J. A., A comparative study of the role of the support on the behaviour of iron based ammonia SCR catalysts, *Microporous and Mesoporous Materials* 104 (2007) 159-170.

Loviat F., Czekaj I., Wambach J. & Wokaun A., Nickel deposition on γ-Al_2O_3 model catalysts: An experimental and theoretical investigation, *Surface Science* 603 (2009) 2210-2217.

Lox E. S. J., Engler B. H., Janssen F. J., Garten R. L., Dalla Betta R. A., Schlatter J. C., Ainbinder Z., Manzer L. E., Nappa M. J., Parmon V. N. & Zamaraev K. I. (2008). *Handbook of Heterogeneous Catalysis*, pp. 1569-1595: Wiley-VCH Verlag GmbH.

Maier S. M., Jentys A., Janousch M., van Bokhoven J. A. & Lercher J. A., Unique Dynamic Changes of Fe Cationic Species under NH_3-SCR Conditions, *The Journal of Physical Chemistry C* 116 (2012) 5846-5856.

Maier S. M., Jentys A., Metwalli E., Müller-Buschbaum P. & Lercher J. A., Determination of the Redox Processes in FeBEA Catalysts in NH3−SCR Reaction by Mössbauer and X-ray Absorption Spectroscopy, *The Journal of Physical Chemistry Letters* 2 (2011) 950-955.

Mangold S., Steininger R., Rolo T. d. S. & Göttlicher J., Full field spectroscopic imaging at the ANKA-XAS- and -SUL-X-Beamlines, *Journal of Physics: Conference Series* 430 (2013) 012130.

Marinkovic N. S., Wang Q., Barrio L., Ehrlich S. N., Khalid S., Cooper C. & Frenkel A. I., Combined in situ X-ray absorption and diffuse reflectance infrared spectroscopy: An attractive tool for catalytic investigations, *Nuclear Instruments and Methods in Physics Research Section A: Accelerators, Spectrometers, Detectors and Associated Equipment* 649 (2011) 204-206.

Marturano P., Drozdova L., Pirngruber G. D., Kogelbauer A. & Prins R., The mechanism of formation of the Fe species in Fe/ZSM-5 prepared by CVD, *Physical Chemistry Chemical Physics* 3 (2001) 5585-5595.

Matam S., Korsak O., Bocher L., Logvinovich D., Hug P., Weidenkaff A. & Ferri D., Lab Scale Fixed-Bed Reactor for Operando X-Ray Absorption Spectroscopy for Structure Activity Studies of Supported Metal Oxide Catalysts, *Topics in Catalysis* 54 (2011) 1213-1218.

Mercuri F. (2011). *Adsorption of organic molecules on Al/gamma-Al_2O_3 surfaces and interfaces,* http://surfaces.wikispaces.com/page/diff/Molecules+on+gamma+alumina/227784172 (13.07.2014).

Mercury software (CCDC), version 3.0, http://www.ccdc.cam.ac.uk/mercury/ (13.01.2014).

Metkar P. S., Salazar N., Muncrief R., Balakotaiah V. & Harold M. P., Selective catalytic reduction of NO with NH3 on iron zeolite monolithic catalysts: Steady-state and transient kinetics, *Applied Catalysis B: Environmental* 104 (2011) 110-126.

Meunier F. C., The design and testing of kinetically-appropriate operando spectroscopic cells for investigating heterogeneous catalytic reactions, *Chemical Society Reviews* 39 (2010) 4602-4614.

Mittasch A. & Frankenburg W. (1950). Vol. Volume 2. *Advances in Catalysis,* edited by V. I. K. W.G. Frankenburg & E. K. Rideal, pp. 81-104: Academic Press.

Mo S.-D., Xu Y.-N. & Ching W.-Y., Electronic and Structural Properties of Bulk γ-Al_2O_3, *Journal of the American Ceramic Society* 80 (1997) 1193-1197.

Nelson A. E., Sun M. & Adjaye J., Reply to "Comments on 'Examination of Spinel and Nonspinel Structural Models for γ-Al_2O_3 by DFT and Rietveld Refinement Simulations'", *The Journal of Physical Chemistry B* 110 (2006) 20724-20726.

Okazaki N., Osada S. & Tada A., Deactivation by sulfur dioxide of alumina-based catalysts for selective catalytic reduction of nitrogen monoxide by ethene, *Applied Surface Science* 121–122 (1997) 396-399.

Paglia G., Buckley C. E. & Rohl A. L., Comment on "Examination of Spinel and Nonspinel Structural Models for γ-Al_2O_3 by DFT and Rietveld Refinement Simulations", *The Journal of Physical Chemistry B* 110 (2006) 20721-20723.

Perbandt C., Bacher V., Groves M., Schwefer M., Siefert R. & Turek T., Kinetics and Reactor Design for N2O Decomposition in the EnviNOx® Process, *Chemie Ingenieur Technik* 85 (2013) 705-709.

Perdew J. P., Density-functional approximation for the correlation energy of the inhomogeneous electron gas, *Physical Review B* 33 (1986) 8822-8824.

Petit P.-E., Farges F., Wilke M. & Solé V. A., Determination of the iron oxidation state in Earth materials using XANES pre-edge information, *Journal of Synchrotron Radiation* 8 (2001) 952-954.

Pinto H. P., Nieminen R. M. & Elliott S. D., *Ab initio* study of γ-Al_2O_3 surfaces *Physical Review B* 70 (2004) 125402.

Pirngruber G. D., Grunwaldt J.-D., Roy P. K., van Bokhoven J. A., Safonova O. & Glatzel P., The nature of the active site in the Fe-ZSM-5/N_2O system studied by (resonant) inelastic X-ray scattering, *Catalysis Today* 126 (2007) 127-134.

Pirngruber G. D., Grunwaldt J.-D., van Bokhoven J. A., Kalytta A., Reller A., Safonova O. V. & Glatzel P., On the Presence of Fe(IV) in Fe-ZSM-5 and $FeSrO_{3-x}$ Unequivocal Detection of the $3d^4$ Spin System by Resonant Inelastic X-ray Scattering, *The Journal of Physical Chemistry B* 110 (2006) 18104-18107.

Pirngruber G. D., Roy P. K. & Prins R., On determining the nuclearity of iron sites in Fe-ZSM-5-a critical evaluation, *Physical Chemistry Chemical Physics* 8 (2006) 3939-3950.

Pirngruber G. D., Roy P. K. & Weiher N., An in situ X-ray Absorption Spectroscopy Study of N_2O Decomposition over Fe-ZSM-5 Prepared by Chemical Vapor Deposition of $FeCl_3$, *The Journal of Physical Chemistry B* 108 (2004) 13746-13754.

Quartieri S., Riccardi M. P., Messiga B. & Boscherini F., The ancient glass production of the Medieval Val Gargassa glasshouse: Fe and Mn XANES study, *Journal of Non-Crystalline Solids* 351 (2005) 3013-3022.

Ravel B. & Newville M., ATHENA, ARTEMIS, HEPHAESTUS: data analysis for X-ray absorption spectroscopy using IFEFFIT, *Journal of Synchrotron Radiation* 12 (2005) 537-541.

Ressler T., Walter A., Scholz J., Tessonnier J. P. & Su D. S., Structure and properties of a Mo oxide catalyst supported on hollow carbon nanofibers in selective propene oxidation, *Journal of Catalysis* 271 (2010) 305-314.

Río M. S. d., Sodo A., Eeckhout S. G., Neisius T., Martinetto P., Dooryhée E. & Reyes-Valerio C., Fe K-edge XANES of Maya blue pigment, *Nuclear Instruments and Methods in Physics Research Section B: Beam Interactions with Materials and Atoms* 238 (2005) 50-54.

Ristić A., Tušar N. N., Arčon I., Logar N. Z., Thibault-Starzyk F., Czyzniewska J. & Kaučič V. e., Large-Pore FAPO-36: Synthesis and Characterization, *Chemistry of Materials* 15 (2003) 3643-3649.

Rochet A., Moizan V., Pichon C., Diehl F., Berliet A. & Briois V., In situ and operando structural characterisation of a Fischer–Tropsch supported cobalt catalyst, *Catalysis Today* 171 (2011) 186-191.

Roe A. L., Schneider D. J., Mayer R. J., Pyrz J. W., Widom J. & Que L., X-ray absorption spectroscopy of iron-tyrosinate proteins, *Journal of the American Chemical Society* 106 (1984) 1676-1681.

Rossano S., Balan E., Morin G., Bauer J. P., Calas G. & Brouder C., ^{57}Fe Mössbauer spectroscopy of tektites, *Physics and Chemistry of Minerals* 26 (1999) 530-538.

Royer S. & Duprez D., Catalytic Oxidation of Carbon Monoxide over Transition Metal Oxides, *ChemCatChem* 3 (2011) 24-65.

Rozita Y., Brydson R. & Scott A. (2010). *Journal of Physics Conference Series*, p. 2096.

Ruggeri M. P., Grossale A., Nova I., Tronconi E., Jirglova H. & Sobalik Z., FTIR in situ mechanistic study of the NH3NO/NO2 "Fast SCR" reaction over a commercial Fe-ZSM-5 catalyst, *Catalysis Today* 184 (2012) 107-114.

Santhosh Kumar M., Schwidder M., Grünert W., Bentrup U. & Brückner A., Selective reduction of NO with Fe-ZSM-5 catalysts of low Fe content: Part II. Assessing the function of different Fe sites by spectroscopic in situ studies, *Journal of Catalysis* 239 (2006) 173-186.

Sayers D. E., Stern E. A. & Lytle F. W., New Technique for Investigating Noncrystalline Structures: Fourier Analysis of the Extended X-Ray Absorption Fine Structure, *Physical Review Letters* 27 (1971) 1204-1207.

Schlögl R., Catalytic Synthesis of Ammonia—A "Never-Ending Story"?, *Angewandte Chemie International Edition* 42 (2003) 2004-2008.

Schmid R., Wilke M., Oberhänsli R., Janssens K., Falkenberg G., Franz L. & Gaab A., Micro-XANES determination of ferric iron and its application in thermobarometry, *Lithos* 70 (2003) 381-392.

Schneider S., Bazin D., Dubuisson J. M., Ribbens M., Sonneville H., Meunier G., Garin F., Maire G. & Dexpert H., Development of a reactive cell for Exafs in~situ studies of automotive postcombustion catalytic converters, *Journal of X-Ray Science and Technology* 8 (1998) 221-230.

Schrader G. L. & Cheng C. P., Laser Raman spectroscopy of cobalt-molybdenum/.gamma.-aluminum oxide catalysts. Characterization using pyridine adsorption, *The Journal of Physical Chemistry* 87 (1983) 3675-3681.

Schwidder M., Kumar M. S., Klementiev K., Pohl M. M., Brückner A. & Grünert W., Selective reduction of NO with Fe-ZSM-5 catalysts of low Fe content: I. Relations between active site structure and catalytic performance, *Journal of Catalysis* 231 (2005) 314-330.

Shelef M., Selective Catalytic Reduction of NOx with N-Free Reductants, *Chemical Reviews* 95 (1995) 209-225.

Simonsen S. B., Chakraborty D., Chorkendorff I. & Dahl S., Alloyed Ni-Fe nanoparticles as catalysts for NH_3 decomposition, *Applied Catalysis A: General* 447–448 (2012) 22-31.

Sun M., Nelson A. E. & Adjaye J., Examination of Spinel and Nonspinel Structural Models for γ-Al_2O_3 by DFT and Rietveld Refinement Simulations, *The Journal of Physical Chemistry B* 110 (2006) 2310-2317.

te Velde G. & Baerends E. J., Precise density-functional method for periodic structures, *Physical Review B* 44 (1991) 7888-7903.

Teo B.-K. (1981). *EXAFS Spectroscopy,* edited by B. K. Teo & D. C. Joy, pp. 13-58: Springer US.

Tepluchin M., Casapu M., Boubnov A., Lichtenberg H., Wang D., Kureti S. & Grunwaldt J.-D., Fe and Mn-Based Catalysts Supported on γ-Al_2O_3 for CO Oxidation under O_2-Rich Conditions, *ChemCatChem* 6 (2014) 1763-1773.

Thompson P., Cox D. E. & Hastings J. B., Rietveld refinement of Scherrer synchrotron X-ray data from Al_2O_3, *Journal of Applied Crystallography* 20 (1987) 79-83.

Topsøe H., Developments in operando studies and in situ characterization of heterogeneous catalysts, *Journal of Catalysis* 216 (2003) 155-164.

van Beek W., Safonova O. V., Wiker G. & Emerich H., SNBL, a dedicated beamline for combined in situ X-ray diffraction, X-ray absorption and Raman scattering experiments, *Phase Transitions* 84 (2011) 726-732.

van Lenthe E. & Baerends E. J., Optimized Slater-type basis sets for the elements 1–118, *Journal of Computational Chemistry* 24 (2003) 1142-1156.

van Lenthe E., Baerends E. J. & Snijders J. G., Relativistic total energy using regular approximations, *The Journal of Chemical Physics* 101 (1994) 9783-9792.

Verwey E. J. W., Electrolytic conduction of a solid insulator at high fields The formation of the anodic oxide film on aluminium, *Physica* 2 (1935) 1059-1063.

Wagloehner S., Reichert D., Leon-Sorzano D., Balle P., Geiger B. & Kureti S., Kinetic modeling of the oxidation of CO on Fe2O3 catalyst in excess of O2, *Journal of Catalysis* 260 (2008) 305-314.

Waychunas G., Apted M. & Brown G., Jr., X-ray K-edge absorption spectra of Fe minerals and model compounds: Near-edge structure, *Physics and Chemistry of Minerals* 10 (1983) 1-9.

Webb S. M., SIXpack: a graphical user interface for XAS analysis using IFEFFIT, *Physica Scripta* 2005 (2005) 1011-1014.

Weckhuysen B. M., Determining the active site in a catalytic process: Operando spectroscopy is more than a buzzword, *Physical Chemistry Chemical Physics* 5 (2003) 4351-4360.

Weckhuysen B. M. (2004). *In-situ spectroscopy of catalysts*. American Scientific Publishers Stevenson Ranch, CA.

Westre T. E., Kennepohl P., DeWitt J. G., Hedman B., Hodgson K. O. & Solomon E. I., A Multiplet Analysis of Fe K-Edge 1s → 3d Pre-Edge Features of Iron Complexes, *Journal of the American Chemical Society* 119 (1997) 6297-6314.

Wilke M., Farges F., Petit P. E., Brown G. E. & Martin F., Oxidation state and coordination of Fe in minerals: An Fe K-XANES spectroscopic study, *American Mineralogist* 86 (2001) 714-730.

Wilke M., Hahn O., Woodland A. B. & Rickers K., The oxidation state of iron determined by Fe K-edge XANES-application to iron gall ink in historical manuscripts, *Journal of Analytical Atomic Spectrometry* 24 (2009) 1364-1372.

Wilke M., Partzsch G. M., Bernhardt R. & Lattard D., Determination of the iron oxidation state in basaltic glasses using XANES at the K-edge, *Chemical Geology* 220 (2005) 143-161.

Wong S. T., Lee J. F., Cheng S. F. & Mou C. Y., In-situ study of MCM-41-supported iron oxide catalysts by XANES and EXAFS, *Applied Catalysis A: General* 198 (2000) 115-126.

Worch D., Suprun W. & Gläser R., Fe- and Cu-oxides supported on γ-Al2O3 as catalysts for the selective catalytic reduction of NO with ethanol. Part I: catalyst preparation, characterization, and activity, *Chemical Papers* 68 (2014) 1228-1239.

Wu Q., Chiarello G. L., Boubnov A., Christensen J. M., Temel B., Jensen A. D. & Grunwaldt J.-D., Formation of bulk and supported molybdenum carbides studied by simultaneous in situ XAS and XRD, (in preparation).

Wu Q., Duchstein L. D. L., Chiarello G. L., Christensen J. M., Damsgaard C. D., Elkjær C. F., Wagner J. B., Temel B., Grunwaldt J.-D. & Jensen A. D., In Situ Observation of Cu–Ni Alloy Nanoparticle Formation by X-Ray Diffraction, X-Ray Absorption Spectroscopy, and Transmission Electron Microscopy: Influence of Cu/Ni Ratio, *ChemCatChem* 6 (2014) 301-310.

Yamamoto T., Assignment of pre-edge peaks in K-edge x-ray absorption spectra of 3d transition metal compounds: electric dipole or quadrupole?, *X-Ray Spectrometry* 37 (2008) 572-584.

Publications

A. Boubnov, S. Dahl, E. Johnson, A. P. Molina, S. B. Simonsen, F. M. Cano, S. Helveg, L. J. Lemus-Yegres and J.-D. Grunwaldt, *Structure–activity relationships of Pt/Al_2O_3 catalysts for CO and NO oxidation at diesel exhaust conditions*, Applied Catalysis B: Environmental 126 (2012) 315-325.

A. Boubnov, A. Gänzler, S. Conrad, M. Casapu and J.-D. Grunwaldt, *Oscillatory CO Oxidation Over Pt/Al_2O_3 Catalysts Studied by In situ XAS and DRIFTS*, Topics in Catalysis 56 (2013) 333-338. Part of Chapter 2 in this thesis.

A. Boubnov, H. Lichtenberg, S. Mangold and J.-D. Grunwaldt, *Structure and reducibility of a Fe/Al_2O_3 catalyst for selective catalytic reduction studied by Fe K-edge XAFS spectroscopy*, Journal of Physics: Conference Series 430 (2013) 012054. Part of Chapter 3 in this thesis.

M. Tepluchin, M. Casapu, A. Boubnov, H. Lichtenberg, D. Wang, S. Kureti and J.-D. Grunwaldt, *Fe and Mn-Based Catalysts Supported on γ-Al_2O_3 for CO Oxidation under O_2-Rich Conditions*, ChemCatChem 6 (2014) 1763-1773.

A. Boubnov, H. W. P. Carvalho, D. E. Doronkin, T. Günter, E. Gallo, A. J. Atkins, C. R. Jacob and J.-D. Grunwaldt, *Selective catalytic reduction of NO over Fe-ZSM-5: Mechanistic insights by operando HERFD-XANES and valence-to-core XES spectroscopy*, Journal of the American Chemical Society 136 (37) (2014) 13006-13015. Part of Chapter 4 in this thesis.

A. Boubnov, H. Lichtenberg, S. Mangold and J.-D. Grunwaldt, *Identification of iron oxidation state and coordination geometry in iron oxide- and zeolite-based catalysts using pre-edge XAS analysis*, Journal of Synchrotron Radiation 22 (2015) 410-426. Part of Chapter 4 in this thesis.

A. Gänzler, M. Casapu, A. Boubnov, O. Müller, S. Conrad, H- Lichtenberg, R. Frahm and J.-D. Grunwaldt, *Operando spatially and time-resolved X-ray absorption spectroscopy and infrared thermography during oscillatory CO Oxidation*, Journal of Catalysis (accepted). Part of Chapter 2 in this thesis.

A. Boubnov, A. Pacher, M. Kundrat, S. Mangold, B. Reznik, C. Jacob, S. Kureti, J.-D. Grunwaldt, *Towards advanced structural analysis of iron oxide clusters on the surface of γ-Al_2O_3 using EXAFS* (in preparation). Part of Chapter 3 in this thesis.

Curriculum Vitae

Name: Alexey Boubnov

Born 8th October 1984 in Moscow

Danish citizen

Married, two children

Education

1990 – 1999	Primary and secondary school in Copenhagen
1999 – 2003	High school in Copenhagen
09/2003 – 10/2007	Bachelor studies in Nanotechnology at the University of Copenhagen
10/2006 – 06/2007	Two semesters at the Swiss Federal Institute of Technology in Zurich
10/2007 – 09/2009	Master studies in Nanotechnology at the University of Copenhagen
02/2010 – 10/2014	Ph.D. thesis under the supervision of Prof. Dr. Jan-Dierk Grunwaldt at the Institute for Chemical Technology and Polymer Chemistry, Karlsruhe Institute of Technology (KIT)